UNIVERSITÄT BONN
Physikalisches Institut

Measurement of beauty and charm photoproduction using inclusive secondary vertexing with the ZEUS detector at HERA

by

Verena Ellen Schönberg

Photoproduction of heavy quarks in events with two jets has been measured with the ZEUS detector at HERA using data recorded in the years 2006–2007 corresponding to an integrated luminosity of $128\,\mathrm{pb}^{-1}$. The beauty and charm content was extracted using the decay-length significance of the b and c hadrons and the invariant mass of the decay vertices. Differential cross sections as a function of P_T^{Jet} and η^{Jet} were compared with the PYTHIA leading order plus parton shower Monte Carlo and QCD predictions calculated at next-to-leading order. In order to study the theoretical description of higher-order effects correlations between the two highest energy jets were also investigated.

Postal address:
Nußallee 12
D-53115 Bonn
Germany

BONN-IR-2010-05
Bonn University
April 2010
ISSN-0172-8741

UNIVERSITÄT BONN
Physikalisches Institut

Measurement of beauty and charm photoproduction using inclusive secondary vertexing with the ZEUS detector at HERA

by
Verena Ellen Schönberg

Dieser Forschungsbericht wurde als Dissertation von der Mathematisch-Naturwissenschaftlichen Fakultät der Universität Bonn angenommen und ist auf dem Hochschulschriftenserver der ULB Bonn http://hss.ulb.uni-bonn.de/diss_online elektronisch publiziert.

Referent:	Prof. Dr. Ian C. Brock
Korreferent:	Prof. Dr. Norbert Wermes

Angenommen am:	21.12.2009
Tag der Promotion:	05.03.2010

Contents

Chapter 1

Introduction

The Standard Model of particle physics comprises all known constituents of matter and the fundamental forces acting between them. In its basic principles it has been an established model since the 1970s and could be confirmed by a vast amount of measurements. One component of the Standard Model that is of particular interest for this thesis is Quantum Chromodynamics (QCD), the theory of the strong interactions. Theoretical predictions for QCD, which are needed for the comparison with the experimental results, are difficult to obtain, as QCD scattering processes cannot be computed exactly and must be approximated via perturbative calculations. Furthermore, the parton density functions (PDFs), which represent the probabilities for finding a certain parton in the proton or photon that may participate in the hard scatter, are not calculable in perturbative QCD and can only be determined in experiments.

An environment where both aspects could be studied was provided by the HERA accelerator at the Deutsches Elektronen-Synchrotron (DESY) in Hamburg. At HERA electrons or positrons and protons were accelerated and brought to collision, such that the electrons (positrons) were scattered off the constituents of the protons. Thus the scattered lepton as well as the other particles produced in the hard scatter could provide information about the internal structure of the proton. This information can be extracted by means of PDFs, the determination of which was one of the major aspects of the HERA physics programme.

The intention of the analysis presented in this thesis was in particular the test of perturbative Quantum Chromodynamics (pQCD) via the measurement of beauty and charm production cross sections using data taken with the ZEUS detector. Such measurements are particularly suitable for probing pQCD, since the high quark masses provide sufficiently hard scales to make perturbation theory applicable. Several measurements of beauty and

charm production at HERA were performed in the past; though a general agreement of the pQCD predictions with the experimental results was found, a trend was observed in the beauty measurements for the data to exceed the predictions. Thus one of the main aims of this analysis was to improve the precision of the measurement in order to draw more substantive conclusions about the description of the data by the theoretical predictions.

For heavy quark production measurements made with the ZEUS detector so far only semileptonic b and c decays or selected D meson decay channels had been considered. The analysis presented here was not restricted to a specific decay channel, but was kept fully inclusive which lead to a substantial gain in statistics. The extraction of the b and c signals was done using lifetime tagging techniques; for this purpose new methods that were not exclusively designed for the identification of single particles needed to be developed. The fine-tuning of these methods was challenging, as a precise tracking and vertexing as well as a good understanding of the detector and an adequate simulation were indispensable; thus the progress of this analysis was strongly correlated with improvements in the track reconstruction and detector simulation.

This thesis is organised as follows: in Chapter 2 an overview of the HERA accelerator complex and the ZEUS detector is given; the detector components that are particularly important for this analysis are described in more detail. The basic theoretical aspects of heavy quark production and the experimental context focusing on HERA are the subject of Chapter 3. In Chapter 4 the leading-order and next-to-leading-order theoretical predictions are presented. Since a great part of the work on this analysis was associated with improving and developing specific reconstruction techniques, Chapter 5 is dedicated to track reconstruction and vertex finding at ZEUS. In Chapter 6 the selection of data samples and events is described; the heavy flavour tagging method used and the extraction of the signals are covered in Chapter 7. The measured cross sections in the central region of the detector and the comparison with theoretical predictions are discussed in Chapter 8; Chapter 9 then deals with the corresponding systematic uncertainties. In Chapter 10 an outlook is given in terms of the extension of the kinematic range of the analysis to the forward region of the detector. Additional studies analysing dijet correlations are addressed in Chapter 11. Finally, Chapter 12 summarises the essential aspects and results of this thesis.

Chapter 2

HERA and ZEUS

In this chapter I will give an overview of the HERA accelerator complex and the ZEUS detector. Furthermore the detector components which are the most relevant ones for this analysis will be described in more detail.

2.1 HERA

The HERA accelerator (**H**adron-**E**lektron-**R**ing**a**nlage) was located at the Deutsches Elektronen-Synchrotron (DESY) in Hamburg. High energetic collisions of leptons and protons were studied at various experiments. The two separate rings for the electrons (or positrons[1]) and the protons were installed in a tunnel of 6 km circumference 10–25 m below ground. The four main experiments, at which the particle collisions were detected and analysed, were located in experimental halls around the HERA ring (see Fig. 2.1). Electrons and protons were accelerated in several pre-accelerators (LINAC, DESY, PETRA, see Fig. 2.2) and finally injected into HERA in so-called bunches. Each bunch contained about 10^{10} particles. Some of the bunches were left empty and could be used for systematic studies. Inside HERA electrons and protons were accelerated from 12 GeV and 40 GeV to their final energies of 27.5 GeV and 920 GeV, respectively.

At a centre-of-mass energy of $\sqrt{s} \approx 318\,\text{GeV}$ the electron and the proton beam were brought to collision each 96 ns at the two interaction points, where the particle detectors H1 (north hall) and ZEUS (south hall) were located. The HERMES detector (east hall) was a so-called beam-target-experiment and used only the electron beam, which was directed at a polarised target. The data collected in this way were exploited to investigate the spin struc-

[1] In the following, the term electrons will be used for electrons and positrons unless stated otherwise.

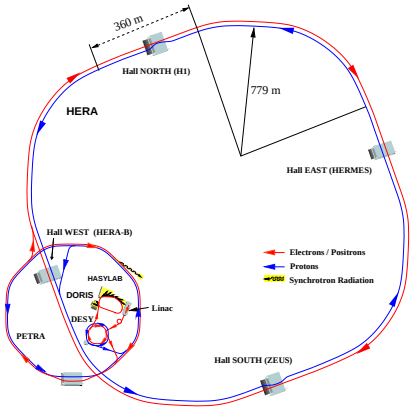

Figure 2.1: The HERA ring including its pre-accelerators.

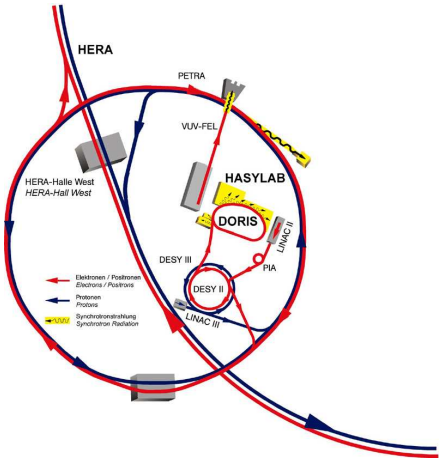

Figure 2.2: The system of pre-accelerators in detail.

ture of the nucleons. The fourth detector, HERA-B, at the west side of the HERA ring was a beam-target-experiment as well and used only the proton beam. The initial objective of the HERA-B physics programme was the measurement of production and decay properties of b hadrons with an emphasis on CP violation and constraining the angles of the unitarity triangle. More information on all experiments can be found in [1–4].

The data-taking at HERA is divided into two periods, HERA I from 1996–2000 and HERA II from 2003–2007. During the shutdown from 2000 to 2002 several machine and detector upgrades were undertaken. One of the main aims of the HERA upgrade was the use of polarised electron beams, which opened up a new sector in the physics programme of both collision experiments. Therefore spin rotator pairs were installed in front of the interaction regions of H1 and ZEUS in order to flip the spins of the particles into the direction of the beam and back on the other side of the detectors. Furthermore the integrated luminosity could be increased in the course of the HERA upgrade. The upgrades of the ZEUS detector will be described in Section 2.3. During the last few months of data-taking the proton energy was decreased to $E_p = 575\,\text{GeV}$ and $E_p = 460\,\text{GeV}$. The three different centre-of-mass energies of 318 GeV, 251 GeV and 225 GeV were used for structure function measurements [5].

2.2 Luminosity

The luminosity is a crucial parameter at particle accelerators. It is defined as the number of particles which can collide per unit time and unit area. At HERA it can be written as follows:

$$\mathcal{L} = \frac{N_e \cdot N_p \cdot N_b \cdot f}{4\pi \cdot \sigma_x \sigma_y}$$

N_e and N_p denote the numbers of electrons and protons per bunch, N_b the number of bunches, f the bunch-crossing frequency and σ_x and σ_y are the standard deviations of the beam cross section at the interaction point.

A high luminosity is essential for achieving high statistics and to be able to also detect and analyse rare processes. The HERA luminosity is measured indirectly by two lead-scintillator calorimeters, which detect photons from the Bethe-Heitler process $ep \to e'p\gamma$. The luminosity can be calculated from the number of detected photons and the cross section, which is well-known for this process. Figure 2.3 displays the integrated HERA luminosity that has been achieved throughout the whole data-taking from 1996 to 2007 as well as the ZEUS luminosity during the HERA II data-taking. The increase in the integrated luminosity that could be achieved through the HERA upgrade is clearly visible; during the HERA II data-taking period HERA delivered roughly three times more luminosity than for HERA I. Data corresponding to $\mathcal{L} \approx 0.5\,\mathrm{fb}^{-1}$ in total were recorded by each collision experiment.

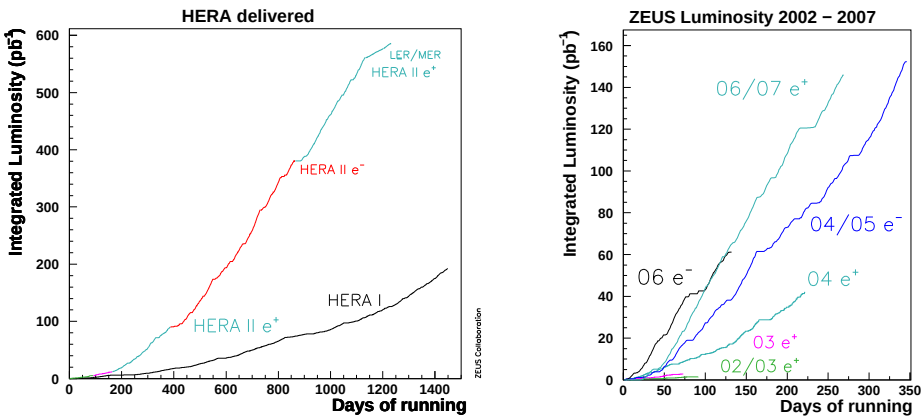

Figure 2.3: HERA delivered luminosity for the whole data-taking (left) and ZEUS gated luminosity for the HERA II data-taking periods (right).

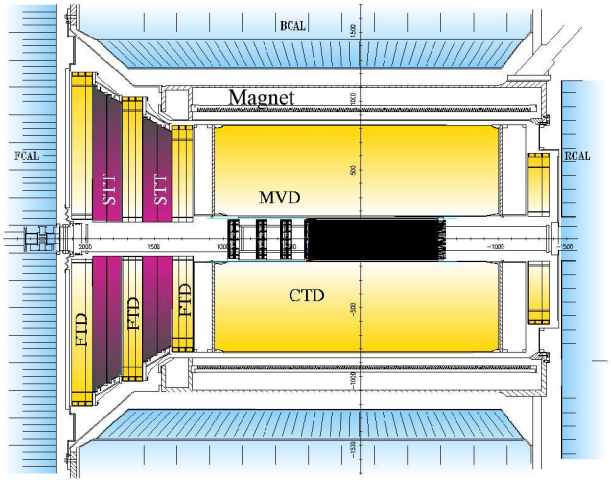

Figure 2.4: The ZEUS inner detector. It consists of the microvertex detector (MVD), the central tracking detector (CTD) and the forward tracking detectors FTD 1–3 and STT.

2.3 ZEUS detector

2.3.1 Overview

Like most of the modern detectors in particle physics the ZEUS detector was constructed onion-like and covered almost the complete 4π range around the interaction region. Such a constellation allows a precise measurement of the position, momentum and energy of the detected final-state particles. A detailed description of the ZEUS detector can be found in [1].

Figure 2.4 shows the inner part of the ZEUS detector. The microvertex detector (MVD) was installed closest to the collision region in order to reconstruct secondary vertices using precisely measured tracks close to the primary vertex. It also supported the track measurement of the central tracking detector (CTD), which surrounded the MVD. A superconducting solenoid around the drift chamber provided a, to a large extent, homogeneous magnetic field of 1.43 T in the proton direction. In forward (i.e. proton) direction followed the forward detector (FDET), which consisted of three planar drift chambers FTD 1–3 as well as the two modules of the straw-tube tracker (STT). The rear tracking detector (RTD) followed in rear direction. It was identical in construction to the FTDs and was therefore considered as part of the forward detector as well.

Around the inner part of the ZEUS detector the uranium scintillator

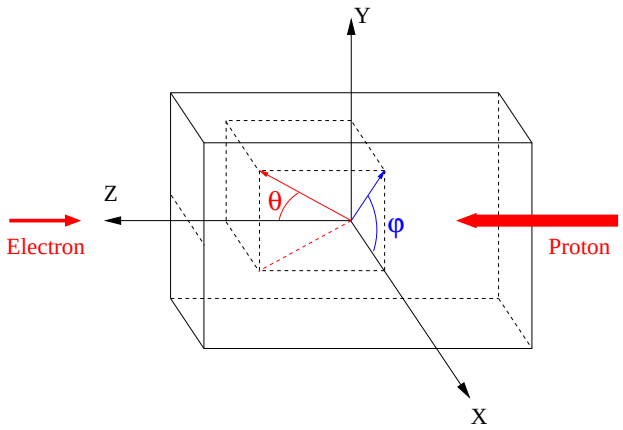

Figure 2.5: The ZEUS coordinate system.

calorimeter was located, which measured the energy depositions of the penetrating particles. It was divided into three geometrical parts; the forward calorimeter (FCAL), the central part (barrel calorimeter, BCAL) and the rear calorimeter (RCAL). Each of the three parts was subdivided into an inner electromagnetic section (EMC) and in the case of the RCAL one, otherwise two outer hadronic sections (HAC). If a particle deposited its whole energy in the electromagnetic section, it could be identified as an electron or photon with high probability; particles which reached or completely passed the hadronic section had to be identified with the help of additional criteria or other detector components. High-energetic muons for instance lost energy, but completely crossed the calorimeter and were detected and identified in the muon chambers (F/BMUON), which surrounded the whole detector. All types of particles were decelerated within the calorimeter and deposited at least parts of their energy there; only neutrinos remained undetected because of their weak interaction with matter.

Furthermore the asymmetric design was a noteworthy characteristic of the detector. It accounted for the difference of the beam energies and the resulting boost of the centre of mass of $\beta \approx 0.93$ in proton direction.

The origin of the ZEUS coordinate system, which is depicted in Figure 2.5, is the geometrical centre of the detector. Note that during the whole HERA II data-taking period the main interaction point was shifted by $\approx 1.3\,\text{cm}$ in X and by $\approx 0.2\,\text{cm}$ in Y with respect to $(0, 0, 0)$. The Z-axis points in the forward direction, i.e. the flight direction of the proton, the X-axis to the centre of the HERA ring. The Y-axis is perpendicular to the X and Z directions. The polar angle θ is defined with respect to the Z-axis, the azimuthal angle ϕ with respect to the X-axis. It is furthermore important

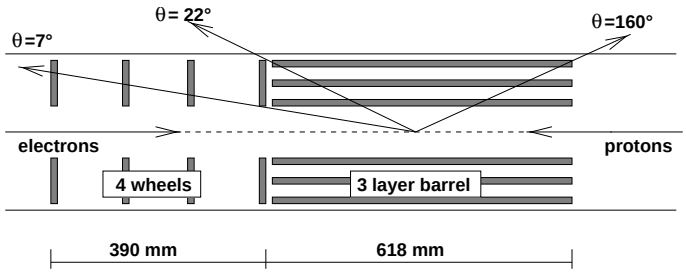

Figure 2.6: Side-view of the microvertex detector.

to introduce the pseudorapidity, η, which is defined as

$$\eta = -\ln(\tan\frac{\theta}{2})$$

In contrast to θ itself it is Lorentz-invariant and therefore usually the preferred observable.

In the following sections the detector components which are of considerable interest for this analysis will be described in detail. Furthermore the track reconstruction, the ZEUS trigger chain and the basic concepts of the detector simulation will be introduced.

2.3.2 Microvertex detector (MVD)

The microvertex detector (MVD, [6]) was one of the two components that were installed in the ZEUS detector during the shutdown in 2000–2002. Its main purpose was the improvement of the vertex finding and the track reconstruction in the immediate vicinity of the interaction point (see also Section 5.1).

The MVD was a silicon-strip detector and was subdivided into a barrel (BMVD) and a forward (FMVD) part. A schematic overview of the MVD is shown in Fig. 2.6.

The BMVD consisted of 30 ladders, which were placed cylindrically around the beampipe in three layers. The innermost layer could not surround the beampipe completely because of its elliptic shape (see Fig. 2.7). Each ladder consisted of five modules, which themselves were composed of two half-modules. Each half-module was made of two silicon sensors. The strips of these sensors were perpendicular to each other; one sensor measured the position in Z direction, the other one provided the $r-\phi$ information. Thus a track could at most produce two hits per layer. There were 512 strips per

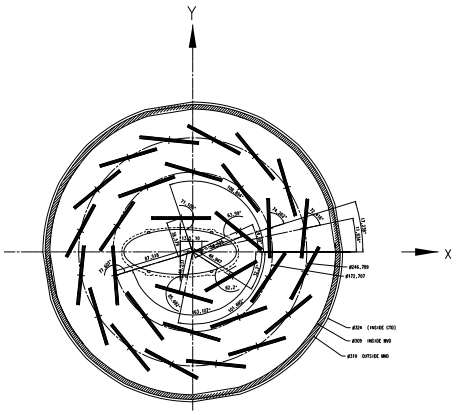

Figure 2.7: The barrel MVD.

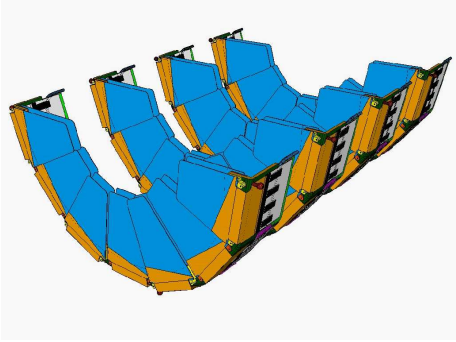

Figure 2.8: Lower half of the forward MVD.

sensor that were read out with a distance (the so-called *pitch*) of 120 μm between them.

The FMVD consisted of four wheels, which were mounted perpendicular to the beampipe. They were composed of 14 sectors; each sector contained an inner and an outer sensor, which were mounted back-to-back. In contrast to the BMVD sensors the FMVD sensors were wedge-shaped and the angle between an inner and an outer sensor was 180°/14. Some of the 112 FMVD sensors were shortened in order to leave enough space for the beampipe. The composition of the FMVD wheels is also shown in Fig. 2.8.

The MVD was able to detect tracks with polar angles of 7–160 °. With its design resolution of $\approx 10\,\mu$m for track and vertex finding it was the crucial component for this analysis.

2.3.3 Central tracking detector (CTD)

The purpose of the central tracking detector (CTD) was the measurement of tracks and to provide information about their charges, momenta and creation points. It consisted of 72 cylindric layers, which were grouped in 9 superlayers. Each superlayer was divided into 32–96 cells with superlayer 1 having 32 cells and each further superlayer having 8 cells more than the previous one; each cell contained 8 signal wires. In the odd-numbered superlayers the wires ran parallel to the Z-axis (axial layers), in the even-numbered ones with an alternating angle of 5° with respect to the Z-axis (stereo layers). The orientation of the wires was chosen in such a way to allow the determination

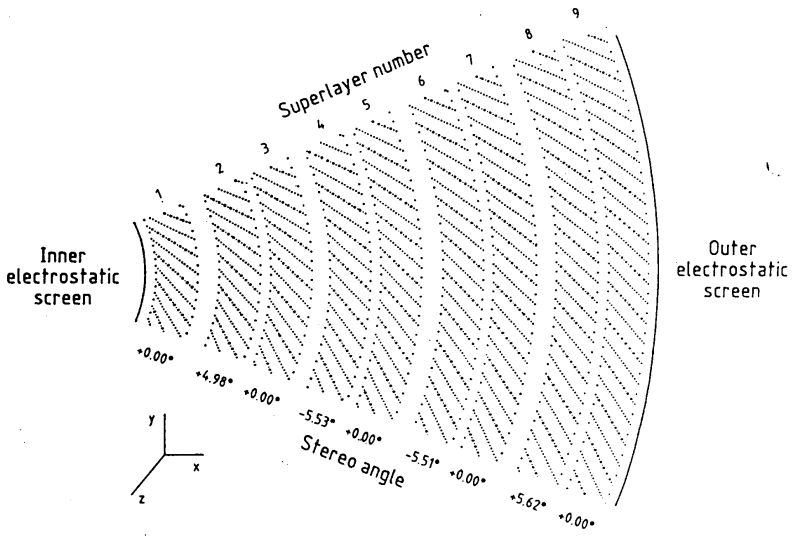

Figure 2.9: An octant of the central tracking detector (CTD) in the X-Y view.

of the Z position of a signal. A second opportunity was the simultaneous readout on both sides of all 8 signal wires in superlayer 1 and of 4 wires in superlayers 3 and 5 (Z-by-timing method). As chamber gas $Ar/C_2H_6/CO_2$ was used. Figure 2.9 shows an octant of the CTD in the X-Y view.

The endplates of the CTD at $Z = -100\,\text{cm}$ and $Z = +105\,\text{cm}$, between which the signal wires were spanned, was made of aluminium and has a thickness of 2 cm. This could lead to the production of particle showers (especially by electrons) and many particles in forward direction. In order to be able to cope with this in the track reconstruction, a good resolution and a reliable detection were indispensable in this part of the detector. The CTD covered the angular range of $15\,^\circ < \theta < 165\,^\circ$. The track reconstruction was supposed to be reliable if a particle had crossed 3 superlayers, reducing the angular range to $20\,^\circ < \theta < 160\,^\circ$. The spatial resolutions achieved were $\approx 300\,\mu$m in $r - \phi$ and 1–5 mm in Z.

2.3.4 Forward tracking detector (FDET)

Due to the asymmetry of the beam energies and the decreasing track reconstruction efficiency at small angles of the CTD, additional drift chambers were installed in the forward region of the ZEUS detector. As described before, the forward detector (FDET) consisted of the three FTDs and the two STT modules in forward direction and the RTD in rear direction.

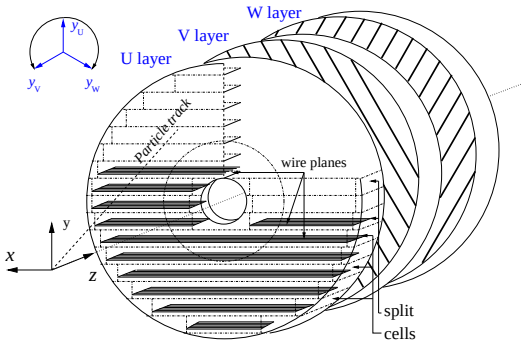

Figure 2.10: Composition of an FTD chamber.

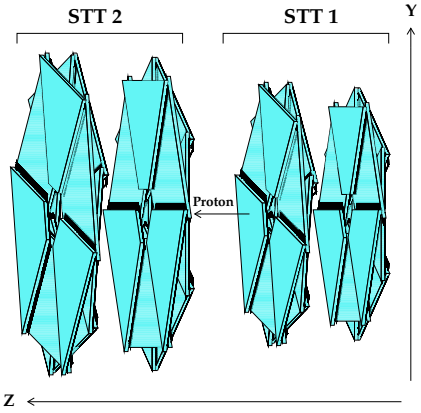

Figure 2.11: Composition of the STT and subdivision into modules and superlayers.

The FTD and RTD drift chambers supported the track reconstruction at very small ($7^\circ < \theta < 28^\circ$) and very large angles ($160^\circ < \theta < 170^\circ$), respectively. All four chambers were identical in construction; they had a circular shape, leaving a hole for the beampipe in the middle (Fig. 2.10). They only differed in their diameter, which increased in the Z direction (i.e. from FTD1 to FTD3) proportionally to the distance from the nominal interaction point. This ensured equal acceptance ranges for all chambers. Each chamber was subdivided into three layers (U,V,W), which were rotated by 120° with respect to each other and themselves consisted of cells, in which the signal wires made of gold-plated tungsten were spanned. As drift gas Ar/C_2H_6 was used. With the given experimental setup spatial resolutions of $250\,\mu$m could be achieved.

In contrast to the FTDs and the RTD, which had been a part of the ZEUS detector from the beginning, the straw tube tracker (STT) was only installed during the upgrade in 2000, replacing the transition radiation detector (TRD). The STT was subdivided into two modules (Fig. 2.11), which were located between the FTDs. They were able to detect tracks in the angular range of $6^\circ < \theta < 25^\circ$. Each module consisted of 24 sectors, which were grouped into four superlayers containing six sectors each. Three sectors at a time were installed at exactly the same Z position, forming a layer. A superlayer, i.e. the combination of two layers that were rotated by 60° with respect to each other, covered the whole azimuthal angle. The four STT superlayers were again rotated with respect to each other, the angular difference between superlayers 1 and 2 as well as 3 and 4 was 30°, between superlayers 2 and 3

only 15 °. A single sector consisted of three layers of so-called straws with a diameter of 7.5 mm. Each straw represented an independent drift chamber with a cover made of capton foil coated with aluminium and carbon serving as the cathode and a signal wire as anode in the middle. When a charged particle traversed a straw, the gas inside (Ar/CO_2) was ionised and the electrons drifting to the anode produced a signal, which is often also called a *hit*. Since the positions of the wires were known, these hits gave information on the course of the particle's track through the detector. Just like the FTDs, the two STT modules were supposed to have equal acceptance ranges as well; therefore the sectors in STT2 were larger than those in STT1, containing 88 straws per layer instead of 64. In total the STT consisted of 10944 straws.

Since the solenoid only surrounded the CTD, the magnetic field was inhomogeneous inside the forward detector. But highly energetic particles, which were usually mainly of interest, went parallel to the magnetic field direction and therefore their tracks could be approximated by straight lines.

More detailed descriptions of the forward tracking detector can be found in [7–9].

2.3.5 Trigger system

The ZEUS trigger system is displayed schematically in Fig. 2.12. Since computing power and storage space of each computing system are limited, it is impossible to store the complete amount of incoming data from all the detector components. Therefore a three-level trigger system was developed in order to select interesting events and substantially reduce the initial amount of data. Its purpose was to discard non-ep-collision events and select interesting physics events. On the first, hardware-based level (First Level Trigger, FLT), all information about an event were stored temporarily in pipelines, until it was accepted or discarded by the local FLTs of the different detector components and eventually combined by the global trigger (GFLT). Already at this stage, the event rate was reduced from initially 10.4 MHz to far below 1 kHz.

The second, software-based level (Second Level Trigger, SLT) made use of the time information of the different components and carried out a first, rough track reconstruction. For instance, on the basis of coincidence measurements beam-gas events were excluded. The event rate now amounted to approximately 50–100 Hz.

In case an event had not been discarded by the first two trigger levels, the different components transmitted their data to the so-called *event builder*, which collected all information and performed a rough reconstruction of the event. Afterwards the third trigger level (Third Level Trigger, TLT) cut on

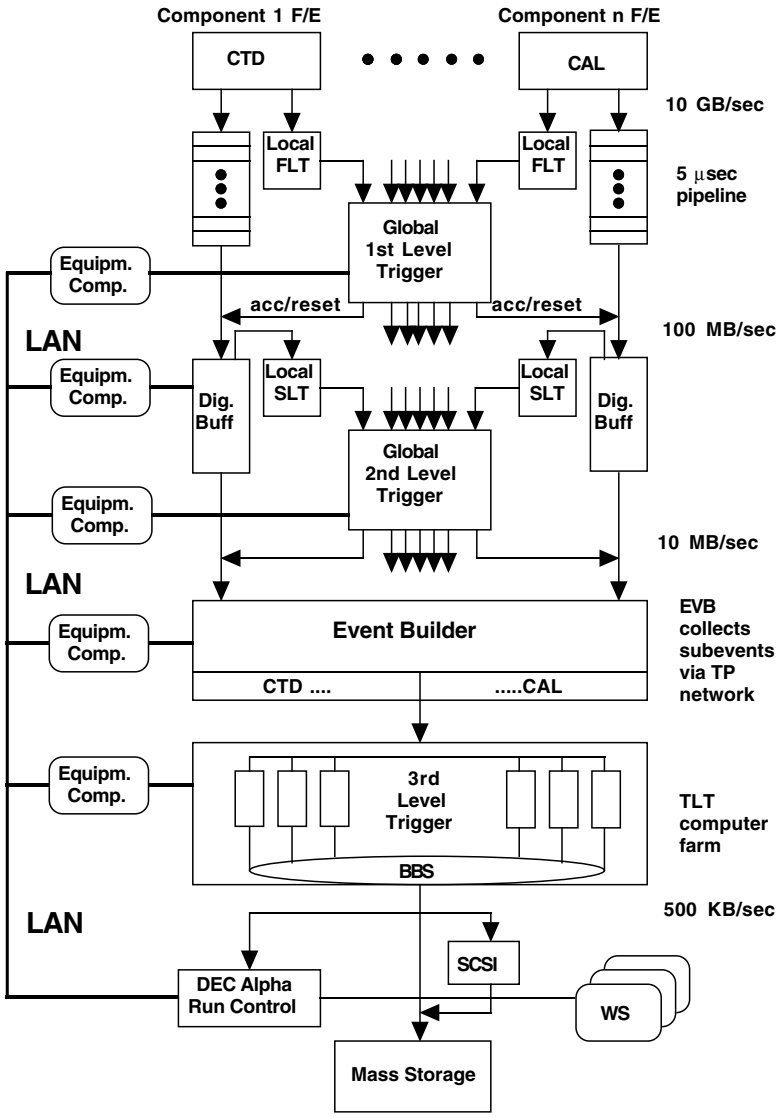

Figure 2.12: The ZEUS trigger system.

certain input variables obtained from the reconstruction and finally decided, if the event was stored for further analysis. After having passed the TLT the event rate was of the order of just a few Hz.

The data of the selected events were stored in ADAMO[2] tables, which could be processed by the offline reconstruction programme ZEPHYR (cf Section 4.1.2).

In the context of this work the trigger system can only be roughly sketched. Several changes, improvements and further developments were undertaken; for example, a Global Tracking Trigger (GTT) was installed in the system [11].

On analysis level various TLT triggers can be tested in order to select events of a certain type depending on the cuts implemented in the trigger in question; for the analysis presented in this thesis a trigger for dijet photoproduction events was used (cf Chapter 6).

[2]ADAMO = **A**leph **Da**ta **Mo**del [10]

Chapter 3

Heavy quark production

In Section 3.1 I will briefly summarise the Standard Model of particle physics. The key aspects concerning the physics of heavy quarks that are most relevant for this thesis are addressed in Section 3.2. Section 3.3 comprises the basics of *ep*-scattering with a focus on heavy flavour photoproduction. Finally, after a short review on the discovery of the heavy quarks, some of the experimental results on beauty production at HERA that have been achieved so far and the relevance of such measurements for future experiments at the Large Hadron Collider (LHC) are discussed in Section 3.5.

3.1 Standard Model

The Standard Model of particle physics comprises all elementary particles which matter is made of and their interactions. It is summarised in Table 3.1, which contains all elementary particles and forces that are known today. There are four fundamental forces (electromagnetic, weak and strong force and gravitation) which are mediated by so-called *gauge bosons*. The electromagnetic force acts on charged particles and is mediated by the photon. Electromagnetic processes are based on the theory of *Quantum Electrodynamics* (QED). The gluon is the mediator of the strong force, which is described by *Quantum Chromodynamics* (QCD), the theory of strong interactions. $W^{\pm}$ and Z are the mediators of the weak force. Gravitation, the fourth force, is supposed to be mediated by the so-called *graviton*. In contrast to the other bosons, which all carry spin 1, it is assumed to be a spin-2 particle; so far it has not been discovered. The Higgs boson, which is supposed to be responsible for the origin of mass [12, 13], has also not been observed yet. All other elementary particles are so-called *fermions* and carry spin $\frac{1}{2}$. The fermions can be divided into leptons (electron, muon, tau and their antiparticles as

		Generation			Electric charge
		1st	2nd	3rd	(e)
Fermions	Leptons	$e^{\pm}$	$\mu^{\pm}$	$\tau^{\pm}$	± 1
		$\nu_e/\bar{\nu}_e$	$\nu_\mu/\bar{\nu}_\mu$	$\nu_\tau/\bar{\nu}_\tau$	0
	Quarks	$u/\bar{u}$	$c/\bar{c}$	$t/\bar{t}$	$\pm\frac{2}{3}$
		$d/\bar{d}$	$s/\bar{s}$	$b/\bar{b}$	$\mp\frac{1}{3}$

	Mediator	Force
Bosons	γ	electromagnetic
	$W^{\pm}, Z$	weak
	g	strong
	(*graviton*)	gravitational

Table 3.1: The Standard Model of particle physics. The upper part displays the elementary particles of matter with their electric charges in units of the electron charge. The lower part contains the four fundamental forces and their mediator bosons.

well as the corresponding (anti)neutrinos) and quarks (up, down, strange, charm, beauty[1] and top) and they are arranged in three generations. Due to their small masses of $\mathcal{O}$(MeV) the up, down and strange quarks are usually referred to as *light quarks*, while the other three (with masses of $\mathcal{O}$(GeV) are called *heavy quarks*. For the analysis presented in this thesis, the beauty (b) and charm (c) quarks are of particular interest; at HERA they are produced in substantial amounts. They are also the heaviest quarks that may be studied at HERA, as the mass of the top quark is too high ($m_t \approx 175\,\text{GeV}$).

A more detailed description of the Standard Model can be found in any introductory particle physics textbook, such as [14, 15].

3.2 Strong interactions

As already mentioned before the strong interactions are described by Quantum Chromodynamics (QCD), which is a local gauge theory based on the

[1]The b quark is usually referred to as bottom quark, while the term *beauty* is the nomenclature typically used at HERA experiments.

gauge group SU(3). The six quarks and the corresponding antiquarks that were introduced in Section 3.1 are the interacting spinors and the strong force between them is mediated by a set of massless gauge bosons, the gluons. Both quarks and gluons carry colour charge, such that all quarks come in three colours, whereas there are eight colour combinations for the gluons. In contrast to QED this also offers the possibility of boson (gluon) self-interaction.

The calculation of physical quantities, such as scattering cross sections and decay rates, can be subdivided into two parts: According to Fermi's "Golden Rule"

$$d\Gamma = \frac{2\pi}{\hbar}|\mathcal{M}|^2 \times (\text{phase space})$$

the determination of the transition rate, $d\Gamma$, for any such interaction consists of the evaluation of the *amplitude* or *matrix element*, $\mathcal{M}$, for the given process and the *phase space* available. The former contains all dynamical information that can be described with the help of the Feynman calculus, while the latter provides the kinematics and depends on the properties of the participating particles. Generally $\mathcal{M}$ cannot be computed exactly and must be approximated via perturbative calculations (pQCD). Therefore it is usually expressed as a power series in the coupling constant of the strong force, α_s.

If the process in question is of higher order than leading order, quark and gluon loops enter the calculation and the integrals involved in the evaluation of the amplitude are often found to diverge. In order to solve this problem a so-called *renormalisation scheme* was developed introducing a cutoff parameter, μ_R, with the dimension of a mass which renders the integrals finite without spoiling for instance its Lorentz-invariance. Furthermore, the infinities get absorbed by replacing the "bare" quantities that the amplitude initially depended on by renormalised or *effective* masses and coupling constants, which are now functions of the energies involved. Figure 3.1 (left) displays the *running* of the strong coupling, α_s, as a function of the renormalisation scale, μ_R, obtained by combining measurements from various experiments. Furthermore, three sets of measurements performed by ZEUS and H1 as well as the DØ experiment at Tevatron are shown in Fig. 3.1 (right). The latter also includes a DØ fit of the average of the strong coupling constant at the Z mass, $\alpha_s(M_Z)$.

In order not to depend on the renormalisation scale, μ_R, physical observables must fulfill the renormalisation group equation

$$\mu\frac{\partial\alpha_s(\mu)}{\partial\mu^2} = 2\beta(\alpha_s(\mu)) = -\frac{\beta_0}{2\pi}\alpha_s^2 - \frac{\beta_1}{4\pi^2}\alpha_s^3 - \ldots \tag{3.1}$$

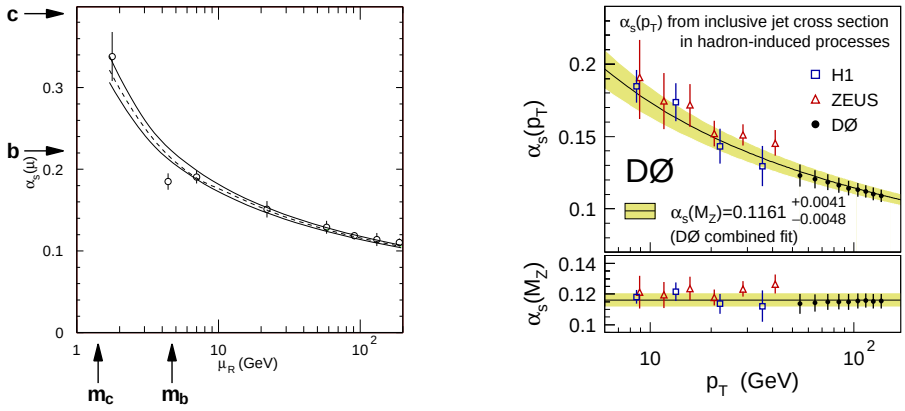

Figure 3.1: Dependence of the strong coupling, α_s, on the renormalisation scale, μ_R, including the $\pm 1\sigma$ limits denoted by the solid lines (left [16]). The data points correspond to measurements from various experiments. On the right, three sets of measurements performed by ZEUS, H1 and DØ are shown, including a DØ fit of the average $\alpha_s(M_Z)$ [17].

describing the previously mentioned dependence of α_s on μ_R. The β function is a perturbative expansion in α_s and unfolds as follows:

$$\begin{aligned} \beta_0 &= 11 - \frac{2}{3} n_f \\ \beta_1 &= 51 - \frac{19}{3} n_f \\ &\vdots \quad \vdots \quad \vdots \end{aligned}$$

At leading order the solution to Eqn. 3.1 is given by

$$\alpha_s(\alpha_s^0, \mu) = \frac{4\pi}{\beta_0 \ln\left(\frac{\mu_R}{\Lambda^2_{QCD}}\right)} \tag{3.2}$$

with

$$\Lambda^2_{QCD} = \mu_R^2 e^{-\frac{4\pi}{\beta_0 \alpha_s^0}}$$

depending on the bare coupling, α_s^0. The value of Λ_{QCD} has to be determined experimentally and was found to be $\approx 200\,\text{MeV}$ at leading order using a strong coupling constant $\alpha_s(M_Z)$ at the Z^0 pole. From Eqn. 3.2 it can be concluded that at high energies and small distances ($\mu \gg \Lambda_{QCD}$), partons can be considered as free partners in the scattering process, which is also referred to as *asymptotic freedom*. Here pQCD is applicable with e.g. the masses of the heavy quarks, m_c and m_b, being sufficiently large to provide

a hard scale as displayed in Fig. 3.1. Hence, heavy quark production is a stringent probe for perturbative QCD. On the other hand, the perturbative calculations become invalid for $\mu \to \Lambda_{QCD}$, which results in *confinement* for small energies and long distances. This explains why no free quarks can be observed; they fragment into hadrons, i.e. mesons ($q\bar{q}$ bound states) or baryons (qqq or $\bar{q}\bar{q}\bar{q}$ bound states). The hadronisation process will be discussed in more detail in Chapter 4.

Table 3.2 lists the properties of the most frequently produced beauty and charm hadrons at HERA. It is particularly noteworthy that both beauty and charm hadrons are rather long-lived with b hadrons having even somewhat longer lifetimes than c hadrons.

Hadron	Quark content	Mass (MeV)	$c\tau$ (μm)
$B^{\pm}$	$u\bar{b}/\bar{u}b$	5279.15 ± 0.31	491.1
$B^0/\bar{B}^0$	$d\bar{b}/\bar{d}b$	5279.53 ± 0.33	458.7
$B_s^0/\bar{B}_s^0$	$s\bar{b}/\bar{s}b$	5366.30 ± 0.60	441.0
$\Lambda_b^0/\bar{\Lambda}_b^0$	$udb/\bar{u}\bar{d}\bar{b}$	5620.20 ± 1.60	415.0
$D^{\pm}$	$c\bar{d}/\bar{c}d$	1869.62 ± 0.20	311.8
$D^0/\bar{D}^0$	$c\bar{u}/\bar{c}u$	1864.84 ± 0.17	122.9
$D_s^{\pm}$	$c\bar{s}/\bar{c}s$	1968.49 ± 0.34	149.9
$\Lambda_c^{\pm}$	$udc/\bar{u}\bar{d}\bar{c}$	2286.46 ± 0.14	59.9

Table 3.2: Quark content, mass and lifetime, $c\tau$, of the most frequently produced beauty and charm hadrons [16].

In order to understand this it is necessary to introduce the quark mixing matrix or *Cabibbo-Kobayashi-Maskawa (CKM) matrix*, V_{CKM}, which contains information on the strength of flavour-changing weak decays:

$$V_{CKM} = \begin{pmatrix} V_{ud} & V_{us} & V_{ub} \\ V_{cd} & V_{cs} & V_{cb} \\ V_{td} & V_{ts} & V_{tb} \end{pmatrix} \tag{3.3}$$

$$= \begin{pmatrix} 0.97419 \pm 0.00022 & 0.2257 \pm 0.0010 & 0.00359 \pm 0.00016 \\ 0.2256 \pm 0.0010 & 0.97334 \pm 0.00023 & 0.0415 \,{}^{+\,0.0010}_{-\,0.0011} \\ 0.00874 \,{}^{+\,0.00026}_{-\,0.00037} & 0.0407 \pm 0.0010 & 0.999133 \,{}^{+\,0.000044}_{-\,0.000043} \end{pmatrix}.$$

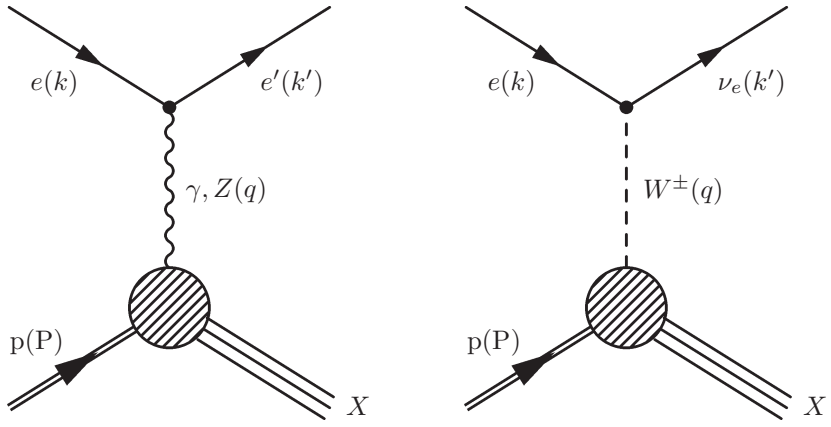

(a) Neutral Current (b) Charged Current

Figure 3.2: Electron-proton scattering at leading order. The electron and proton interact by exchanging either a neutral vector boson, γ or Z (a), or a $W^{\pm}$ (b). X denotes the hadronic final-state.

Equation 3.3 presents the currently best determination of the magnitudes of all CKM matrix elements according to [16]. It can be observed that decays within the same generation are favoured over decays between generations. In particular, V_{cb} which is the matrix element representing the probability of a $b \to c$ decay is much smaller than V_{cs}, the corresponding matrix element for the most probable charm decay. Due to the larger phase space available this directly results in a longer lifetime for b hadrons and indicates that any lifetime-related quantity may be helpful for separating b hadrons from c hadrons.

3.3 Electron-proton scattering

At lowest order, electron-proton (ep) scattering occurs via the electroweak exchange of a vector boson between the incoming lepton and proton. If a neutral boson, i.e. a photon (γ) or Z, is exchanged the process is called *neutral current* (NC). The case in which a $W^{\pm}$ is exchanged and a neutrino appears in the final state is called *charged current* (CC). The lowest-order diagrams for such NC and CC events are depicted in Fig. 3.2. Electron-proton scattering events are characterised by the following Lorentz-invariant

kinematic variables:

$$Q^2 = -q^2 = -(k - k')^2 \tag{3.4}$$
$$\sqrt{s} = \sqrt{(k + P)^2} \tag{3.5}$$
$$x = \frac{Q^2}{2P \cdot q} \tag{3.6}$$
$$y = \frac{P \cdot q}{P \cdot k}. \tag{3.7}$$

Here, Q^2 denotes the negative square of the four-momentum transfer of the exchanged boson and is often also called the *photon virtuality*. $\sqrt{s}$ is the centre-of-mass energy of the lepton-proton system. With beam energies of $E_p = 920\,\text{GeV}$ and $E_e = 27.5\,\text{GeV}$ (see Chapter 2) this results in a HERA centre-of-mass energy of

$$\sqrt{s} = \sqrt{4E_pE_e} \approx 318\,\text{GeV}.$$

x, which is also referred to as the Björken scaling variable, represents the fraction of the momentum of the incoming proton that is carried by the struck quark. The meaning of the inelasticity, y, becomes clear if it is transferred into the proton rest-frame:

$$y = \frac{1}{2}(1 - \cos\theta_e) = \sin^2\left(\frac{\theta_e}{2}\right).$$

It is directly dependent on the scattering angle of the lepton, θ_e, with respect to the direction of the incoming lepton beam. Therefore a large value of y corresponds to a large scattering angle and thus a large fraction of the initial lepton energy that is transferred to the proton; at low y the lepton hardly changes its direction and less energy is transferred. The four quantities are related by

$$Q^2 = s \cdot x \cdot y.$$

For $Q^2 \gg 1\,\text{GeV}^2$ the ep events are referred to as *deep inelastic scattering* (DIS)[2]. Events with low Q^2 are predominantly characterised by the exchange of a quasi-real photon and are referred to as *photoproduction*. This is the dominant part of the HERA cross section and also the regime used for the analysis presented in this thesis. As the W and Z cross sections depend on

$$\frac{Q^2}{(M_{W/Z}^2 + Q^2)^2}$$

[2]The limit of $1\,\text{GeV}^2$ is solely a convention; $Q^2 \ll m_p^2$ with m_p being the proton mass or $Q^2 \approx 0\,\text{GeV}^2$ is often used as well to define the photoproduction regime and to separate it from DIS.

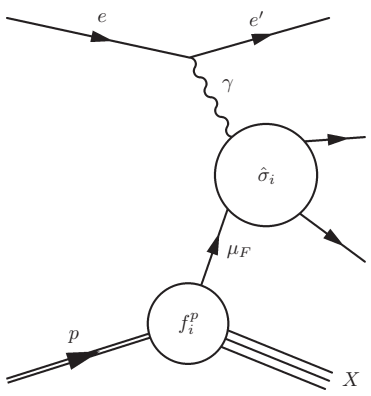

Figure 3.3: Factorisation of the ep scattering process into the hard subprocess, $\hat{\sigma}_i$, and soft processes hidden in the partonic structure functions, f_i^p, of the proton.

the exchange of $W^{\pm}$ or Z is suppressed at low Q^2; therefore photoproduction processes are often also referred to as γp collisions. While in DIS the hard scale that allows perturbative calculations to be performed is provided by the large photon virtuality, Q^2, this is not the case in the photoproduction regime. However, the large masses of the heavy quarks or the large transverse momenta of jets may replace Q^2 and serve as hard scales.

According to the QCD factorisation theorem [18] the inclusive ep cross section can be factorised into the cross section of the hard subprocess, $\hat{\sigma}_i$, on parton level and the partonic structure functions, f_i^p; it can thus be written as

$$\sigma^{ep} = \sum_{i=q,\bar{q},g} \hat{\sigma}_i(\mu_F) \otimes f_i^p(\mu_F).$$

The structure functions are directly proportional to linear combinations of the parton densities. The scale dependences of the latter are known as *parton density functions* (PDFs), which represent the probability for finding a parton i in the proton or photon, respectively. Both $\hat{\sigma}_i$ and f_i^p depend on the *factorisation scale*, μ_F, which separates the hard scatter from the soft processes as depicted in Fig. 3.3. The parton density functions are not calculable in pQCD, but must be extracted from experimental data using *parton evolution models*, which describe the evolution of the quark and gluon momentum distributions in Q^2. The leading-order predictions used for the analysis presented in this thesis are for instance based on the Dokshitzer-Gribov-Lipatov-Altarelli-Parisi (DGLAP) evolution equations [19]. Figure 3.4 shows the dependence on x of parton density functions determined by the ZEUS and H1 collaborations from DIS data for $Q^2 = 10\,\mathrm{GeV}^2$. It can be observed

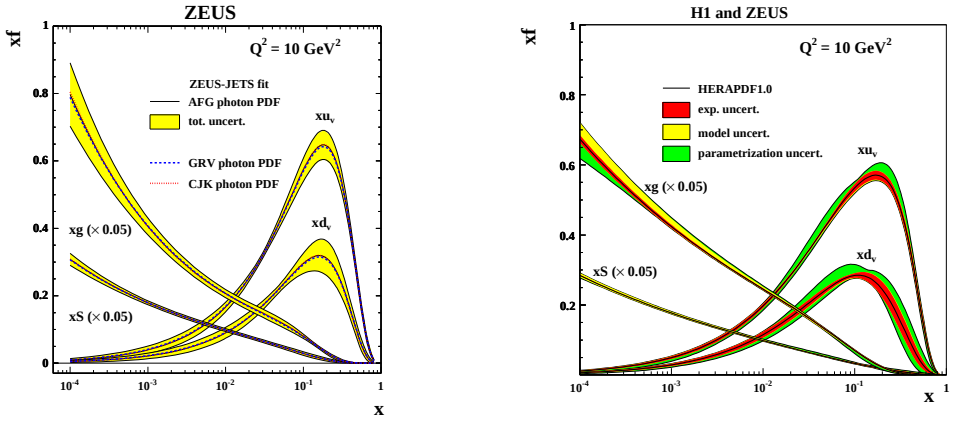

Figure 3.4: Parton distribution functions determined from a ZEUS next-to-leading order QCD fit (left) and from a combined H1 and ZEUS fit (right) at $Q^2 = 10\,\mathrm{GeV}^2$. Shown are the distributions for the valence quarks u (xu_v) and d (xd_v) as well as for gluons (xg) and sea quarks (xS); note that the latter are scaled by 0.05 [20, 21].

that the valence quarks u and d are dominant at high x. The gluon and sea quark PDFs are scaled by 0.05 and dominate at low x. The PDFs on the left were determined from ZEUS data and a corresponding ZEUS fit alone, while the right figure shows the ZEUS-H1 combination. The latter has considerably reduced uncertainties and represents the first set of HERA PDFs which will be a valuable input for the LHC experiments. There are several working groups evaluating such sets of parton density functions. Apart from the group at ZEUS there is for instance the CTEQ collaboration; their PDFs as well as the ZEUS PDFs will be used later on in this analysis. Although the analysis is restricted to the photoproduction regime, i.e. low four-momentum transfers, the distributions shown in Fig. 3.4 are still relevant, since the scale used there is of roughly the same order as the factorisation scale chosen for the perturbative calculations that will be compared with the measurements.

3.3.1 Beauty and charm production

The dominant production mechanism for heavy quarks is boson-gluon fusion. In *direct* boson-gluon fusion a photon (γ) or Z emitted by the incoming electron interacts with a gluon from the proton producing a heavy quark ($b\bar{b}$ or $c\bar{c}$) pair. This process, in which the photon acts as a point-like particle, is

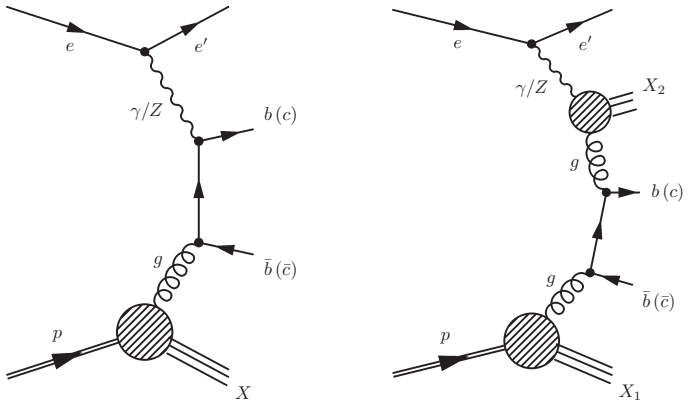

Figure 3.5: Direct (left) and resolved (right) boson-gluon fusion.

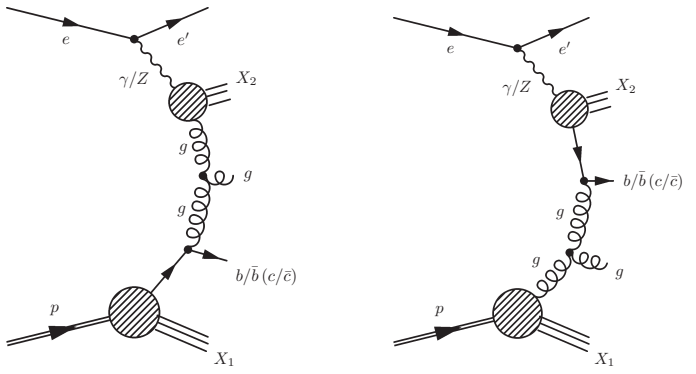

Figure 3.6: Excitation in the proton (left) and excitation in the photon (right).

illustrated in Fig. 3.5 (left). The photon may also act as a source of partons by fluctuating into $q\bar{q}$ pairs and hence creating hadronic structures. This process in which the heavy quark pair is subsequently produced via gluon-gluon fusion as depicted in Fig. 3.5 (right), is called *resolved* boson-gluon fusion. Here only a fraction of the initial momentum of the photon participates in the hard scatter. Due to such processes it makes sense to introduce photon structure functions using the same formalism as for the proton PDFs (cf Section 3.3). While in the processes shown in Fig. 3.5 quark pairs are produced, a single quark can also originate directly from the proton or from a hadron produced by the photon. These processes are called *excitation in the proton* and *excitation in the photon*, respectively, and are usually also classified as resolved boson-gluon fusion events. Figure 3.6 illustrates both excitation

processes. The distinction between excitation and non-excitation processes gains in importance in double-tagging analyses, in which both b or c quarks produced in the hard scatter or correlations between them are examined (cf Chapter 11). There the excitation processes are suppressed with respect to the direct and resolved interactions depicted in Fig. 3.5.

3.4 Heavy flavour tagging

Various experimental techniques are applicable for tagging heavy flavours. Most of them are tailored to a specific hadronic final state. In Fig. 3.7 an example for a b hadron decay is sketched. Here the $\bar{b}$ quark emerging from the hard subprocess and a d quark fragmented into a B^0 hadron, which subsequently decays. The $\bar{b}$ decays semileptonically via a W^+ exchange, leaving a $\bar{c}$ to combine with the d and form a D^{*-} meson. The semileptonic decay can either produce a μ^+ and a muon neutrino, ν_μ, or a positron, e^+, and an electron neutrino, ν_e; the branching ratio for both processes is $\mathcal{BR}(W \to \mu\nu_\mu/e\nu_e) \approx 10\,\%$. Decays into $\tau\nu_\tau$ occur with almost the same probability, but they possess a more difficult signature, since the τ decays mostly hadronically; τ decays into muons or electrons have only a branching ratio of $\approx 17\,\%$. In analogy to the semileptonic decay depicted in Fig. 3.7 there might also be $b \to c$ cascades with subsequent semileptonic charm decays. Equivalent processes occur for all other b hadrons.

In order to tag such b events one can for instance make use of the properties of the final-state lepton that was produced in the semileptonic decay.

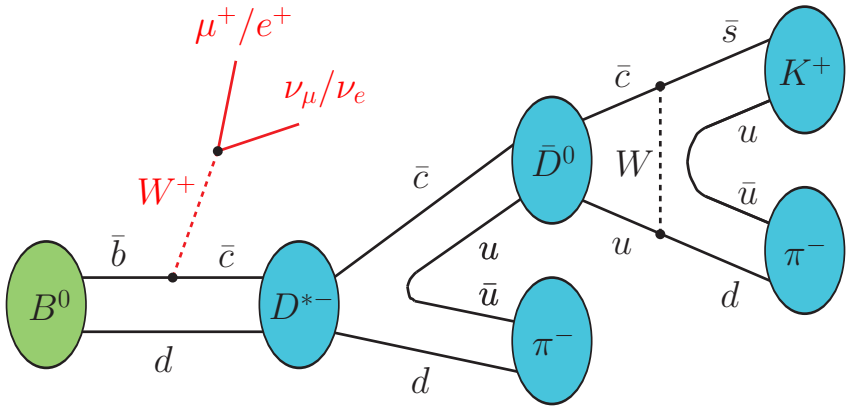

Figure 3.7: Example B decay chain with $B^0 \to D^*$ decay and subsequent golden decay $D^* \to D^0\pi \to K\pi\pi$.

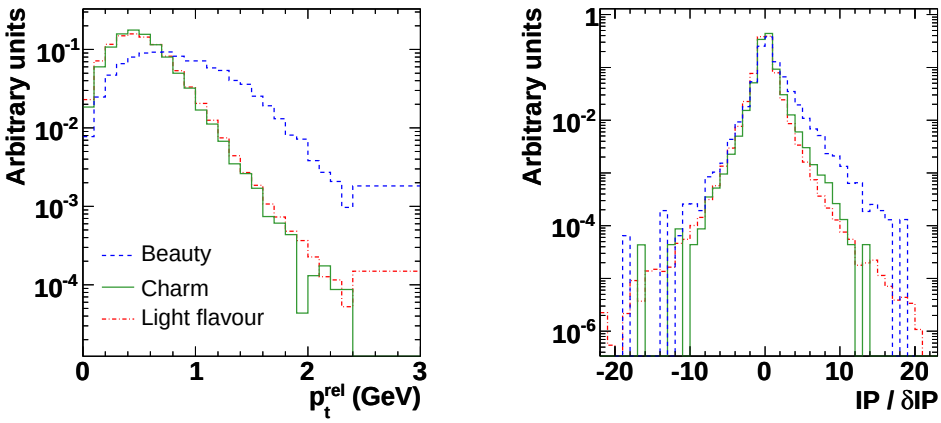

Figure 3.8: p_t^{rel} and impact-parameter significance distributions for electrons from semileptonic decays [22]. The distributions for beauty, charm and light flavours are denoted by the blue, green and red histograms.

One possibility is to use its transverse momentum relative to the jet axis, p_t^{rel}, which is known to have a harder spectrum for leptons from b hadron decays than for those originating from other sources. An example for such a p_t^{rel} distribution for electrons from semileptonic decays is displayed in Fig. 3.8 (left). It is visible that p_t^{rel} provides a good separation of beauty from charm and light flavours, but the latter two are almost indistinguishable. Due to the long lifetime of b hadrons muons or electrons from semileptonic b hadron decays are produced at a certain distance from the main interaction point and can therefore also be identified via impact-parameter tagging. The impact parameter, IP, is defined as the point of closest approach of the lepton track with respect to the interaction point. It has a positive sign if the track crosses the axis of the associated jet within the jet hemisphere, otherwise it is negative. The impact-parameter significance is defined as the impact parameter divided by its error, δIP. In Fig. 3.8 (right) the impact-parameter significance distribution is shown for electrons from semileptonic decays. In contrast to p_t^{rel} it also reveals some separation power to distinguish charm and light flavours; however, the distinction between beauty and the other flavours is much more pronounced. If no b decay channel is specified it is still possible to exploit the long lifetime of b hadrons by determining their decay lengths through the reconstruction of secondary vertices. This will be the central topic of the analysis presented in this thesis.

D^* tagging is a commonly used method for the identification of charm events. In Fig. 3.7 the so-called *golden decay* of a D^{*-} into $\bar{D}^0\pi^-$ and the

subsequent decay of the $\bar{D}^0$ into $K^+\pi^-$ is depicted; the branching ratio corresponds to $\mathcal{BR}(D^* \to K\pi\pi) \approx 36\,\%$. This decay channel will also be of interest for systematic studies in the context of this analysis and will be addressed again in Section 10.3.2. The previously described techniques are often also combined or used for double tagging by e.g. tagging a D^* originating from one b decay as well as a semileptonic muon from the decay of the other b produced in the hard subprocess.

3.5 Experimental results

In this section I will first review the discovery of the heavy quarks and summarise previous measurements that provided useful input for the work presented in this thesis. Since it is impossible to do justice to all measurements on heavy quark production that have been performed so far, I will focus on recent analyses of beauty photoproduction at HERA. A collection of measurements from fixed-target experiments and results from other collider experiments can for instance be found in [76, 77]. Finally, I will briefly discuss the impact of the beauty analyses performed at HERA on future experiments, particularly at the LHC.

3.5.1 Discovery of heavy flavours

Until 1974, the only quarks known were the light quarks u,d and s. However, the idea of a fourth flavour had already been introduced by Björken, Glashow, Iliopoulos and Maiani [23], since there was an intriguing parallel between the lepton and quark families. So far four leptons, but only three quarks had been established. The charm quark turned up with the discovery of the J/ψ meson at Brookhaven and SLAC, which represents a bound state of the charm quark and its antiquark. The discovery of the J/ψ came to be known as the *November revolution* and in the following years further charmed mesons ($D^0 = c\bar{u}$, $D^+ = c\bar{d}$, $D_s = c\bar{s}$) and baryons ($\Lambda_c^+ = udc$, $\Sigma_c^{++} = uuc$) were found.

The quark model could have been regarded as complete now, if there had not been the discovery of the third charged lepton, the τ. It temporarily spoiled the symmetry of the established model, until in 1977 the Υ, a bound state of a beauty quark and its antiquark ($b\bar{b}$) was found. Subsequently several hadrons containing beauty - such as $B^0(b\bar{d})$, $B^-(b\bar{u})$ and $\Lambda_b(ubd)$ - were discovered.

Finally, in 1995 the discovery of the "missing" top quark at the $p\bar{p}$ collider

Tevatron at Fermilab completed the Standard Model as it is known today[3]. In the following - in particular in Section 3.5.3 - it will be shown why even 35 years after the discovery of the charm quark the study of heavy quarks is still one of the main components of the physics programme of high energy physics experiments.

3.5.2 Beauty production at HERA

The ZEUS collaboration has measured beauty production in events with two jets and a muon or an electron from b-quark semileptonic decays [48–51]. In the $b \to \mu$ analysis that was based on part of the HERA II dataset the beauty component was separated from charm and light flavour backgrounds using the transverse momentum of the lepton relative to the axis of the associated jet (p_T^{rel}) and the impact parameter of the muon. Two other $b \to \mu$ analyses, which were based on HERA I data, made use of p_T^{rel} alone in order to determine the b content of the sample. In one of those analyses the μ-jet cross sections were also extrapolated to obtain the cross sections for b-jets in dijet events, $\sigma(ep \to e'jjX)$. In the HERA I $b \to e$ analysis several variables sensitive to both the electron identification as well as semileptonic decays were combined in a likelihood test function for the extraction of the beauty content. An analysis on beauty production using $D^*\mu$ correlations has been performed as well [52].

Similar analyses using muon tags and $D^*\mu$ correlations have been published by the H1 collaboration [53]. In Fig. 3.9 a summary of the differential cross sections for b-quark production as a function of the transverse b-quark momentum, p_t^b, as measured in various independent ZEUS and H1 analyses is presented. Good agreement with the theoretical predictions calculated in next-to-leading order is observed.

All HERA measurements on beauty photoproduction that have been published so far were restricted to a certain b hadron decay channel which leads to a substantial loss of statistics. By keeping the measurement fully inclusive as it was done in the analysis presented in this thesis a significant improvement of the precision can be expected. At the same time new techniques for heavy flavour tagging are required for an analysis in which no attempt is made to identify final-state particles. Hence a method that exploits the long lifetime of b hadrons via secondary vertexing for determining the beauty contribution of the sample (see Chapter 7) was developed for this analysis for the first time.

[3]The tau neutrino, ν_τ, which was postulated, but only observed in 2000, shall be disregarded here.

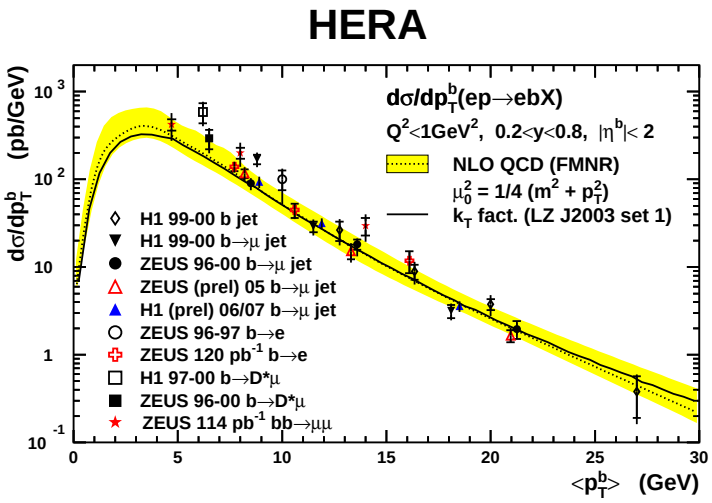

Figure 3.9: Summary of differential cross sections for b-quark production as a function of p_t^b as measured by the ZEUS and H1 collaborations. The measurements are shown as points with the inner error bars being the statistical errors and the outer bars representing the statistical and systematic errors added in quadrature. The solid black line and the yellow band denote the next-to-leading order QCD prediction and its uncertainty.

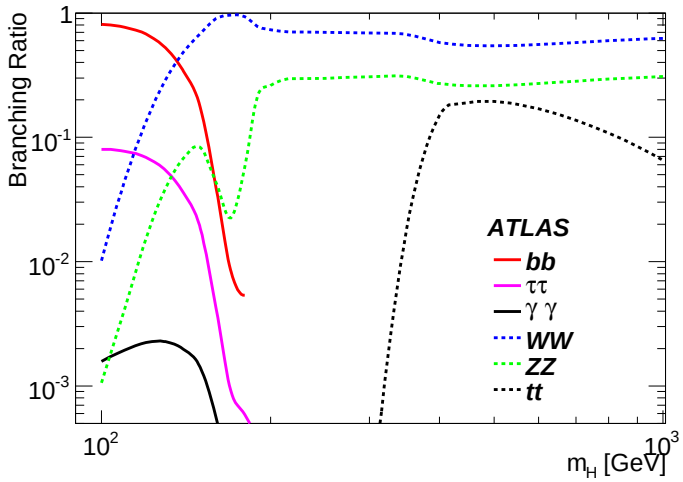

Figure 3.10: Branching ratios for the relevant decay modes of the Standard Model Higgs boson as a function of its mass, m_H [54].

3.5.3 Beauty production at the LHC

One reason why the study of beauty production and decay at HERA is of great importance, is the era of physics at the pp-collider LHC at CERN that has just begun. Two of the main topics of interest heavily rely on a good understanding of QCD in general and in particular of the physics of b-quarks: top-quark production (and decay) and the search for the Higgs boson.

Since top quarks predominantly decay into a b-quark and a W boson (which subsequently decays either hadronically into $q\bar{q}$ or leptonically into $l\nu_l$), it is essential to have reliable b-tagging methods at hand to allow precise studies of top-quark production and decay. All the ZEUS and H1 results presented in 3.5.2 provide valuable input for these LHC analyses.

Furthermore, the Standard Model Higgs boson, which is expected to be discovered at the LHC, may decay into $b\bar{b}$, $t\bar{t}$, WW or ZZ with branching ratios depending on the Higgs mass (see Fig.3.10). For all of these processes that directly or indirectly involve the production and decay of b-quarks and may provide evidence for the existence of the Higgs boson in the future, a reliable identification of b-jets is mandatory.

Chapter 4

Theoretical predictions

In this chapter the two different types of theoretical predictions, to which the measured cross sections were compared, will be presented. In Section 4.1 the leading-order plus parton shower (LO+PS) Monte Carlo (MC) samples will be introduced, while the next-to-leading order (NLO) pQCD predictions will be discussed in Section 4.2.

4.1 Monte Carlo simulation

Typically the recorded physics events are compared to so-called leading-order plus parton shower (LO+PS) Monte Carlo events of the same event type. The MC events are used for several purposes:

- to optimise the event selection and contribute to the improvement of the reconstruction (cf Chapter 5);
- to test the accuracy of the underlying physics model;
- to transform measurements from *detector level (DL)* to *hadron level (HL)* by means of acceptances (cf Chapter 8);
- to transform NLO QCD calculations from *parton level (PL)* to hadron level by means of hadronic corrections (cf Chapters 8, 10 and 11).

The event generation process and the distinction between detector level, hadron level and parton level are illustrated in Fig. 4.1: The leading-order (LO) calculation corresponds to the hard subprocess in which the $q\bar{q}$ pair is produced. The additional radiation of gluons is called parton showering (PS). Commonly this stage of the generation process combining LO and PS is referred to as *parton level (PL)*. In the next step the quarks fragment into

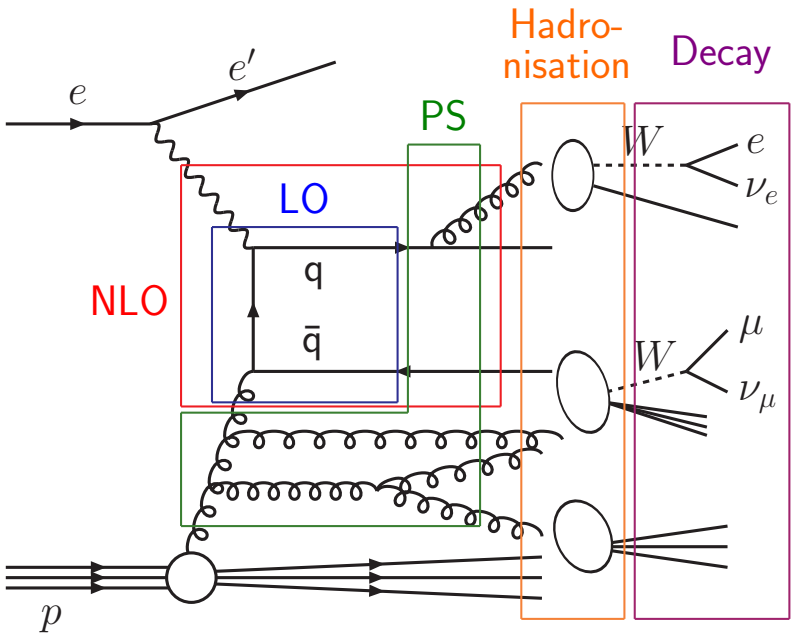

Figure 4.1: Illustration of the different steps in the event generation of an *ep* scattering process consisting of leading-order (LO) calculation, parton showering (PS), hadronisation and decays. The components that are used for NLO QCD predictions are indicated as well.

hadrons, therefore this stage is named *hadron level (HL)*. The fragmentation is due to the strong force between the partons at large distances. In this regime α_s is large and perturbative calculations are not applicable anymore. The hadronisation process is simulated with the help of fragmentation models, two of which will be presented in Section 4.1.1. Subsequently, the hadrons decay into the final state particles that are visible on *detector level (DL)*. The decay products are usually accumulated in spatially limited bundles, so called *jets*. Thus the reconstruction of jets plays an important role in the event selection; it will be discussed further in the context of the event selection for this analysis (cf Chapter 6). Simulated MC events contain information about all stages of the generation process and are therefore a useful tool for extracting "truth level information" by relating detector-level quantities within the simulated events to the corresponding ones on hadron or parton level. In particular the HL information is needed to enable a meaningful comparison of measured cross sections between different experiments, since it is independent of experimental limitations such as detector coverage,

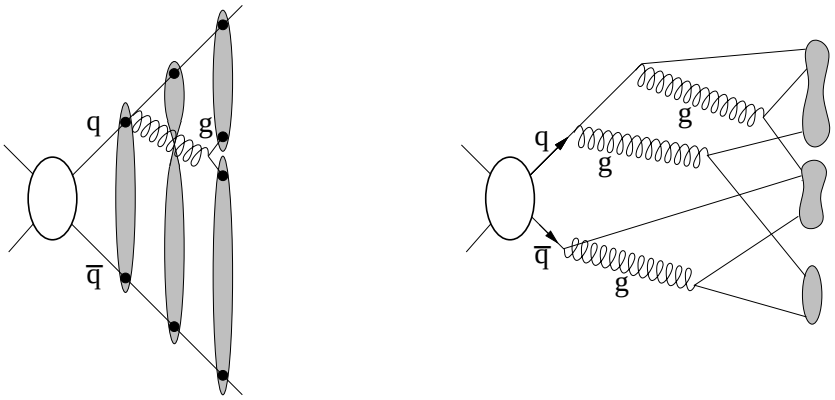

Figure 4.2: Fragmentation models: In case of the string fragmentation (left) the energy increases linearly with the separation of the outgoing $q\bar{q}$ pair. At a certain energy density the string is forced to break up such that new $q\bar{q}$ pairs are formed [27]. In case of the cluster fragmentation (right) the formation of new $q\bar{q}$ pairs happens via parton showering and gluon splitting [28].

resolutions and acceptances.

The process of producing a MC event can be subdivided into the previously discussed event generation, which is completely independent of the detector-related issues mentioned above, and the detector simulation and event reconstruction. The event generator used for this analysis as well as the simulation of the detector response will be the topics of the following two sections.

For the comparison with data enough events must be generated in order to obtain a sufficient statistical significance.

4.1.1 PYTHIA

The photoproduction events needed for the analysis presented in this thesis were generated with the PYTHIA programme [24], version 6.023. As PDFs CTEQ5L and GRVG-LO were used for the proton and the photon, respectively [25, 26]. Furthermore, it incorporates the LUND string fragmentation model [27] as depicted in Fig. 4.2. The partons are connected by so-called *strings*, which gain more and more energy the further the partons move away from each other. Finally, they break up and new $q\bar{q}$ pairs are formed. When there is not enough energy left to separate the partons further, bound states, i.e. hadrons, are formed. The cluster fragmentation [28] that is also sketched in Fig. 4.2, is an alternative model and for instance used by the HERWIG

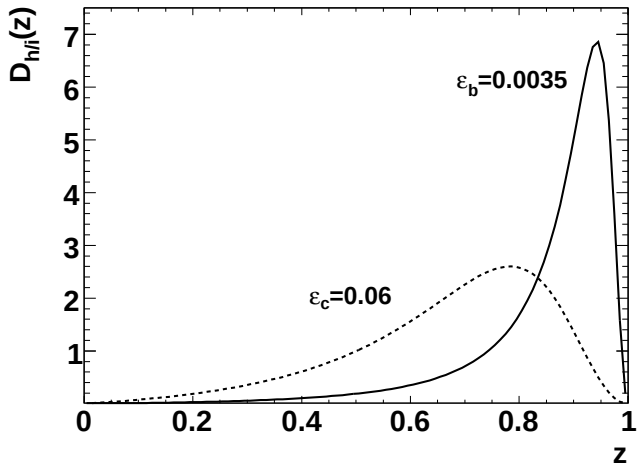

Figure 4.3: The Peterson fragmentation functions $D_{h/i}(z)$ for beauty and charm using $\varepsilon_b = 0.0035$ and $\varepsilon_c = 0.06$. Both functions were normalised to one.

programme [29], which is also used frequently for generating the same kind of processes. The fragmentation process is included in the event simulation by convoluting the final-state parton cross sections with a function $D_{h/i}(z)$ parametrising the fragmentation of a final-state parton, i, into a hadron, h. For heavy quarks most generators (including PYTHIA) make use of the Peterson fragmentation function [30]:

$$D_{h/i}(z) = \mathcal{P}_{h/i} \cdot \frac{A}{z \cdot (1 - \frac{1}{z} - \frac{\varepsilon}{1-z})^2}. \tag{4.1}$$

In Eqn. 4.1 $z = E_h/E_i$ denotes the ratio of the hadron and parton energies, $\mathcal{P}_{h/i}$ the total probability for the parton i to fragment into the hadron h and A a normalisation constant. The Peterson parameter ε is determined experimentally [31]. In Fig. 4.3 the fragmentation function $D_{h/i}(z)$ is shown for ε values for beauty and charm that are typically used for theoretical predictions (cf Section 4.2). For heavy quarks a peak close to one is expected, since the hadron absorbs most of the quark's energy. Usually the LUND symmetric fragmentation function is used for light flavours [32].

In Table 4.1 all processes which are included in the generated samples are listed. They are classified according to the distinction of process types presented in Section 3.3.1. The names of the samples (*beauty*, *charm* and *light flavours*) correspond to the flavours of the quarks being produced in

Beauty (Charm)		Light flavours	
Direct	Resolved	Direct	Resolved
$\gamma g \to b\bar{b}$ (84)	$q\bar{q} \to b\bar{b}$ (81)	$\gamma q \to qg$ (33)	$qq \to qq$ (11)
	$gg \to b\bar{b}$ (82)	$\gamma g \to q\bar{q}$ (54)	$q\bar{q} \to q\bar{q}$ (12)
Excitation γ	Excitation p		$q\bar{q} \to gg$ (13)
$bq \to bq$ (11)	$bq \to bq$ (11)		$qg \to qg$ (28)
$b\bar{b} \to b\bar{b}$ (12)	$bg \to bg$ (28)		$gg \to q\bar{q}$ (53)
$bg \to bg$ (28)	$b\gamma \to b\gamma$ (33)		$gg \to gg$ (68)

Table 4.1: Beauty, charm and light flavour Monte Carlo samples and contributing processes. In brackets the PYTHIA process IDs are listed.

the hard scatter. In case of the light flavour MC the excitation processes are included in the sample labelled "Resolved". The contribution of some of the photoproduction processes to the inclusive cross section is displayed in Fig. 4.4.

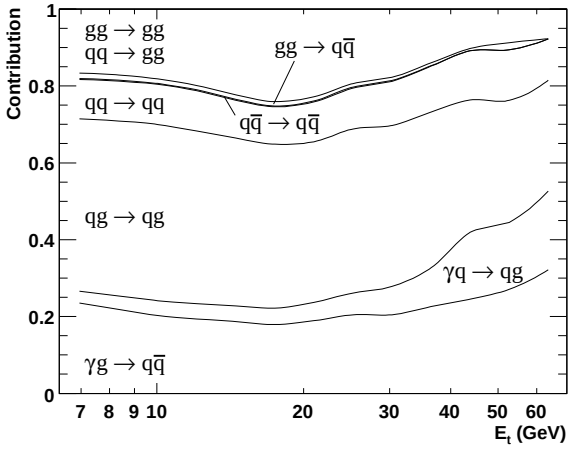

Figure 4.4: Relative contributions of the γp processes to the inclusive jet production cross section as a function of the transverse jet energy, E_t. The contributions are drawn stacked, i.e. the area below each line includes the sum of all contributions below [33].

4.1.2 Detector simulation and event reconstruction

The production of MC events including detector simulation and reconstruction is illustrated in Fig. 4.5. At the beginning, the desired physics processes are generated. All generators commonly used at ZEUS are integrated in the AMADEUS package. Its main purpose is to convert the generator output into the ADAMO format which can be handled by the programmes used in further steps. Subsequently the MOZART[1] package [34], which is based on Geant 3.21 [35], simulates the interaction of particles with matter as well as the detector geometry and response. It is set up such that the detector configuration can be simulated separately for each data-taking period, which for instance allows the implementation of new sub-detectors (as done after the HERA upgrade, cf Chapter 2) and additional material like cables or cooling pipes.

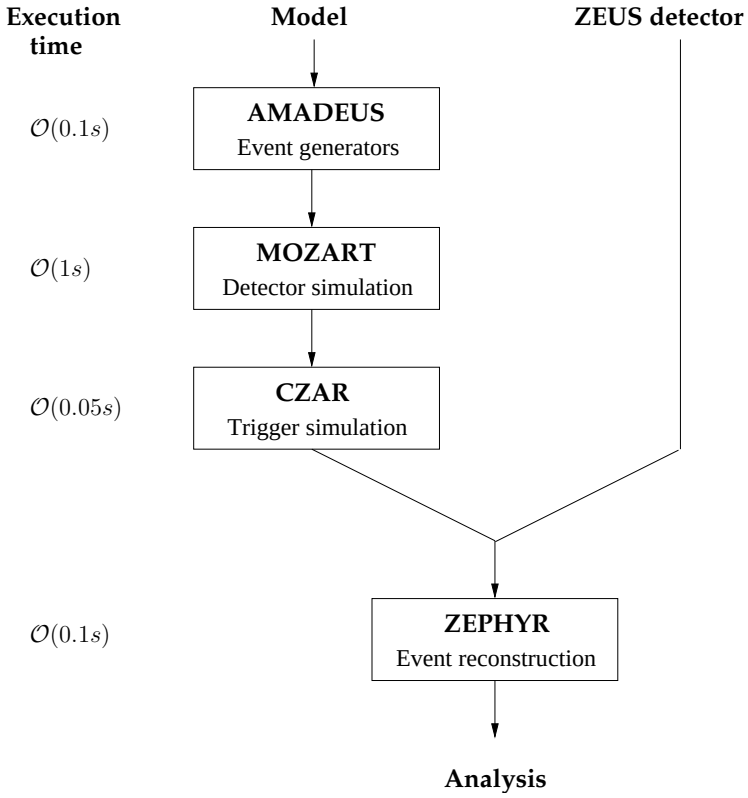

Figure 4.5: Flow chart of the ZEUS Monte Carlo simulation software.

[1]MOZART = **Mo**nte Carlo for **Z**EUS **A**nalysis, **R**econstruction and **T**rigger.

The CZAR[2] package is responsible for simulating the different trigger levels (cf Section 2.3.5). It combines the programmes ZGANA[3], which is responsible for the FLT and SLT simulation, and the TLT simulation software TLTZGANA. Finally, the events are reconstructed by the ZEPHYR[4] package. It is identical for data and Monte Carlo except for the truth information on hadron and parton level which the simulated events contain in addition. Therefore a MC event has the same structure as a data event and can thus be analysed in exactly the same way. The combination of MOZART, CZAR and ZEPHYR is usually referred to as the *funneling process*. The execution times for the different stages of the MC production are also displayed in Fig. 4.5 [36]. The exact numbers depend on the available computing power; however, it is visible that the detector simulation takes roughly 10 times longer than the generation and the event reconstruction. More information on the event simulation at ZEUS can be found in [37].

4.2 NLO QCD calculations

In addition to the LO+PS Monte Carlo simulations described in the previous section NLO QCD calculations were made using the FMNR programme [38, 39]. It is based on the Fixed Flavour Number Scheme (FFNS)[5], in which u, d and s are the only active flavours in the structure functions of the proton and the photon. The heavy flavours are generated dynamically in the matrix elements and therefore only produced in the hard scatter. This is valid for $\mu^2 \approx \mathcal{O}(m_q^2)$, with q being the beauty or charm quark (or the corresponding antiquark). As PDFs CTEQ5M [25] and GRVG-HO [26] were used for the proton and the photon, respectively. In a second set of predictions which will be used later CTEQ5M was replaced by the ZEUS-S PDF [40]. Among the parameters that need to be adjusted for calculating the appropriate predictions are the quark masses m_b and m_c, the renormalisation and factorisation scales,

$$\mu = \mu_R = \mu_F = \frac{\mu_0}{2} = \frac{1}{2}\sqrt{(p_t^b)^2 + m_b^2},$$

as well as the fragmentation parameters ε_b and ε_c used in the Peterson fragmentation function (cf Section 4.1.1). The central values for all parameters described above are listed in Table 4.2. Jets were reconstructed by running

[2]CZAR = **C**omplete **Z**GANA **A**nalysis **R**outines
[3]ZGANA = **Z**EUS **G**eant **A**nalysis
[4]ZEPHYR = **ZE**US **Phy**sics **R**econstruction
[5]The Fixed Flavour Number Scheme is often also referred to as the *massive scheme*.

Parameter	Beauty	Charm
m_q	4.75 GeV	1.50 GeV
μ	$\frac{\mu_0}{2}$	$\frac{\mu_0}{2}$
ε_q	0.0035	0.06

Table 4.2: Central values of the parameters used for the NLO QCD predictions calculated with the FMNR programme [39]. q denotes the beauty or charm quark.

the k_t algorithm (cf Chapter 6) on the four-momenta of the two b quarks and the third light parton (if present) generated by the programme.

The NLO cross sections which correspond to parton level predictions as indicated in Fig. 4.1 were corrected for hadronisation effects to allow a direct comparison with measured hadron-level cross sections. The correction factors, C_{had}, were derived from the MC simulation as the ratio of the number of hadron-level jets to the number of parton-level jets. The size of these corrections will be discussed in Chapters 8, 10 and 11, where the results of the analysis are presented. Furthermore, all hadronisation corrections are also listed in the cross-section tables in Appendices C and D.

In order to evaluate the uncertainty of the NLO calculations the renormalisation and factorisation scale μ was varied between $\mu_0/4$ and μ_0 and the quark masses by $\pm 0.25\,\text{GeV}$ for beauty and $\pm 0.2\,\text{GeV}$ for charm. For the determination of the total uncertainty, both contributions were added in quadrature.

Due to the fact that the mass of the b quark, m_b, is three times larger than the charm mass, m_c, and thus provides a harder scale, more reliable predictions are expected for the beauty cross sections (cf Section 3.2). Consequently, the uncertainties will be largest for the predictions of the charm cross sections at low scales. This issue will again be addressed in the context of the discussion of the analysis results presented in Chapter 8.

Chapter 5

Tracking and vertexing

A precise tracking was essential for the analysis presented in this thesis, hence the most important aspects, i.e. the general track reconstruction procedure and the vertex finding, will be discussed in this chapter. Furthermore, the Grand Reprocessing (GR) effort will be introduced which enabled the provision of consistent datasets for the whole HERA II data-taking period. These datasets were not yet available when this analysis was done, but many analysis-related tracking studies were performed in its context on pre-GR data and lead to considerable improvements, which could already be used as default for the final Grand-Reprocessed data. These studies and the corrections that consequently had to be applied to the pre-GR data will be described in detail, as they were crucial for the analysis.

5.1 Track reconstruction

A major achievement in the past few years was the so-called global tracking, which uses the hits in all tracking detectors, i.e. MVD, CTD and STT, for a combined pattern recognition. In a first step a group of hits in the most outward component, which is the STT in the forward region and the CTD elsewhere, is defined as the track *seed*. Seeds in the STT were required to have at least eight hits; if there were less than eight hits the CTD was also in the forward region used for finding the track seed. The seed serves as a starting point and is connected to the interaction point with the help of an approximate estimation of the momentum and charge of the track. This connection roughly establishes the direction in which will be looked for further matching hits. Subsequently, the signals produced in the inner tracking chambers along the way to the beam-spot are continuously picked up until a *road* of hits from the STT or CTD through the MVD to the

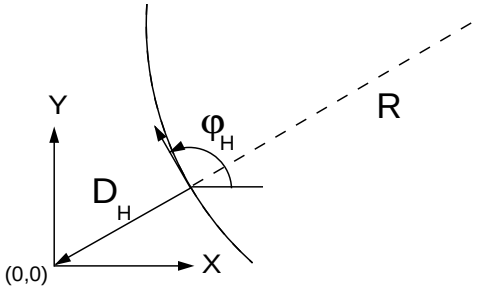

Figure 5.1: Parametrisation of a track helix [43].

interaction point has been created [41]. After the pattern recognition a track fit is done using the selected hits on the road in order to determine the final track helix[1]. The parametrisation of the helix is based on the definition of the *point of closest approach*, i.e. the point on the helix which is closest to the chosen reference point in X-Y. Five parameters are needed for a full description of the helix:

$$(\varphi_H, Z_H, D_0, \cot(\theta), W).$$

φ_H is the azimuthal angle of the direction vector of the helix at the point of closest approach, Z_H the Z position of the point of closest approach and $D_0 = QD_H$ its distance to the reference point multiplied by the charge. The sign of D_H depends on whether the reference point is located within the helix or outside. θ denotes the polar angle of the track and $W = Q/R$ the quotient of its charge and the radius of curvature. Figure 5.1 illustrates the definition of the helix parameters with respect to a given reference point which is placed in the origin of the coordinate system. The track reconstruction procedure is generally not restricted to tracks with hits in all three tracking chambers, i.e. CTD, MVD and STT; it also allows the reconstruction of CTD-only, MVD-only, CTD+MVD and MVD+STT tracks. Further information on pattern recognition and track fit can be found in [42, 43].

[1]The helix shape is caused by the magnetic field created by the solenoid around the CTD, see Section 2.3.

5.2 Vertex reconstruction

5.2.1 Primary vertex and beam-spot

Initially the event primary vertex was determined by selecting a set of properly reconstructed tracks, calculating a weighted centre-of-gravity for those tracks and minimising the χ^2 of the fit. Within this procedure tracks were discarded that lead to a higher χ^2 than a certain χ^2 limit. This method was later refined by following a *thermodynamical approach* and replacing the χ^2 cuts by a smooth temperature-dependent weight function

$$w(\chi^2, T) = \frac{1}{1 + exp(\frac{\chi^2 - \chi^2_{cut}}{2T})}, \tag{5.1}$$

the so-called *Deterministic Annealing Filter (DAF)*. The vertex that was determined using the initial approach and the tracks fitted to it served as a starting point. Then a weight according to Equation 5.1 with a high temperature, T, was assigned to each track. After updating the weighted fit, the temperature was reduced. Subsequently, these steps were iterated until a certain T or convergence was reached. Figure 5.2 displays the dependence of the weight, $w(\chi^2, T)$, on χ^2 for several values of the temperature, T. In addition outlier tracks, i.e. tracks that were too far away from the vertex to be properly fitted to it, were removed by constraining the vertex to be close to the interaction point, the so-called *beam-spot*. The term beam-*spot* is misleading, since it was not a well-defined spot but a 3D distribution of the beam-beam collisions. Its width was roughly $80 \times 20\,\mu$m in X-Y and 8 cm in

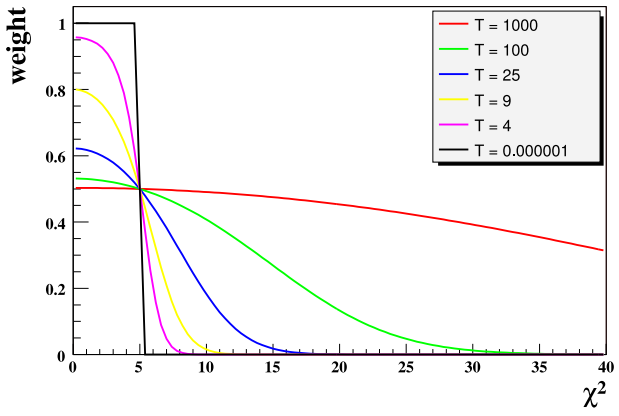

Figure 5.2: Weight $w(\chi^2, T)$ as used in the Deterministic Annealing Filter (DAF) for several fixed values of the temperature, T, and $\chi^2_{cut} = 5$ [47].

Z. The beam-spot could move with time and was therefore determined for periods of 2000 events by fitting the X, Y and Z distributions of the initial primary vertex. Furthermore, the beam tilt expressed by the slopes of the incoming beams in X and Y with respect to the Z axis was evaluated by slicing the X and Y vertex distributions into several Z intervals and fitting those with single Gaussians; subsequently the mean values were fitted with straight lines representing the X and Y slopes. The error on the position and the beam-spot width were also evaluated within this procedure. More information on the determination of the beam-spot can be found in [44]. The DAF method with beam-spot constraint considerably improved the efficiency of the vertexing as well as the resolution, therefore it was established as the default procedure for primary vertex finding at ZEUS. Further details and studies can be found in [45]. The re-vertexing function containing the method explained above and several similar routines that are based on it were combined in the tLite software package [46].

5.2.2 Secondary vertices

In addition to the event primary vertex also secondary vertices were reconstructed in a similar way. This standard reconstruction of secondary vertices does not sufficiently cover all possible topologies automatically, therefore many context-dependent re-vertexing techniques are needed at analysis level. The dedicated re-vertexing that was in particular developed for the b-tagging analyses was done as follows:

As described in Chapter 3 the b quarks that are produced in the hard subprocesses of boson-gluon fusion (cf Fig. 3.5 and 3.6) hadronise and subsequently decay with the decay products appearing in the detector as jets of final-state particles. Because of the long lifetime of b and c hadrons the reconstruction of their decay vertices was of great interest for this analysis, since it provides a useful tool for separating the beauty signal from other (short-lived) particles. The idea therefore was to fit a vertex for each jet using well-reconstructed tracks that could be geometrically associated to it. For the track selection the following cuts were applied:

- $p_t \geq 0.5\,\text{GeV}$,
- # MVD hits ≥ 4,
- # CTD superlayers ≥ 3 or # STT hits ≥ 1.

As described in Section 5.1, at least eight hits were needed for an STT track seed. Thus the request for at least one STT hit effectively corresponds to

requiring eight hits. Furthermore, the tracks had to be associated to a jet with a maximal distance $\Delta R = \sqrt{(\Delta\eta)^2 + (\Delta\phi)^2} < 1$ to the closest jet. If two or more such tracks were associated to a jet, a candidate vertex was fitted from all associated tracks using the DAF algorithm introduced in the previous section. For the purpose of fitting these jet vertices the beam-spot constraint was of course removed from the fit in order not to artificially pull the vertices towards the interaction point. The vertexing routine returned the vertex position including its error matrix as well as the track parameters, weights and the invariant mass, m_{vtx}, of the fitted tracks. For the calculation of m_{vtx} the pion mass $m(\pi^{\pm}) = 139.57\,\mathrm{MeV}$ was assumed for each track.

Figure 5.3 displays control distributions for all selected tracks that were used in the vertex fits. The data distributions for the transverse momentum, p_t, the azimuthal angle, ϕ, the number of passed CTD superlayers and the number of MVD hits were found to be described well by the MC. The η distribution and the number of STT hits revealed some discrepancies. However, these deviations were expected at the time the distributions were made, since the simulation of the forward detector as well as the alignment of the FMVD and the STT had not yet been finalised. For this reason the forward region was explicitly excluded in the analysis at this stage, such that the observed discrepancies did not affect the results.

Conceptually the vertexing procedure could also be applied to jets originating from $c\bar{c}$ production which should be separable from light flavour jets in the same way. The commonly used term for such vertices was *secondary vertices*, which is rather misleading, because in reality they did not necessarily represent the true b hadron decay vertices. If for instance the b hadron decayed in a cascade via a charmed hadron only one vertex was fitted which was likely to be located between the two true decay vertices of the b and c hadrons. Furthermore, additional tracks that did not originate from the b hadron decay could happen to be picked up and associated to the jet as well. For light flavours there should not exist any strongly displaced vertices at all, but still candidate vertices were fitted for each jet also in light flavour events. Nevertheless the term *secondary vertices* has been established in the past and therefore the jet vertices will be referred to as such in the following to simplify matters.

After all possible secondary vertices had been reconstructed in an event, the remaining tracks that had not been associated to any of them were used to fit a new primary vertex, the so-called *reduced primary vertex*. Like in the case of the event primary vertex (see Section 5.2.1) its reconstruction contained a beam-spot constraint. The reduced primary vertex offered the possibility to use an interaction point which was entirely independent of the secondary vertices and the tracks associated to them.

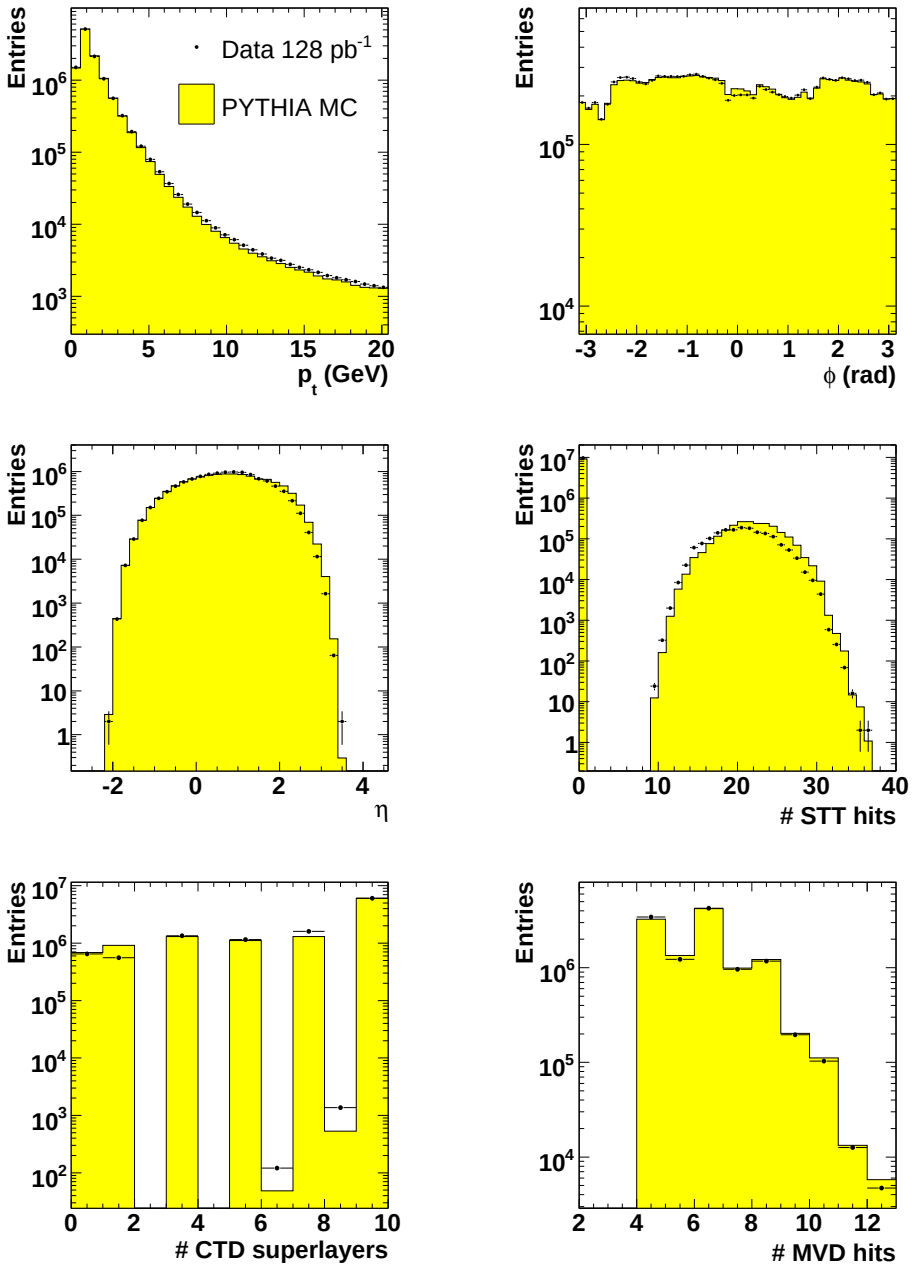

Figure 5.3: Control distributions for p_t, ϕ, η, number of STT hits, number of passed CTD superlayers and number of MVD hits for all selected secondary vertex tracks. The data are denoted by the black points, while the yellow histograms represent the PYTHIA MC distributions.

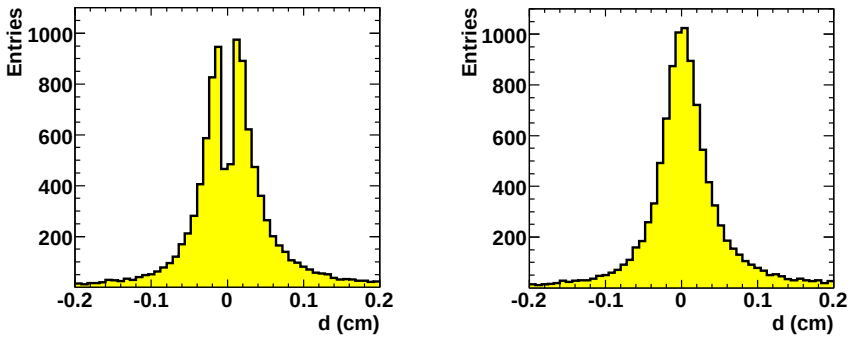

Figure 5.4: Two-dimensional decay length, d, before (left) and after the projection onto the axis of the associated jet (right). Shown are the total PYTHIA MC distributions.

5.2.3 Decay length

As already mentioned in Section 5.2.2 the idea was to separate the beauty and charm signal from the light flavour background by making use of the long lifetimes of the b and c hadrons. A quantity closely related to the lifetime is the decay length, d, which can easily be calculated as the distance between the interaction point at which the hadron is created, i.e. the beam-spot or the primary vertex, and the secondary vertex. Studies showed that there was no visible difference between the usage of the beam-spot or the (beam-spot-constrained) event primary vertex as the reference point for the decay-length calculation. It was decided to use the beam-spot and to restrict the decay length to two dimensions, i.e. to calculate its projection onto the X-Y plane; the latter was done to reduce potential systematic effects which might have occurred due to the much larger width of the beam-spot in Z than in X-Y. The beam-spot position in X and Y was evaluated at $Z = Z_{Vtx}$ taking into account the beam tilt. Although the secondary vertex may not exactly represent the decay vertex of the hadron, it still gives an adequate measure for how long heavy-flavoured hadrons fly before they decay compared to light-flavoured ones. The sign of the decay length was assigned using the axis of the jet the vertex is associated to: if the decay length, $\vec{d}$, was in the same hemisphere as the jet axis, $\vec{j}$, i.e. the scalar product, $\vec{d} \cdot \vec{j}$, was > 0, a positive sign was assigned to it; otherwise the sign of the decay length was negative. Furthermore, the two-dimensional decay length was projected onto the axis of the associated jet. Figure 5.4 displays the decay length before and after the projection onto the jet axis. It is visible that the non-projected decay

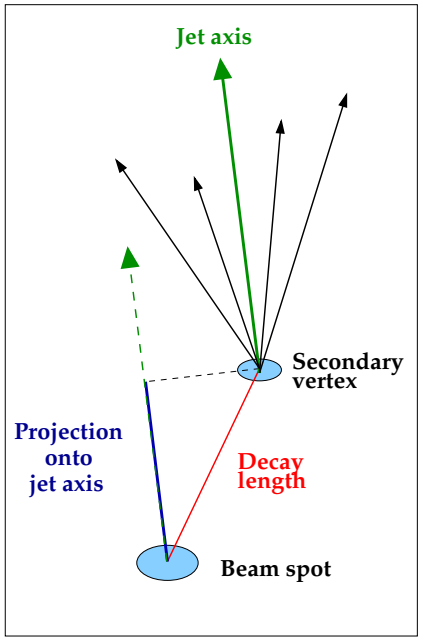

Figure 5.5: Sketch illustrating the determination of the decay length projected onto the axis of the associated jet.

length has a minimum at zero. This is caused by vertices for which the decay length is approximately perpendicular to the jet direction; here the sign of the decay length flips, but the decay length itself is rather unlikely to have a small value which would fill the gap. In order to obtain a continuous Gaussian-like distribution the projection onto the jet axis was done.

Equation 5.2 summarises the calculation of the decay length as discussed above:

$$\begin{aligned} d &= \vec{d}_{2D} \cdot \frac{\vec{j}_{2D}}{|\vec{j}_{2D}|} \\ &= \begin{pmatrix} \Delta X \\ \Delta Y \end{pmatrix} \cdot \frac{\vec{j}_{2D}}{|\vec{j}_{2D}|} \\ &= \begin{pmatrix} X_{vtx} - X_{bsp} \\ Y_{vtx} - Y_{bsp} \end{pmatrix} \cdot \frac{\vec{j}_{2D}}{|\vec{j}_{2D}|}. \end{aligned} \tag{5.2}$$

Here X_{vtx} and Y_{vtx} represent the X and Y position of the secondary vertex, while the beam-spot position is denoted by X_{bsp} and Y_{bsp}.

Figure 5.5 illustrates the determination of the decay length as described previously. The projection onto the jet axis is denoted by the blue line,

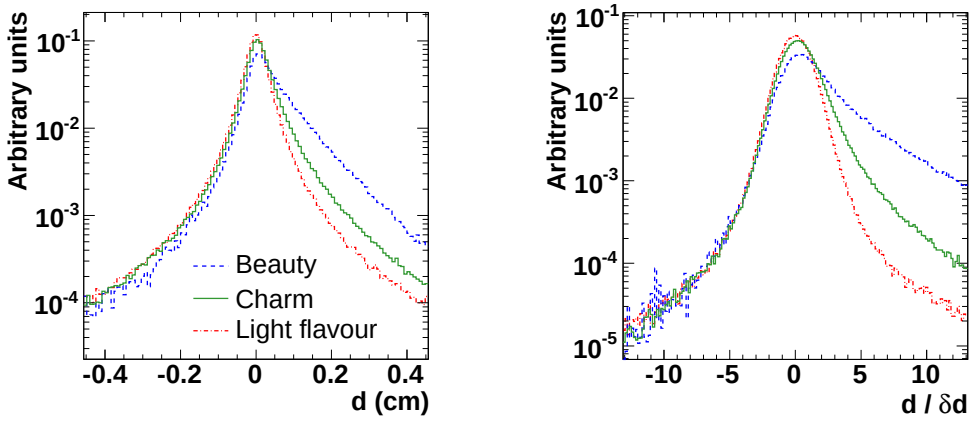

Figure 5.6: 2D decay length, d, projected onto the axis of the associated jet (left) and corresponding decay-length significance, $S = d/\delta d$. The distributions for beauty, charm and light flavours are denoted by the blue, green and red histograms.

while the red line represents the decay length without this projection. The distribution of the 2D decay length is displayed separately for beauty, charm and light flavours in Fig. 5.6 (left). Here the flavour is assigned according to the flavour of the initial partons in the hard subprocess. For light flavours a symmetric distribution around zero was found, while beauty and charm - as expected - revealed a clear asymmetry with an enhancement at large decay lengths which is due to the long lifetime of the b and c hadrons. The negative part of the decay length which originates from secondary vertices being reconstructed opposite to the direction of the associated jets is unphysical and purely caused by detector resolution effects. These effects are independent of any physical process and therefore expected to be identical for all flavours, which is nicely confirmed by the distributions shown in Fig. 5.6. Both the beam-spot as well as the secondary vertices are determined with an uncertainty depicted by the blue ellipses in Fig. 5.5. The calculation of the decay-length error, δd, is thus done as follows:

$$\begin{aligned}(\delta d)^2 &= (\vec{\nabla} d)^T (C^{vtx} + C^{bsp})(\vec{\nabla} d) \\ &= \left(\frac{\partial d}{\partial \Delta X}\right)^2 (C_x^{vtx} + C_x^{bsp}) + 2\frac{\partial d}{\partial \Delta X}\frac{\partial d}{\partial \Delta Y}(C_{xy}^{vtx} + C_{xy}^{bsp}) \\ &\quad + \left(\frac{\partial d}{\partial \Delta Y}\right)^2 (C_y^{vtx} + C_y^{bsp}).\end{aligned}$$

C^{vtx} and C^{bsp} denote the covariance matrices of the secondary vertex and the beam-spot, respectively. The decay-length significance, which will be of great importance for this analysis, is defined as

$$S = \frac{d}{\delta d}.$$

It is a measure for the probability of the vertex being correctly reconstructed at a considerable distance from the interaction point. The significance distributions for beauty, charm and light flavours are displayed in Fig. 5.6 (right). Compared to the decay-length distributions on the left, the significances reveal even larger asymmetries for beauty and charm which implies that the secondary vertices associated to heavy flavour jets could be determined with a higher precision than those associated to light flavour jets.

5.3 Grand Reprocessing

During the HERA II data-taking period the tracking as well as other software packages were continuously improved and extended. Usually the latest developments directly went into the processing of the data that were about to be taken. At regular intervals old datasets were additionally reprocessed in order to adopt the developments that had been implemented since the data were taken. However, following this procedure the different HERA II datasets as well as the corresponding MC simulations were at no time processed with exactly the same software, which made it difficult to combine all datasets in an analysis. This was in particular the case if the analysis in question was heavily relying on the tracking, which was subject to the biggest of all changes. In order to be able to analyse the full HERA II dataset in the future, the *Grand Reprocessing (GR)* effort was started shortly after the end of the data-taking. All software packages were frozen and used for reprocessing the full dataset. At the time this analysis was close to being finalised and published by the ZEUS collaboration as a preliminary result the GR was still in progress and the corresponding MC simulations had not been entirely produced yet. Therefore certain corrections that will be discussed in the following sections were applied to the pre-GR data and MCs in order to obtain datasets which already contained most of the benefits from the GR although they had not been officially Grand-Reprocessed yet. For the extension of the analysis that was done later and will be the topic of Chapter 10, the only fully available GR dataset at that time, namely the 2006/07 positron running, was used.

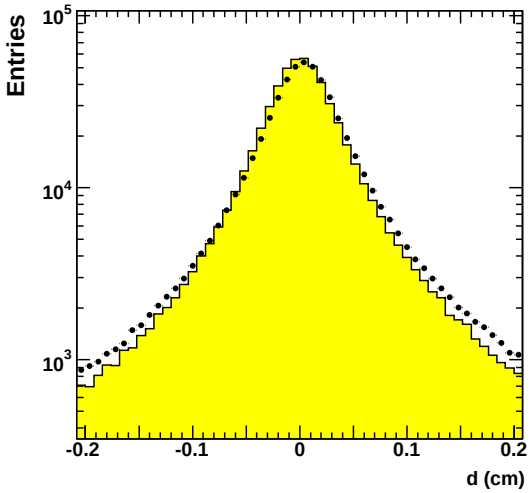

Figure 5.7: 2D decay-length distribution before alignment corrections. The data (black points) are significantly shifted with respect to the MC, represented by the yellow histogram.

5.4 The Z-shift problem

For such a kind of analysis as the one in this thesis is it mandatory to reconstruct tracks and vertices with an accuracy of a few microns. Therefore it is not surprising that several tracking problems became conspicuous only in the course of this work. One of them, the so-called *Z-shift problem*, which was studied in cooperation with the ZEUS tracking group, will be described in the following. Another tracking issue that needed to be dealt with was the study of MVD hit resolutions in data and MC. A correction procedure for adjusting the resolutions in the MC to reproduce the data was developed in the context of this analysis and is discussed in Appendix A.

The Z-shift problem was initially observed indirectly in the basic decay-length distributions. Figure 5.7 shows the 2D decay length for data and MC. The distribution for data is significantly shifted to the right with respect to the MC distribution. The observed shift was found to be independent of quantities like the azimuthal angle, ϕ, of the jets or vertices and the track momenta and it appeared in both 2D and 3D distributions. However, some dependences on the polar angle of the jets, θ, and on the Z position of the primary vertex, Z_{Vtx}, could be seen (see Fig. 5.8). The relative shifts of data and MC with respect to zero were evaluated by fitting the peak

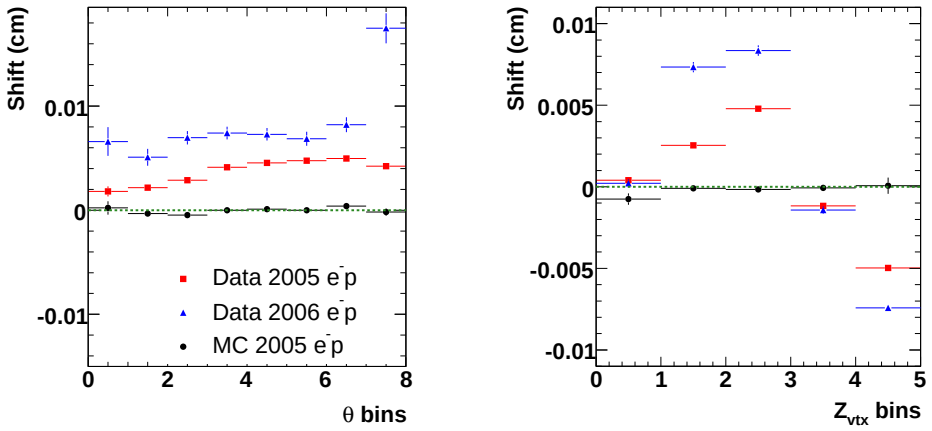

Figure 5.8: Decay-length shift with respect to zero as a function of θ (left) and Z_{Vtx} (right). Two-dimensional and three-dimensional data distributions from the 2005 and 2006 $e^{-}p$ running periods (red and blue squares and triangles) are compared to the corresponding MC samples (black circles).

regions of the distributions with a Gaussian with the mean value of the fit results representing the shift. Figure 5.8 (left) shows the decay-length shift in bins of θ of the jet which the secondary vertex is associated to. 2D and 3D data distributions from two different data sets (red and blue squares and triangles) are compared to the distributions obtained from the corresponding MC samples (black circles). It can be seen that all data distributions reveal large deviations of up to $80\,\mu$m, while the MC distributions are almost flat at zero. A similar behaviour can be found in Fig. 5.8 (right) which displays the decay-length shift in bins of Z_{Vtx}. Here an even stronger dependence can be observed for the data, while the MC is again reasonably stable and flat at zero. Even though also the two-dimensional decay length was used for these studies, the vertex fit that this decay length results from had always been done in three dimensions. In order to verify the dependence of the observed shift on Z, the secondary-vertexing routines were modified such that also the vertex fit itself was performed only in X and Y. Therefore the helix parameters Z_h and $\cot(\theta)$ (see Section 5.1) of all tracks entering the vertex fit as well as all covariance matrix elements depending on them were set to zero. The decay-length distribution obtained from the vertex fit in two dimensions is displayed in Fig. 5.9. Very good agreement between data and MC was observed. Furthermore it was checked and confirmed that the width of the decay-length distribution remained unchanged.

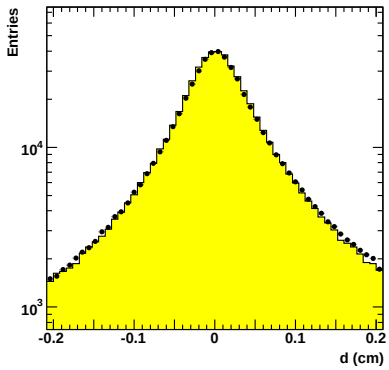

Figure 5.9: Decay-length distribution for data (black points) and MC (yellow histogram) after the vertex fit in two dimensions.

The results of these studies indicated that (at least parts of) the Z-shift problem might originate from inaccuracies in the detector alignment, especially since all Monte Carlo distributions were unaffected. Therefore further studies were performed by members of the ZEUS tracking group, leading to two major improvements in the alignment procedure [56].

In general, the MVD and the forward detector are aligned with respect to the CTD, with the MVD alignment being done first and the alignment constants for the forward detector being determined afterwards. The MVD alignment consists of two parts, which are distinguished by the types of tracks that are selected to align the MVD sensors. In one part tracks from ep collision events, i.e. typical events for physics analyses, are used. The disadvantage of such tracks is that they are not sensitive to certain systematic displacements of sensors (so-called *weak modes*), which do not affect the quality of the track fit. In order to compensate this deficit, in the second part of the alignment procedure cosmic muons which pass through the whole detector are selected. The full information on the detector misalignment can finally be obtained from the combination of ep and cosmics alignment. For detailed information about the MVD alignment procedure see [75].

The first of the two improvements in the alignment procedure concerns the ep collision events. Here the X and Y positions of the beam-spot as well as the Z position of the primary vertex were used as a constraint by adding them as an additional hit. However, the tracks used for the alignment were usually also used for fitting the primary vertex. In order to keep the vertex constraint independent of the reconstruction of the selected tracks, the procedure was changed such that those tracks were removed from the

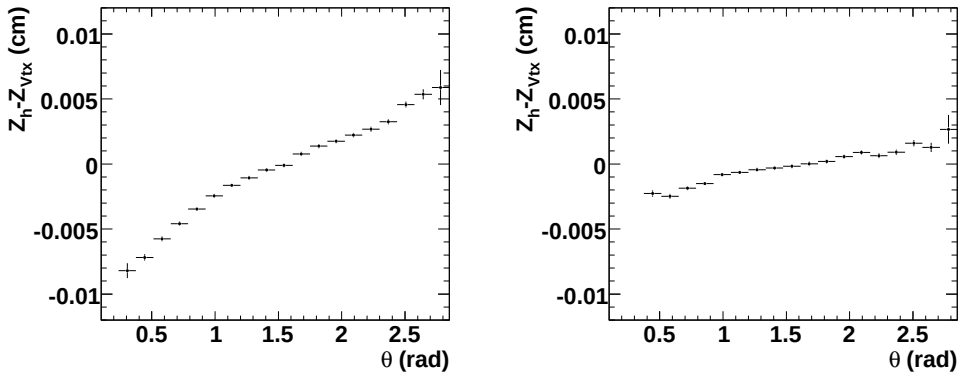

Figure 5.10: Mean $Z_h - Z_{Vtx}$ as a function of θ for all selected tracks after the old (left) and the new cosmics treatment (right) [55].

vertex fit. Subsequently, the re-fitted primary vertex could be used as an independent constraint.

The second improvement was a refinement of the cosmics treatment within the alignment procedure. High-energy cosmic muons can traverse the whole detector. If such a muon happened to pass through the MVD, its track was reconstructed as two tracks originating from the point of closest approach and used as such for the alignment. Given the finite precision of the pattern recognition and the track fit this scenario allowed the two halves of the MVD, in each of which one of the two tracks was reconstructed, to be displaced with respect to each other.

Figure 5.10 (left) shows the Z-shift, which is here defined as $Z_h - Z_{Vtx}$ of all selected tracks, as a function of θ using the cosmics treatment that was explained previously. Here the track helices have been re-referenced such that Z_h denotes the distance in Z direction of the point of closest approach to the beam-spot and not to $(0, 0, 0)$ as described in Section 5.1. A strong linear dependence on θ can be observed confirming the indications obtained from the decay-length studies (see Fig. 5.8). The largest shifts of $\approx$ 60–80 μm with respect to zero occur for tracks going to the very forward and backward parts of the detector. The alignment procedure was subsequently changed such that the cosmics tracks were treated as single tracks fixing the positions of the upper and the lower half of the MVD with respect to each other. The Z-shift as it turns out with the improved cosmics treatment is displayed in Fig. 5.10 on the right. A clear improvement can be seen with the maximum shift being reduced from 80 μm to 20 μm.

5.5 Alignment and beam-spot corrections

When the studies on the Z-shift problem were performed, the Grand Reprocessing (GR) of all data samples (see Section 5.3) was already in preparation. The new alignment was immediately integrated in the tracking software, but due to the tight schedule of the GR no more intermediate pre-GR versions of alignment GAFs[2], software and data samples were foreseen. Furthermore, the inclusive secondary vertexing analysis was the only analysis directly depending on these changes: An effect of a few microns would not have even shown up in most of the other analyses, for which the vertexing precision as well as the statistics were much lower. This is also the reason why these issues had not been spotted earlier. Therefore it was decided to stick to the original schedule and not to create a new pre-GR version of the relevant tracking software packages and GAFs, but to apply the latest MVD alignment by hand in order to be able to proceed with the analysis. This was done by reading in the alignment constants provided by the tracking group [56] and re-running the track fits offline, i.e. on ntuple level. However, it has to be kept in mind that the alignment of the forward detector, which depends on the MVD alignment and is therefore evaluated on top of it, was not renewed. Hence the forward region had to be explicitly excluded from the analysis of pre-GR datasets.

Changing the alignment of the microvertex detector naturally goes along with shifting the event primary vertex and the beam-spot. Since these are needed for the calculation of the decay length, an appropriate correction had to be applied. The movement of the beam-spot caused by the alignment correction was evaluated from the mean impact parameter, IP_{mean}, of the event as a function of the azimuthal angle, ϕ, of the tracks and the Z_{Vtx} position. Here the impact parameter was calculated as D_0 with respect to the beam-spot. In order to determine IP_{mean}, well-reconstructed events and tracks were selected which had to fulfill the following conditions:

- Distance of the primary vertex in X-Y from the beam-spot $< 1\,\mathrm{cm}$,
- $|Z_{Vtx}| < 20\,\mathrm{cm}$,
- Tracks with $p_t \geq 0.5\,\mathrm{GeV}$,
- $|Z_h| < 30\,\mathrm{cm}$,
- # MVD hits ≥ 6.

[2] A *General ADAMO File (GAF)* is a special data bank containing e.g. tables with alignment constants. The structure of these tables is the same as for the tables which are used for storing tracks or similar objects during the production of datasets.

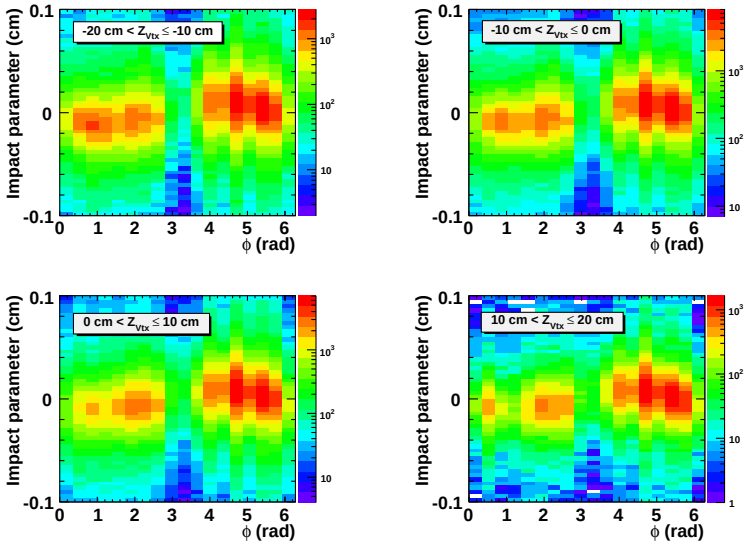

Figure 5.11: Impact parameter as a function of the azimuthal angle, ϕ, in four bins of the Z vertex position.

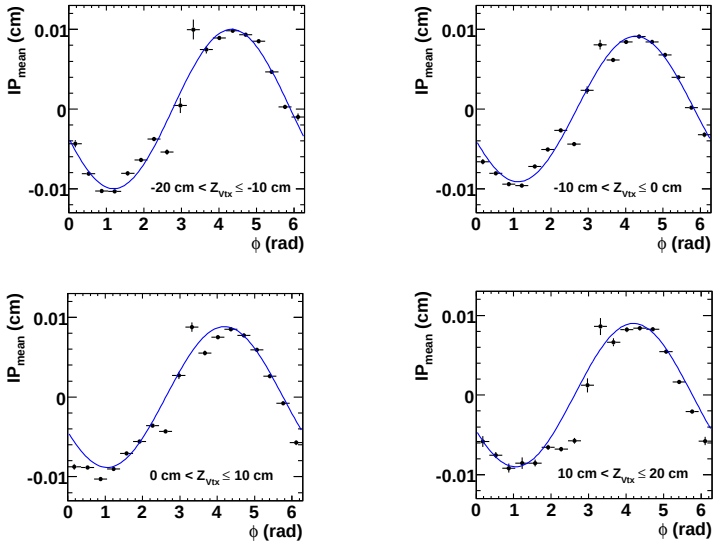

Figure 5.12: Mean impact parameter as a function of the azimuthal angle, ϕ, in four bins of the Z vertex position. The blue line represents the sinusoidal fit function to the data.

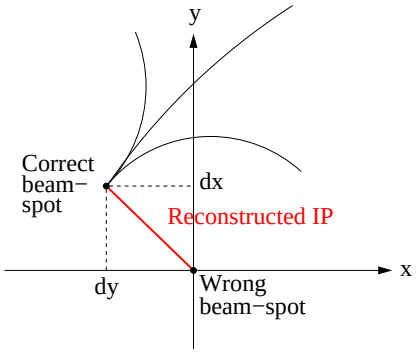

Figure 5.13: Determination of dx and dy. The red line indicates the wrongly measured impact parameter (IP).

Figure 5.11 shows the impact parameter of these tracks as a function of ϕ for four different Z_{Vtx} bins ranging from $Z = -20\,\text{cm}$ to $Z = +20\,\text{cm}$. For geometrical reasons the statistics around $\phi = \pi$ are lower than anywhere else; in this region only two MVD ladders could at most be passed by a track, hence the probability for the tracks to have the required six MVD hits was much lower than in the other ϕ regions. If the beam-spot is determined on condition of a fully aligned detector, the mean impact parameter is expected to be zero. But in the present case, where the detector had been aligned after the determination of the beam-spot, a sinusoidal shape with maximum values of $IP_{mean} = \pm 0.01\,\text{cm}$ could be seen. This indicated that the beam-spot needed to be moved according to the new alignment. The profiles of these two-dimensional distributions, which are shown in Fig. 5.12, were suitable for evaluating the correction values for the beam-spot position. First, the changes in X and Y were determined for each Z_{Vtx} bin with the help of sinusoidal fits to the data. The correction values were calculated as

$$\begin{aligned} -d_x &= IP_{mean}(\phi = \pi/2) \\ d_y &= IP_{mean}(\phi = 0). \end{aligned}$$

Figure 5.13 illustrates the determination of d_x and d_y. While the periodic structure of the mean-impact-parameter distribution as a function of ϕ visualises the displacement in X and Y, the dependence on Z_{Vtx} corresponds to a change of the beam tilt, which completes the parametrisation of the correction. Figure 5.14 displays d_x and d_y as a function of Z_{Vtx} with the straight line representing the linear fit of the data. Thus the new beam-spot position for each event was finally determined from the Z_{Vtx} dependence of

d_x and d_y as

$$\begin{aligned} X_{BSP}^{new} &= X_{BSP} - d_x(Z_{Vtx}) \\ Y_{BSP}^{new} &= Y_{BSP} - d_y(Z_{Vtx}). \end{aligned}$$

After applying the beam-spot correction the impact-parameter distributions as a function of ϕ and Z_{Vtx} were re-done in order to confirm that the procedure worked as expected. Figures 5.15 and 5.16 show that the mean impact parameter, IP_{mean}, as a function of ϕ is now indeed reasonably stable around zero for all Z_{Vtx} bins. The average deviation from zero amounts to $\approx 10\,\mu$m; the larger deviations around $\phi = \pi$ result from a less precise determination of the mean impact parameter due to low statistics as stated before.

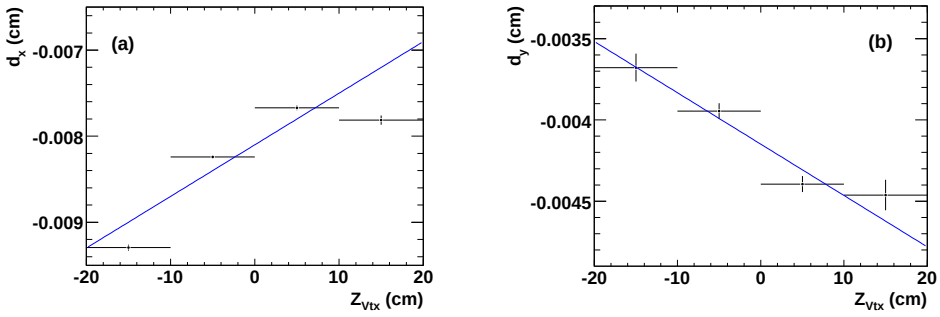

Figure 5.14: Beam-spot corrections for X (a) and Y (b) as a function of the Z vertex position. The lines represent the linear fits to the data.

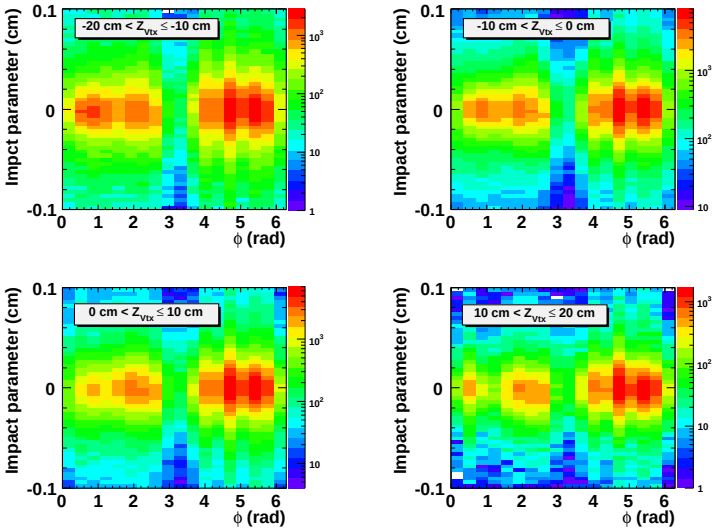

Figure 5.15: Impact parameter as a function of the azimuthal angle, ϕ, in four bins of the Z vertex position after the beam-spot correction has been applied.

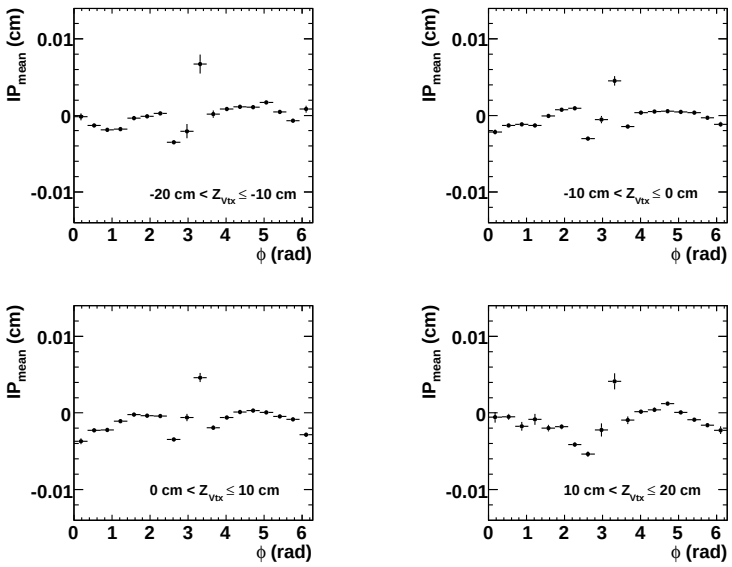

Figure 5.16: Mean impact parameter as a function of the azimuthal angle, ϕ, in four bins of the Z vertex position after the beam-spot correction has been applied.

5.6 Summary of tracking and vertexing

A dedicated secondary-vertexing technique matching the topology of events from beauty and charm jet production was developed. In the course of the vertexing studies it was shown that an analysis using these techniques is sensitive to inaccuracies of $\mathcal{O}(\mu m)$ and that a precise tracking and alignment is crucial for the feasibility of such an analysis. A better precision than for any of the previous analyses is needed and thus the adjustment and fine-tuning of tracking, vertexing and alignment parameters is challenging. In cooperation with the ZEUS tracking group several improvements, which were also directly beneficial for the Grand Reprocessing effort, could be achieved in the context of the analysis. As the Grand Reprocessing was not yet finished at the time the analysis was done, corrections were applied in order to make use of the latest developments also using pre-GR data; after the corrections they were expected to be of a similar quality as the Grand-Reprocessed data. However, one restriction had to be made: Since the simulation and the alignment of the FMVD and the STT had not been finalised yet, the forward direction had to be explicitly excluded in analyses using pre-GR data. Hence the measurement presented in this thesis was first restricted to the barrel region of the detector using jets with $-1.6 \leq \eta^{Jet} < 1.3$ (cf Chapters 6-9) and extended to the full region ($-1.6 \leq \eta^{Jet} < 2.5$) as soon as the Grand-Reprocessed data were available (cf Chapters 10 and 11).

Chapter 6

Event and candidate selection

In this chapter the selection of dijet photoproduction events and secondary vertex candidates will be described.

6.1 Datasets

For this analysis data taken in the 2006/07 e^+p running period with a corresponding integrated luminosity

$$\mathcal{L}_{Data} = 128\,\mathrm{pb}^{-1}$$

were available. This was the only data sample, which was processed with a version of the reconstruction software ZEPHYR (cf Section 4.1.2) that already included the latest tracking developments which were known to be essential for a precise determination of secondary vertices. One of the crucial ingredients was the correct simulation of the MVD hit resolution; studies and details on this issue can be found in Appendix A and in [57]. Together with the corrections discussed in Chapter 5 it could be considered to be of similar quality to the Grand Reprocessing datasets, which were just being processed.

A corresponding set of PYTHIA MC samples subdivided into the different types of physics processes as introduced in Section 4.1.1 was produced. In Table 6.1 all sub-samples and the corresponding integrated luminosities, $\mathcal{L}$, are listed. For the light flavour samples the excitation processes were included in the resolved sample. Since the beauty and charm samples are those containing the signal events for which production cross sections are intended to be measured, they are required to be available in a sufficient quantity to ensure a satisfactory statistical precision. Therefore roughly 10 times the data statistics was produced in case of beauty, while the size of the charm

Process type	Integrated luminosity $\mathcal{L}$ (pb^{-1})		
	Beauty	Charm	Light flavours
Direct	1503	542	140
Resolved	1556	601	134
Excitation γ	1417	563	
Excitation p	1764	540	

Table 6.1: Dijet Monte Carlo samples with corresponding integrated luminosities, $\mathcal{L}$ for the different process types. The light flavour excitation processes are included in the resolved sample.

samples corresponded to approximately $5 \cdot \mathcal{L}_{Data}$. The light flavour samples containing the background events for this analysis were available with an integrated luminosity corresponding to approximately that of the data. In principal an integrated luminosity comparable with $\mathcal{L}_{Beauty}$ would have been desirable for charm and light flavours as well, but due to substantially higher production cross sections huge datasets and consequently a lot of storage space would have been needed. Therefore a compromise had to be made between a sufficient statistical precision and available disk capacities.

6.2 Jets

As for the selection of heavy quark production events high-P_T jets are usually already required at trigger level (cf Section 6.3) a reliable reconstruction of these jets is essential for the identification of heavy quark decays.

Several jet reconstruction algorithms are available, of which two of them have been used in this analysis and will thus be described in the following. The input elements for the algorithms can for example be calorimeter cells, objects combining calorimeter and tracking information (so-called *ZUFOs* [58]) or even hadrons or partons, if jets on truth level are requested. Two properties that are required for any jet finding algorithm are *collinear safety* and *infrared safety*. Observables are collinear safe if in a configuration of n objects which the algorithm is run on they are not affected by replacing any object by a collinear pair of objects. From the experimental point of view this condition corresponds to the jets being unaffected by the resolution of two collinear objects hitting the same CAL cell. Observables are infrared safe if adding an infinitely soft object has no effect on the outcome. In the experiment this corresponds to jets being unaffected by CAL noise or

the exact setting of the signal thresholds for the CAL cells[1]. The conditions of collinear and infrared safety are both fulfilled for the two following jet reconstruction algorithms.

The so-called *cone algorithm* is based on the assumption that the particles belonging to a jet are all located within a cone around the direction of the initial parton. The fundamental concept is the maximisation of the transverse energy, E_T, within a cone of radius

$$R = \sqrt{(\Delta\eta)^2 + (\Delta\phi)^2} \tag{6.1}$$

with $\Delta\eta$ and $\Delta\phi$ denoting the differences in pseudorapidity, η, and azimuthal angle, ϕ, between the objects the algorithm is run on and the jet direction. Usually the maximal radius is set to $R_{max} = 1$. If two jets identified with the cone algorithm overlap and a significant fraction – typically 50-75 % – of the total energy of the less energetic jet is located in the overlap region, the jets are merged; otherwise two jets are reconstructed with the common objects being assigned to the closest jet.

A different approach is used by *cluster algorithms*. A very prominent example is the k_t algorithm, which is based on the successive combination of close object pairs into clusters. For each pair (i, j) a distance, d_{ij}, is calculated as

$$d_{ij} = \min(E_T^i, E_T^j)^2 \Delta R^2 \tag{6.2}$$

with E_T^k denoting the transverse energies of the two objects and R being defined as in Eqn. 6.1. Note that for small angles, ξ, between the objects, i.e. $\Delta R \ll 1$, Eqn. 6.2 results in

$$d_{ij} = \min(E_T^i, E_T^j)^2 \Delta R^2 \approx \min(E^i, E^j)^2 \Delta\xi^2 \approx k_t^2,$$

giving the algorithm its name. Furthermore, for each input object, i, a distance d_{ib} to the beam particles is defined:

$$d_{ib} = (E_T^i)^2 R^2.$$

If the minimum of all distances between paired objects is smaller than the minimum of all distances between single objects and the beam particles, i.e.

$$\min(d_{ij}) < \min(d_{ib}),$$

objects i and j are merged into a cluster. Otherwise, object i is complete and marked as a jet. This procedure is iterated until no more pairs with an

[1] In pQCD the two requirements ensure the evasion of collinear and soft divergences.

energy smaller than a certain fraction, f, of the total energy in the event can be found; for tuning purposes f can be adjusted by means of a cutoff parameter. In contrast to the cone algorithms the k_t cluster algorithm has the advantage that it naturally avoids the problem of overlapping jets.

More information on cone and cluster algorithms can be found in [59]. More recent methods for jet reconstruction starting to be used in high energy physics are the anti-k_t and SISCone algorithms [60, 61].

6.3 Event selection

For the initial pre-selection of γp dijet events the TLT trigger HFL5 was used. It contained the following cuts:

- 2 jets (cone algorithm) with $E_T^{Jet} > 4.5\,\mathrm{GeV}$ and $|\eta^{Jet}| < 2.5$,
- $P_Z/E < 0.95$,
- $E - P_Z < 100\,\mathrm{GeV}$.

Here E denotes the total energy in the event and P_Z the Z-component of the total momentum. Both quantities were calculated from calorimeter information. The jet reconstruction at trigger level was done using the cone algorithm described in the previous section.

Note that in case of the charm and light flavour MC samples the condition of at least two jets per event with $E_T^{Jet} > 4\,\mathrm{GeV}$ and $|\eta^{Jet}| < 3$ was already required during the truth level generation procedure running the k_t cluster algorithm on hadron level. These cuts reduced the samples by a factor 15-30 depending on the process type and thus allowed the production of (dijet) samples corresponding to a higher integrated luminosity (cf Section 6.1).

At analysis level jets reconstructed with the k_t cluster algorithm were used to apply the final selection. Two jets with

$$P_T^{Jet\,1(2)} \geq 7(6)\,\mathrm{GeV} \text{ and } |\eta^{Jet}| < 2.5$$

were required in each event with Jet 1 and Jet 2 being the jets with the largest and second largest transverse momentum, respectively. Previous studies have shown that the HFL5 trigger was not equally efficient in data and MC [63]; therefore a trigger efficiency correction had to be applied. The evaluation of this correction was done on data taken during the 2005 $e^- p$ running and is displayed in Fig. 6.1: On the left the HFL5 trigger efficiency as a function of the transverse momentum of the second highest energetic jet, $P_T^{Jet\,2}$, is shown for data and MC, while their ratio including a linear fit of the dependence on

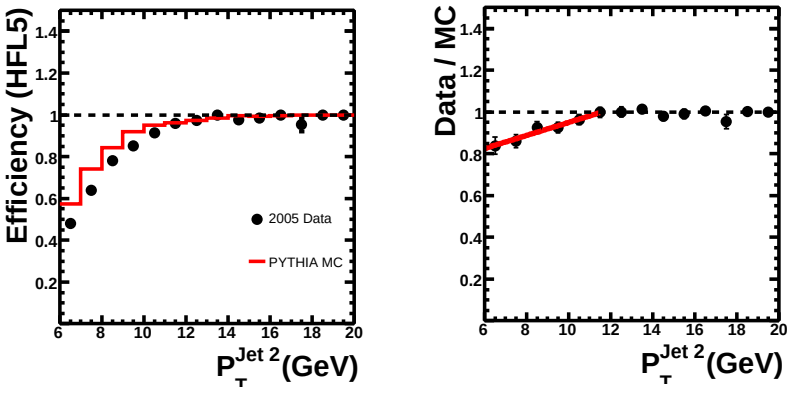

Figure 6.1: HFL trigger efficiency as a function of the transverse momentum of the second highest energetic jet, $P_T^{Jet\,2}$, for data and MC (left) as well as their ratio (right) [63]. The linear fit which represents the trigger efficiency correction is indicated by the red line.

$P_T^{Jet\,2}$ up to 11.5 GeV is depicted on the right. Hence the trigger efficiency correction was applied by assigning a weight

$$w_{trigger} = 0.638 + 0.031 \cdot P_T^{Jet\,2}$$

to all MC events with $P_T^{Jet\,2} < 11.5\,\text{GeV}$.

In order to select events in the photoproduction (γp) regime and to discard those from deep inelastic scattering (DIS), it was required that no candidate for the scattered positron was found. Since the four-momentum transfer is low in γp events the incoming positron is hardly deflected and escapes along the beampipe after the hard scatter. Candidates for the scattered positron were identified by the Sinistra programme [64] and assigned a probability $P_{e'}$. For the final selection events with the most probable candidate having an energy $E_{e'} > 5\,\text{GeV}$, a probability $P_{e'} > 90\,\%$ and an inelasticity $y_{el} < 0.9$ were rejected. The inelasticity, y_{el} (cf Section 3.3), was calculated with the so-called *electron method*, which exclusively uses the scattering angle, θ_e, and the energies before and after the collision, $E_{e/e'}$, for the determination of the kinematic variables:

$$\begin{aligned} Q^2_{el} &= 2E_e E_{e'}(1+\cos\theta_e), \\ y_{el} &= 1 - \frac{E_{e'}}{2E_e}(1-\cos\theta_e), \\ x_{el} &= \frac{Q^2_{el}}{s y_{el}}. \end{aligned}$$

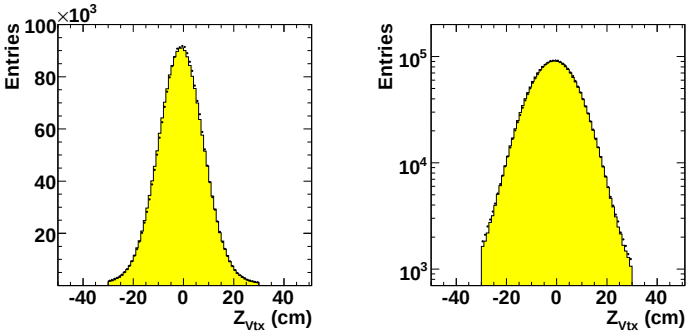

Figure 6.2: Z_{Vtx} distribution on linear (left) and logarithmic scales (right). The data are denoted by the black points, while the histograms represent the PYTHIA MC distributions.

Furthermore, the requirement $0.2 < y_{JB} < 0.8$ was used to reject remaining DIS interactions and beam-gas events. Here, the inelasticity was evaluated using the Jaquet-Blondel method [65]:

$$y_{JB} = \frac{1}{2E_e} \sum_i (E_i - p_{z,i}).$$

The sum runs over all ZUFOs, i.e. final-state objects combining calorimeter and tracking information [58].

Finally, only events with a well-reconstructed primary vertex in the centre of the interaction region were selected by requiring $|Z_{Vtx}| < 30\,\text{cm}$ in order to discard further non-ep interactions. Control distributions for Z_{Vtx} are displayed in Fig. 6.2; good agreement between data and MC was found.

6.4 Secondary vertex candidates

Secondary vertices which provide the main tool for separating the long-lived beauty and charm hadrons from the light flavour background were reconstructed as described in Section 5.2.2. In order to select good quality vertices and reject questionable candidates, further cuts were applied:

$$\begin{aligned} \chi^2/ndf &\leq 6, \\ d_{XY} &< 1\,\text{cm}, \\ d_Z &< 30\,\text{cm}. \end{aligned}$$

d_{XY} and d_Z denote the distances of the vertices to the beam-spot in X-Y and Z, while the fit significance is represented by χ^2/ndf. The cut values

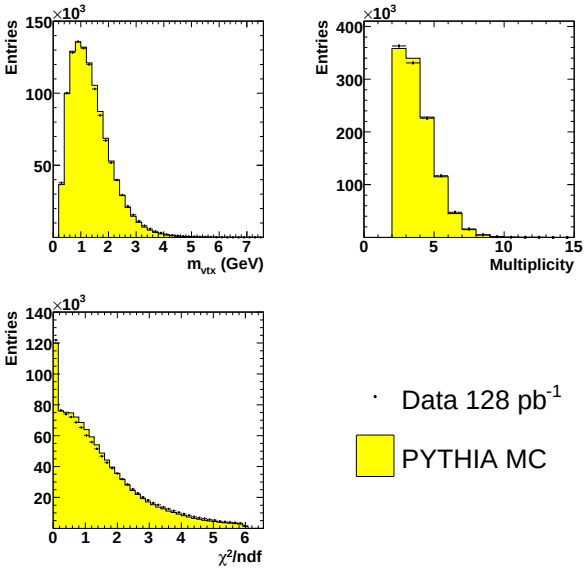

Figure 6.3: Invariant mass of the secondary vertex tracks, m_{vtx}, track multiplicity and χ^2/ndf of secondary vertices. The data are denoted by the black points, while the yellow histograms represent the PYTHIA MC distributions.

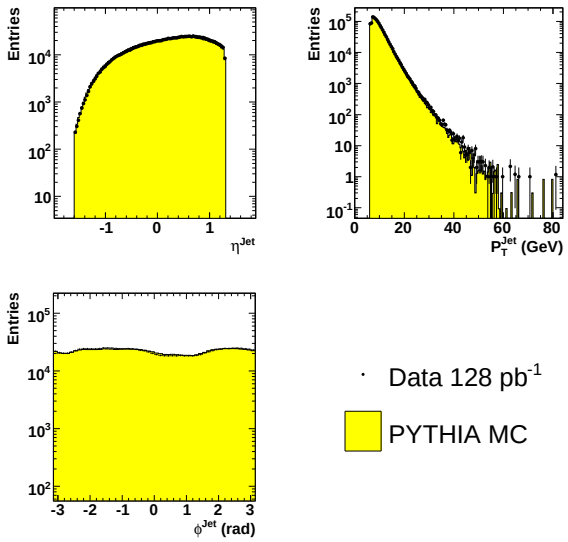

Figure 6.4: Pseudorapidity, η^{Jet}, transverse momentum, P_T^{Jet}, and azimuthal angle, ϕ^{Jet}, for jets with associated vertices. The data are denoted by the black points, while the yellow histograms represent the PYTHIA MC distributions.

were chosen according to previous studies, which confirmed a considerable suppression of background vertices after imposing the quality cuts [66]. In addition, the selected vertices were required to have an invariant mass of the fitted tracks $m_{vtx} < 7.5\,\text{GeV}$, since a beauty signal at significantly higher masses than the nominal b hadron masses of 5–6 GeV is not meaningful.

Only those secondary vertices that were associated to one of the two jets with the highest transverse momenta, P_T^{Jet}, were considered, since these jets were most likely to correspond to the two b jets. As explained in Chapter 5 there was no appropriate alignment of the forward detector yet and the forward region had to be excluded in analyses performed on pre-GR datasets. For this reason secondary vertices which were either associated to jets with $\eta^{Jet} \geq 1.3$ or contained at least one track with $\eta^{track} \geq 1.5$ were discarded.

Figure 6.3 shows control distributions for the selected secondary vertices; displayed are the invariant mass, m_{vtx}, the track multiplicity and the fit significance, χ^2/ndf. In all distributions reasonable agreement between the data and the PYTHIA MC is observed. The strong peak at very small values of χ^2/ndf is caused by vertices with only two fitted tracks. This is expected since it is much more likely to obtain a well-defined vertex from fitting two tracks, if their orientation is such that they most probably originate from the same vertex, than from a fit using three or more tracks. In Fig. 6.4 control distributions for the corresponding jets, i.e. those of the two highest energetic jets per event with associated secondary vertices, are shown. The η^{Jet}, P_T^{Jet} and ϕ^{Jet} distributions are all described well by the MC.

6.5 Summary of cuts

In the following, the cuts for the event, track and secondary vertex candidate selection are summarised.

Photoproduction dijet events:

- HFL 5 trigger:
  - 2 jets (cone algorithm) with $E_T^{Jet} > 4.5\,\text{GeV}$ and $|\eta^{Jet}| < 2.5$,
  - $P_z/E < 0.95$,
  - $E - P_z < 100\,\text{GeV}$;
- "Offline" jet selection:
  2 jets (k_t algorithm) with $P_T^{Jet1(2)} > 7(6)\,\text{GeV}$ and $|\eta^{Jet}| < 2.5$;
- $0.2 < y_{JB} < 0.8$;

- No scattered positron candidate with
  $E_e > 5\,\text{GeV} \wedge P_e > 90\,\% \wedge y_e < 0.9$;
- $|Z_{Vtx}| < 30\,\text{cm}$.

Tracks for secondary vertexing:

- $p_t \geq 0.5\,\text{GeV}$;
- # MVD hits ≥ 4;
- # CTD superlayers ≥ 3 or # STT hits ≥ 1;
- Jet association within $\Delta R < 1$.

Secondary vertex candidates:

- $\chi^2/ndf \leq 6$;
- Distance from the interaction point $d_{XY} < 1\,\text{cm}$ in X-Y;
- Distance from the interaction point $d_Z < 30\,\text{cm}$ in Z;
- Association to one of the two highest energetic jets, if $\eta^{Jet} < 1.3$;
- No fitted track with $\eta^{track} < 1.5$;
- $m_{vtx} < 7.5\,\text{GeV}$.

Chapter 7

Extraction of the beauty fraction

As described in the previous chapter events containing secondary vertex candidates that fulfilled the criteria listed in Section 6.4 were selected for the signal extraction. In Fig. 7.1 and 7.2 control distributions for the selected vertices and the associated jets are shown. Here and in all following figures blue and green are used for the signal contributions from beauty and charm, respectively, while the total MC distributions are represented by the yellow histograms. The comparison with the data that are denoted by the black points demonstrates good agreement. Note that the different MC con-

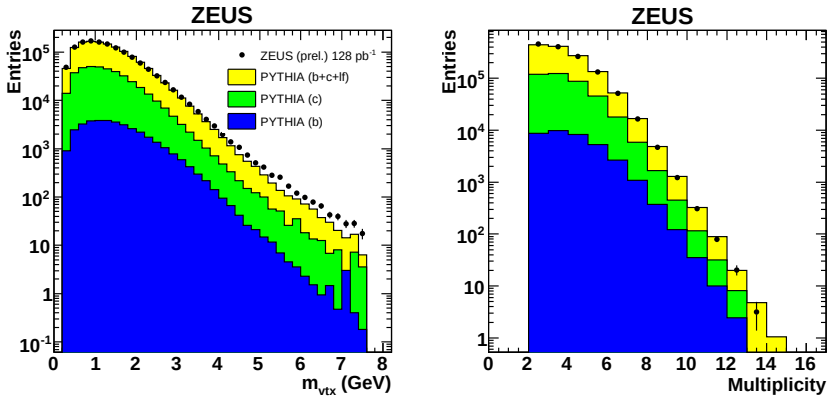

Figure 7.1: Distribution of the invariant vertex mass, m_{vtx}, (left) and the track multiplicity of the selected secondary vertices (right), displaying the data and total MC distributions as well as the contributions from the beauty and charm MC subsamples normalised according to the fractions obtained from the fit.

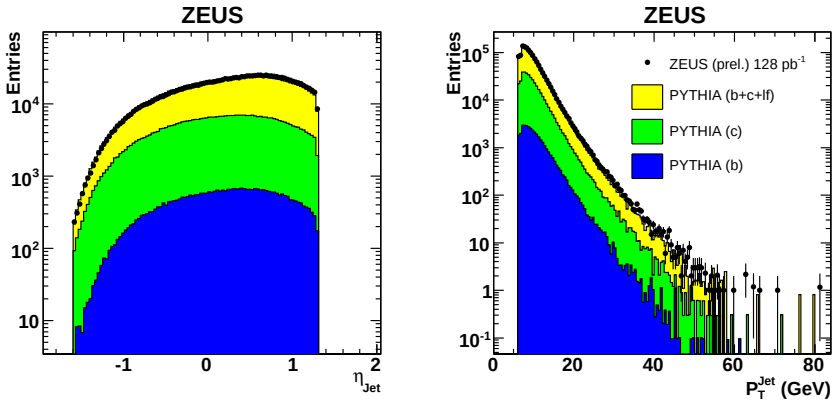

Figure 7.2: Distribution of η^{Jet} (left) and P_T^{Jet} (right), displaying the data and total MC distributions as well as the contributions from the beauty and charm MC subsamples normalised according to the fractions obtained from the fit. Only jets associated to a selected secondary vertex are taken into account.

tributions have already been scaled with the results obtained from the fit explained below.

The vertex candidates were defined as beauty or charm *signal* according to whether the event contained at least one b or c quark. This included heavy quarks from the hard subprocess as well as those originating from gluon splitting ($g \to q\bar{q}$) in light flavour events.

For each candidate vertex the two-dimensional decay length projected onto the axis of the associated jet was calculated according to Equation 5.2. The heavy flavour content of the sample was then determined by means of the decay-length significance, S, which is defined as the decay length, d, divided by its error, δd. It was combined with the invariant mass, m_{vtx}, of the tracks contributing to the secondary vertex fit to enhance the discriminating power: The decay-length significance distribution was divided into different m_{vtx} bins in order to provide an almost pure beauty region at $2\,\text{GeV} \leq m_{vtx} < 7.5\,\text{GeV}$, while the lower mass bins were dominated by charm. Figure 7.3 shows S for the total m_{vtx} range and for $2\,\text{GeV} \leq m_{vtx} < 7.5\,\text{GeV}$. The contributions from beauty and charm are indicated by the blue and green lines; the red lines represent the light flavour content. It is notable that an almost pure beauty sample can be obtained if secondary vertices with $m_{vtx} \geq 2\,\text{GeV}$ and $S \geq 8$ are selected (cf Section 8.2). The negative side of the significance (S^-, $S < 0$), which is unphysical and caused by detector-related effects, was then mirrored onto and subtracted from the positive side (S^+, $S > 0$). A minimisation of the light flavour (background) contribution was expected fol-

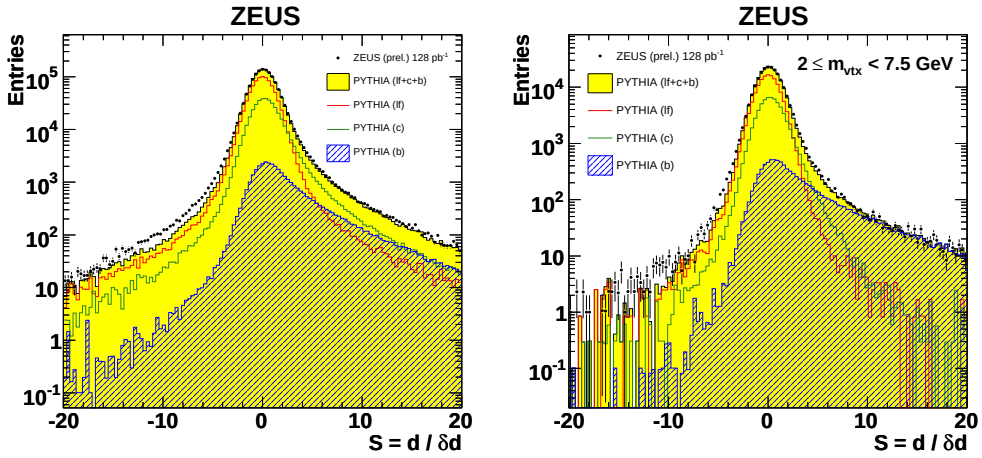

Figure 7.3: Distribution of decay-length significance, S, for the total secondary vertex mass range (left) and for $2\,\text{GeV} \leq m_{vtx} < 7.5\,\text{GeV}$ (right) displaying the data and total MC distributions as well as the contributions from the three MC subsamples normalised according to the fractions obtained from the fit.

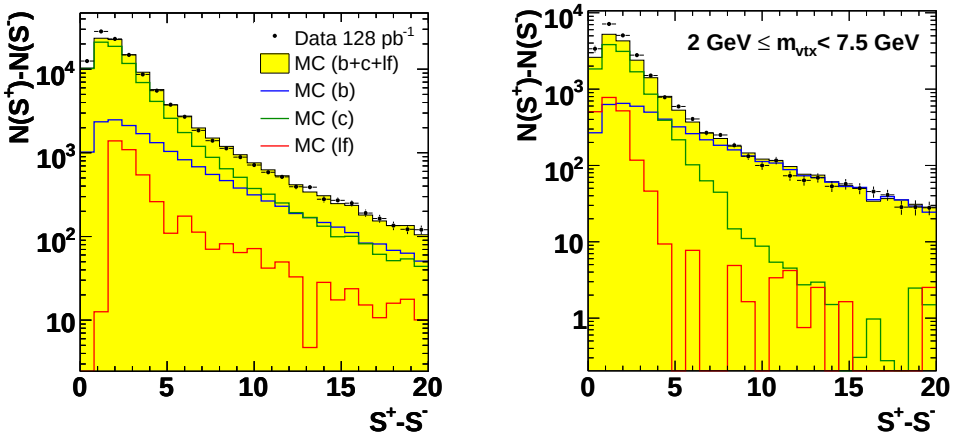

Figure 7.4: Mirrored and subtracted decay-length significance, $S^+ - S^-$, for the total secondary vertex mass range (left) and for $2\,\text{GeV} \leq m_{vtx} < 7.5\,\text{GeV}$ (right). Displayed are the data and total MC distributions as well as the contributions from the three MC subsamples normalised according to the fractions obtained from the fit.

lowing this procedure, since the unmirrored decay-length significance is to a great extent symmetric around zero in contrast to the same distributions for heavy flavours (cf Section 5.2.3). An additional advantage of the mirroring was the reduction of potential systematic effects which might arise from the discrepancies between the data and the MC that could be seen in the tails of the unmirrored decay-length significance. This disagreement was due to the fact that the track resolution was not sufficiently well simulated (see also Appendix A). A study of the discrepancies found in the unmirrored distribution was included in the systematic checks (cf Chapter 9).

In Fig. 7.4 the mirrored and subtracted significance distributions, $S^+ - S^-$, are shown for the total m_{vtx} range as well as for $2\,\mathrm{GeV} \leq m_{vtx} < 7.5\,\mathrm{GeV}$. In general one can observe that the light flavour fraction has decreased significantly, such that charm dominates for low secondary vertex masses and beauty for $m_{vtx} \geq 2\,\mathrm{GeV}$. For the highly beauty-enriched region, i.e. mirrored significances above $S^+ - S^- \simeq 3$, the MC describes the data well; however, some discrepancies at low $S^+ - S^-$ can be observed.

In order to extract the contributions from beauty, charm and light flavours the $S^+ - S^-$ distributions were divided into three m_{vtx} bins; the beauty-dominated region was chosen as shown in Fig. 7.3 and 7.4, i.e. as $2\,\mathrm{GeV} \leq m_{vtx} < 7.5\,\mathrm{GeV}$, while the low mass region was further split into two bins, namely below 1.4 GeV and above. Subsequently a binned χ^2 fit of the three MC distributions to the data was performed simultaneously for all three distributions. The overall MC normalisation was constrained by adjusting the relative normalisation of the three MC subsamples to be consistent with the normalisation of the data in the unmirrored significance distribution. Hence the fit function to be minimised was defined as follows:

$$\chi^2 = \sum_{i=1}^{N_S} \sum_{j=1}^{N_M} \frac{(N_{ij}^{Data} - k_b \cdot N_{ij}^b - k_c \cdot N_{ij}^c - k_{lf} \cdot N_{ij}^{lf})^2}{(\delta_{ij}^{Data})^2 + (k_b \cdot \delta_{ij}^b)^2 + (k_c \cdot \delta_{ij}^c)^2 + (k_{lf} \cdot \delta_{ij}^{lf})^2} + \frac{(N_{tot}^{Data} - k_b \cdot N_{tot}^b - k_c \cdot N_{tot}^c - k_{lf} \cdot N_{tot}^{lf})^2}{(\delta_{tot}^{Data})^2 + (k_b \cdot \delta_{tot}^b)^2 + (k_c \cdot \delta_{tot}^c)^2 + (k_{lf} \cdot \delta_{tot}^{lf})^2}. \tag{7.1}$$

The sums run over all $S^+ - S^-$ bins i and the three m_{vtx} bins j. N_{ij}^l denotes the number of entries for the sample $l \in \{Data, b, c, lf\}$ in bin (i, j) and δ_{ij}^l represents the corresponding errors. For the MC samples the number of entries was obtained by adding up the MC subsamples weighted according to their integrated luminosities and normalising the sum to the data luminosity. Since a trigger efficiency correction had to be applied (cf Section 6.3) an additional weight representing the trigger efficiency entered the calculation. The free parameters of the fit consist in the three scaling factors k_m (so-called

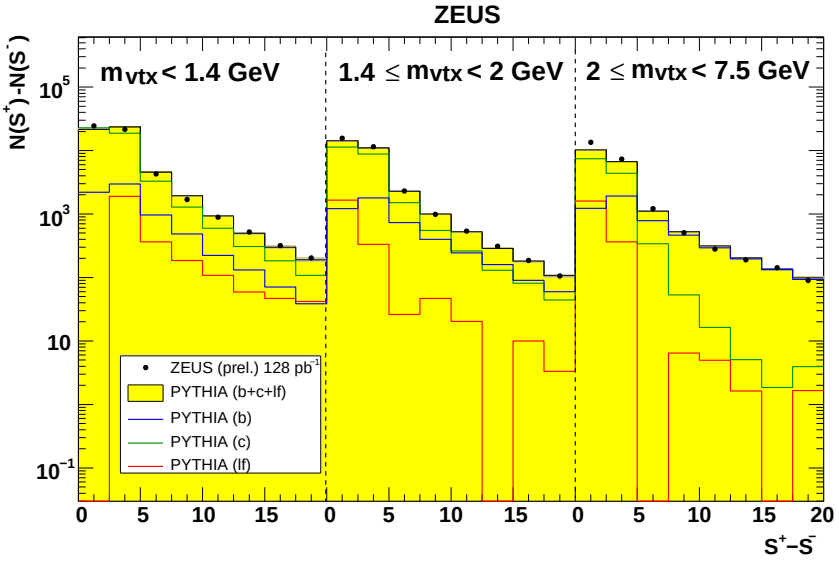

Figure 7.5: Distribution of the mirrored decay-length significance, $S^+ - S^-$ in three bins of the invariant mass of the secondary vertices, m_{vtx}. Displayed are the data (denoted by the black points) and total the MC distribution (represented by the yellow histogram) as well as the contributions from the three MC subsamples (indicated by the solid lines) normalised according to the fractions obtained from the fit.

k-factors) for the beauty, charm and light flavour MC samples. Due to the normalisation to the data luminosity they directly correspond to the scaling factors that will appear in the cross sections. The constraint of the overall normalisation is given by the second line in Equation 7.1; here the number of entries and the error in a given bin have been replaced by the total number of entries in the unmirrored distribution and its error.

Figure 7.5 shows the $S^+ - S^-$ distribution in the three chosen m_{vtx} bins after the fit. Note that the scaling factor for beauty is almost solely determined by the high significance bins at $m_{vtx} \geq 2\,\text{GeV}$; therefore the deviations at small mirrored significances as observed in Fig. 7.4 were expected to have a negligible effect on the beauty measurement. The fit resulted in the following k-factors for the three flavours:

$$\begin{aligned} k_b &= 1.12 \pm 0.034, \\ k_c &= 1.29 \pm 0.021, \\ k_{lf} &= 0.89 \pm 0.006. \end{aligned} \tag{7.2}$$

The correlations between beauty, charm and light flavours emerged as follows:

	b	c	lf
b	1.00	-0.52	0.39
c	-0.52	1.00	-0.81
lf	0.39	-0.81	1.00

It is visible that charm and beauty as well as charm and light flavours are anti-correlated, while beauty and light flavours are moderately correlated.

In general, good agreement between data and MC was found after the fit. However, the discrepancies at small mirrored significances that were mentioned before are still visible and consistent with what was observed previously in the corresponding control distributions. This resulted in a fit significance of $\chi^2/ndf = 107/22 = 4.8$. In order to check the impact on the measurement and to investigate the stability of the results, several cross-checks including additional cuts on m_{vtx} and variations of the fit range were performed; they will be presented and discussed in Chapter 9.

The same fit as displayed in Fig. 7.5 was done in several differential bins of $P_{\mathrm{T}}^{\mathrm{Jet}}$ and η^{Jet}; the corresponding fit distributions can be found in Fig. B.1 and B.2 in Appendix B.

The application of a normalisation constraint as introduced in Equation 7.1 should be discussed in somewhat more detail. As explained before one benefit of the mirroring procedure was the minimisation of the light flavour content. On the other hand such small contributions, which can even become negative due to the mirroring, can cause large fluctuations in a fit. An example fit without normalisation constraint is displayed in Fig 7.6 (top). The instability of this fit is visualised by the large errors on the total MC distribution and the size of the light flavour contribution, which was scaled up to an unreasonably large fraction. In order to cross-check if the instability was indeed caused by the small light flavour content, the same fit was repeated with beauty and charm contributions only as shown in Fig 7.6 (middle). Neglecting the light flavour contribution the fit yielded a reasonable result with proper errors. Finally, the normalisation term in Equation 7.1 was introduced constraining the total normalisation and in particular the relative contribution of light flavours with respect to beauty and charm. The fit result after applying the constraint is displayed in Fig 7.6 (bottom). The fluctuations that had been observed previously were now avoided and reasonable results were obtained for all contributions.

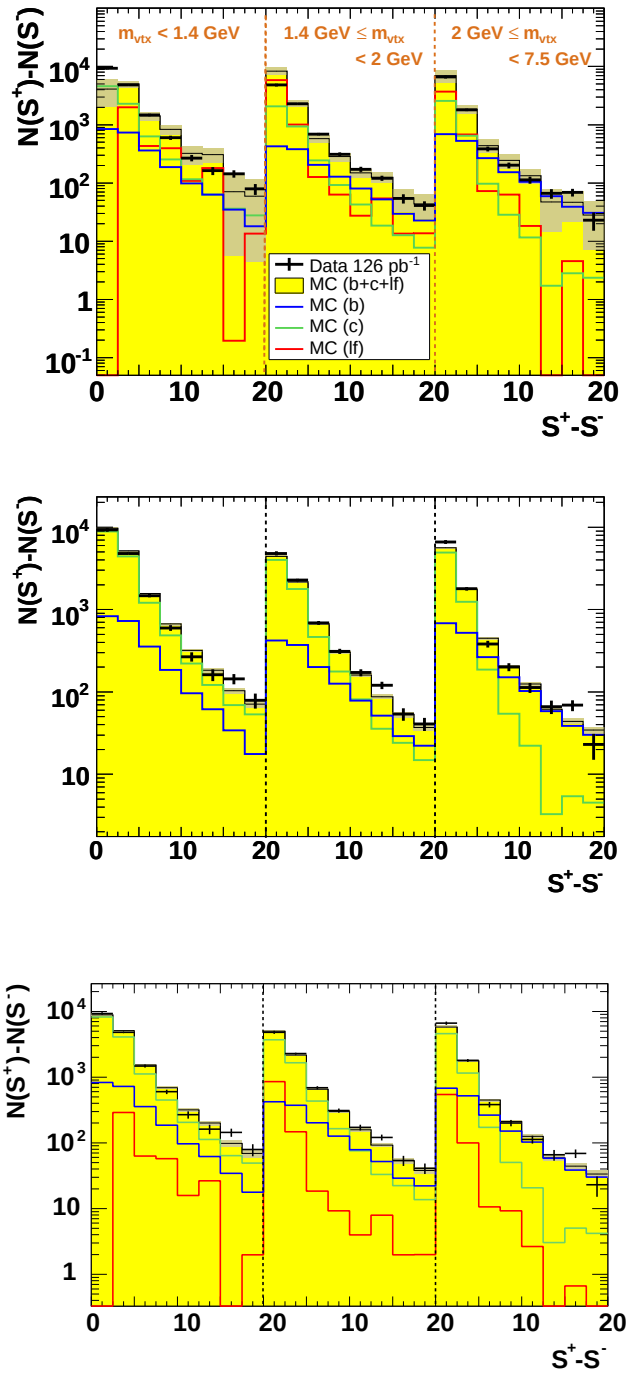

Figure 7.6: Fits of the mirrored significance distributions, $S^+ - S^-$, in three m_{vtx} bins without normalisation constraint (top), without constraint removing the light flavour contribution (middle) and with constraint including all three MC distributions (bottom). For further information see also the caption of Fig. 7.5. The uncertainty of the total MC distribution is represented by the shaded bands.

Chapter 8

Cross-section measurements in the central region

In this chapter the calculation of the total and single-differential cross sections for beauty and charm production is described. The measurements are presented and compared with both the PYTHIA LO+PS Monte Carlo simulation and the NLO QCD predictions calculated with the FMNR programme. Furthermore a method for selecting beauty- and charm-enriched regions is introduced. As a cross-check the results were re-evaluated on Grand-Reprocessed datasets using the identical procedure as before and are compared to the cross sections obtained from the pre-GR analysis.

The measurements on pre-GR data were approved and published as preliminary results by the ZEUS collaboration. The extension of the analysis to the forward region that is done on Grand-Reprocessed datasets is still in progress and is thus presented in a separate chapter (cf Chapter 10).

8.1 Cross sections

The total cross section, σ, of a given process is defined as the number of events, N, in the sample containing the process in question divided by the integrated luminosity, $\mathcal{L}_{Data}$:

$$\sigma = \frac{N}{\mathcal{L}_{Data}}.$$

Hence the formula for the inclusive beauty jet production cross section can be written as

$$\sigma^b = \frac{N_b^{rec,Data}}{\mathcal{A}_b \cdot \mathcal{L}_{Data}}. \tag{8.1}$$

Here, $\mathcal{A}_b$ refers to the beauty acceptance and $N_b^{rec,Data}$ to the number of reconstructed beauty jets in data, which had to be determined from the fit using

$$N_b^{rec,Data} = k_b \cdot N_b^{rec,MC}. \tag{8.2}$$

The number of reconstructed beauty events in the MC is here and in the following denoted by $N_b^{rec,MC}$, but is equivalent to N_{tot}^b in Eqn. 7.1. Defining the acceptance as

$$\mathcal{A}_b = \frac{N_b^{rec,MC}}{N_b^{true,HL}} \tag{8.3}$$

Equation 8.1 can be transformed into

$$\sigma^b = \frac{k_b \cdot N_b^{true,HL}}{\mathcal{L}^{Data}}. \tag{8.4}$$

Here, k_b denotes the beauty scaling factor obtained from the fit (cf Chapter 7) and $N_b^{true,HL}$ the number of generated beauty jets on hadron level (HL). Hadron level jets were obtained running the k_t cluster algorithm (cf Section 6.2) on all final-state MC particles before the decay of the weakly decaying b and c hadrons as depicted in Fig. 4.1. Therefore true b or c jets could be defined as all hadron level jets containing a b or c hadron, respectively, including all b and c baryons and excitations. In the case that the true hadron jet contained a b hadron as well as a c hadron originating from a cascade decay, the candidate was counted as beauty signal. Furthermore, signatures with b or c hadrons resulting from gluon splitting ($g \to q\bar{q}$) were also included in the respective signal independently of the quark flavours in the hard subprocess.

The single-differential beauty jet production cross section as a function of a given variable, v, is defined accordingly:

$$\begin{aligned} \frac{d\sigma^b}{dv} &= \frac{N_b^{rec,Data}}{\mathcal{A}_b \cdot \mathcal{L}^{Data} \cdot \Delta v} \\ &= \frac{k_b \cdot N_b^{true,HL}}{\mathcal{L}^{Data} \cdot \Delta v}. \end{aligned} \tag{8.5}$$

Here, Δv refers to the width of the given v bin. The total and single-differential charm cross sections were determined accordingly.

With the calculus above at hand, total and single-differential beauty and charm cross sections were measured for the processes

$$\begin{aligned} e^+p &\to e^+b\bar{b}X \\ e^+p &\to e^+c\bar{c}X \end{aligned}$$

in the kinematic range

$$\begin{aligned} Q^2 &< 1\,\mathrm{GeV}^2, \\ 0.2 &< y < 0.8, \\ P_T^{Jet\,1(2)} &> 7(6)\,\mathrm{GeV}, \\ -2.5 \;\leq\; \eta^{Jet\,1(2)} &< 2.5 \end{aligned}$$

with at least one of the jets within $-1.6 \leq \eta^{Jet\,1(2)} < 1.3$. The total beauty and charm jet production cross sections were measured as

$$\begin{aligned} \sigma_b^{vis} &= 648 \pm 20(stat.)^{+\ 57}_{-\ 96}(syst.) \pm\ 19(lum.)\,\mathrm{pb}, \\ \sigma_c^{vis} &= 5209 \pm 84(stat.)^{+580}_{-590}(syst.) \pm 160(lum.)\,\mathrm{pb}. \end{aligned}$$

The errors given correspond to the statistical uncertainties, the total systematic uncertainties and the errors due to the uncertainty in the luminosity measurement. The evaluation of the systematic uncertainties will be discussed in detail in Chapter 9. The measurements were compared to NLO QCD predictions calculated with the FMNR programme using the specifications introduced in Section 4.2:

$$\begin{aligned} \sigma_b^{NLO} \otimes C_{had}^b &= 648^{+\ 170}_{-\ 100}\,\mathrm{pb}, \\ \sigma_c^{NLO} \otimes C_{had}^c &= 5382^{+2900}_{-1500}\,\mathrm{pb}. \end{aligned}$$

Hadronisation corrections of $C_{had}^b = 0.80$ and $C_{had}^c = 0.81$ were applied to the NLO QCD predictions in order to allow the comparison of the cross sections on hadron level. Very good agreement within the statistical and systematic errors between the measured cross sections and the NLO predictions was observed.

The differential cross sections as a function of P_T^{Jet} and η^{Jet} are displayed in Fig. 8.1 for beauty and in Fig. 8.2 for charm; the inner error bars denote the statistical uncertainty, while the outer error bars correspond to the statistical and systematic errors summed in quadrature. The measurements are compared to the Pythia LO+PS predictions, which were scaled with the k-factors obtained from the total $S^+ - S^-$ fit (cf Eqn. 7.2), as well as the NLO QCD predictions. The NLO uncertainty was evaluated as described in Section 4.2. Differential hadronisation corrections, C_{had}, were evaluated and again used to transfer the NLO predictions from parton level to hadron level. The correction factors are shown in Fig. 8.3 and were found to be consistent for beauty and charm. All cross sections are also listed in Tables C.1 and C.2 in Appendix C. In general, good agreement between the measurements and both predictions is observed within the statistical, systematic and theoretical uncertainties. At large η^{Jet} the measured charm cross sections are

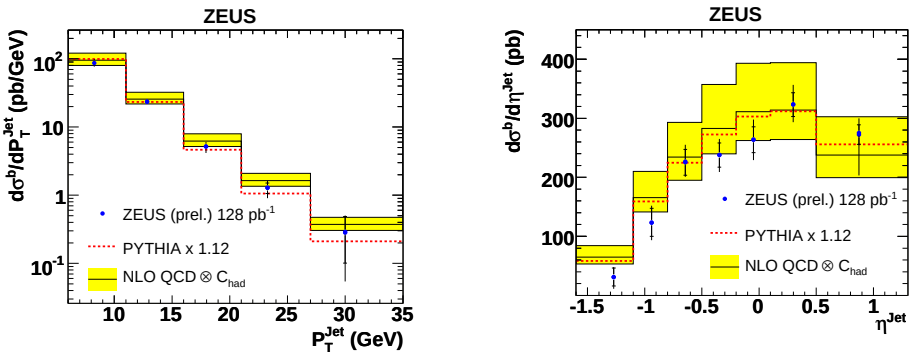

Figure 8.1: Differential beauty jet cross section as a function of P_T^{Jet} (left) and η^{Jet} (right) for events with $Q^2 < 1\,\mathrm{GeV}^2$, $0.2 < y < 0.8$, $P_T^{Jet\,1(2)} > 7(6)\,\mathrm{GeV}$ and $-2.5 \leq \eta^{Jet\,1(2)} < 2.5$ using jets with $-1.6 \leq \eta^{Jet\,1(2)} < 1.3$. The black points show the results measured in this analysis. The inner error bars are statistical uncertainties, while the external error bars show the statistical and systematic uncertainties added in quadrature. The solid line and the yellow band represent the NLO QCD predictions and their uncertainties.

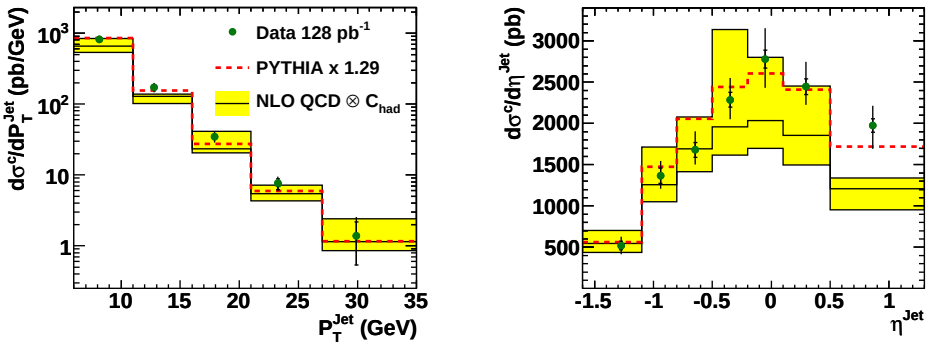

Figure 8.2: Differential charm cross section as a function of P_T^{Jet} (left) and η^{Jet} (right). For further information see the caption of Fig. 8.1

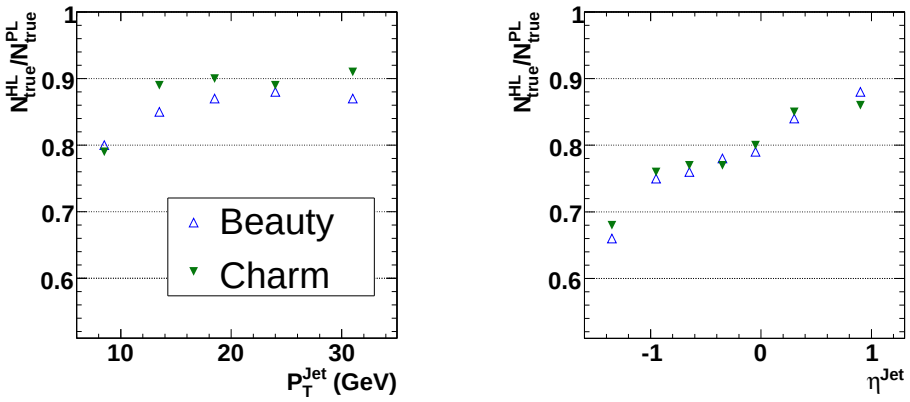

Figure 8.3: Hadronisation corrections as a function of P_T^{Jet} and η^{Jet} for beauty (open triangles) and charm (filled triangles).

consistent with the PYTHIA LO+PS prediction, but lie systematically above the NLO QCD predictions. However, the FMNR predictions for the charm cross sections show large fluctuations especially for the upper uncertainty, which consists of the quadratic sum of the variations using a factorisation scale of $\mu_0/4$ instead of $\mu_0/2$ and a charm mass of $m_c = 1.3\,\text{GeV}$. Due to increase of the value of α_s at smaller scales the predictions became less reliable in this regime as expected (cf Fig. 3.1 and Section 4.2).

The cross sections as a function of η^{Jet} were additionally compared to a previously published HERA I measurement in which muons from semileptonic b decays and associated jets with $-1.6 \leq \eta^{Jet} < 1.4$ were analysed [49]. In the previous analysis the inclusive beauty jet production cross section was obtained by extrapolating the measured μ-jet cross sections with the help of the $b \to \mu$ branching ratio. The comparison of the two measurements is displayed in Fig. 8.4; they agree well within the statistical and systematic errors. Although the two analyses were performed on datasets with similar integrated luminosities the errors on the measurement could be substantially reduced compared to the previous analysis; this directly expresses the advantages of the new b tagging technique.

In Fig. 8.5 the updated summary distribution showing the differential cross sections for b-quark production as a function of the transverse momentum of the b-quark, p_t^b, is presented (cf Section 3.5.2). The b-jet cross sections were converted into b-quark cross sections by scaling the measurements with the ratio of the NLO predictions for b-quark production and b-jet production. Good agreement with the NLO QCD prediction is observed for a variety of independent ZEUS and H1 measurements, giving a consistent picture of b

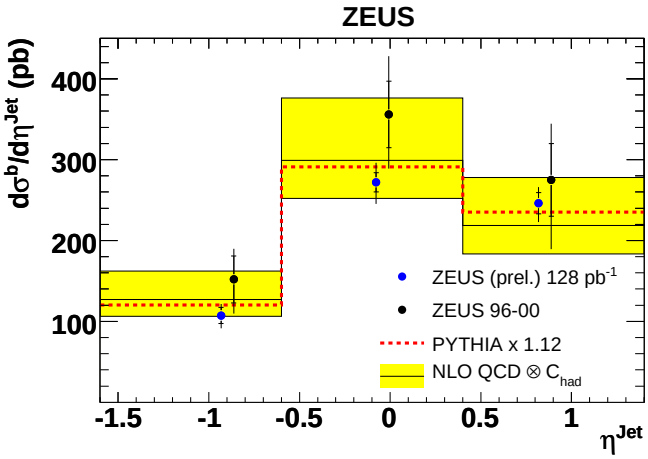

Figure 8.4: Differential cross section as a function of η^{Jet} for events with $Q^2 < 1\,\mathrm{GeV}^2$, $0.2 < y < 0.8$, $P_T^{Jet\,1(2)} > 7(6)\,\mathrm{GeV}$ and $-2.5 \leq \eta^{Jet\,1(2)} < 2.5$ using jets with $-1.6 \leq \eta^{Jet\,1(2)} < 1.4$. The blue points show the results from this analysis, the black ones the results from the previously published HERA-I measurement. The inner error bars are statistical uncertainties, while the external error bars show the statistical and systematic uncertainties added in quadrature. The band represents the NLO QCD prediction and the theoretical uncertainties.

quark photoproduction over a wide range of p_t^b. The cross sections obtained from this analysis are denoted by the red stars; they represent the most precise measurement of b-quark production at HERA that has been achieved so far. It is interesting to note that for most of the recent measurements the experimental uncertainty is smaller than the theoretical uncertainty. Furthermore the p_t^b range of the measurement could be extended to larger values with respect to previous analyses.

The control distributions shown in Figs. 7.1 and 7.2, the fitted $S^+ - S^-$ distribution in Fig. 7.5 as well as the jet production cross sections in Figs. 8.1, 8.4 and 8.5 indicated by "ZEUS (prel.) 128 pb^{-1}" were made public by the ZEUS collaboration as preliminary results for the DIS09 conference[1].

[1]XVII International Workshop on Deep-Inelastic Scattering and Related Subjects, 26$^{\mathrm{th}}$-30$^{\mathrm{th}}$ April 2009, Madrid, Spain.

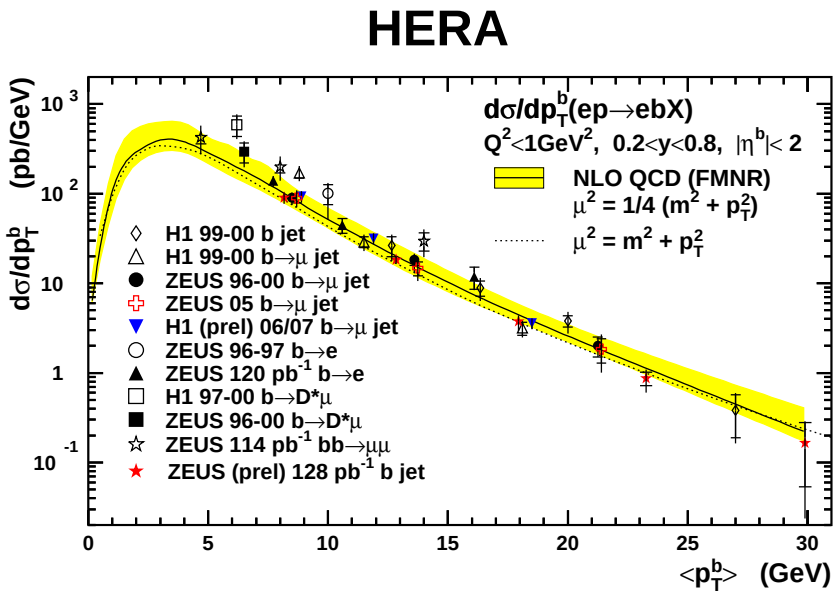

Figure 8.5: Summary of differential cross sections for b-quark production as function of p_t^b as measured by the ZEUS and H1 collaborations. The measurements are shown as points, with the result of this measurement shown as red stars. The inner error bars are the statistical errors, the outer bars show the statistical and systematic errors added in quadrature. The band represents the NLO QCD prediction and the theoretical uncertainties.

8.2 Beauty and charm enrichment

One of the main features of the method used in this analysis was that requiring $m_{vtx} \geq 2\,\text{GeV}$ and $S^+ - S^- > 8$ it was possible to obtain an almost pure beauty sample with a beauty fraction of 95 % and a charm contamination of 4 %. In Fig. 8.6 and 8.7, the η^{Jet}, P_T^{Jet}, m_{vtx} and track multiplicity distributions as well as the mirrored decay-length significance, $S^+ - S^-$, are shown for the beauty-enriched region. In general, reasonable agreement between data and MC could be observed, although in the mirrored significance distribution the data tend to lie slightly below the MC prediction for $8 \leq S^+ - S^- < 13$. However, it has to be kept in mind that only a very small fraction of the beauty content of the whole sample could be selected for such highly beauty-enriched distributions; therefore it is doubtful whether a perfect description can be expected. The beauty-enriched distributions were included in the ZEUS preliminary result as well, as denoted in the figures.

The possibility to select a charm-enriched region is of interest as well. By requiring $m_{vtx} < 2\,\text{GeV}$ a charm fraction of 84 % could be achieved, while the remaining beauty contribution amounted to 14 %. The corresponding control distributions are displayed in Fig. 8.9 and 8.8.

In case of the charm-enriched sample some discrepancies between data and MC, especially in the η^{Jet}, m_{vtx} and mirrored decay-length significance distributions, could be observed. Since the systematic checks for the preliminary results which will be discussed in Chapter 9 focused on the beauty analysis, it was not clear if the charm systematics were entirely under control yet. Therefore the charm results were not yet made public by the ZEUS collaboration. In the course of repeating and extending the analysis on the GR dataset, this issue was studied in greater detail (see Section 10.3).

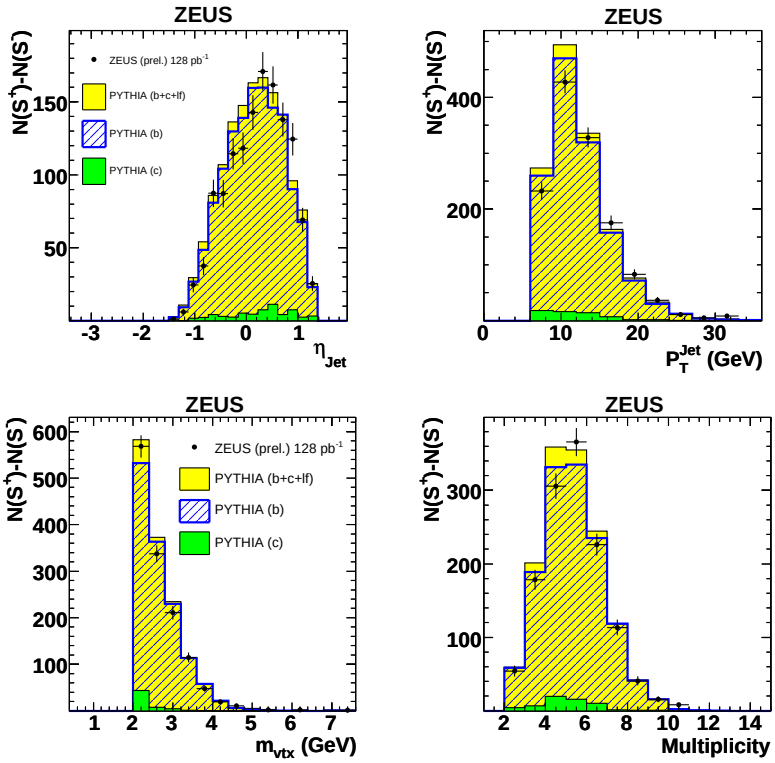

Figure 8.6: Distribution of η^{Jet} (top left), P_T^{Jet} (top right), m_{vtx} (bottom left) and vertex multiplicity (bottom right) for the beauty-enriched sample. The black points represent the data, while the total MC distribution as well as the contributions from beauty and charm are denoted by the yellow, blue and green histograms.

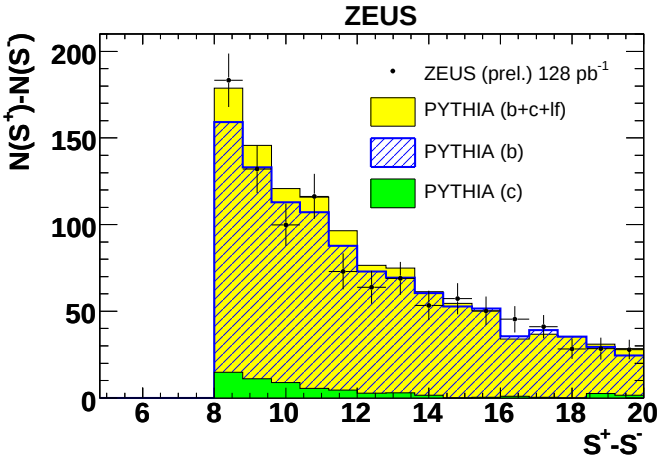

Figure 8.7: Mirrored decay-length significance, $S^+ - S^-$, for the beauty-enriched sample. For further details see the caption of Fig. 8.6.

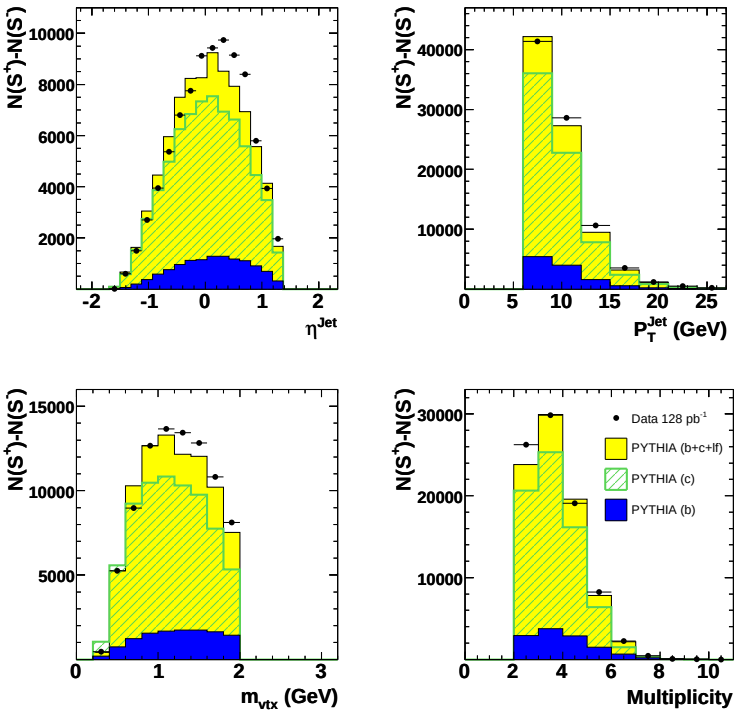

Figure 8.8: Distribution of η^{Jet} (top left), P_T^{Jet} (top right), m_{vtx} (bottom left) and vertex multiplicity (bottom right) for the charm-enriched sample. For further details see the caption of Fig. 8.6.

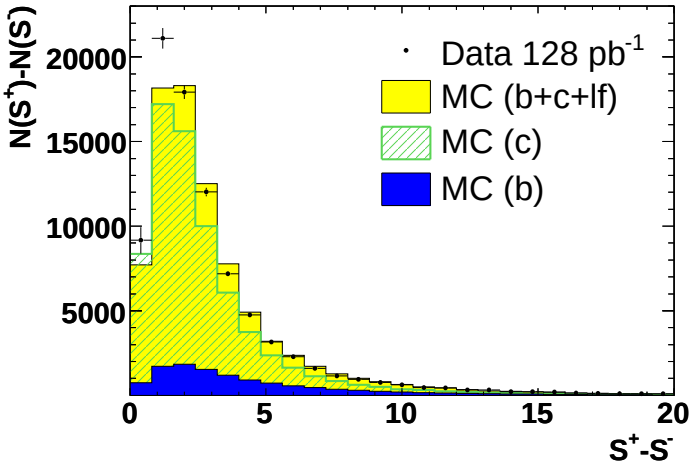

Figure 8.9: Mirrored decay-length significance, $S^+ - S^-$, for the charm-enriched sample. For further details see the caption of Fig. 8.6.

8.3 Analysis on Grand-Reprocessed data

Shortly after the results presented in Sections 8.1 and 8.2 were made public as preliminary results, the Grand-Reprocessed (GR) data and the corresponding Monte Carlo simulations became available. As already discussed in Section 5.5 the dataset used for the measurements was corrected such that it was supposed to be as similar as possible to the final Grand-Reprocessed dataset. In order to verify this, the analysis was re-done using the GR data and MC.

Figure 8.10 shows the comparison of the cross sections determined on pre-GR (denoted by the open circles) and GR data (denoted by the filled circles); for the latter only statistical errors are shown. The measurements were also compared to the Pythia LO prediction as obtained from the GR version of the Monte Carlo simulation. Very good agreement between the two results was found, which retrospectively justifies the usage of the corrected pre-GR data for the public results. It is also visible that the statistical errors are slightly smaller for the measurement using GR data, although the two datasets were of almost the same size; this was due to the fact that the description of the mirrored decay-length significance had improved considerably and thus the fit yielded more significant and more precise results (cf Chapter 10).

Further developments which became possible with the availability of the GR datasets will be discussed in Chapter 10.

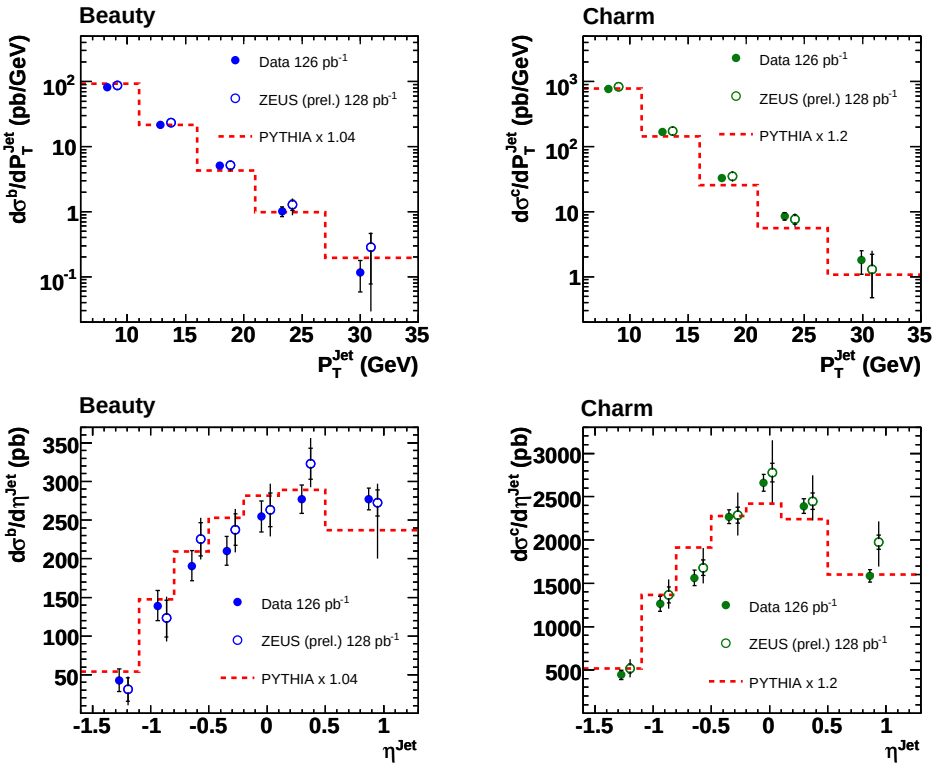

Figure 8.10: Differential cross sections as a function of P_T^{Jet} (top) and η^{Jet} (bottom). The results obtained on pre-GR data as shown in Fig. 8.1 and 8.2 are denoted by the open circles and compared to the measurement on Grand-Reprocessed data (filled circles). For the latter only statistical errors are shown. The dashed red line represents the PYTHIA LO+PS prediction.

Chapter 9

Systematics for the central region

Various sources of systematic effects have been studied in the context of this analysis in order to evaluate the total uncertainty on the measurements. In this chapter all systematic checks that were done for the results presented in Chapter 8 will be discussed. Studies which were changed or added in the course of extending the analysis will be addressed in Chapter 10.

9.1 Hadronic energy scale

In order to account for the uncertainty of the energy measurement in the calorimeter and its description by the simulation the jet energies in the MC were varied by $\pm 3\,\%$ according to dedicated studies [62]. Subsequently, the whole analysis was re-run using the altered jet energies. The variation mainly affected the event selection cuts on P_T^{Jet} and the cross section as a function of P_T^{Jet}. A constant uncertainty was expected for the cross section as a function of η^{Jet}.

For the total cross sections uncertainties of $\pm 0.5\,\%$ and $\pm 6.5\,\%$ were determined for beauty and charm, respectively. Furthermore, a P_T^{Jet} dependence was observed, resulting in uncertainties of 5–22 % and 3–17 % on the measurements as a function on P_T^{Jet}. In terms of η^{Jet} no dependence was found and the average uncertainties were of a similar size as for the total cross sections.

9.2 Trigger correction

As explained in Section 6.3 a trigger correction was applied by weighting all MC events with $P_T^{Jet\,2} < 11.5\,\text{GeV}$ with

$$w_{trigger} = 0.638 + 0.031 \cdot P_T^{Jet\,2}.$$

according to previous studies [63]. Since the size of the trigger correction had been evaluated on a different data sample than the one used for this analysis, a rather conservative variation of the correction of $\pm 50\,\%$ was included as a systematic check. It led to shifts of the total beauty and charm cross sections of $\pm 3.3\,\%$ and $\pm 5.5\,\%$, respectively.

9.3 Fit range

The uncertainty originating from the fit procedure was estimated by varying the fit range. For the measurement the full range of the mirrored decay-length significance, $S^+ - S^-$, was used in each bin of the secondary vertex mass, m_{vtx} (see Fig. 7.5). In order to evaluate a potential systematic uncertainty that might in particular be caused by the discrepancies observed in the low mirrored significance region (cf Fig. 7.4), lower cuts on $S^+ - S^-$ were applied restricting the fit range to the region which is dominated by beauty and charm. In Fig. 9.1 the scaling factors for beauty, charm and light flavours as obtained from the fraction fits are displayed as a function of the (mirrored)

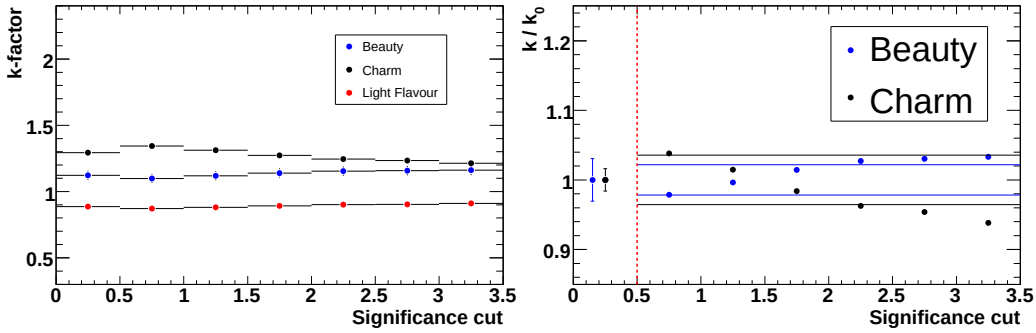

Figure 9.1: Dependence of the scaling factors for beauty (blue points), charm (black points) and light flavours (red points) as a function of the lower cut on the mirrored decay-length significance, $S^+ - S^-$ (left). On the right, the ratios with respect to the nominal scaling factor, k_0, as well as the average deviations are shown for beauty and charm.

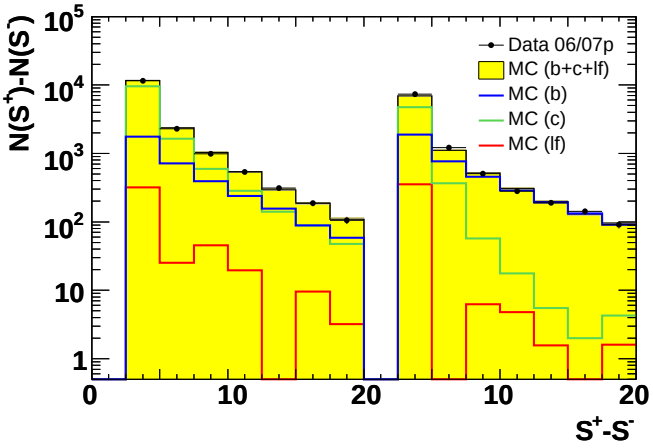

Figure 9.2: Significance fit with restricted fit range removing the low mass region ($m_{vtx} < 1.4\,\mathrm{GeV}$) and cutting on $S^+ - S^- \geq 2$.

significance cut. The k-factor for light flavour shows hardly any dependence on the cut, while the k-factors for beauty (charm) slightly increase (decrease) with increasing cut value. Furthermore, the ratios of the k-factors obtained after cutting on the significance and the nominal k-factor, here referred to as k_0, are displayed in Fig. 9.1. The solid horizontal lines represent the average deviations from the nominal k-factors for beauty and charm, which were taken as the final systematic uncertainties. These uncertainties were determined for the total kinematic range as well as for each differential bin in P_T^{Jet} and η^{Jet} and consistently found to be of the same size as the statistical errors or smaller. The corresponding figures for all bins in P_T^{Jet} can be found in Appendix E, Figs. E.1 and E.2.

As an additional check - in particular for the beauty cross section - the fit of the mirrored significance distribution was repeated removing the low mass region, $m_{vtx} < 1.4\,\mathrm{GeV}$, which should not have a big influence on the beauty result and cutting on $S^+ - S^- \geq 2$. The fit result is displayed in Fig. 9.2 and led to k-factors for beauty and charm of

$$\begin{aligned} k_b &= 1.10 \pm 0.036 \\ k_c &= 1.40 \pm 0.033 \end{aligned}$$

and a fit significance of $\chi^2/ndf = 0.97$. The value for beauty was consistent within statistical errors with what had previously been found for the total fit (cf Chapter 7). The charm result turned out to be $\approx 9\,\%$ higher than before; however, in contrast to beauty the charm fraction was not entirely

determined by the two high m_{vtx} bins and removing the mass region below 1.4 GeV is equivalent to cutting away a non-negligible amount of the charm signal region.

9.4 Decay-length smearing

As already shown in Chapter 7, the tails of the decay length (significance) distribution were not fully described by the MC. The effect of this discrepancy on the measurement was estimated by smearing the MC to reproduce the data. Therefore, an empirical smearing function was developed consisting of a Gaussian for the peak region and a logarithmic function for smearing the tails [67].

The smearing function contained four free parameters A, B, C and D and was only dependent on the decay-length error, δd, which ensured the correlations between the decay length and its error to be taken into account. For smearing the peak region a small fraction A of all decay lengths, d, was modified as follows:

$$d_{smeared} = d \pm B \cdot \delta d$$

In order to additionally adjust the extreme tails of the decay-length distribution, a fraction $C \cdot \delta d$ of all decay lengths was modified such that

$$d_{smeared} = d + \frac{R}{|R|} \cdot \frac{\ln(1 - |R|)}{-D}$$

with R being a random number within [-1,1]. The four parameters were empirically chosen such that the negative side of the decay-length distribution, which is only caused by detector resolution effects and supposed to be independent of any physics process, shows good agreement between data and MC. The values for the four parameters were found to be

$$\begin{aligned} A &= 0.15 \\ B &= 1.5 \\ C &= 0.1\,/\text{cm} \\ D &= 5\,/\text{cm}. \end{aligned}$$

Figure 9.3 shows the negative side of the decay-length significance distribution. The data which are denoted by the black points are compared to the unsmeared MC distribution in red and the smeared one in blue. In particular the agreement for the extreme tail of the distribution was improved considerably and a generally good description of the data could be observed after

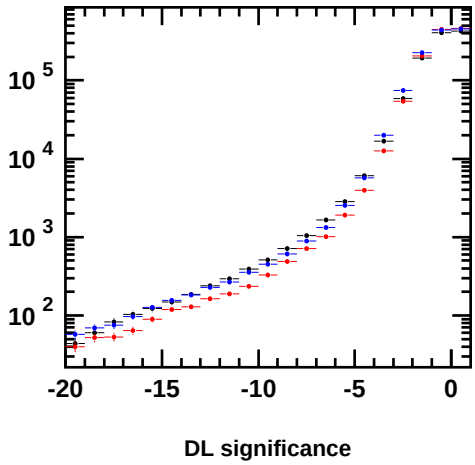

Figure 9.3: Negative side of the decay-length significance distribution before and after smearing. The black points represent the data, while the unsmeared MC distribution is denoted by the red points and the smeared MC by the blue points [68].

the smearing. The systematic uncertainties were evaluated by applying the smearing procedure and subsequently re-doing all fits. For the total beauty and charm cross sections systematic uncertainties of -13 % and -5.4 % were determined, respectively.

9.5 Reweighting of P_T^{Jet} and η^{Jet}

In Fig. 9.4 the P_T^{Jet} and η^{Jet} distributions are shown on linear scale. The figures on the left are obtained from the standard datasets without applying any further corrections. In both distributions there are discrepancies between data and MC visible. In order to study the effect of this disagreement on the cross sections the background (light flavour) contribution was reweighted according to the differences between data and MC assuming a correct description of beauty and charm. This reweighting procedure was simultaneously done for both distributions. The figures on the right display the result of the reweighting; a reasonable agreement between data and MC could be achieved.

The systematic uncertainty on the total beauty and charm cross sections due to this reweighting was found to be negligible. However, it was still taken into account in the calculation of the systematic uncertainties, since

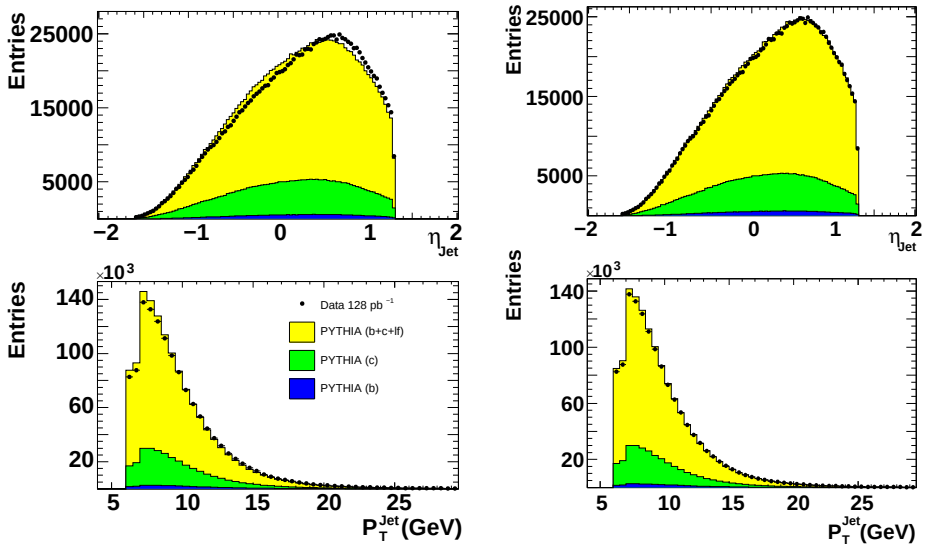

Figure 9.4: P_T^{Jet} and η^{Jet} distributions before (left) and after (right) reweighting. The data points are compared to the MC distributions denoted by the yellow histograms. The beauty and charm contributions are indicated by the blue and green histograms.

a dependence on P_T^{Jet} and η^{Jet} was expected. In some of the differential bins of the beauty cross sections systematic uncertainties of up to 3 % were evaluated.

9.6 Mass reweighting

In Chapter 7 it was shown that the distribution of the invariant mass of the secondary vertex tracks, m_{vtx}, revealed slight discrepancies between data and MC at large values of m_{vtx}. In order to evaluate the impact of these discrepancies on the measurement, the light flavour contribution was re-weighted according to the differences between data and MC. Repeating the analysis using the re-weighted mass distribution, the effect on the cross sections was found to be negligible. Therefore the mass re-weighting was treated as a consistency check rather than a systematic uncertainty and did consequently not contribute to the systematic errors.

Since the analysis was focused on the beauty measurement at that stage in order to make this result public the discrepancies observed in the m_{vtx} distribution of the charm-enriched sample were not investigated further. However,

in the context of extending the analysis to the forward region a systematic study was done resulting in a reweighting of the charm m_{vtx} distribution to determine the contribution to the systematic uncertainties (cf Chapter 10).

9.7 Others

Apart from the systematic checks discussed above, which were particularly important for this analysis, a few general systematic effects were additionally taken into account.

The analysis strongly relied on the track and vertex reconstruction efficiency of the microvertex detector and its description by the MC simulation. In order to take the influence of an imperfect simulation of the MVD hit efficiency on the results into account, corresponding systematic errors were estimated by studying the MVD hit distributions and comparing those studies to similar checks which had previously been done in the course of a D^+ analysis. The systematic uncertainty was found to be $\pm 3\,\%$ on average.

The polarisation switch from positively polarised to negatively polarised positrons in the middle of the 06/07p running period went along with a drop of the event rate, i.e. the number of events per luminosity, that was observed to be $\approx 3\,\%$ larger than expected by the theory. Details on these observations and related studies can be found in [73, 74]. Since the reason for this effect is not yet understood, a conservative systematic uncertainty of $+5\,\%$ was assigned.

For the uncertainty on the luminosity measurement a systematic error of $\pm 3\,\%$ was assigned.

9.8 Summary of systematics

Table 9.1 summarises the impact of the studied systematic effects on the total beauty and charm cross sections. As explained before, the mass reweighting was treated as a consistency check and not included in the calculation of the systematic errors; therefore it is not listed here. The uncertainty on the luminosity measurement was also not taken into account in the evaluation of the systematic errors, but quoted separately (see Section 8.1). The total systematic uncertainty for each bin of the differential cross sections is listed in Tables C.1 and C.2 in Appendix C.

Uncertainty	Beauty (%)	Charm (%)
Hadronic energy scale	± 0.5	±6.5
Trigger efficiency correction	± 3.3	±5.5
Fit range	± 2.2	±3.6
Decay-length smearing	−13.0	−5.4
Reweighting of P_T^{Jet} and η^{Jet}	–	–
MVD hit efficiency	± 3.0	±3.0
Event yield	+ 5.0	+5.0
Luminosity	± 3.0	±3.0

Table 9.1: Summary table of uncertainties included in the systematic errors. Presented are the uncertainties on the total beauty and charm cross sections. The uncertainty due to a reweighting of P_T^{Jet} and η^{Jet} contributed with less than 1 %, therefore no number is quoted here (see also Section 9.5).

Chapter 10

Extension to the forward region

For the analysis presented in Chapters 6–8 the forward region of the detector was explicitely excluded by discarding jets with $\eta^{Jet} \geq 1.3$ and tracks with $\eta^{track} \geq 1.5$. As explained before, this was done, because the final simulation of the forward part of the MVD as well as the STT was not yet implemented in the latest version of the MC. This included resolution corrections as well as an accurate mapping of dead channels in both detector components. Furthermore, the alignment of the barrel MVD was corrected offline as described in Section 5.5, but there was no matching version of the STT alignment available yet. Thus the forward tracks were neither well-reconstructed nor simulated appropriately and therefore they could not be used for the secondary vertexing.

In the following I will briefly review the method and status of the STT dead-channel simulation before the Grand Reprocessing and describe how it was further improved and finalised. Afterwards I will present the first steps towards extending the inclusive secondary vertexing analysis to the forward region and discuss the current problems and possibilities.

10.1 STT dead-channel simulation

The mapping of faulty STT channels was started after the 03/04 positron running, which was the first data-taking period after the installation of the STT in the ZEUS detector. The procedure of determining the efficiencies of single STT channels, so-called *straws*, was completely data-driven. As described in Section 2.3.4 each of the 48 STT sectors consisted of three layers of straw tubes. For the extraction of the faulty straws the hits-per-straw distributions of each layer in each sector were examined. As an example, Fig. 10.1 shows the hits-per-straw distribution for sector 29 and run 51078

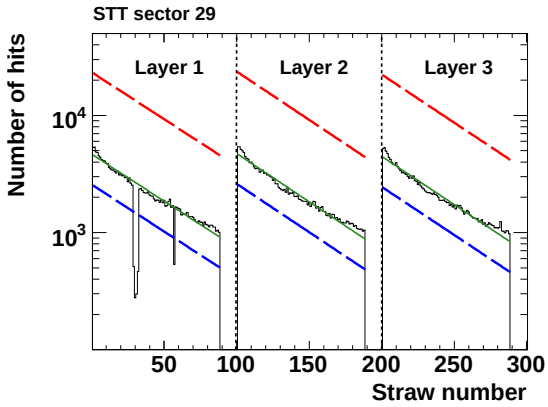

Figure 10.1: Hits-per-straw distribution for STT sector 29 and run 51078; the three layers of straw tubes are indicated by the dashed vertical lines. The exponential fits are shown as green solid lines, the cuts for a classification as dead or hot are denoted by the dashed red and blue lines.

on logarithmic scale with the three different layers of straws being indicated by the dashed vertical lines. A few faulty straws, for instance in bins 29–32 of layer 1, are clearly visible.

The hits-per-straw distribution of each layer was fitted with an exponential function, which gave a simple and convenient description of the distribution. The measured number of hits per straw was subsequently compared to the expectation as obtained from the fit. If it was below 55 % or above 300 % of the fit value, the straw was considered as dead or hot, respectively. This procedure was carried out separately for each run within the 03/04p data-taking period. Afterwards, the fraction of runs within the whole period, in which a straw was declared as dead, was determined. The distribution of those fractions for all 11000 straws is displayed in Fig. 10.2 on the left. It is notable that most entries are in the first bin, i.e. most of the straws were never declared as dead at all. On the other hand, a few hundred straws always had a number of hits that corresponded to less than 55 % of their expectation value and therefore ended up in the highest bin. The entries in between were almost negligible, so the cut value for the final decision whether a straw should be mapped as dead or not could be set rather arbitrarily. In the end, all straws which had been declared as dead in more than 40 % of all runs were considered as dead and mapped accordingly in the STT status GAFs. The value was chosen to lie approximately at the median of the distribution excluding the lowest and highest bins. This ensured the description to be accurate on average for the whole data-taking period.

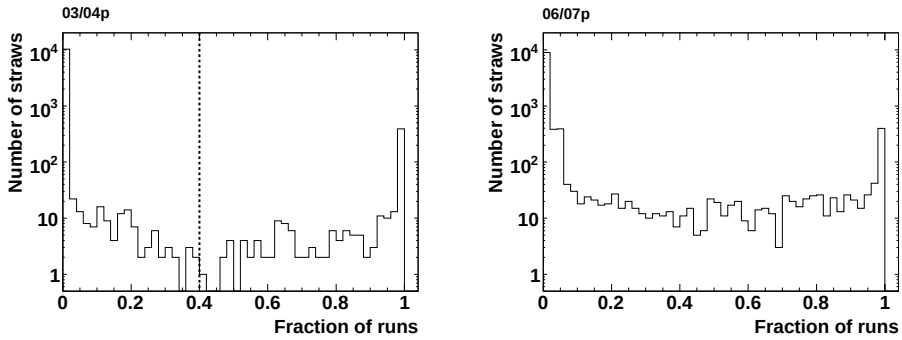

Figure 10.2: Number of straws as a function of the fraction of runs, in which a straw has been declared as dead, for the 03/04p (left) and 06/07p (right) data-taking periods. The dotted line in the left figure denotes the cut value of 40 %.

In terms of the hot straws, i.e. those that had a number of hits far above the expectation value, it turned out that only six of the 11000 straws showed such a behaviour; therefore they were neglected and not considered in the mapping of faulty straws.

More details about the previously described procedure as well as the impact on the efficiency of the forward tracking can be found in [9].

After the 2005 electron running, in which the STT was not included in the data-taking, the mapping of the faulty STT channels was continued for the other HERA II data-taking periods. The final aim was to have an accurate mapping available for the whole HERA II dataset shortly after the end of the HERA running. For the 06/07 running periods, the fit procedure for the initial classification as to whether or not a straw was working properly during a single run was kept unchanged. However, the distribution of the fraction of runs, in which straws had been declared as dead, indicated some differences with respect to the previous distribution from 03/04p. The direct comparison of the two distributions is shown in Fig. 10.2. It was conspicuous that the number of straws, which could not clearly be regarded as dead or as properly working, was not negligible anymore. Further studies revealed that the number of dead straws had gradually increased during the 06/07 running periods; therefore the method for classifying these straws needed to be refined and improved. Further studies showed that the growing number of dead straws with time was mainly due to three STT sectors becoming more and more inefficient[1]. In Fig. 10.3, the number of dead straws as a function

[1]The reason for this efficiency loss is as yet unknown and still under investigation; therefore here the emphasis is put only on the accurate mapping of the inefficiencies.

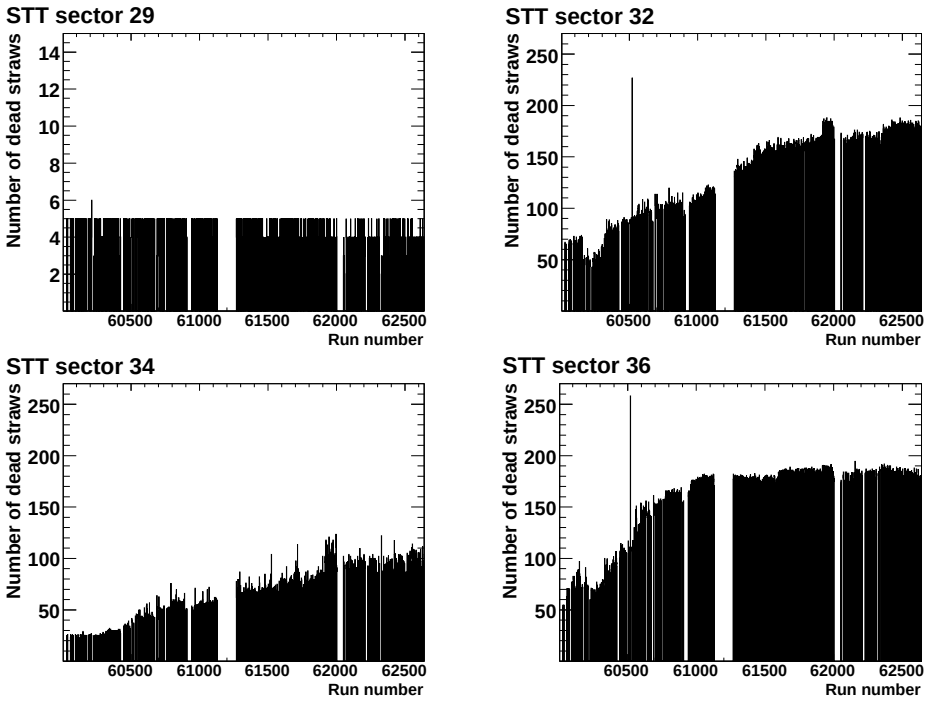

Figure 10.3: Number of dead straws in sectors 29, 32, 34 and 36 as a function of the run number. Note the different vertical scale in the top left figure.

of the run number, i.e. time, is shown for the three sectors mentioned above (sectors 32, 34 and 36) as well as for sector 29, which represents the properly working sectors typically exhibiting only very few dead channels.

In the following, the classification procedure was changed such that a third category was added for those straws that could neither be regarded as dead nor as working properly (*flaky* straws). In addition to the status the efficiency according to the distribution in Fig. 10.2 was also stored for each flaky straw. The corresponding software was modified such that a random number was generated for each MC event and compared to the straw efficiency; in case the random number was larger than the efficiency the straw was regarded as dead and discarded from the pattern recognition, otherwise it was taken. Since the three conspicuous sectors all belonged to the same layer and more similarities in such groups of three sectors could be spotted, the random number was generated simultaneously for all straws in a whole STT layer in order to take the observed correlations into account. For the same reasons as already discussed in Section 5.5 the modified software was not used for any further pre-GR Monte Carlo versions, but directly included in the Grand Reprocessing.

10.2 Further modifications

With the improvements of the STT dead-channel simulation described in Section 10.1 as well as the final MVD alignment and a matching STT alignment in hand, some first steps towards including the forward region could be undertaken. On the other hand, it was known that at least two more developments were still in progress: The tuning of the STT resolution in the MC simulation was ongoing and an appropriate simulation of the dead channels in the forward MVD was missing. However, both developments were expected to have only little impact on the analysis results.

For the extension of the analysis the Grand-Reprocessed data and corresponding MCs were used. The integrated luminosity of the new data sample was slightly lower than before:

$$\mathcal{L}_{Data}^{GR} = 126\,\mathrm{pb}^{-1}.$$

The loss of $2\,\mathrm{pb}^{-1}$ was due to technical reasons: for a few runs the beam-spot was not determined and thus those events were not usable for decay-length calculations.

The trigger correction was refined and re-evaluated on the GR datasets using the same data as in the analysis [69,70]. It was found to be considerably smaller than assumed for the preliminary results as described in Section 6.3, justifying the conservative choice of a 50 % variation for the systematic errors which well covered this effect. Studies showed that the correction function should be parametrised as

$$w_{trigger} = 0.12 + 0.18 \cdot P_T^{Jet\,2} - 0.01 \cdot (P_T^{Jet\,2})^2$$

for all MC events with $P_T^{Jet\,2} < 9.5\,\mathrm{GeV}$. Thus the maximum correction at low $P_T^{Jet\,2}$ was of the order of 5 %. The evaluation of the trigger efficiency is also displayed in Fig. 10.4 with the fit determining the weight function being indicated by the blue line.

The secondary vertexing procedure remained unchanged for jets and tracks in the barrel part of the detector, while some modifications for the forward region were necessary. In Fig. 10.5 on the left the η^{Jet} distribution for all jets with an associated secondary vertex is shown. The region beyond $\eta^{Jet} \approx 1.6$ is obviously not described by the MC simulation. The corresponding distribution for the mirrored decay-length significance, $S^+ - S^-$, is displayed in Fig. 10.6 (top). It is restricted to $1.3 \leq \eta^{Jet} < 2.5$ and divided into the three m_{vtx} bins that have previously been used for all fraction fits. Large discrepancies between data and MC could be observed. Furthermore, the data as well as the MC revealed large negative contributions at low significance values, which made a reasonable fit impossible. Several jet and track

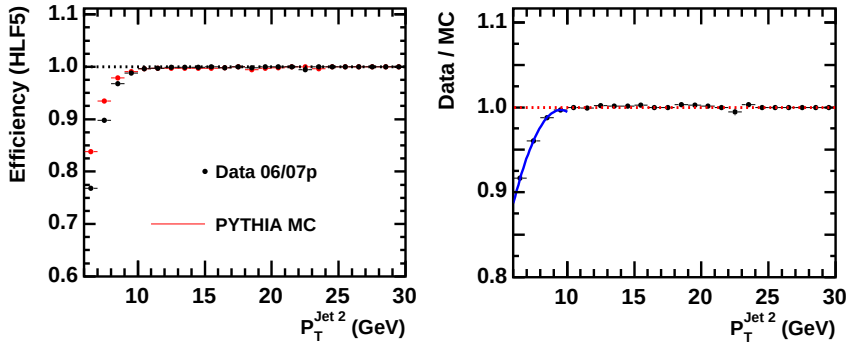

Figure 10.4: HFL trigger efficiency as a function of the transverse momentum of the second highest energetic jet, $P_T^{Jet\,2}$, for data and MC (left) as well as their ratio (right), taken from [69]. The fit which represents the trigger efficiency correction is indicated by the blue line.

properties were studied. The distributions could be substantially improved by tightening the track selection cuts for forward tracks used in the reconstruction of secondary vertices. Tracks with $\eta \geq 1.5$ were required to have a transverse momentum $p_t \geq 3\,\text{GeV}$ and to be MVD-only or MVD+STT tracks, i.e. tracks which were reconstructed without any CTD information. With the new selection for forward tracks, the secondary vertices were refitted. Furthermore, a general event cleaning cut was applied by discarding all events with more than 70 tracks which did not fulfill the criteria of the track selection for the secondary vertexing.

The improvement due to these changes is displayed in Fig. 10.5 (right) and Fig. 10.6 (bottom), where the η^{Jet} and $S^+ - S^-$ distributions obtained with the re-fitted secondary vertices are shown. The η^{Jet} distribution was found to be well-described by the MC simulation and a substantial improvement in terms of the agreement between data and MC as well as the occurrence of negative contributions could also be observed for $S^+ - S^-$. The restrictions that were imposed on the track selection indicate an inefficiency in the combined forward tracking with its exact origin being currently under investigation. Using the additional cuts described previously and removing the upper cuts on η^{Jet} and η^{track} that had been applied before (cf Chapter 6) the measurement could finally be extended to the forward region. In Fig. 10.7 the $S^+ - S^-$ distributions are shown for the full η^{Jet} region. On the left $S^+ - S^-$ is displayed for the total secondary vertex mass range, while on the right m_{vtx} was restricted to $2\,\text{GeV} \leq m_{vtx} < 7.5\,\text{GeV}$. Very good agreement between data and MC was observed; in particular the low $S^+ - S^-$ did not

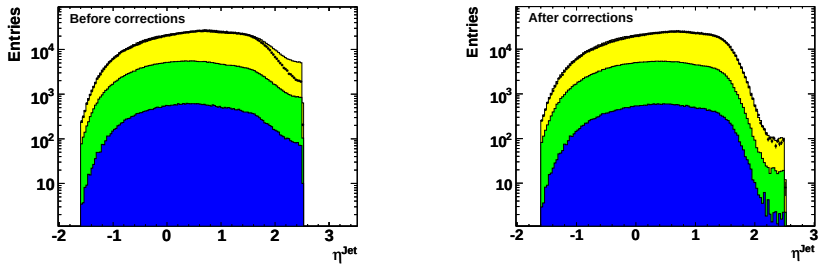

Figure 10.5: η^{Jet} distribution including forward region before (left) and after corrections (right). The data which are denoted by the black points are compared to the MC simulation (yellow histogram). In addition the contributions from beauty and charm are shown as blue and green histograms.

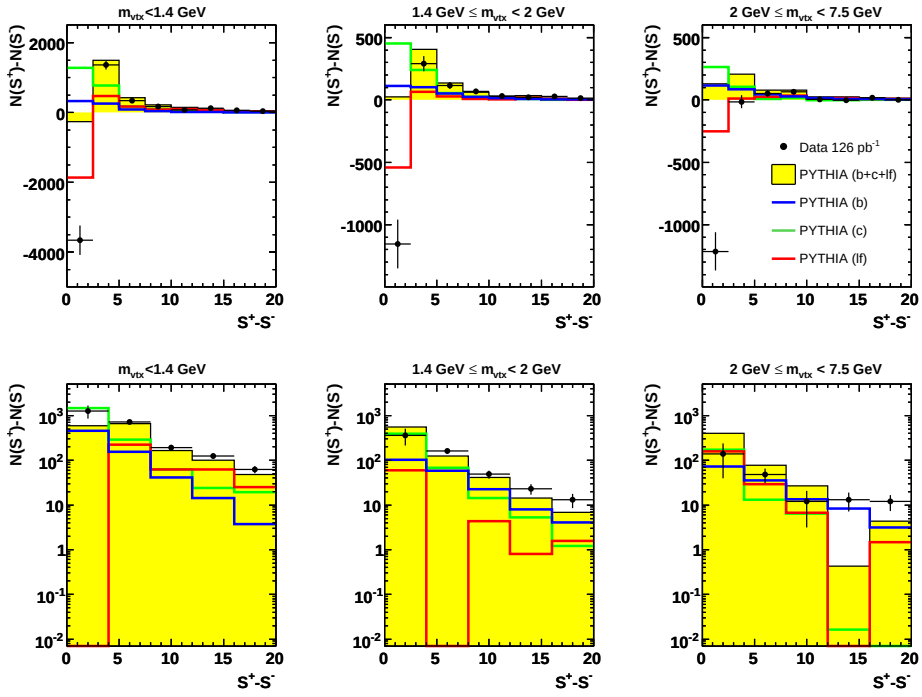

Figure 10.6: Mirrored and subtracted significance distribution in three m_{vtx} bins for $1.3 \leq \eta^{Jet} < 2.5$ before (top) and after corrections (bottom). The data which are denoted by the black points are compared to the MC simulation (yellow histogram). In addition the contributions from beauty, charm and light flavours are shown as blue, green and red lines.

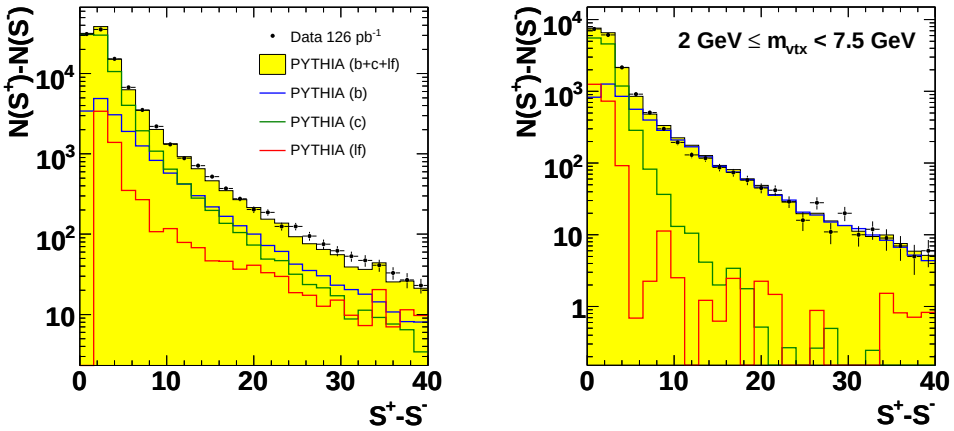

Figure 10.7: Mirrored and subtracted decay-length significance, $S^+ - S^-$, for the total secondary vertex mass range (left) and for 2 GeV $\leq$ m_{vtx} $<$ 7.5 GeV (right) after changing the track selection for forward tracks. Displayed are the data and total MC distributions as well as the contributions from the three MC subsamples normalised according to the scale factors obtained from the fit.

reveal any significant discrepancies anymore (cf Fig. 7.4). This indicated that further improvements which had not yet been accounted for in the corrections described in Chapter 5 were incorporated in the GR versions of the datasets.

In analogy to the results that were made public the two-dimensional decay-length significance was used throughout the analysis. In Fig. 10.8 the direct comparison between the 2D and 3D mirrored decay-length significances is shown. The accuracy of the description by the MC is similar, which implies that in principal also the three-dimensional decay-length significance can be used in the future.

10.3 Systematics

The calculation of the systematic uncertainties as described in Chapter 9 was fully repeated on the Grand-Reprocessed data and MC samples. The reweighting of P_T^{Jet} and η^{Jet} was re-done, but not included in the error bars anymore, since the effect on the results was found to be negligible compared to the other contributions.

In the following, the systematic checks which were changed or added will be discussed in detail.

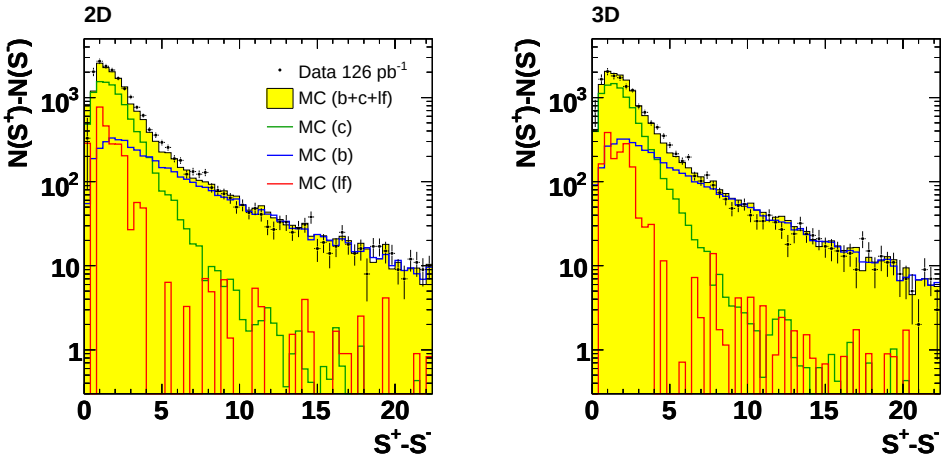

Figure 10.8: 2D and 3D mirrored and subtracted decay-length significance, $S^+ - S^-$, for $2\,\text{GeV} \leq m_{vtx} < 7.5\,\text{GeV}$ after changing the track selection for forward tracks. Displayed are the data and total MC distributions as well as the contributions from the three MC subsamples.

10.3.1 Hadronic energy scale

The procedure of calculating an uncertainty for the energy measurement in the calorimeter was slightly modified in order to increase the reliability of the systematic error. In addition to the 3 % variation described in Section 9.1 the energy scale was furthermore varied by ±1.5 % and ±6 %. In Fig. 10.9 the variation of the total beauty and charm cross sections is shown as a function of the energy-scale variation.

In the relevant region, i.e. between −3 % and +3 % (cf Chapter 9), the variation reveals an approximately linear behaviour. Therefore the data were fitted with with a linear fit function excluding the points corresponding to an energy-scale variation of ±6 %. The fit is shown as a solid line, while the fit uncertainty is indicated by the dashed curves. Subsequently, the values for the deviation of the cross sections corresponding to an energy-scale variation of ±3 % were extracted from the fit. Using this method the determination of the hadronic energy-scale uncertainty was robust against fluctuations that might occur when varying by only one fixed value. For the total beauty cross section an uncertainty of ±2 % was determined, while for charm values of +9 % and −7 % could be extracted.

The procedure described above was repeated for all differential bins in η^{Jet} and P_T^{Jet}, the corresponding distributions can be found in Appendix E, Figs. E.3 and E.4. In Fig. 10.10 the dependence of the deviation of the cross

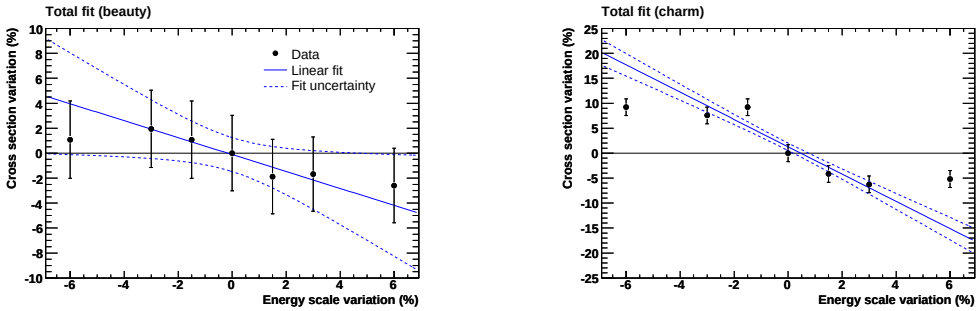

Figure 10.9: Variation of the total beauty (left) and charm (right) cross sections as a function of the energy-scale variation. The linear fit is denoted by the solid line, its uncertainty by the dashed lines. The points corresponding to an energy-scale variation of $\pm 6\,\%$ were excluded from the fits.

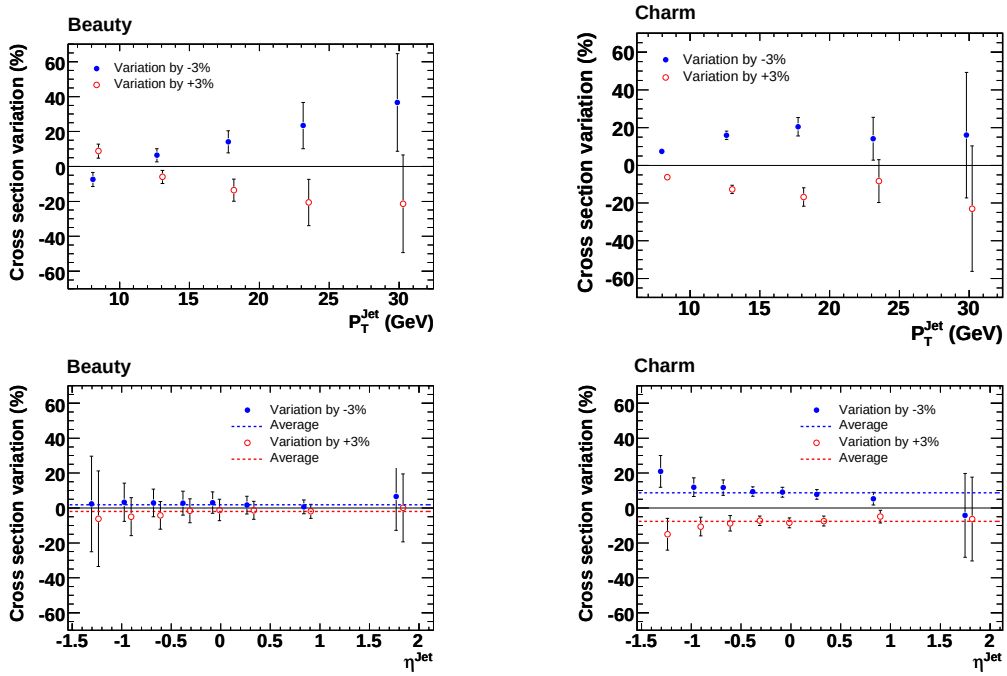

Figure 10.10: Dependence of the cross-section variation on P_T^{Jet} (left) and η^{Jet} (right) due to an energy-scale variation of $\pm 3\,\%$. The data corresponding to a positive variation are denoted by the open circles, those corresponding to a negative variation by filles circles. In the case of η^{Jet}, the average deviations from the measured cross sections are additionally indicated by the dashed lines.

section due to the energy-scale variation is shown as a function of P_T^{Jet} (top) and η^{Jet} (bottom) for beauty (left) and charm (right). The data corresponding to a variation of $+3\,\%$ are denoted by the open circles, those corresponding to a variation of $-3\,\%$ by filled circles. Constant deviations were found for η^{Jet}, while a clear dependence on P_T^{Jet} was observed as expected (see Section 9.1).

In case of η^{Jet} the average deviations as indicated by the dashed lines were used for the calculation of the systematic errors. In order to account for the dependence on P_T^{Jet} the individual values presented in Fig. 10.10 were applied for the determination of the corresponding uncertainties.

10.3.2 Charm reweighting

Since the distribution of the invariant mass of the secondary vertices, m_{vtx}, was not entirely described by the MC after selecting a charm-enriched sample (cf Section 8.2), the mass distribution of the charm content in the non-enriched sample was reweighted as a systematic check.

The weights were determined in the context of an ongoing D^* analysis [72], in which the so-called *golden decay channel*,

$$D^{*+} \rightarrow D^0\pi^+_{\text{slow}} \rightarrow K^-\pi^+\pi^+_{\text{slow}}$$

and its charge-conjugate, was studied. For the purpose of extracting weights for the systematic study in question, the kinematic range was chosen to be identical to the one used in this analysis. A clean charm sample was selected by reconstructing D^* candidates, which were required to be associated to one of the two highest-energetic jets in an event with a maximum distance $\Delta R(D^*, jet) = 0.4$ in the η-ϕ plane. In the following these associated jets will be referred to as *tagged D^* jets*. The D^* candidates were obtained by selecting combinations of three tracks corresponding to K, π and π_{slow} with requirements on the quality of those tracks and the reconstructed D^* and D^0 candidates (see [72]). The final charm signal was extracted subtracting the distributions with wrong-charge combinations ($K^+\pi^+\pi^-$ and $K^-\pi^-\pi^+$) from those containing the right-charge combinations ($K^+\pi^-\pi^-$ and $K^-\pi^+\pi^+$)[2]. In order to study jets and events as selected in this analysis those jets among the two highest-energetic jets in an event that were not tagged as D^* jets (*untagged jets*) were selected and investigated. Furthermore, the untagged jets were required to have an associated secondary vertex fulfilling the cuts described in Section 6.4.

[2] All other possible combinations correspond to Doubly Cabbibo suppressed decays and were therfore discarded.

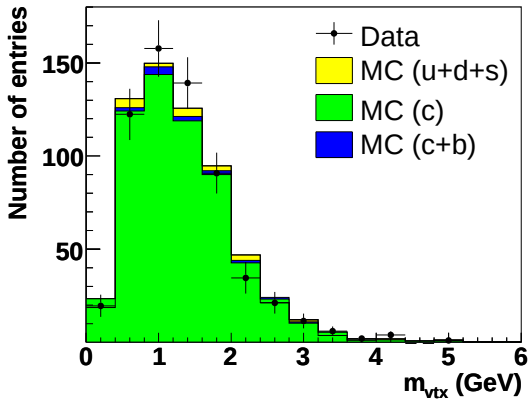

Figure 10.11: Invariant mass, m^{vtx}, of the secondary vertices associated to the untagged jets [71].

Figure 10.11 shows the distribution of the invariant mass, m_{vtx}, of the secondary vertices being associated to the untagged jets. The data points are compared to the MC denoted by the yellow histogram; in addition the contributions from the charm MC as well as from the sum of the beauty and charm MCs are shown as green and blue histograms. Reasonable agreement between data and MC could be observed. In order to reweight the m_{vtx} distribution of the charm content in this analysis three weights were extracted for the m_{vtx} bins which were previously used for the significance fits. The determination of these weights was done such that the MC reproduced the data well and at the same time the overall normalisation remained unchanged. The same procedure was repeated for several differential bins in P_T^{Jet} and η^{Jet} (see also Table E.1 in Appendix E). The widths were chosen such that the statistics were roughly equal in all bins of the given variable. In Fig. 10.12 the dependence of the weights on P_T^{Jet} and η^{Jet} is displayed for all three m_{vtx} bins as denoted in the legend. For η^{Jet} an approximately constant behaviour was observed for all mass bins, while some small differences between the two P_T^{Jet} bins could be found. Therefore the weights as a function of η^{Jet} were fitted with a constant function for each m_{vtx} bin, again ensuring the overall normalisation to be fixed as previously done for the total range. In the case of P_T^{Jet} the two bins were kept separate fixing the normalisation in each of the bins. The weights that were finally extracted and applied to the charm distributions that enter the significance fits shown in Chapter 7 are indicated by the dashed lines in Fig. 10.12. Additionally it was examined how many of the untagged jets were true charmed hadron jets and how big the contribution from beauty and light flavour jets was. This classification is depicted in

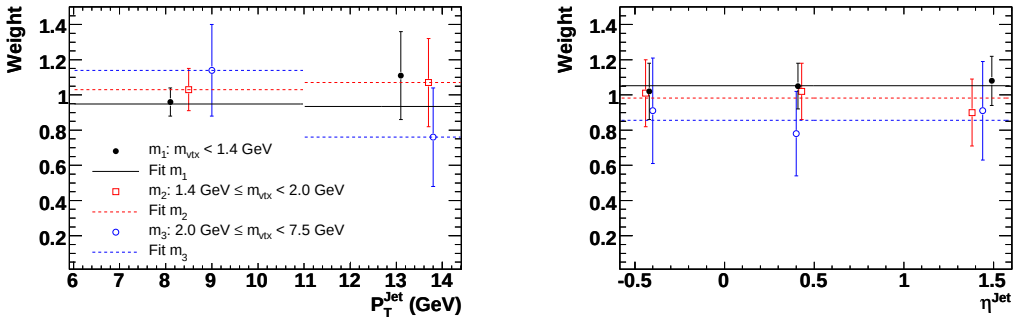

Figure 10.12: Weights for the three m_{vtx} bins as a function of P_T^{Jet} and η^{Jet}.

Fig. 10.13 on the left; the contribution from true charm jets was found to be $\approx 80\,\%$. The charm jets in the beauty and light flavour MCs originated from cascade decays ($b \to c$) and gluon splitting ($g \to c\bar{c}$), respectively. Since true charm jets cannot be selected in data, it was important to verify that despite the $20\,\%$ contamination by beauty and light flavour jets the m_{vtx} distribution in Fig. 10.11 was appropriate for extracting the weights. Therefore the MC m_{vtx} distribution shown previously was compared to a second distribution using only jets with a matched true charm jet. The comparison is shown in Fig. 10.13 (right) with the two distributions being denoted by the filled and open circles, respectively. The third distribution, which was inserted as an additional cross-check and is represented by the open triangles, requires sec-

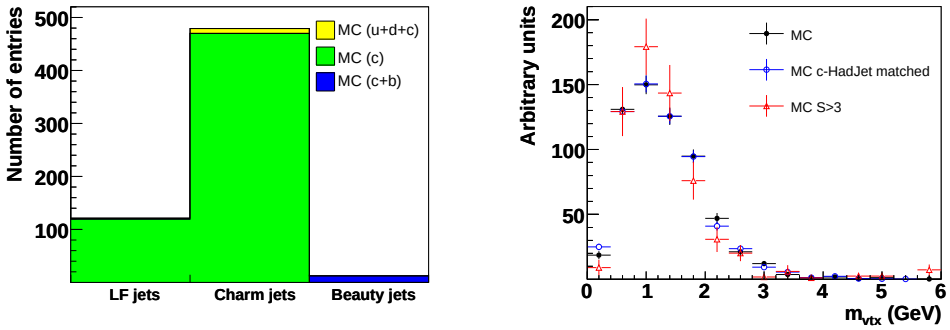

Figure 10.13: Type of the untagged jets extracted from MC truth information (left) and comparison of the m_{vtx} distributions for all detector-level jets in the MC, for those with a matched hadron jet and for those with a decay-length significance $S > 3$ (right) [71].

ondary vertices with decay-length significances, S, above 3. All distributions were normalised to the MC distribution without additional cuts.

The three m_{vtx} distributions were found to be consistent within errors confirming that the use of the m_{vtx} distribution displayed in Fig. 10.11 does not yield any additional systematic effects. For a quantitative comparison the corresponding mean and RMS values are listed in Table 10.1.

Cut	Mean (GeV)	RMS (GeV)
None	1.33	0.72
Matched true charm jet	1.33	0.71
$S > 3$	1.35	0.81

Table 10.1: Mean and RMS for the m_{vtx} MC distribution without any restriction, requiring a matched true charm jet and applying a cut on the decay-length significance of $S > 3$ [71].

Finally, the impact of the charm mass reweighting on the analysis results was evaluated by applying the extracted weights to the charm contribution of the mirrored decay-length significance, $S^+ - S^-$, and repeating all fits as presented in Chapter 7. For the total cross sections systematic uncertainties of $+5.2\,\%$ and $-1.8\,\%$ were calculated.

10.3.3 Summary of systematics

Table 10.2 summarises the systematic uncertainties calculated for the total beauty and charm cross sections.

It is worth noting that some of the systematic uncertainties are considerably smaller compared to those that were calculated for the analysis on pre-GR data (see Table 9.1). In particular the influence of the decay-length smearing was substantially reduced. This additionally indicates that the description of the decay-length significance by the MC has improved after the Grand Reprocessing as already observed in Fig. 10.7; since the smearing widens the MC distributions symmetrically, it has less impact on the result the better the shapes of the data and MC distributions agree. The systematic uncertainty for the event yield was kept as it was for the public results; this effect is still under study and the error can probably be substantially reduced in the future. The same applies to the uncertainty due to an imperfect simulation of the MVD hit efficiency; the same uncertainty was assumed as for the public results, especially since the simulation of the MVD resolution has not been finalised yet.

Uncertainty	Beauty (%)	Charm (%)
Hadronic energy scale	$^{+1.9}_{-2.2}$	$^{+9.5}_{-6.9}$
Trigger correction	± 2.1	± 4.3
Fit range	± 1.7	± 3.2
Decay-length smearing	$+0.2$	-1.7
Charm mass reweighting	$+5.2$	-1.8
MVD hit efficiency	± 3.0	± 3.0
Event yield	$+5.0$	$+5.0$
Luminosity	± 3.0	± 3.0

Table 10.2: Summary table of uncertainties included in the systematic errors. Presented are the uncertainties on the total beauty and charm cross sections.

10.4 Results for the central and forward region

After the modifications described in the previous sections all mirrored decay-length significance fits were re-done. The fit for the total kinematic range resulted in the following k-factors for the three flavours:

$$\begin{aligned} k_b &= 1.05 \pm 0.032 \\ k_c &= 1.18 \pm 0.020 \\ k_{lf} &= 0.92 \pm 0.006. \end{aligned}$$

Due to the improved description of the decay-length significance the χ^2/ndf was reduced to $52/22 = 2.38$.

The measured differential beauty and charm cross sections as a function of P_T^{Jet} and η^{Jet} are shown in Fig. 10.14. The data which are displayed with statistical and systematic errors and are compared to the scaled PYTHIA LO+PS prediction and the NLO QCD prediction calculated with the FMNR programme. The specifications are again the same as described in Chapter 4. In addition to the prediction using CTEQ5M as the proton PDF the central value of a second FMNR prediction, for which CTEQ5M was replaced by the ZEUS-S PDF, is shown. The latter was found to lie systematically above the central value, but within the uncertainty of the prediction using CTEQ5M. Hadronisation corrections were applied to both NLO QCD predictions; the correction factors, C_{had}, as a function of P_T^{Jet} and η^{Jet} for both

beauty and charm are displayed in Fig. 10.15. The measurements and the PYTHIA LO+PS predictions as well as the QCD NLO calculations were found to be in good agreement within the statistical and systematic uncertainties. All cross sections, NLO predictions and hadronisation correction factors are also listed in Tables C.3 and C.4 in Appendix C.

The differential cross section as a function of η^{Jet} was furthermore compared to the corresponding preliminary result as shown in Fig. 10.16; very good agreement between both measurements could be observed. Due to the extension of the kinematic range in η^{Jet} it was not possible to directly compare the cross section as a function of P_T^{Jet}.

Finally the beauty-enriched and charm-enriched distributions were redone as well (cf Section 8.2). As an example the two $S^+ - S^-$ distributions are displayed in Fig. 10.17. While in the beauty-enriched $S^+ - S^-$ distribution the data are still slightly below the MC for $8 \leq S^+ - S^- < 13$, clear improvements for the charm distribution are visible resulting in a significantly better description than observed on the pre-GR datasets.

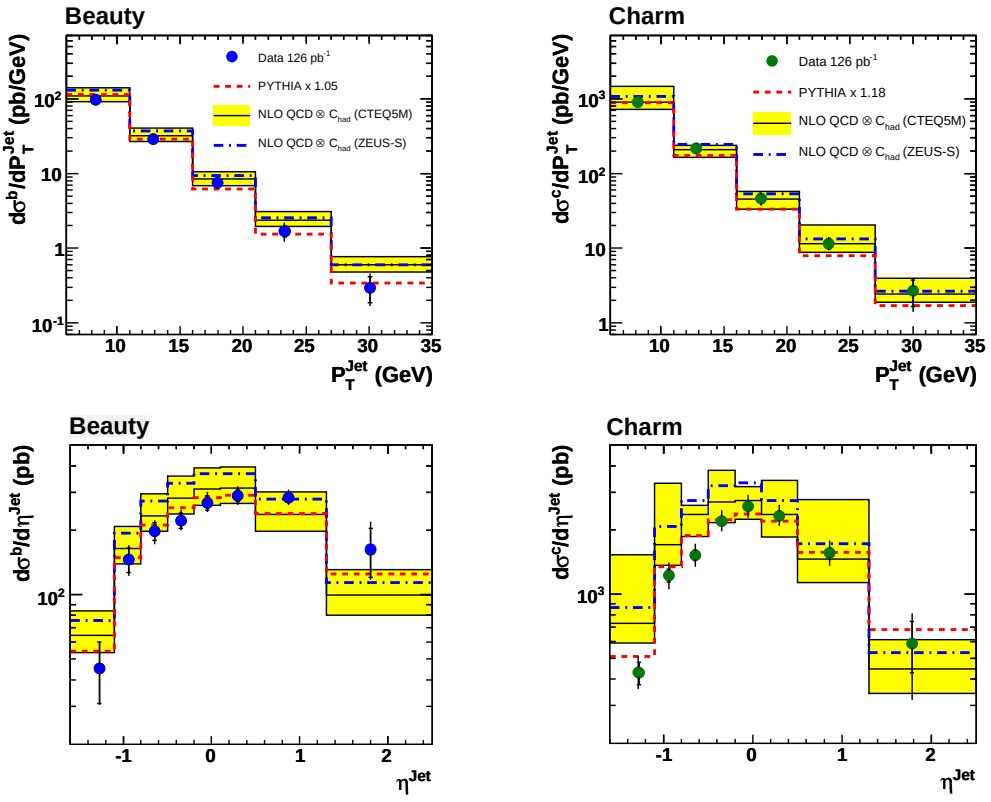

Figure 10.14: Differential beauty and charm cross sections as a function of P_T^{Jet} (top) and η^{Jet} (bottom) for events with $Q^2 < 1\,\mathrm{GeV}^2$, $0.2 < y < 0.8$, $P_T^{Jet\,1(2)} > 7(6)\,\mathrm{GeV}$ and $-2.5 \leq \eta^{Jet\,1(2)} < 2.5$ using jets with $-1.6 \leq \eta^{Jet\,1(2)} < 2.5$. The black points show the results from this analysis. The inner error bars are statistical uncertainties, while the external error bars show the statistical and systematic uncertainties added in quadrature. The band represents the NLO QCD prediction using CTEQ5M as proton PDF and its uncertainties. In addition the central value of the NLO QCD prediction using Zeus-S instead of CTEQ5M is shown.

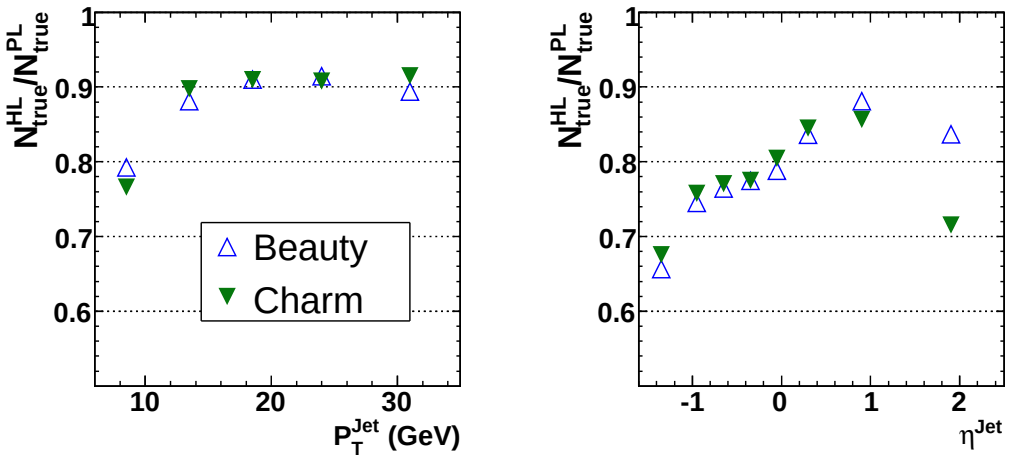

Figure 10.15: Hadronisation corrections as a function of P_T^{Jet} and η^{Jet} for beauty (open triangles) and charm (filled triangles).

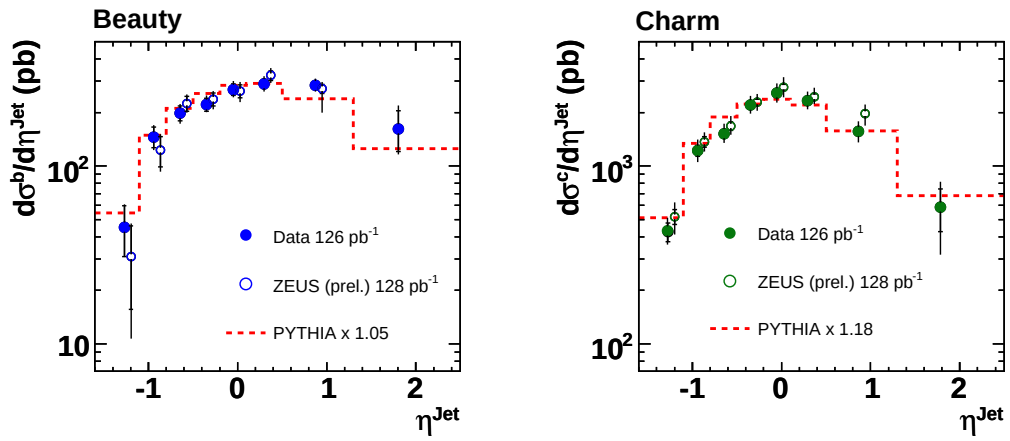

Figure 10.16: Differential beauty and charm cross sections as a function of η^{Jet}. The filled circles represent the results from this analysis including the forward region and are compared to the preliminary results denoted by the open circles. The inner error bars are statistical uncertainties, while the external error bars show the statistical and systematic uncertainties added in quadrature.

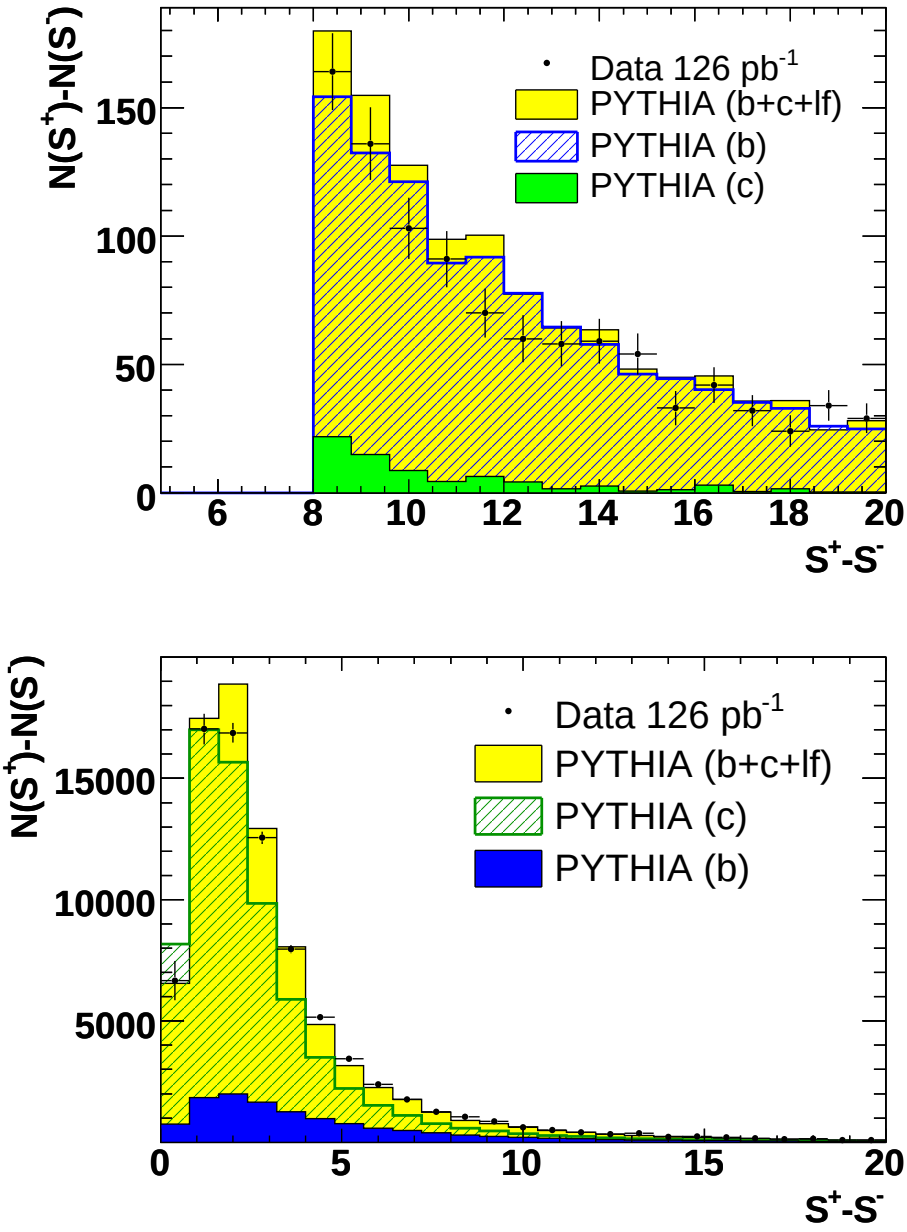

Figure 10.17: Mirrored decay-length significance, $S^+ - S^-$, for the beauty-enriched and charm-enriched samples. The black points represent the data, while the total MC distribution as well as the contributions from beauty and charm are denoted by the yellow, blue and green histograms.

Chapter 11

Dijet correlations

The inclusive secondary vertexing analysis and in particular the event selection it is based on also allows the study of dijet correlations. This topic was already addressed in the course of previous studies, in which semileptonic B decays into jets and muons were analysed [77, 78]. However, after the evaluation of the results it was difficult to draw substantive conclusions, because the statistics for such analyses focusing on a dedicated b decay channel was rather limited. The inclusiveness of the beauty analysis presented in this thesis and the resulting gain in statistics therefore suggested to repeat the dijet correlation studies and try to extract more conclusive results.

The methods and cuts used in the following are based on recent studies covered in [79]. After a short introduction I will describe the two methods that were used for the extraction of the correlation cross sections. The results obtained from both methods will be presented, compared and discussed.

11.1 Introduction

At leading order, the two highest energetic jets[1] will typically be produced back-to-back in the x-y plane. The distribution of the angular difference in this plane, $\Delta\phi$, will therefore have a strong peak at $\Delta\phi = \pi$ and decrease rapidly towards lower values. Higher orders, which are present in the data, but are not fully included in the Monte Carlo simulation, allow for additional gluon radiation, which results in extra jets. Due to the presence of these jets, the angular difference between the two highest energetic jets will be reduced and the $\Delta\phi$ distribution will be softened. In order to further investigate these higher-order effects, cross sections as a function of $\Delta\phi$ and four other corre-

[1] In the following, the two highest energetic jets ordered according to their transverse momenta, $p_T^{Jet\,1(2)}$, will be called Jet 1 and Jet 2 unless stated otherwise.

lation variables were determined and compared to LO+PS MC predictions as well as NLO QCD calculations. For both predictions the same datasets and parameters as described in Chapter 4 were used.

The five correlation variables, which were examined in this study, are defined as follows:

- The angular difference of Jet 1 and Jet 2 in the x-y plane:
  $\Delta\phi := \sphericalangle(\phi^{Jet\,1}, \phi^{Jet\,2})$
- The difference in η of Jet 1 and Jet 2:
  $\Delta\eta := \eta^{Jet\,1} - \eta^{Jet\,2}$
- $\Delta R := \sqrt{\Delta\phi^2 + \Delta\eta^2}$
- $\cos\theta^* := \tanh(\frac{\Delta\eta}{2})$
- The invariant mass of Jet 1 and Jet 2:
  $M^{jj} := \sqrt{E^{Jet\,1} \cdot E^{Jet\,2} - \vec{p}^{\,Jet\,1} \cdot \vec{p}^{\,Jet\,2}}$.

The initial motivation for using $\cos\theta^*$ in addition to $\Delta\eta$ was the fact that it represents the scattering angle of the dijet system with respect to the proton axis in the dijet rest frame. It distinguishes between the highest energetic jet being produced in the proton ($\cos\theta^* > 0$) or in the photon direction ($\cos\theta^* < 0$) and can thus provide information about the production process. However, stable theoretical predictions are difficult to obtain, since there a clear distinction between the two highest energetic jets is impossible. This problem does not occur in analyses using for instance semileptonic decays into muons, as the jet associated to the muon can be used as the tagged jet and $\cos\theta^*$ can be calculated using the μ-jet and the other b-jet. In order to make a comparison with theoretical predictions possible in the following only the absolute values of $\cos\theta^*$ were used. The same argument holds for $\Delta\phi$ and $\Delta\eta$. Although $|\cos\theta^*|$ cannot directly differentiate between the production processes it was kept for the cross-section measurement and for additional process-dependent studies.

Control distributions of all five variables are shown in Fig. 11.1. The data are compared to the Pythia LO+PS Monte Carlo simulation and clearly reveal the expected higher-order effects discussed above: In particular, the $|\Delta\phi|$ distribution shows significant deviations at $|\Delta\phi| = \pi$. Related discrepancies are observed in ΔR. The $|\Delta\eta|$ and $|\cos\theta^*|$ distributions are also not entirely described by the MC; these discrepancies will be discussed briefly at the end of this chapter.

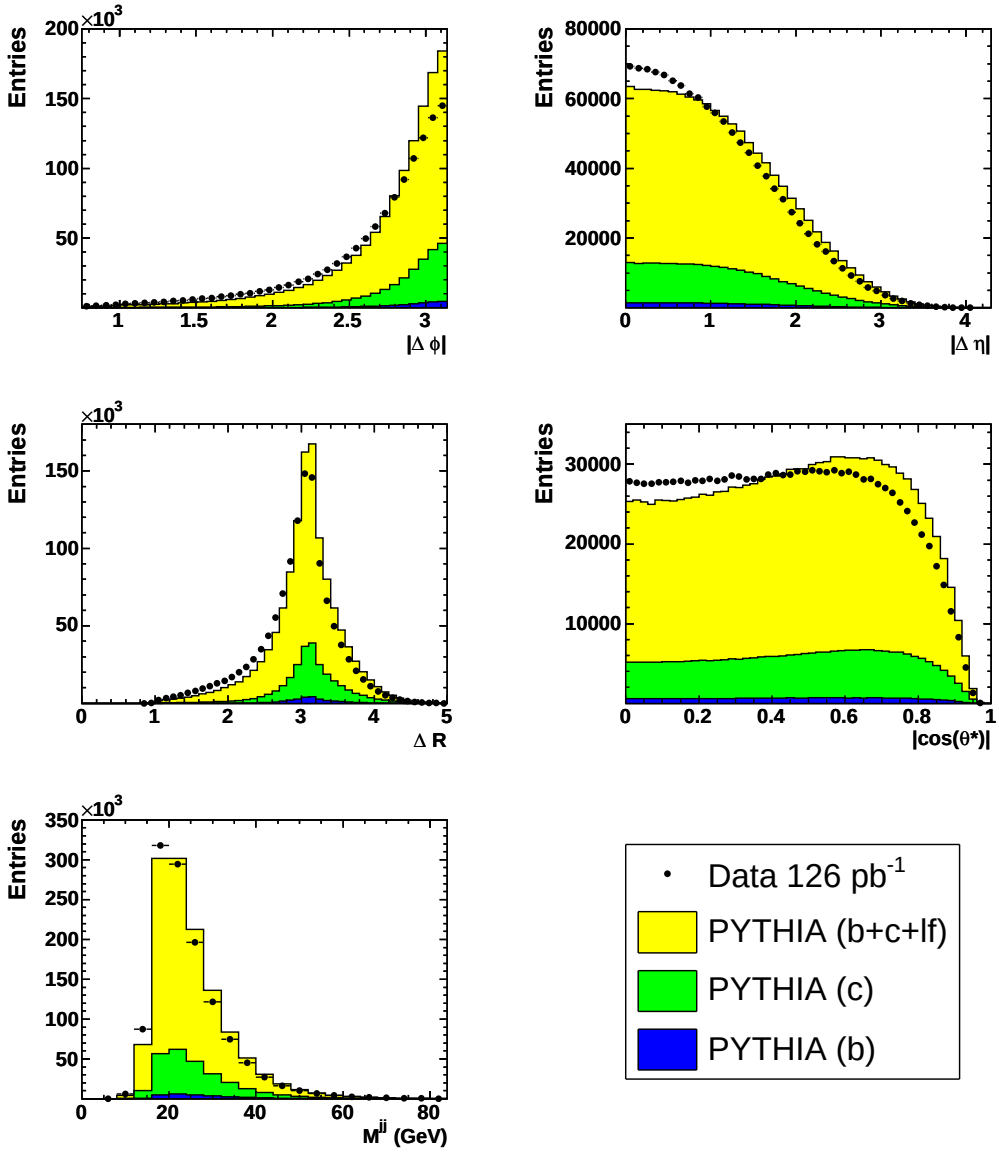

Figure 11.1: Control distributions for the dijet correlation variables $|\Delta\phi|$, $|\Delta\eta|$, ΔR, $|\cos\theta^*|$ and M^{jj}. The data are compared to the PYTHIA MC simulation. Furthermore, the contributions from beauty and charm are shown.

All events in the 2006/07 e^+p Grand-Reprocessed data that fulfilled the selection criteria listed in Section 6.3 and those jets among the two highest energetic ones per event with $-1.6 \leq \eta^{Jet} < 2.5$ were considered in the analysis. Furthermore, at least one of the two highest energetic jets was required to have a secondary vertex associated to it with the secondary vertices being reconstructed in the same way as for the results presented in Chapter 10.

Hadronic corrections were also evaluated from the MC; they are shown in Fig. 11.3 for both beauty and charm. The NLO QCD predictions were corrected with these values in order to ensure the consistency between them and the measured cross sections, which make use of the acceptance determined from truth information on hadron level (cf Section 4.2). The large corrections ($\approx 80\,\%$) for small values of $|\Delta\phi|$ and ΔR are due to the fact that using hadron level (HL) b jets the number of events as a function of $|\Delta\phi|$ decreases continuously towards small values as it is also seen on detector level in both data and MC, while for the parton level (PL) a local minimum around $|\Delta\phi| = 1.3$ and an increase towards $|\Delta\phi| = 0$ is observed. The direct comparison between the number of events on PL and HL as a function of $|\Delta\phi|$ is shown in Fig. 11.2. It is not yet understood why the MC predicts such a large number of events with an angular difference $|\Delta\phi| < 1$ between the two highest energetic parton level b jets, which leads to a considerable downscaling of the NLO QCD predictions in this region.

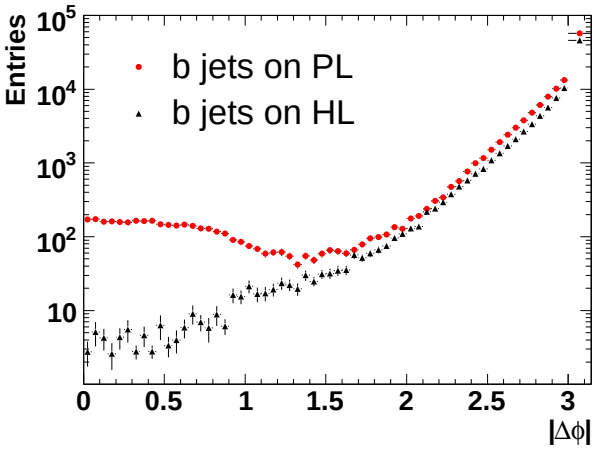

Figure 11.2: Number of events on parton level (PL) and hadron level (HL) as a function of $|\Delta\phi|$.

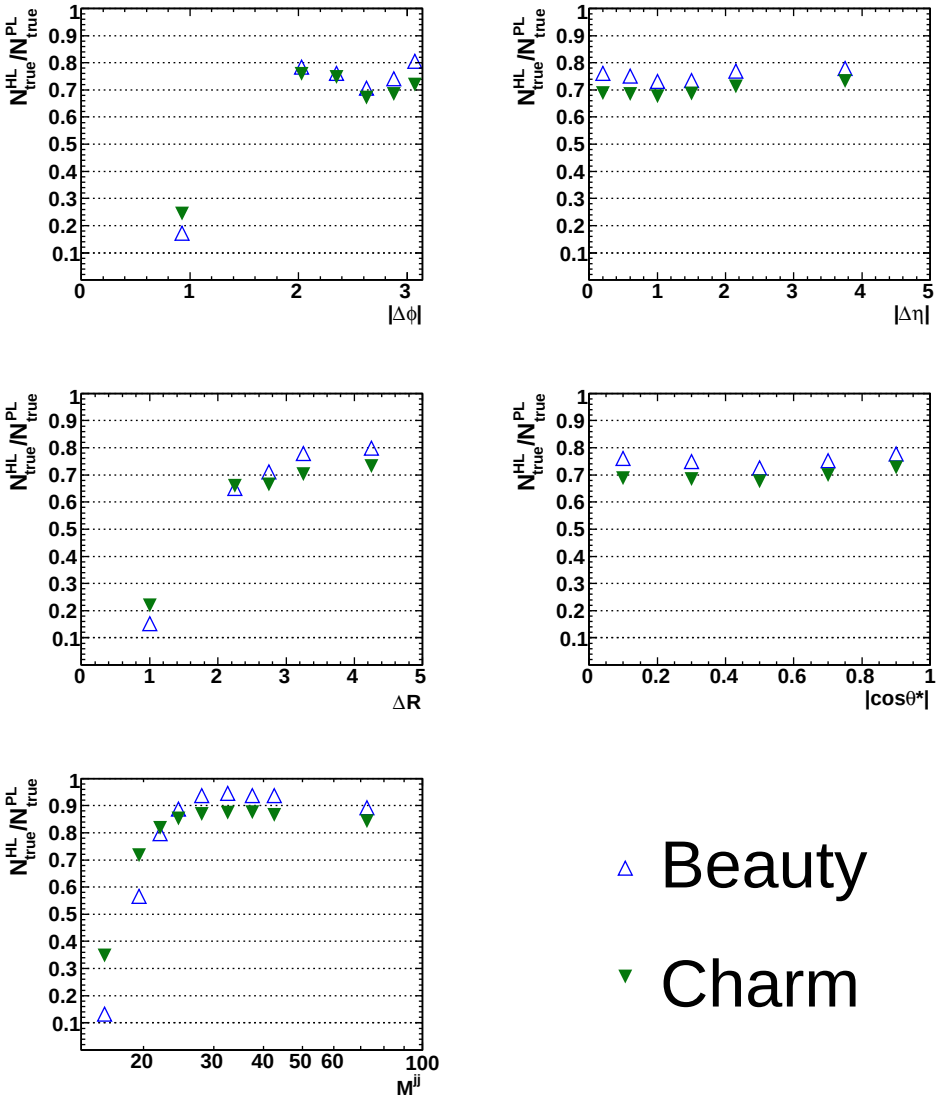

Figure 11.3: Hadronisation corrections for beauty (open triangles) and charm (filled triangles) as a function of the dijet correlation variables $|\Delta\phi|$, $|\Delta\eta|$, ΔR, $|\cos\theta^*|$ and M^{jj}.

11.2 Methods

In the following two independent methods for the determination of the beauty content and the extraction of the differential cross sections as a function of the correlation variables introduced in the previous section will be described. The first method also allows for a simultaneous measurement of charm di-jet correlation cross sections. The two methods were expected to deliver consistent results and were therefore used to cross-check each other.

11.2.1 Fit of $S^+ - S^-$

The first approach is identical to the procedure explained in Chapter 7: in order to separate beauty from charm and light flavours, the mirrored decay-length significance, $S^+ - S^-$, was split into three bins of the invariant mass of the secondary vertex tracks, m_{vtx}. In order to evaluate the differential cross sections as a function of the five correlation variables, $S^+ - S^-$ was fitted simultaneously in all three m_{vtx} bins for each bin in $|\Delta\phi|$, ΔR, $|\Delta\eta|$, $|\cos\theta^*|$ and M^{jj}. For the fit, the χ^2 in equation 7.1 was minimised and scaling factors for the beauty, charm and light flavour contributions could be obtained. As an example, the fitted $S^+ - S^-$ distributions for six $\Delta\phi$ bins are shown in Fig. 11.4. The corresponding distributions for all other correlation variables are displayed in Fig. D.1- D.4 in Appendix D. All fits yielded stable results with χ^2/ndf values between 1 and 1.5 on average.

In analogy to Section 8.1 the differential beauty cross section as a function of a given correlation variable, v, was calculated as follows:

$$\frac{d\sigma^b}{dv} = \frac{k_b \cdot N_b^{true,HL}}{\mathcal{L}^{Data} \cdot \Delta v}.$$

Here, k_b denotes the beauty scaling factor obtained from the fit and $N_b^{true,HL}$ the number of b events on hadron level for a given v bin, Δv. $\mathcal{L}^{Data}$ refers to the integrated luminosity of the used data sample. The differential cross sections for charm were determined accordingly.

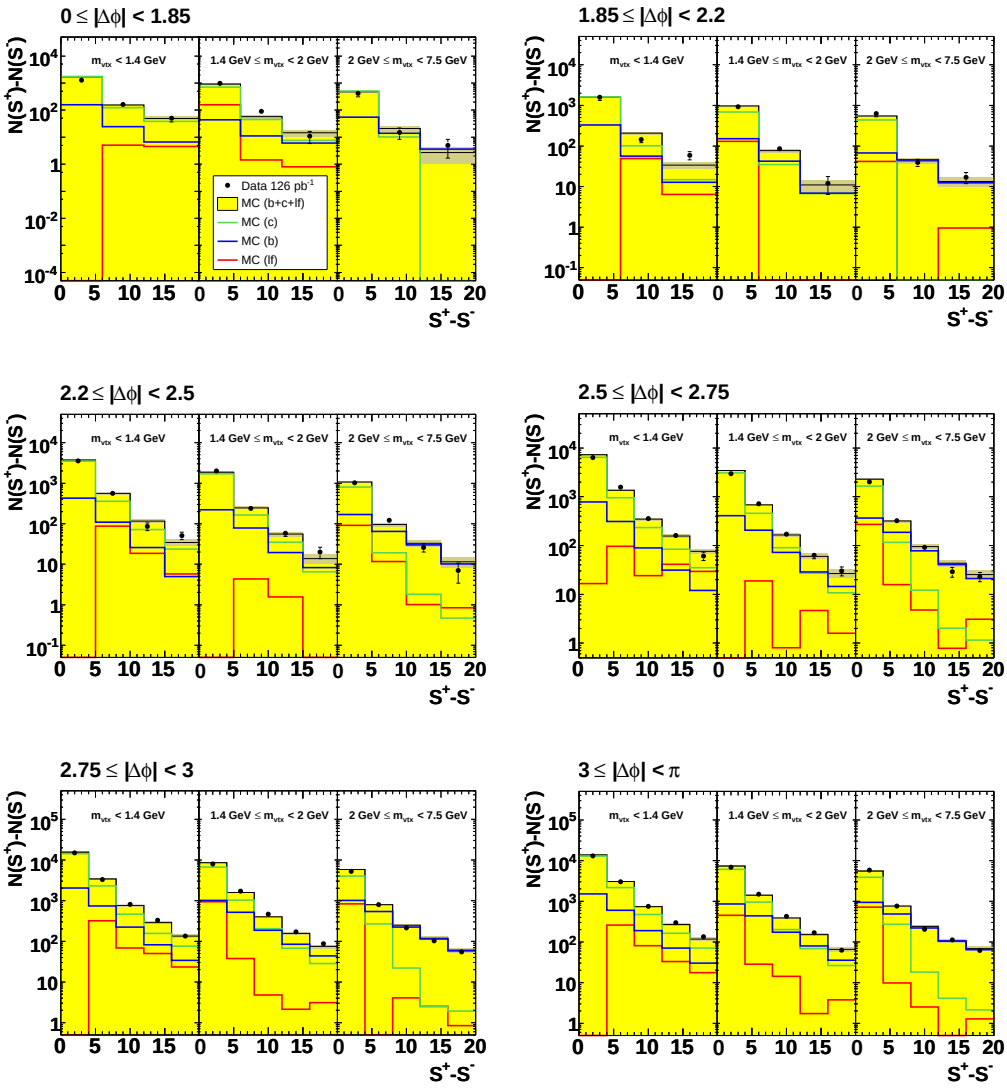

Figure 11.4: Mirrored significance fits in three m_{vtx} bins for all $|\Delta\phi|$ bins. The contributions from beauty, charm and light flavours are scaled with the factors obtained from the fit and denoted by the blue, green and red solid lines. The data are represented by the black points, the scaled MC sum is shown as a yellow histogram with shaded error bands.

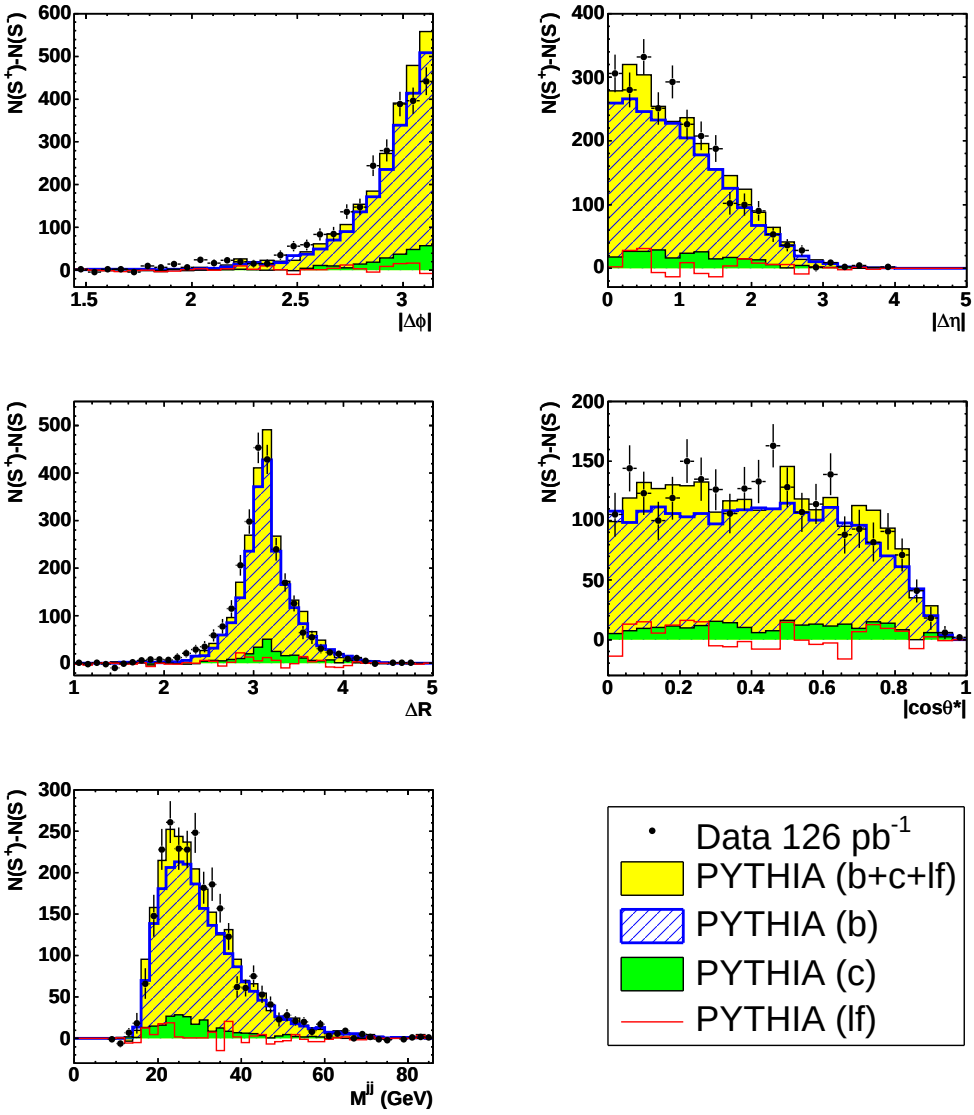

Figure 11.5: Beauty-enriched control distributions for the dijet correlation variables $|\Delta\phi|$, $|\Delta\eta|$, ΔR, $|\cos\theta^*|$ and M^{jj}. The data are compared to the PYTHIA MC simulation. Furthermore, the contributions from beauty, charm and light flavours are shown.

11.2.2 Beauty enrichment

The second approach made use of the highly beauty-enriched region for the extraction of the differential cross sections. It was selected in the same way as before (see Section 8.2) by requiring:

- $m_{vtx} \geq 2\,\mathrm{GeV}$,
- $S^+ - S^- > 6$.

The cut on the mirrored significance was reduced from 8 to 6 in order to provide enough statistics for the measurement. In Section 8.2 the beauty-enriched region was only used for obtaining the corresponding vertex and jet control distributions. In contrast to this, the aim now was to calculate differential cross sections as a function of event variables (e.g. $|\Delta\phi|$) rather than jet or vertex variables; therefore the difficulty here consisted in properly taking into account events with both of the two highest energetic jets having an associated secondary vertex. Since in such a situation there are two vertices the cuts listed above could be applied to, weights w were applied to the selected events such that

$$w = \mathrm{sign}(S_1) + \mathrm{sign}(S_2)$$

with S_i being the decay-length significances corresponding to the two secondary vertices. If there was no vertex associated to a jet, $\mathrm{sign}(S)$ was set to 0 for the calculation of the event weight. Hence the event was not considered at all in the case that none of the two jets had an associated secondary vertex. This procedure particularly took into account that an event with two positive decay-length significances was most probably indeed a $b\bar{b}$ event; thus it was enhanced in weight. This weighting scheme, which is also summarised in Table 11.1, was applied in a similar way to the events on hadron level in order to ensure a consistent treatment of the reconstructed and true quantities used for the acceptance calculation later on.

Figure 11.5 shows the five dijet correlation variables after beauty-enrichment. The beauty fraction - denoted by the shaded area - now amounts to 90 %, the contribution from charm and light flavours can be regarded as negligible. In the $|\Delta\phi|$ distribution the expected deviation of the MC from the data due to higher order effects can still be observed; it is also visible in ΔR in terms of a slight shift of the data towards lower values compared to the MC simulation. The other three distributions show a reasonable agreement between data and MC within the limits of the given statistical precision.

A high and stable beauty fraction, f_b (see Fig. 11.6), was necessary for a reliable extraction of the cross sections. The differential cross section as a

Jet 1 \ ***Jet 2***	$S_2 > 0$	$S_2 < 0$	*No vertex*
$S_1 > 0$	+2	0	+1
$S_1 < 0$	0	-2	-1
No vertex	+1	-1	0

Table 11.1: Weighting scheme for the dijet correlation variables in the beauty-enriched region.

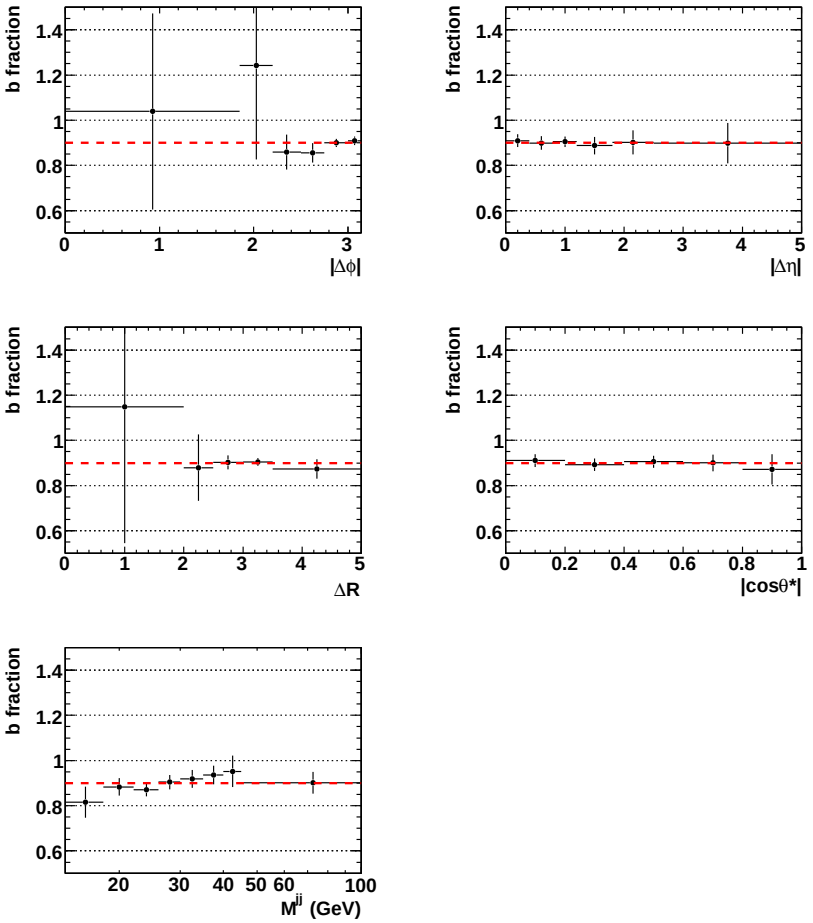

Figure 11.6: Beauty fraction as a function of the dijet correlation variables $|\Delta\phi|$, $|\Delta\eta|$, ΔR, $|\cos\theta^*|$ and M^{jj}. The beauty fraction of the total sample is indicated by the dashed line.

function of a given correlation variable, v, was calculated as follows:

$$\begin{aligned}\frac{d\sigma^b}{dv} &= \frac{N_b^{Data}}{\mathcal{A}_b \cdot \mathcal{L}^{Data} \cdot \Delta v} \\ &= \frac{N^{Data} \cdot f_b}{\mathcal{A}_b \cdot \mathcal{L}^{Data} \cdot \Delta v}.\end{aligned}$$

Here, $\mathcal{L}^{Data}$ refers to the integrated luminosity of the used data sample and f_b to the beauty fraction. N^{Data} denotes the number of data entries and $\mathcal{A}_b$ the beauty acceptance in a given bin, Δv. The acceptance

$$\mathcal{A}_b = \frac{N_{rec}}{N_{true}^{HL}}$$

is calculated as the number of reconstructed beauty events divided by the number of generated beauty events on hadron level (HL). In Fig. D.5 in Appendix D it is shown as a function of all correlation variables.

Unfortunately, it was impossible to also achieve a charm enrichment of comparable purity, therefore only beauty production cross sections were extracted using this method.

11.3 Results on dijet correlations

The differential cross sections for beauty and charm production as obtained with the fit method are displayed in Fig. 11.7-11.9. The measurements are compared with the PYTHIA LO+PS predictions as well as both NLO QCD calculations obtained from the FMNR programme using CTEQ5M and ZEUS-S as proton PDF. The cross section as a function of $|\Delta\phi|$ in Fig. 11.7 is shown on both linear and logarithmic scales. The cross section naturally reveals the same disagreement between data and MC that was discussed before and is due to the missing higher-order effects in the simulation. The NLO QCD prediction agrees well with the measurement, although slight discrepancies in the bins with low statistics, i.e. at low $|\Delta\phi|$, can be observed. The same behaviour was found for the cross section as a function of ΔR, which is shown in Fig. 11.8. The cross sections depending on $|\Delta\eta|$, $|\cos\theta^*|$ and M^{jj} are described well by both the MC simulation and the NLO QCD predictions. The cross-section numbers and hadronisation corrections are listed in Tables D.3-D.6 in Appendix D.

In Fig. 11.10 the differential beauty production cross sections as obtained after beauty enrichment are shown. These measurements are also compared to the PYTHIA LO+PS predictions as well as the NLO QCD calculations. The cross-section numbers are listed in Tables D.1 and D.2 in Appendix D.

Figure 11.11 shows the direct comparison of the measurements obtained with the two methods presented in Sections 11.2.1 and 11.2.2. Both results are in very good agreement and therefore demonstrate the consistency of the two methods. Since the measurements are hardly distinguishable, the ratio, i.e. the result after beauty enrichment divided by the result as obtained from the fits, is displayed as well with the shaded band indicating a $\pm 10\,\%$ deviation from 1. Except for very few bins with low statistics the ratio is always found to lie within this band.

For the evaluation of the systematic errors the studies discussed in Chapters 9 and 10 were repeated in all bins of the five correlation variables. The contributions of the different sources were found to be of a similar size as for the cross sections as a function of η^{Jet} and P_T^{Jet} presented earlier.

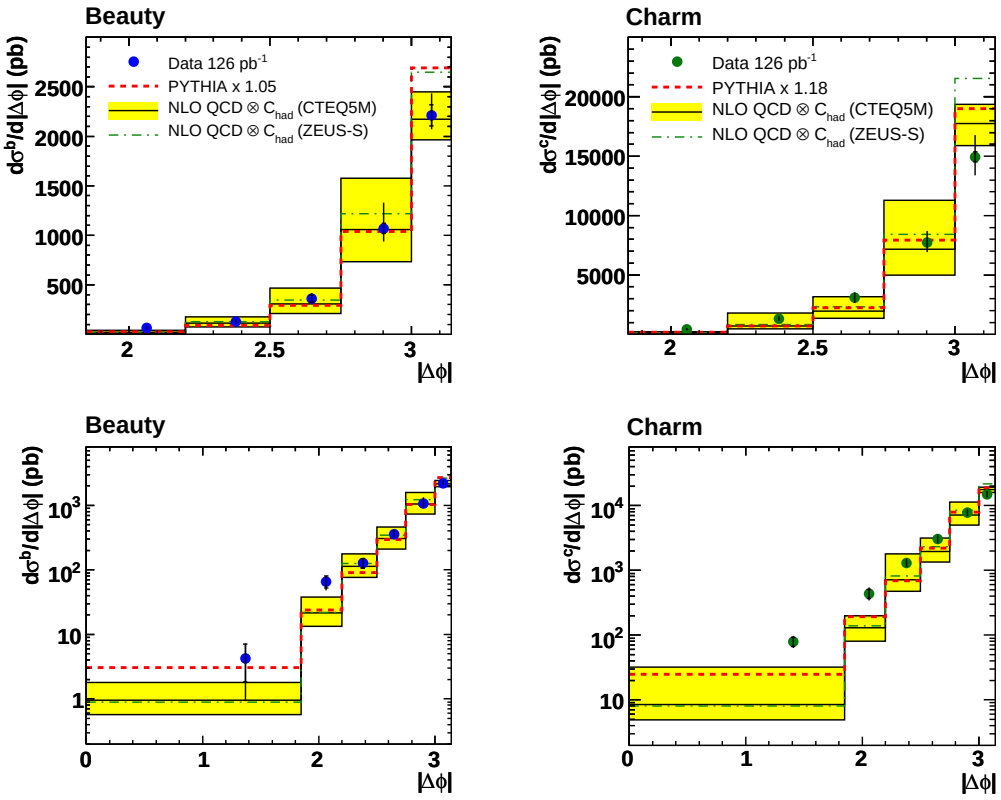

Figure 11.7: Differential cross sections as a function of the dijet correlation variable $|\Delta\phi|$ on linear (top) and logarithmic scales (bottom) as obtained from the mirrored decay-length significance fit. The measurements are compared to the scaled PYTHIA LO+PS prediction denoted by the red dashed lines as well as the two NLO QCD predictions using CTEQ5M (solid line and yellow uncertainty bands) and ZEUS-S (green dashed line) as proton PDF. Note that for clarity the first $|\Delta\phi|$ bin is not shown in the upper figures.

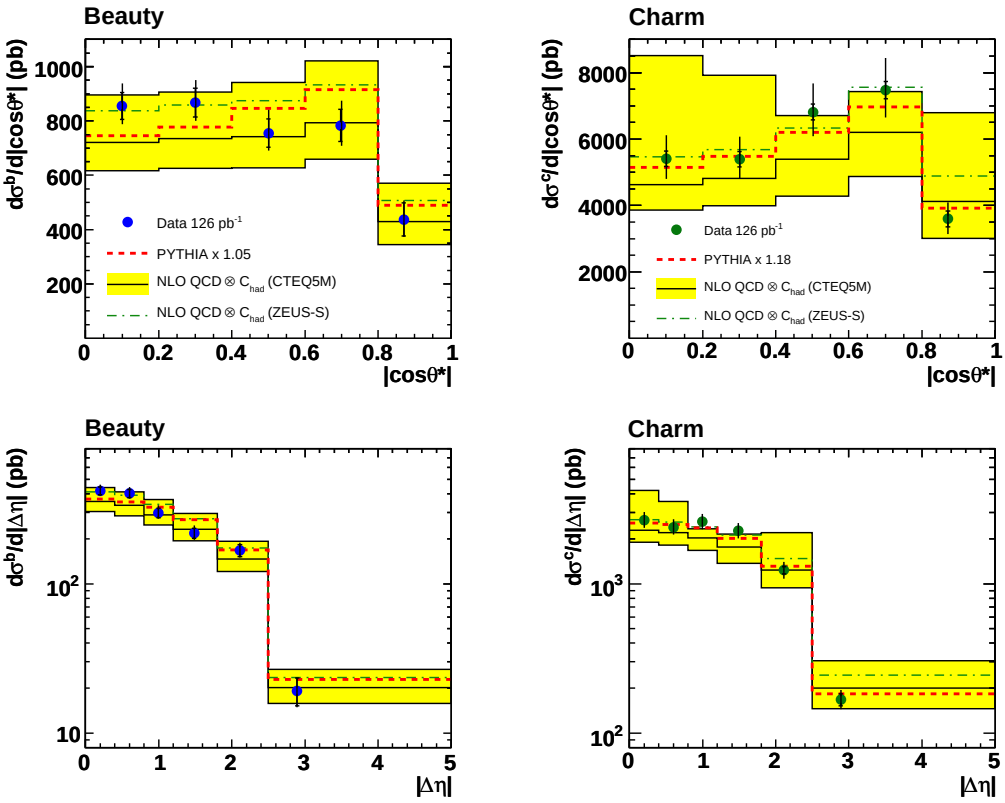

Figure 11.8: Differential cross sections as a function of the dijet correlation variables $|\cos\theta^*|$ and $|\Delta\eta|$ as obtained from the mirrored decay-length significance fit. For more details see the caption of Fig. 11.7.

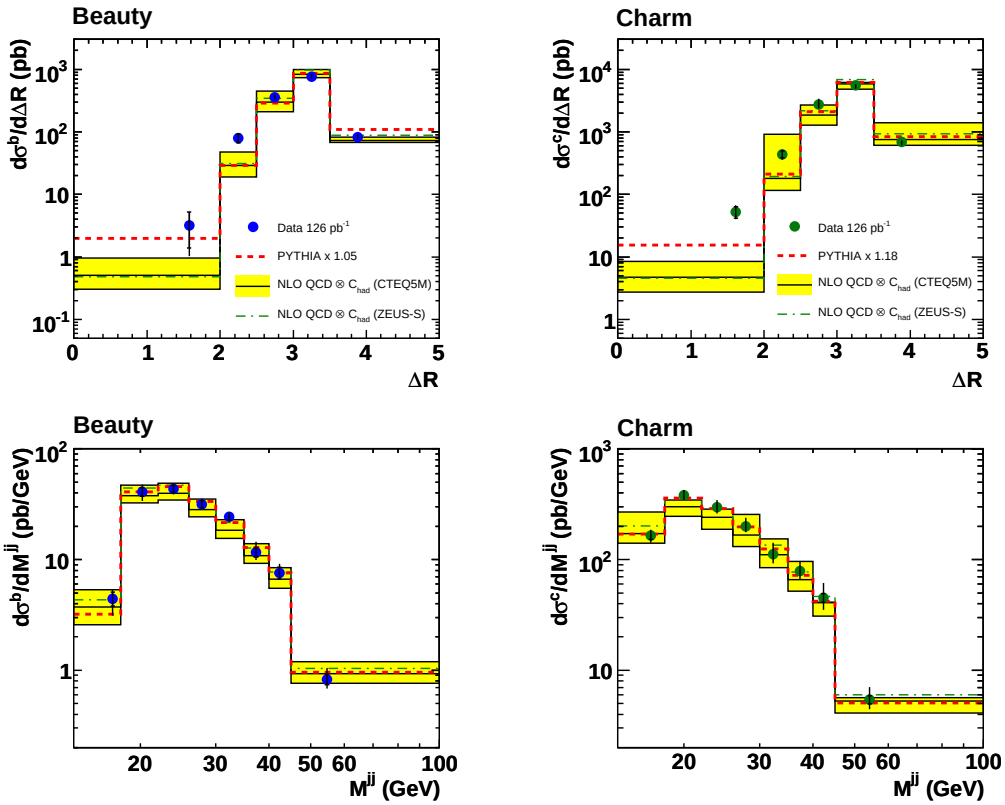

Figure 11.9: Differential cross sections as a function of the dijet correlation variables ΔR and M^{jj} as obtained from the decay-length significance fit. For more details see the caption of Fig. 11.7.

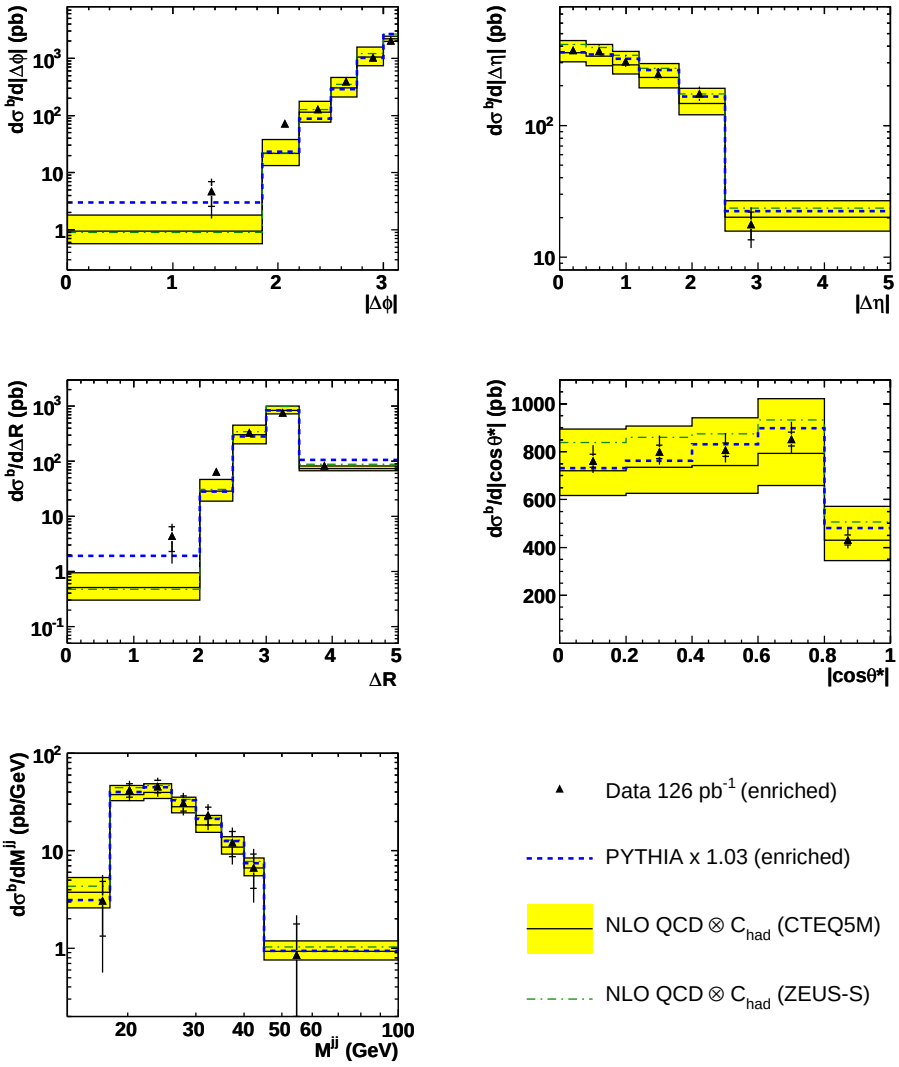

Figure 11.10: Differential beauty cross sections as a function of the dijet correlation variables $|\Delta\phi|$, $|\Delta\eta|$, ΔR, $|\cos\theta^*|$ and M^{jj} as obtained from the beauty-enriched sample. The measurements are compared to the scaled PYTHIA LO+PS prediction represented by the blue dashed line as well as the two NLO QCD predictions using CTEQ5M (solid line and yellow uncertainty bands) and ZEUS-S (green dashed line) as proton PDF, respectively.

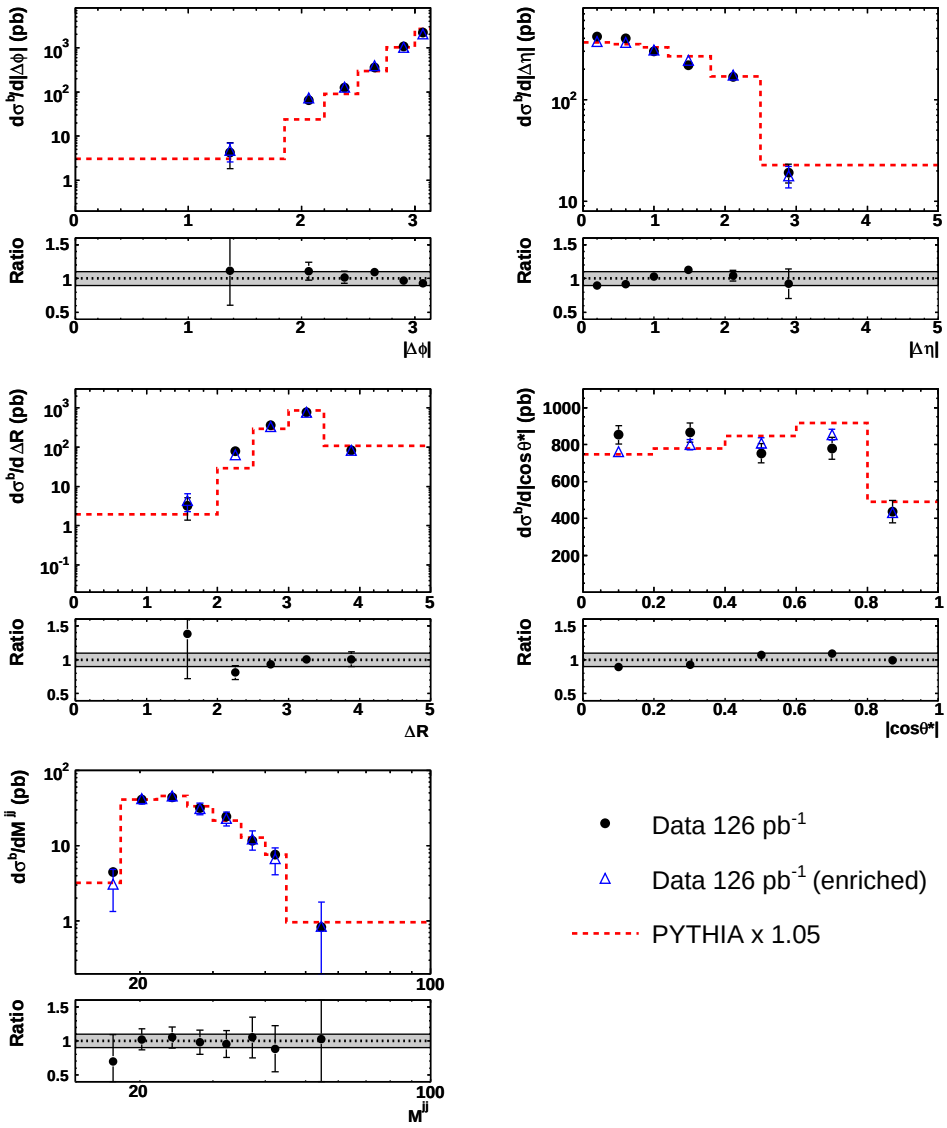

Figure 11.11: Direct comparison of the differential beauty cross sections as a function of the dijet correlation variables $|\Delta\phi|$, $|\Delta\eta|$, ΔR, $|\cos\theta^*|$ and M^{jj}. The measurements as obtained from the decay-length significance fit (circles) and the beauty-enriched sample (triangles) are compared to the scaled PYTHIA LO+PS prediction denoted by the dashed line. In addition the ratio, i.e. the result after beauty enrichment divided by the result as obtained from the fits, is shown. The shaded band indicates a $\pm 10\,\%$ deviation from 1.

11.4 Outlook

With two independent and consistent methods for the determination of the beauty content at hand, the dijet correlation analysis can be extended and studied in greater detail. For instance the sample can be split into a direct-enriched region and a resolved-enriched region by means of

$$x_\gamma^{obs} = \frac{1}{2yE_e} \sum_{i \in Jet\,1,2} E_{t,i} e^{-\eta_i},$$

which represents the fraction of E_e, i.e. the energy of the incoming electron, that is transferred to the photon. $E_{t,i}$ and η_i denote the transverse energies and the pseudorapidities of the two highest energetic jets in the event. The resolved-enriched region also includes excitation processes.

This distinction is worth studying since the resolved-enriched part contains a non-negligible hadron-like contribution and is thus sensitive to the gluon content in the photon. The basic control distributions for $|\Delta\phi|$ and $|\cos\theta^*|$ that are displayed in Fig. 11.12 already show differences between the two regimes: the $|\Delta\phi|$ distribution peaks much more strongly around $|\Delta\phi| = \pi$ in the direct-enriched sample. This behaviour is expected since in direct photoproduction it is more likely to tag two back-to-back jets originating from two quarks that are produced in the hard subprocess (cf Chapter 3). On the other hand there is a bigger discrepancy between the data and the LO+PS Monte Carlo simulation for the resolved-enriched sample. The latter can also be observed in the $|\cos\theta^*|$ distribution: Most of the deviations observed in the description using the whole sample (cf Fig. 11.1) seem to be due to the resolved part, since the direct part is reasonably well simulated. Because of to those discrepancies a better understanding and more detailed studies are necessary before it is possible to extract final results.

Finally, it is desirable to also compare the separate measurements for the direct-enriched and resolved-enriched regimes to NLO QCD predictions in order to further probe the applicability and adequacy of perturbative QCD calculations.

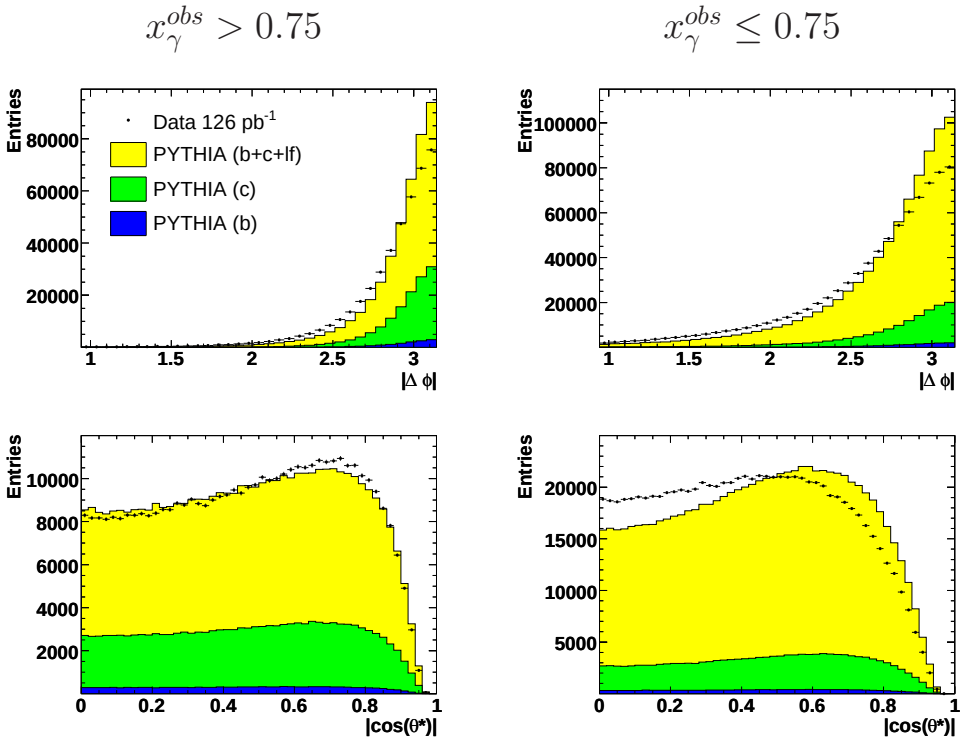

Figure 11.12: Control distributions for $|\Delta\phi|$ and $|\cos\theta^*|$ for the direct-enriched ($x_\gamma^{obs} > 0.75$) and the resolved-enriched region ($x_\gamma^{obs} \leq 0.75$). The data are denoted by the black points, while the total MC distributions are represented by the yellow histograms. The contributions from beauty and charm are indicated by the blue and green histograms.

Chapter 12

Summary and conclusions

The main topic of the analysis presented in this thesis was the measurement of total and single-differential cross sections for beauty and charm jet production at HERA at a centre-of-mass energy $\sqrt{s} = 318\,\text{GeV}$. The analysis was performed using data taken with the ZEUS detector during the 2006/07 positron-proton running corresponding to an integrated luminosity of $\mathcal{L} = 128\,\text{pb}^{-1}$. Kinematically it was restricted to the photoproduction regime which is characterised through four-momentum transfers $Q^2 < 1\,\text{GeV}^2$. High-P_T dijet events were selected representing the signature of boson-gluon-fusion processes that are dominant for heavy quark production at HERA.

The beauty and charm content of the sample was extracted by exploiting the long lifetimes and large masses of b and c hadrons. For this purpose secondary vertices representing candidates for the b and c decay vertices were reconstructed from tracks that could be associated to the two highest energetic jets. Subsequently the two-dimensional decay-length significance was calculated for each candidate vertex yielding a good separation power of both signal contributions from the light flavour background as well as between the beauty and the charm signals themselves. Making use of the fact that candidates from light flavours exhibit a to a great extent symmetric decay-length significance distribution around zero the contribution of the light flavour events in the sample was minimised by mirroring the negative side of the decay-length significance and subtracting it from the positive side. At large values the resulting mirrored and subtracted decay-length significance distribution, $S^+ - S^-$, revealed a clear separation between beauty and charm, while the light flavour contribution that had dominated the unmirrored distribution could be substantially suppressed. In order to further enhance the separation the $S^+ - S^-$ distribution was split into different bins of the invariant mass of the secondary vertex tracks, m_{vtx}, providing a highly

beauty-enriched region for $m_{vtx} \geq 2\,\text{GeV}$ and a low-mass region dominated by charm. With these two quantities it was possible to obtain an almost pure beauty sample and an enriched sample of charm events, which were used to cross-check the description of the data by the MC. Finally, the signal contributions were determined from $S^+ - S^-$, in m_{vtx} bins by fitting Monte Carlo templates for beauty, charm and light flavours to the data distribution. The fact that the region of large vertex masses and high mirrored significances almost exclusively contained beauty and thus determined the beauty fraction in the fit made the procedure remarkably stable and insusceptible to any inadequacy in the charm and light flavour description in the MC. Hence at the beginning of this analysis the main focus was on measuring beauty production cross sections, while the charm cross sections were determined simultaneously as a by-product.

The measured total beauty and charm cross sections as well as the single-differential cross sections as a function of P_T^{Jet} and η^{Jet} were found to be in good agreement with the LO+PS Monte Carlo simulation as well as with NLO QCD predictions. In contrast to previous measurements this analysis was not restricted to a dedicated decay channel, but kept fully inclusive and could thus benefit from a considerable gain in statistics. Hence the precision of the results could be considerably improved compared to previous analyses resulting in the most precise measurement of beauty production that could be achieved at HERA so far. The differential cross section as a function of the transverse momentum of the b quark, p_t^b, could be extended to higher values that had not been reached in previous analyses. Furthermore for the first time the inclusive beauty and charm jet production cross sections could be measured without the need for a knowledge of exclusive branching fractions. It is interesting to note that the beauty and charm scaling factors obtained from the fraction fits in this analysis are much smaller than the ones determined in previous (exclusive) measurements. Compared with e.g. the latest HERA II results using semileptonic b decays to electrons, in which the beauty and charm contributions were scaled with $k_b = 2.07$ and $k_c = 1.45$ [22], the scale factors obtained from the inclusive measurements are $\approx 15\,\%$ smaller for charm and even $\approx 50\,\%$ smaller for beauty.

The results of the beauty production measurement have been approved by the ZEUS collaboration and been shown at international conferences. A paper on this analysis using Grand-Reprocessed data and with the aim of extending the systematic checks for the charm results in order to also include them in the publication is in progress.

The secondary vertexing technique that was developed in the context of this analysis was used for the first time for the determination of inclusive heavy quark production cross sections at ZEUS. However, the new technique

heavily relied on a precise track and vertex reconstruction as well as an adequate simulation. For the first time the target precisions of the alignment and the reconstruction in various detector components was not only desired but needed in order to perform measurements based on lifetime information. Hence in close collaboration with the ZEUS tracking group several weaknesses of the reconstruction, alignment and simulation that had not been spotted earlier were revealed and great efforts were undertaken to cure them during this work. An improved simulation of resolutions as well as faulty channels in the MVD and the STT and the finalisation of the barrel MVD alignment were indispensable ingredients and finally made this analysis possible. Furthermore, the measurement using newly reprocessed data demonstrated the achievements of the Grand Reprocessing and the corresponding simulation, in particular through a considerable reduction of the main systematic errors. However, both the reconstruction and the simulation, particularly in the forward region, are not final yet and further improvements are necessary, but still the analysis could be extended to the high-η region and for the first time forward tracks could be used for a measurement.

Finally, the studies of dijet correlations that had already been addressed in the context of previous measurements were repeated in the context of this fully inclusive analysis. Two methods were developed and used to cross-check each other: in the first case the beauty content was determined by means of a template fit using the $S^+ - S^-$ distributions in different m_{vtx} bins as before. For the second method a highly beauty-dominated region with a constant b fraction was selected avoiding the necessity of a fraction fit and thus allowing for a straightforward determination of the cross sections. Both methods were found to be consistent within the statistical and systematic uncertainties. Differential cross sections as a function of several correlation variables were calculated and found to be in good agreement with NLO QCD predictions. The comparison with the LO+PS Monte Carlo simulation revealed higher-order effects that are present in the data, but were missing in the simulation as expected.

Future analyses at ZEUS will be able to benefit from the experience regarding the physical aspects as well as tracking and secondary vertexing techniques that could be gained in the course of this work. For example, a complementary analysis focusing on the DIS regime has already been started, in the course of which the structure functions $F_2^{b\bar{b}}$ and $F_2^{c\bar{c}}$, which describe the beauty and charm content in the proton, will be extracted. This information will be of particular interest and importance for the experiments at the LHC that has just started its operation; a deep understanding of beauty production for the study of signal and background processes will be crucial for all analyses.

Appendix A

MVD hit smearing

As pointed out in Chapter 7, the decay length as well as its error and the decay-length significance were not entirely described by the MC using the default reconstruction. In particular, the MC distributions were found to be too narrow with respect to the data indicating an imperfect simulation of the MVD resolution. In order to correct for this discrepancy on analysis level a smearing procedure was developed. As a first approach the mean position, $\langle x \rangle$, of all MVD clusters used on tracks was smeared as follows:

$$\langle x \rangle_{smeared} = \langle x \rangle + R \cdot \frac{y}{p}$$

with R being a random number generated from a Gaussian distribution with mean 0 and width 1 and y an empirical value, which was expressed in units of the pitch of the MVD, $p = 120\,\mu$m. The direction perpendicular to the MVD strips within the local coordinate system of the MVD sensor is denoted with x. The best value for y was found to be $40\,\mu$m; it was furthermore shown to be independent of the azimuthal angle, ϕ, and the transverse momentum, p_t, of the tracks. Details concerning the smearing procedure and further studies can be found in [66].

Although a considerable improvement in the agreement between data and MC could be observed, the description by the MC was still not entirely satisfactory; therefore the smearing procedure was revised and further developed. For the evaluation of a new MVD hit smearing method a subsample of the data taken during the 2006 e^+p running corresponding to an integrated luminosity of $\mathcal{L} \approx 5\,\text{pb}^{-1}$ was used. Since the aim was not only to perform purely tracking-related studies, but also to visualise the impact on a physics analysis at the same time, the event selection was kept equivalent to the one presented in Section 6.3. The main purpose of the refinement of the smearing procedure was to take into account the dependence of the MVD resolution on

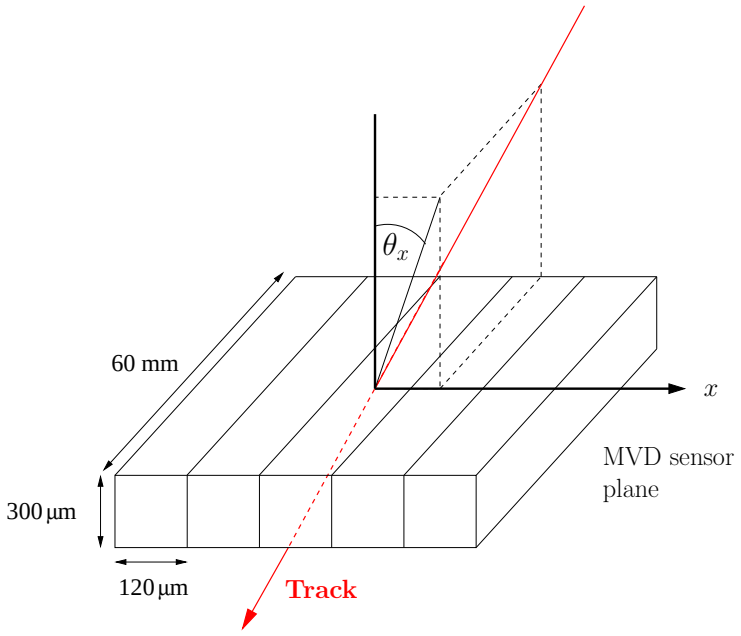

Figure A.1: Definition of the impact angle, θ_x, of a track onto an MVD sensor.

the impact angle, θ_x, of the tracks on the MVD sensors. More precisely, θ_x is defined as the angle between the perpendicular on the MVD sensor plane and the projection of the track onto the plane perpendicular to the sensor strips; this definition is also illustrated in Fig. A.1. The MVD hit residual distribution as a function of θ_x was provided by the ZEUS tracking group [80] and is displayed in Fig. A.2 for data (left) and MC (right). Parametrisations σ_{Data} and σ_{MC} for both residuals were evaluated by fitting the distributions, yielding

$$\begin{aligned} \sigma_{Data} &= \frac{24.2}{\cos(\theta_x)} + 13.3 \cdot \theta_x^2 \\ \sigma_{MC} &= \frac{14.9}{\cos(\theta_x)} + 16.5 \cdot \theta_x^2 \end{aligned} \tag{A.1}$$

with θ_x in radians. A smearing function was then extracted from Equations A.1 as

$$s\,(\theta_x) = \sqrt{\sigma^2_{Data}(\theta_x) - \sigma^2_{MC}(\theta_x)}.$$

For $|\theta_x| > 70\,^\circ$ the smearing value, s, was assumed to be constant. Subse-

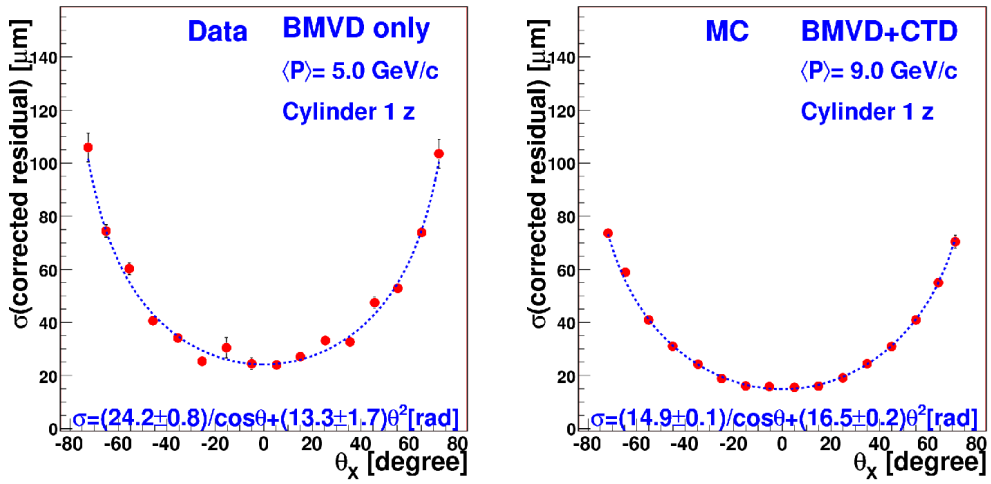

Figure A.2: MVD hit resolution as a function of the impact angle, θ_x, of the tracks onto the MVD sensors for data (left) and MC (right), taken from [80].

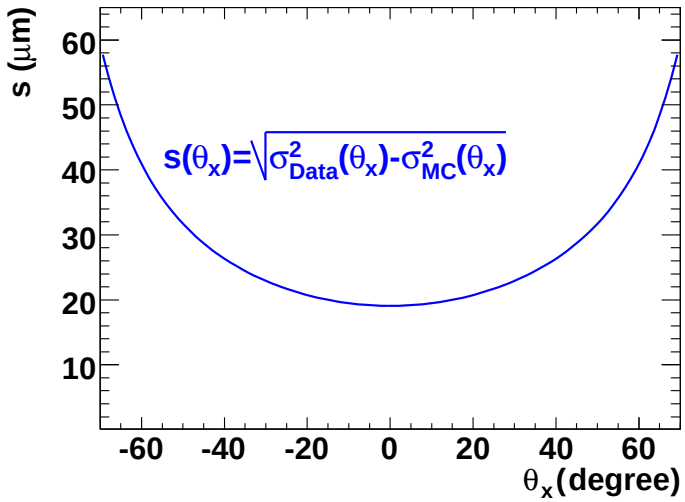

Figure A.3: Smearing function, $s(\theta_x)$, as determined from the MVD hit residual distributions in Fig. A.2.

quently, the smearing was applied as before

$$\langle x \rangle_{smeared} = \langle x \rangle + R \cdot \frac{s(\theta_x)}{p}$$

replacing the empirical value y with the θ_x-dependent smearing function, $s(\theta_x)$, which is also visualised in Fig. A.3. Most of the tracks hit the MVD sensors almost perpendicularly; for those tracks the needed smearing was found to be of the order of 20–25 μm, i.e. roughly half of the empirical value that was determined before. For tracks with large impact angles a larger smearing had to be applied.

In Fig. A.4 the two-dimensional decay length, d, projected onto the axis of the associated jet (cf Section 5.2.3), its error, δd, as well as the decay-length significance, $d/\delta d$, are shown before (left) and after the θ_x-dependent MVD hit smearing (right). A considerable improvement due to the smearing could be observed, such that the MC simulation agreed well with the data. However, in Fig. A.4 (right) a slight shift of the data with respect to the MC is still visible in the decay length and significance distributions. This is due to the fact that the alignment and beam-spot corrections described in Section 5.5 had not yet been implemented when the resolution studies presented here were performed.

In the end it was decided not to correct for the MVD resolution effects on analysis level, but to implement a similar procedure at an earlier stage [57]. The tuning of these resolution corrections is still ongoing and final conclusions have not been drawn yet.

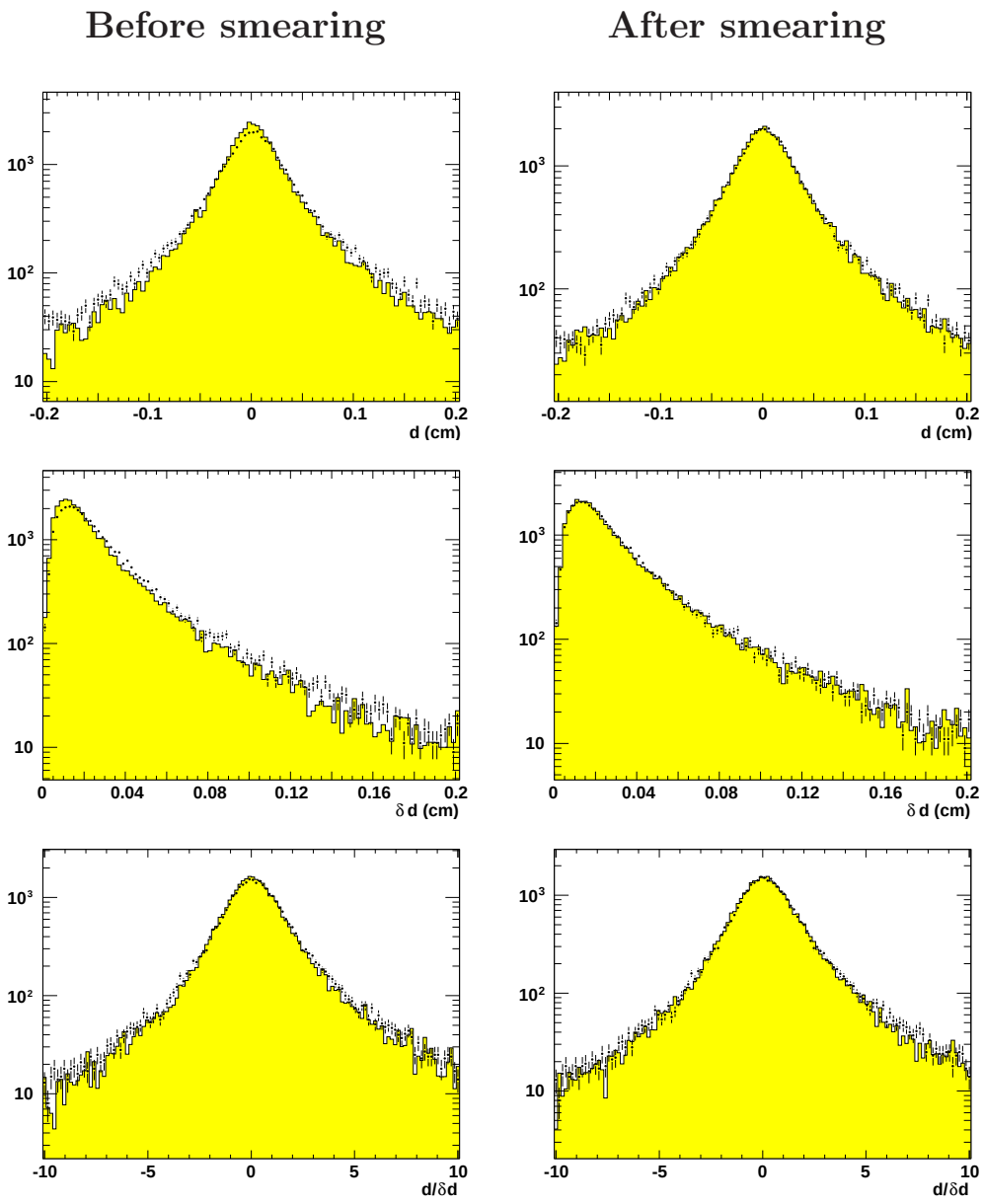

Figure A.4: Two-dimensional decay length, d, decay-length error, δd, and decay-length significance, $d/\delta d$, before (left) and after MVD hit smearing (right). The data are denoted by the black points, while the MC is represented by the yellow histograms.

Appendix B

Fit distributions

In this appendix the results of the mirrored decay-length significance fits corresponding to the cross sections as a function of P_T^{Jet} and η^{Jet} presented in Chapter 8 are shown. The corresponding distributions for the results discussed in Chapter 10 were not included, as they do not differ much from the shown ones and do not provide any further information.

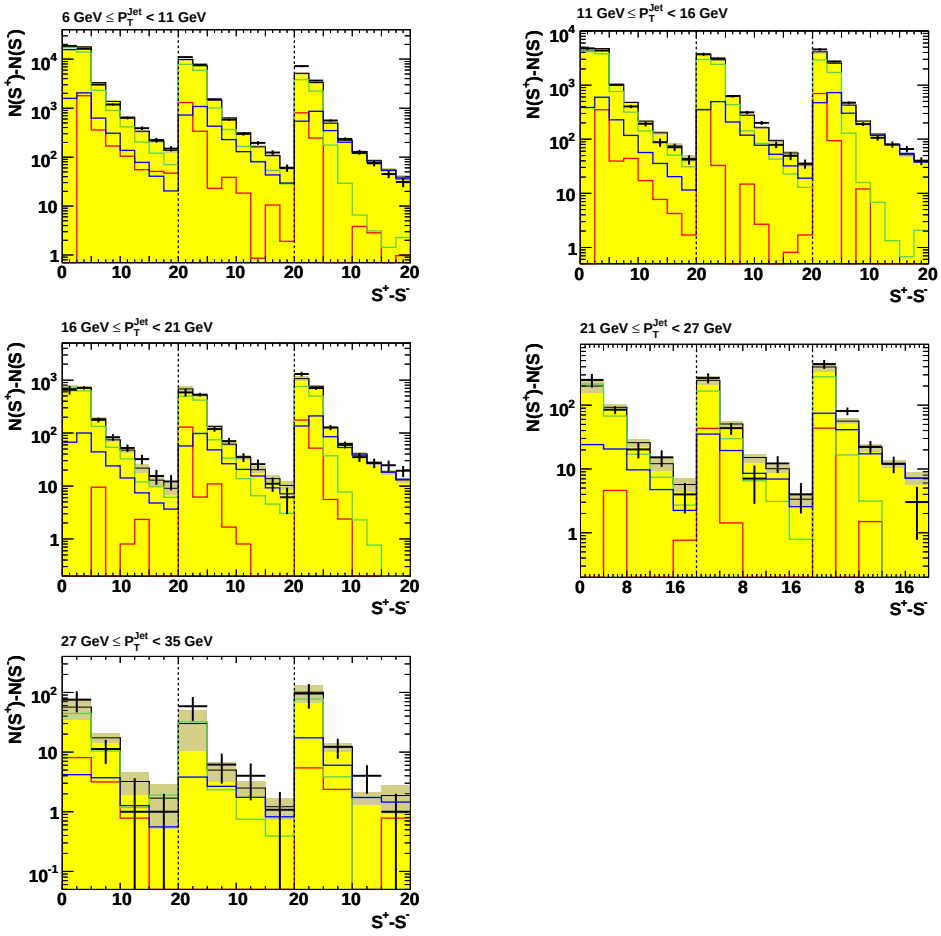

Figure B.1: Mirrored decay-length significance fits in three m_{vtx} bins for all P_T^{Jet} bins. The contributions from beauty, charm and light flavours are scaled with the factors obtained from the fit and denoted by the blue, green and red solid lines. The data are represented by the black points, the scaled MC sum is shown as a yellow histogram with shaded error bands.

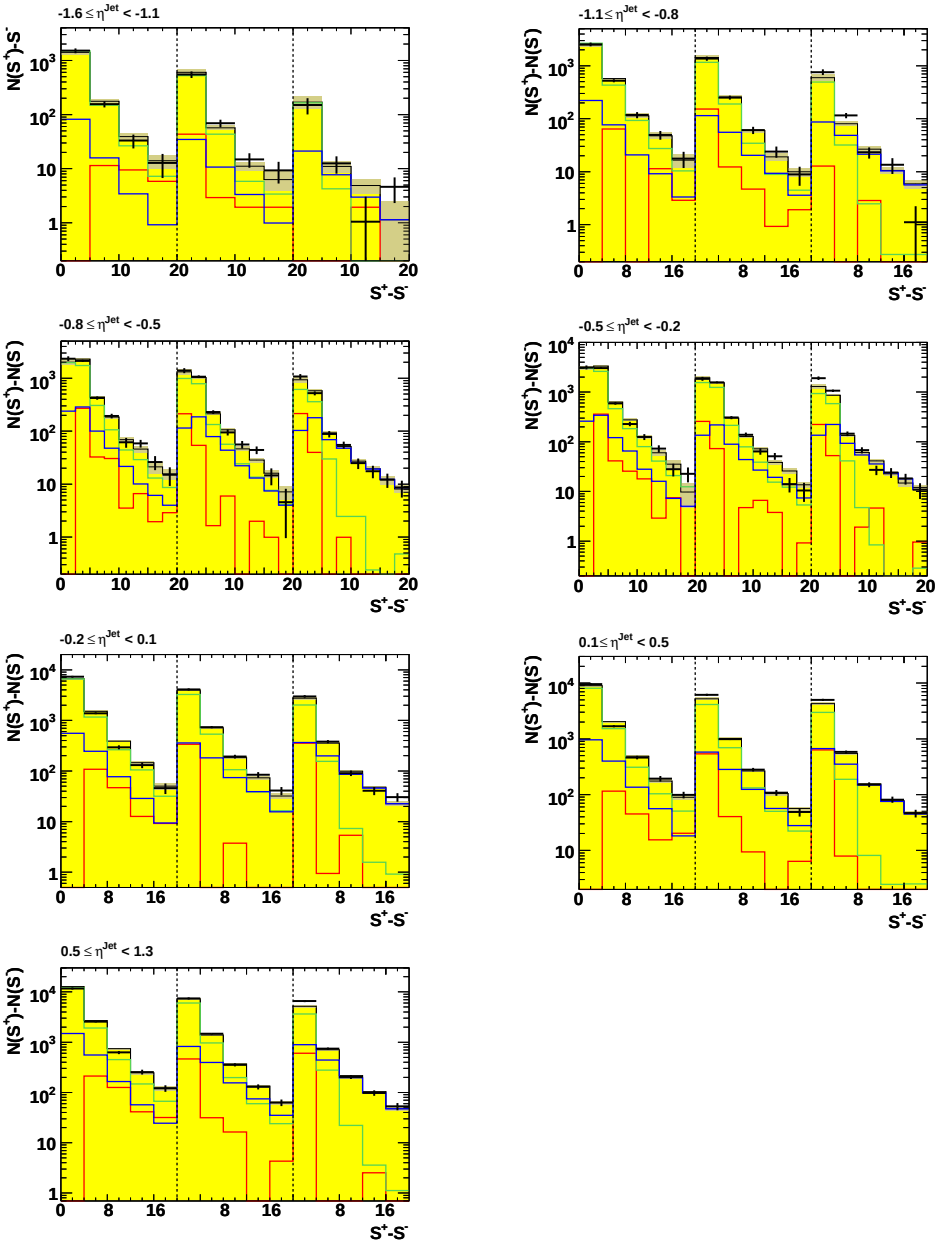

Figure B.2: Mirrored decay-length significance fits in three m_{vtx} bins for all η^{Jet} bins. For further details see caption of Fig. B.1.

Appendix C

Cross sections

In this appendix all measured differential beauty and charm jet production cross sections including statistical and systematic uncertainties and the corresponding NLO QCD predictions including hadronisation corrections are listed. The measurements were performed on events with

$$\begin{aligned} Q^2 &< 1\,\mathrm{GeV}^2, \\ 0.2 &< y < 0.8, \\ P_T^{Jet\,1(2)} &> 7(6)\,\mathrm{GeV}, \\ -2.5 \leq \eta^{Jet\,1(2)} &< 2.5. \end{aligned}$$

Tables C.1 and C.2 contain the cross sections as a function of P_T^{Jet} and η^{Jet} corresponding to the results presented in Chapter 8. Here jets with $-1.6 \leq \eta^{Jet\,1(2)} < 1.3$ were used. In Tables C.3 and C.4 the corresponding cross sections for the extended η^{Jet}-range ($-1.6 \leq \eta^{Jet\,1(2)} < 2.5$, cf Chapter 10) are listed.

The differential beauty and charm cross sections for the dijet correlation measurements can be found in Appendix D.

C.1 Restricted η^{Jet} range

C.1.1 Beauty cross sections

P_T^{Jet} (GeV)	$d\sigma^b/dP_T^{Jet}$ (pb/GeV)	$d\sigma^b_{NLO}/dP_T^{Jet} \otimes C^b_{had}$ (pb/GeV)	C^b_{had}
6 : 11	$86.8 \pm 4.7\ ^{+12}_{-\ 9.0}$	$96\ ^{+26}_{-15}$	0.80
11 : 16	$23.5 \pm 1.1\ ^{+\ 1.9}_{-\ 1.5}$	$25.6\ ^{+\ 6.8}_{-\ 3.9}$	0.85
16 : 21	$5.19 \pm 0.44^{+\ 0.70}_{-\ 0.94}$	$6.3\ ^{+\ 1.6}_{-\ 1.1}$	0.87
21 : 27	$1.28 \pm 0.23^{+\ 0.24}_{-\ 0.32}$	$1.63^{+\ 0.50}_{-\ 0.24}$	0.88
27 : 35	$0.28 \pm 0.20^{+\ 0.06}_{-\ 0.15}$	$0.37^{+\ 0.10}_{-\ 0.07}$	0.87

η^{Jet}	$d\sigma^b/d\eta^{Jet}$ (pb)	$d\sigma^b_{NLO}/d\eta^{Jet} \otimes C^b_{had}$ (pb)	C^b_{had}
−1.6 : −1.1	$31 \pm 15^{+\ 7}_{-13}$	65^{+20}_{-11}	0.66
−1.1 : −0.8	$123 \pm 24^{+15}_{-18}$	165^{+44}_{-25}	0.75
−0.8 : −0.5	$225 \pm 22^{+18}_{-14}$	233^{+62}_{-36}	0.76
−0.5 : −0.2	$238 \pm 20^{+17}_{-21}$	282^{+76}_{-44}	0.78
−0.2 : 0.1	$264 \pm 22^{+26}_{-27}$	312^{+79}_{-51}	0.79
0.1 : 0.5	$323 \pm 20^{+26}_{-23}$	315^{+80}_{-49}	0.84
0.5 : 1.3	$272 \pm 17^{+18}_{-70}$	237^{+65}_{-39}	0.88

Table C.1: Summary table of differential beauty jet production cross sections for events with $Q^2 < 1\,\mathrm{GeV}^2$, $0.2 < y < 0.8$, $P_T^{Jet\,1(2)} > 7(6)\,\mathrm{GeV}$ and $-2.5 \leq \eta^{Jet\,1(2)} < 2.5$ using jets with $-1.6 \leq \eta^{Jet\,1(2)} < 1.3$. Listed are the measurements and the NLO predictions using CTEQ5M as proton PDF including uncertainties as well as the hadronisation correction factors, C_{had}.

C.1.2 Charm cross sections

P_T^{Jet} (GeV)	$d\sigma^c/dP_T^{Jet}$ (pb/GeV)	$d\sigma^c_{NLO}/dP_T^{Jet} \otimes C^c_{had}$ (pb/GeV)	C^c_{had}
6 : 11	$840 \pm 12\ ^{+100}_{-\ 83}$	$848\ ^{+530}_{-170}$	0.79
11 : 16	$173.6 \pm 4.9\ ^{+\ 28}_{-\ 24}$	$181\ ^{+\ 30}_{-\ 39}$	0.89
16 : 21	$34.8 \pm 2.1\ ^{+\ 6.6}_{-\ 5.4}$	$37.2^{+\ 6.1}_{-\ 10}$	0.90
21 : 27	$7.7 \pm 1.2\ ^{+\ 1.3}_{-\ 1.3}$	$8.5^{+\ 7.1}_{-\ 1.8}$	0.89
27 : 35	$1.30 \pm 0.82^{+\ 0.80}_{-\ 0.14}$	$1.6^{+\ 1.1}_{-\ 0.4}$	0.91

η^{Jet}	$d\sigma^c/d\eta^{Jet}$ (pb)	$d\sigma^c_{NLO}/d\eta^{Jet} \otimes C^c_{had}$ (pb)	C^c_{had}
−1.6 : −1.1	$519 \pm 51^{+\ 94}_{-\ 94}$	$729^{+\ 810}_{-\ 140}$	0.68
−1.1 : −0.8	$1367 \pm 92^{+160}_{-130}$	$1711^{+1600}_{-\ 350}$	0.76
−0.8 : −0.5	$1679 \pm 90^{+210}_{-150}$	$2362^{+\ 250}_{-\ 500}$	0.77
−0.5 : −0.2	$2287 \pm 91^{+250}_{-220}$	$2709^{+1100}_{-\ 540}$	0.77
−0.2 : 0.1	$2777 \pm 110^{+360}_{-330}$	$2753^{+\ 450}_{-\ 510}$	0.80
0.1 : 0.5	$2446 \pm 95^{+290}_{-200}$	$2364^{+1100}_{-\ 510}$	0.85
0.5 : 1.3	$1974 \pm 83^{+230}_{-270}$	$1462^{+1300}_{-\ 330}$	0.86

Table C.2: Summary table of total and differential charm jet production cross sections for events with $Q^2 < 1\,\mathrm{GeV}^2$, $0.2 < y < 0.8$, $P_T^{Jet\,1(2)} > 7(6)\,\mathrm{GeV}$ and $-2.5 \leq \eta^{Jet\,1(2)} < 2.5$ using jets with $-1.6 \leq \eta^{Jet\,1(2)} < 1.3$. Listed are the measurements and the NLO predictions using CTEQ5M as proton PDF including uncertainties as well as the hadronisation correction factors, C_{had}.

C.2 Full η^{Jet} range

C.2.1 Beauty cross sections

P_T^{Jet} (GeV)	$d\sigma^b/dP_T^{Jet}$ (pb/GeV)	$d\sigma^b_{NLO}/dP_T^{Jet} \otimes C^b_{had}$ (pb/GeV)	C^b_{had}
6 : 11	$101.4 \pm 5.3\ ^{+12}_{-11}$	$110\ ^{+30}_{-18}$ (130)	0.79
11 : 16	$28.2 \pm 1.4\ ^{+\ 2.7}_{-\ 2.0}$	$31.9\ ^{+\ 8.7}_{-\ 5.0}$ (37.1)	0.88
16 : 21	$7.44 \pm 0.61^{+\ 1.2}_{-\ 1.1}$	$8.4\ ^{+\ 2.2}_{-\ 1.6}$ (9.4)	0.91
21 : 27	$1.63 \pm 0.28^{+\ 0.40}_{-\ 0.38}$	$2.36^{+\ 0.74}_{-\ 0.39}$ (2.56)	0.91
27 : 35	$0.30 \pm 0.12^{+\ 0.12}_{-\ 0.07}$	$0.59^{+\ 0.18}_{-\ 0.12}$ (0.59)	0.92

η^{Jet}	$d\sigma^b/d\eta^{Jet}$ (pb)	$d\sigma^b_{NLO}/d\eta^{Jet} \otimes C^b_{had}$ (pb)	C^b_{had}
−1.6 : −1.1	$42 \pm 15^{+\ 5}_{-\ 3}$	65^{+20}_{-11} (76)	0.66
−1.1 : −0.8	$139 \pm 20^{+14}_{-13}$	164^{+44}_{-25} (194)	0.74
−0.8 : −0.5	$191 \pm 20^{+15}_{-17}$	234^{+62}_{-36} (274)	0.76
−0.5 : −0.2	$208 \pm 19^{+20}_{-11}$	282^{+76}_{-44} (332)	0.77
−0.2 : 0.1	$255 \pm 20^{+24}_{-16}$	313^{+79}_{-51} (369)	0.79
0.1 : 0.5	$277 \pm 18^{+23}_{-20}$	315^{+80}_{-49} (368)	0.84
0.5 : 1.3	$277 \pm 14^{+21}_{-15}$	237^{+65}_{-39} (279)	0.88
1.3 : 2.5	$166 \pm 44^{+38}_{-19}$	100^{+31}_{-20} (114)	0.84

Table C.3: Summary table of total and differential beauty jet production cross sections for events with $Q^2 < 1\,\mathrm{GeV}^2$, $0.2 < y < 0.8$, $P_T^{Jet\,1(2)} > 7(6)\,\mathrm{GeV}$ and $-2.5 \leq \eta^{Jet\,1(2)} < 2.5$ using jets with $-1.6 \leq \eta^{Jet\,1(2)} < 2.5$. Listed are the measurements and the NLO predictions using CTEQ5M as proton PDF including uncertainties as well as the hadronisation correction factors, C_{had}. The NLO predictions in brackets correspond to those using ZEUS-S instead of CTEQ5M.

C.2.2 Charm cross sections

P_T^{Jet} (GeV)	$d\sigma^c/dP_T^{Jet}$ (pb/GeV)	$d\sigma^c_{NLO}/dP_T^{Jet} \otimes C^c_{had}$ (pb/GeV)	C^c_{had}
6 : 11	$889 \pm 21\ ^{+100}_{-\ 83}$	$915\ ^{+550}_{-190}$ (1079)	0.77
11 : 16	$202.0 \pm 5.8^{+\ 36}_{-\ 31}$	$209\ ^{+\ 29}_{-\ 45}$ (246)	0.90
16 : 21	$43.2 \pm 2.7^{+\ 9.4}_{-\ 8.1}$	$45\ ^{+\ 45}_{-\ 12}$ (54)	0.91
21 : 27	$11.0 \pm 1.7^{+\ 1.9}_{-\ 1.2}$	$11.4^{+\ 9.0}_{-\ 2.7}$ (13.2)	0.91
27 : 35	$2.4 \pm 1.0^{+\ 0.5}_{-\ 0.7}$	$2.4^{+\ 1.5}_{-\ 0.5}$ (2.7)	0.92

η^{Jet}	$d\sigma^c/d\eta^{Jet}$ (pb)	$d\sigma^c_{NLO}/d\eta^{Jet} \otimes C^c_{had}$ (pb)	C^c_{had}
−1.6 : −1.1	$444 \pm 52^{+\ 62}_{-\ 51}$	$728^{+\ 810}_{-\ 140}$ (864)	0.68
−1.1 : −0.8	$1263 \pm 87^{+170}_{-150}$	$1708^{+1600}_{-\ 350}$ (2076)	0.76
−0.8 : −0.5	$1562 \pm 90^{+190}_{-160}$	$2364^{+\ 250}_{-\ 500}$ (2745)	0.77
−0.5 : −0.2	$2254 \pm 79^{+270}_{-220}$	$2711^{+1100}_{-\ 540}$ (3235)	0.78
−0.2 : 0.1	$2660 \pm 98^{+330}_{-300}$	$2752^{+\ 450}_{-\ 510}$ (3324)	0.80
0.1 : 0.5	$2391 \pm 85^{+290}_{-240}$	$2363^{+1100}_{-\ 510}$ (2754)	0.85
0.5 : 1.3	$1586 \pm 73^{+220}_{-190}$	$1462^{+1300}_{-\ 330}$ (1728)	0.86
1.3 : 2.5	$576 \pm 170^{+160}_{-210}$	$446^{+\ 170}_{-\ 100}$ (530)	0.72

Table C.4: Summary table of differential charm cross sections for events with $Q^2 < 1\,\mathrm{GeV}^2$, $0.2 < y < 0.8$, $P_T^{Jet\,1(2)} > 7(6)\,\mathrm{GeV}$ and $-2.5 \leq \eta^{Jet\,1(2)} < 2.5$ using jets with $-1.6 \leq \eta^{Jet\,1(2)} < 2.5$. Listed are the measurements and the NLO predictions using CTEQ5M as proton PDF including uncertainties as well as the hadronisation correction factors, C_{had}. The NLO predictions in brackets correspond to those using ZEUS-S instead of CTEQ5M.

Appendix D

Dijet correlations

This appendix is organised as follows: in Section D.1 the results of the mirrored decay-length significance fits are shown for the differential cross sections as a function of $|\Delta\phi|$, $|\Delta\eta|$, ΔR, $|\cos\theta^*|$ and M^{jj}. In Section D.2 the acceptances after beauty enrichment are shown for all differential beauty cross sections. Section D.3 contains all measured differential beauty and charm cross sections as a function of $|\Delta\phi|$, $|\Delta\eta|$, ΔR, $|\cos\theta^*|$ and M^{jj} including statistical and systematic uncertainties as obtained from the mirrored decay-length significance fits and after beauty enrichment. In Tables D.1 and D.2 the differential cross sections for beauty dijet correlations determined from the two methods are compared directly. The results obtained from the mirrored decay-length significance fits are also compared with the corresponding NLO QCD predictions including hadronisation corrections in Tables D.3 and D.4. In Tables D.5 and D.6 the cross sections for charm dijet correlations are listed and also compared to the NLO QCD predictions. In analogy to the results listed in Appendix C all measurements were performed on events with

$$\begin{aligned} Q^2 &< 1\,\mathrm{GeV}^2, \\ 0.2 &< y < 0.8, \\ P_T^{Jet\,1(2)} &> 7(6)\,\mathrm{GeV}, \\ -2.5 \leq \eta^{Jet\,1(2)} &< 2.5. \end{aligned}$$

using jets with $-1.6 \leq \eta^{Jet\,1(2)} < 2.5$.

D.1 Fit results

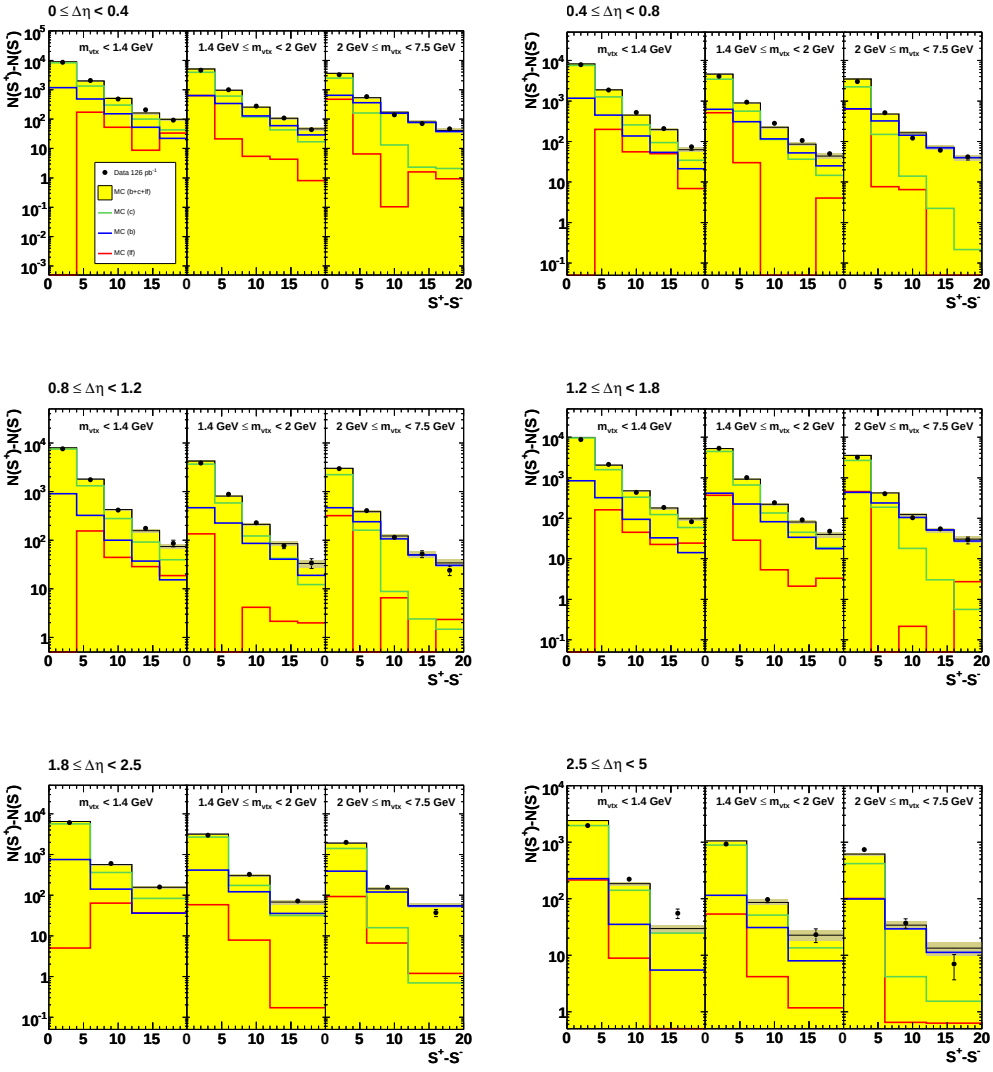

Figure D.1: Mirrored decay-length significance fits in three m_{vtx} bins for all $|\Delta\eta|$ bins. The contributions from beauty, charm and light flavours are scaled with the factors obtained from the fit and denoted by the blue, green and red solid lines. The data are represented by the black points, the scaled MC sum is shown as a yellow histogram with shaded error bands.

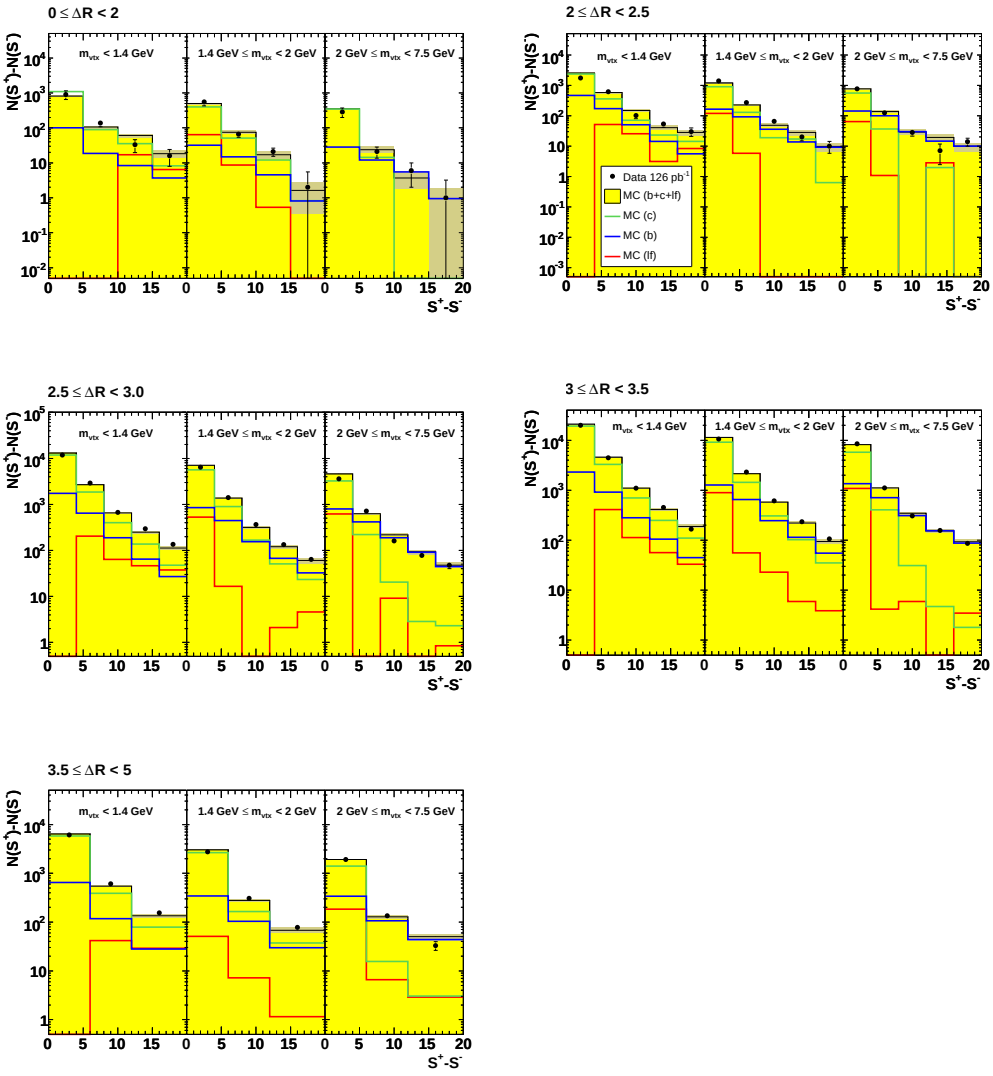

Figure D.2: Mirrored decay-length significance fits in three m_{vtx} bins for all ΔR bins. For further details see caption of Fig. D.1.

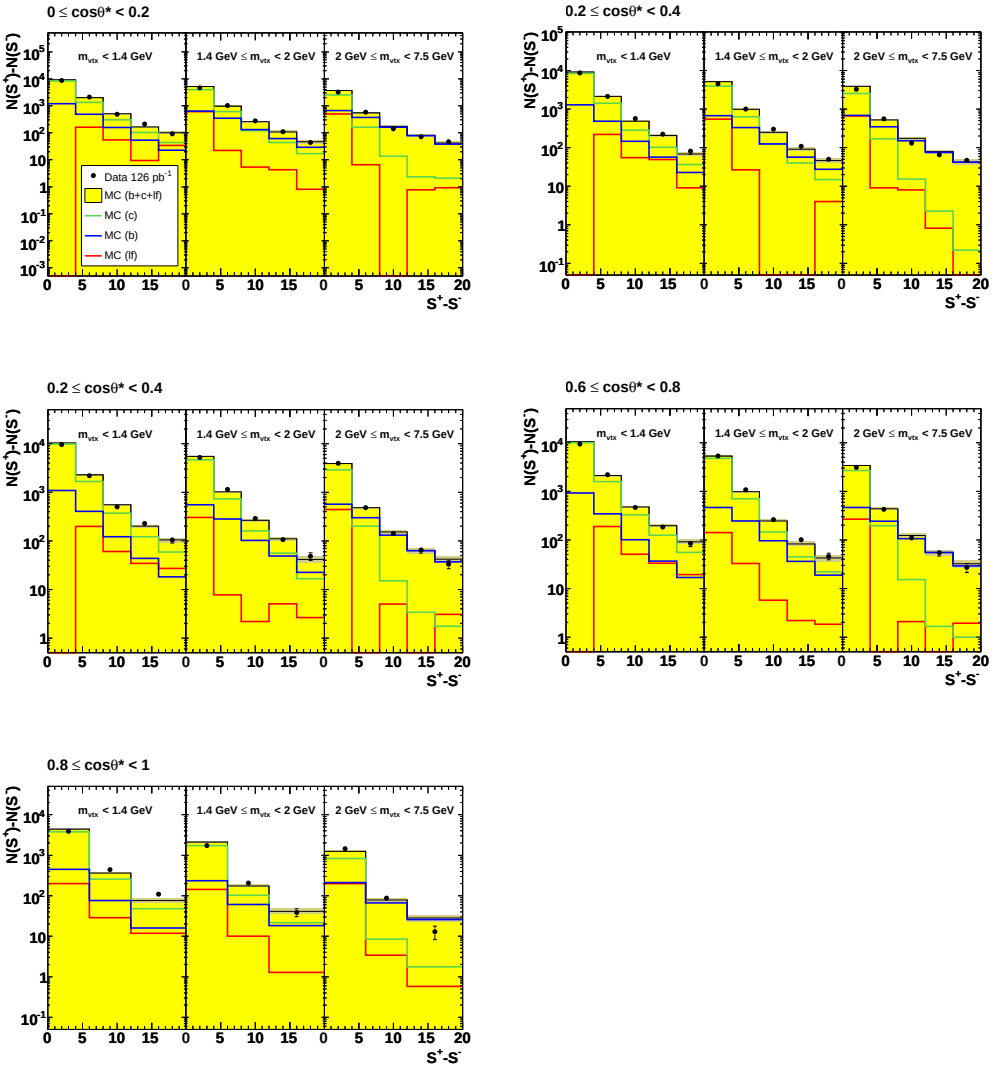

Figure D.3: Mirrored decay-length significance fits in three m_{vtx} bins for all $|\cos\theta^*|$ bins. For further details see caption of Fig. D.1.

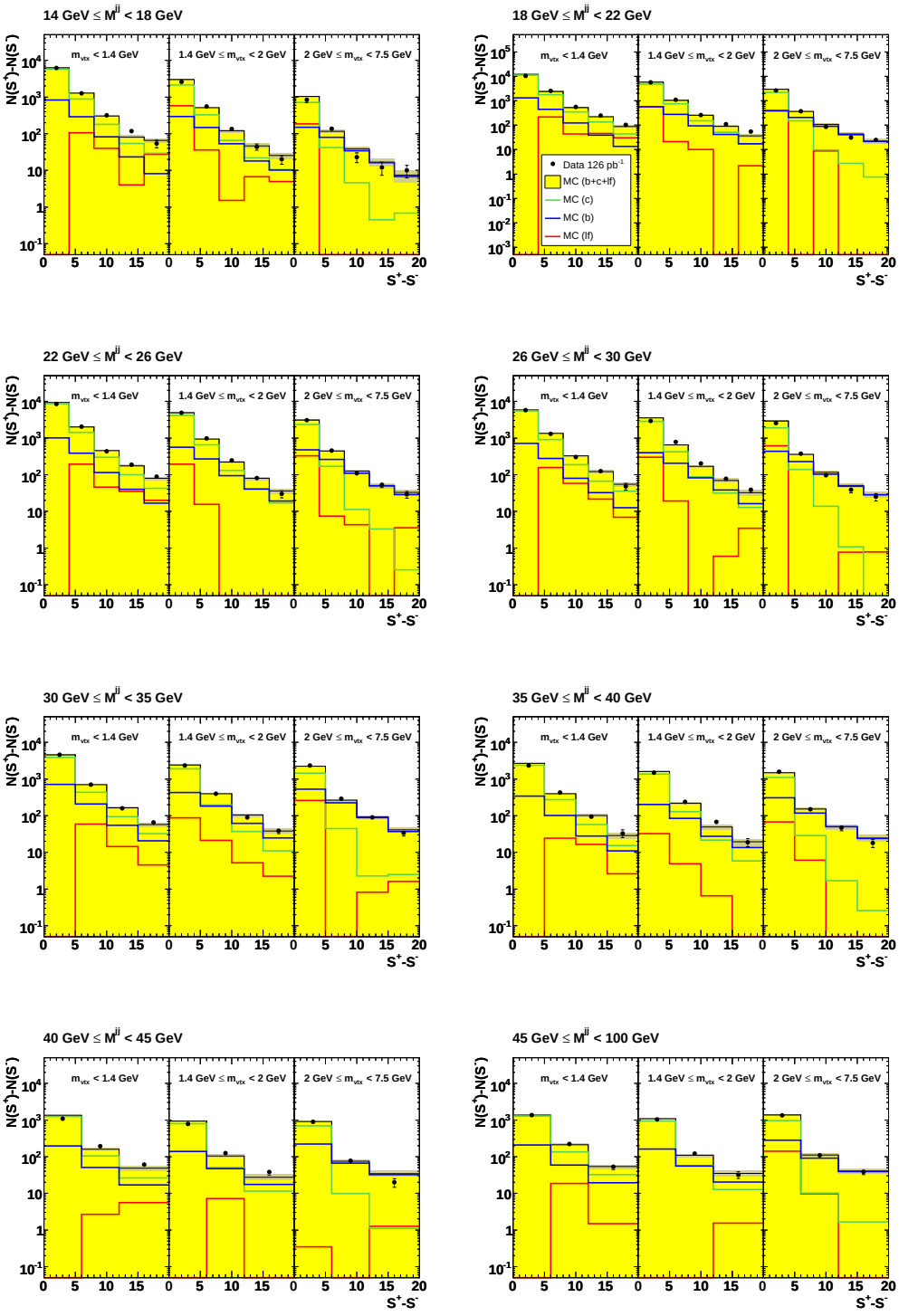

Figure D.4: Mirrored decay-length significance fits in three m_{vtx} bins for all M^{jj} bins. For further details see caption of Fig. D.1.

D.2 Acceptance

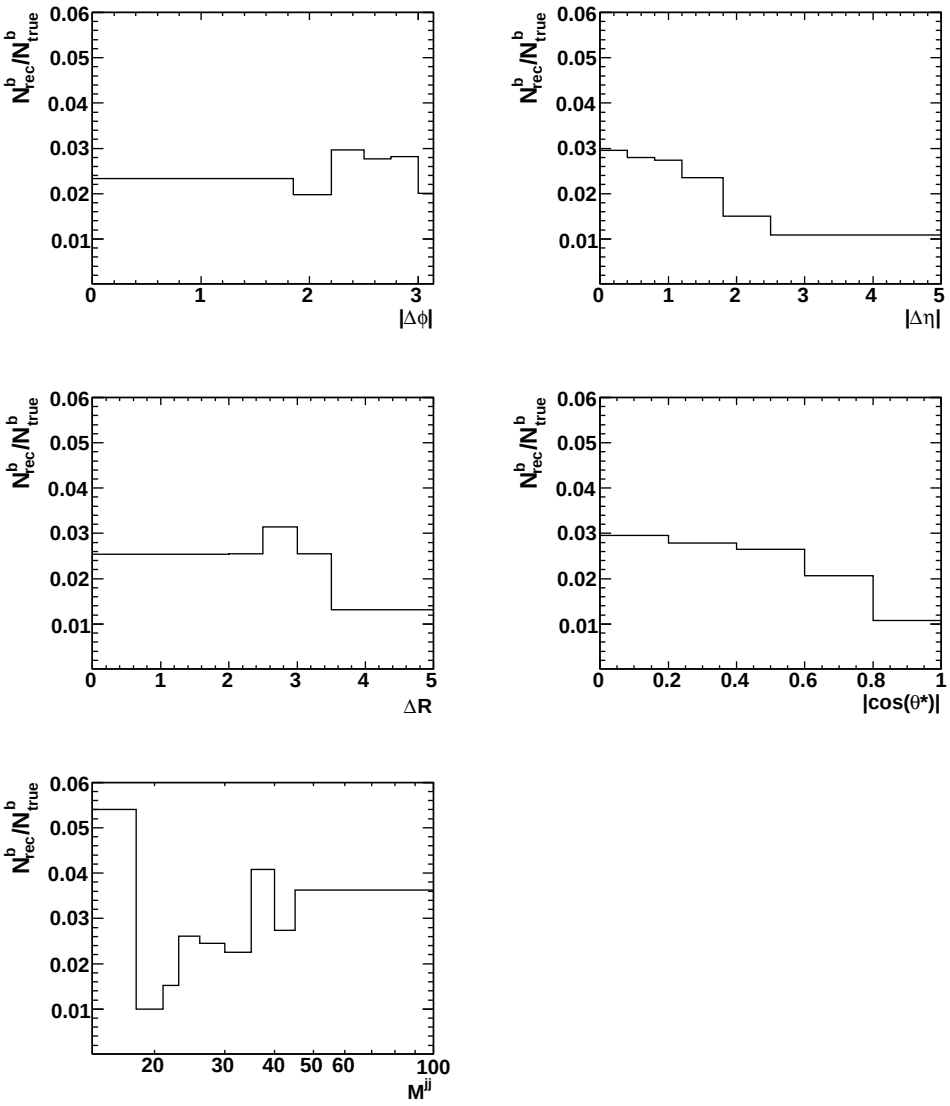

Figure D.5: Acceptance as a function of the dijet correlation variables $|\Delta\phi|$, $|\Delta\eta|$, ΔR, $|\cos\theta^*|$ and M^{jj} after beauty enrichment.

D.3 Cross sections

D.3.1 Beauty cross sections

$\lvert\Delta\phi\rvert$	$d\sigma^b_{fit}/d\lvert\Delta\phi\rvert$ (pb)	$d\sigma^b_{enr}/\lvert d\Delta\phi\rvert$ (pb)
0 : 1.85	$4.3 \pm 2.8^{+\ 1.0}_{-\ 2.3}$	$4.8 \pm 2.2^{+\ 2.2}_{-\ 2.3}$
1.85 : 2.2	$66 \pm 14\ ^{+\ 5.5}_{-\ 12}$	$72.9 \pm 8.5^{+\ 13}_{-\ 11}$
2.2 : 2.5	$127 \pm 22\ ^{+\ 11}_{-\ 8.5}$	$129 \pm 11\ ^{+\ 16}_{-\ 15}$
2.5 : 2.75	$361 \pm 34\ ^{+\ 43}_{-\ 25}$	$395 \pm 20\ ^{+\ 38}_{-\ 31}$
2.75 : 3.0	$1070 \pm 51\ ^{+340}_{-\ 47}$	$1035 \pm 32\ ^{+\ 80}_{-\ 58}$
3.0 : π	$2211 \pm 110\ ^{+190}_{-\ 93}$	$2056 \pm 45\ ^{+140}_{-\ 90}$

$\lvert\Delta\eta\rvert$	$d\sigma^b_{fit}/d\lvert\Delta\eta\rvert$ (pb)	$d\sigma^b_{enr}/d\lvert\Delta\eta\rvert$ (pb)
0 : 0.4	$419 \pm 25\ ^{+35}_{-20}$	$375 \pm 19\ ^{+32}_{-25}$
0.4 : 0.8	$403 \pm 25\ ^{+32}_{-18}$	$368 \pm 19\ ^{+32}_{-25}$
0.8 : 1.2	$299 \pm 23\ ^{+29}_{-13}$	$307 \pm 18\ ^{+28}_{-22}$
1.2 : 1.8	$218 \pm 17\ ^{+21}_{-11}$	$246 \pm 16\ ^{+23}_{-19}$
1.8 : 2.5	$167 \pm 16\ ^{+13}_{-\ 8.1}$	$175 \pm 13\ ^{+19}_{-16}$
2.5 : 5.0	$19 \pm 4.1^{+\ 1.6}_{-\ 1.6}$	$18 \pm 4.2^{+\ 4.4}_{-\ 4.3}$

Table D.1: Summary table of differential beauty dijet correlation cross sections as a function of $|\Delta\phi|$ and $|\Delta\eta|$ for events with $Q^2 < 1\,\mathrm{GeV}^2$, $0.2 < y < 0.8$, $P_T^{Jet\,1(2)} > 7(6)\,\mathrm{GeV}$ and $-2.5 \leq \eta^{Jet\,1(2)} < 2.5$ using jets with $-1.6 \leq \eta^{Jet\,1(2)} < 2.5$. Listed are the results as obtained from the mirrored decay-length significance fits and after beauty-enrichment.

ΔR	$d\sigma^b_{fit}/d\Delta R$ (pb)	$d\sigma^b_{enr}/d\Delta R$ (pb)
0 : 2.0	$3.2 \pm 2.0^{+\ 0.6}_{-\ 1.2}$	$4.4 \pm 2.1^{+\ 2.1}_{-\ 2.2}$
2.0 : 2.5	$79 \pm 13\ ^{+\ 7.1}_{-\ 5.8}$	$64.4 \pm 8.0^{+10}_{-\ 9.4}$
2.5 : 3.0	$357 \pm 21\ ^{+32}_{-18}$	$334 \pm 18\ ^{+31}_{-25}$
3.0 : 3.5	$767 \pm 31\ ^{+69}_{-41}$	$769 \pm 28\ ^{+59}_{-42}$
3.5 : 5.0	$82.8 \pm 8.5^{+\ 6.3}_{-\ 4.1}$	$83.4 \pm 9.1^{+11}_{-10}$

$\lvert\cos\theta^*\rvert$	$d\sigma^b_{fit}/d\lvert\cos\theta^*\rvert$ (pb)	$d\sigma^b_{enr}/d\lvert\cos\theta^*\rvert$ (pb)
0 : 0.2	$853 \pm 50^{+70}_{-41}$	$763 \pm 28^{+59}_{-43}$
0.2 : 0.4	$865 \pm 53^{+69}_{-38}$	$799 \pm 28^{+62}_{-45}$
0.4 : 0.6	$753 \pm 52^{+72}_{-34}$	$808 \pm 28^{+65}_{-45}$
0.6 : 0.8	$780 \pm 59^{+74}_{-40}$	$853 \pm 29^{+68}_{-50}$
0.8 : 1.0	$436 \pm 62^{+35}_{-21}$	$432 \pm 21^{+38}_{-30}$

M^{jj} (GeV)	$d\sigma^b_{fit}/dM^{jj}$ (pb/GeV)	$d\sigma^b_{enr}/dM^{jj}$ (pb/GeV)
14 : 18	$4.44 \pm 0.64^{+0.70}_{-1.17}$	$3.1 \pm 1.8\ ^{+1.8}_{-1.8}$
18 : 22	$41.1 \pm 3.5\ ^{+5.6}_{-6.5}$	$42.0 \pm 6.5\ ^{+8.1}_{-7.3}$
22 : 26	$43.6 \pm 3.2\ ^{+4.3}_{-3.5}$	$45.9 \pm 6.8\ ^{+7.7}_{-7.3}$
26 : 30	$31.7 \pm 2.4\ ^{+2.9}_{-1.9}$	$31.1 \pm 5.6\ ^{+6.2}_{-5.8}$
30 : 35	$24.3 \pm 1.6\ ^{+1.8}_{-1.1}$	$23.1 \pm 4.8\ ^{+5.1}_{-5.0}$
35 : 40	$11.6 \pm 1.1\ ^{+2.7}_{-1.3}$	$12.2 \pm 3.5\ ^{+3.8}_{-3.6}$
40 : 45	$7.59 \pm 0.96^{+1.20}_{-0.42}$	$6.7 \pm 2.6\ ^{+2.7}_{-2.7}$
45 : 100	$0.83 \pm 0.09^{+0.21}_{-0.11}$	$0.85 \pm 0.92^{+0.94}_{-0.93}$

Table D.2: Summary table of differential beauty dijet correlation cross sections as a function of ΔR, $|\cos\theta^*|$ and M^{jj} for events with $Q^2 < 1\,\mathrm{GeV}^2$, $0.2 < y < 0.8$, $P_T^{Jet\,1(2)} > 7(6)\,\mathrm{GeV}$ and $-2.5 \leq \eta^{Jet\,1(2)} < 2.5$ using jets with $-1.6 \leq \eta^{Jet\,1(2)} < 2.5$. Listed are the results as obtained from the mirrored decay-length significance fits and after beauty-enrichment.

$\lvert\Delta\phi\rvert$	$d\sigma^b/d\lvert\Delta\phi\rvert$ (pb)	$d\sigma^b_{NLO}/\lvert d\Delta\phi\rvert \otimes C^b_{had}$ (pb)	C^b_{had}
0 : 1.85	$4.3 \pm 2.8^{+\ 1.0}_{-\ 2.3}$	$0.95^{+\ 0.85}_{-\ 0.38}$ (0.90)	0.17
1.85 : 2.2	$66 \pm 14^{+\ 5.5}_{-\ 12}$	$21.7^{+\ 17}_{-\ 8.3}$ (22.0)	0.78
2.2 : 2.5	$127 \pm 22^{+\ 11}_{-\ 8.5}$	$114^{+\ 64}_{-\ 37}$ (127)	0.76
2.5 : 2.75	$361 \pm 34^{+\ 43}_{-\ 25}$	$305^{+160}_{-\ 95}$ (348)	0.71
2.75 : 3.0	$1070 \pm 51^{+340}_{-\ 47}$	1059^{+520}_{-320} (1220)	0.74
3.0 : π	$2211 \pm 110^{+190}_{-\ 93}$	2172^{+280}_{-210} (2646)	0.81

$\lvert\Delta\eta\rvert$	$d\sigma^b/d\lvert\Delta\eta\rvert$ (pb)	$d\sigma^b_{NLO}/d\lvert\Delta\eta\rvert \otimes C^b_{had}$ (pb)	C^b_{had}
0 : 0.4	$419 \pm 25^{+35}_{-20}$	356^{+85}_{-52} (414)	0.76
0.4 : 0.8	$403 \pm 25^{+32}_{-18}$	335^{+79}_{-51} (391)	0.75
0.8 : 1.2	$299 \pm 23^{+29}_{-13}$	289^{+76}_{-42} (341)	0.73
1.2 : 1.8	$218 \pm 17^{+21}_{-11}$	232^{+64}_{-38} (272)	0.73
1.8 : 2.5	$167 \pm 16^{+13}_{-\ 8.1}$	147^{+45}_{-26} (174)	0.77
2.5 : 5.0	$19.2 \pm 4.1^{+\ 1.6}_{-\ 1.6}$	$20.2^{+\ 6.6}_{-\ 4.4}$ (23.6)	0.78

Table D.3: Summary table of differential beauty dijet correlation cross sections as a function of $|\Delta\phi|$ and $|\Delta\eta|$ for events with $Q^2 < 1\,\mathrm{GeV}^2$, $0.2 < y < 0.8$, $P_T^{Jet\,1(2)} > 7(6)\,\mathrm{GeV}$ and $-2.5 \leq \eta^{Jet\,1(2)} < 2.5$ using jets with $-1.6 \leq \eta^{Jet\,1(2)} < 2.5$. Listed are the measurements and the NLO predictions using CTEQ5M as proton PDF including uncertainties as well as the hadronisation correction factors, C_{had}. The NLO predictions in brackets correspond to those using ZEUS-S instead of CTEQ5M.

ΔR	$d\sigma^b/d\Delta R$ (pb)	$d\sigma^b_{NLO}/d\Delta R \otimes C^b_{had}$ (pb)	C^b_{had}
0 : 2.0	$3.2 \pm 2.0^{+\ 0.6}_{-\ 1.2}$	$0.51^{+\ 0.45}_{-\ 0.20}$ (0.48)	0.15
2.0 : 2.5	$79 \pm 13^{+\ 7.1}_{-\ 5.8}$	$28.9^{+\ 18}_{-\ 9.9}$ (30.9)	0.65
2.5 : 3.0	$357 \pm 21^{+32}_{-18}$	$301^{+150}_{-\ 92}$ (344)	0.71
3.0 : 3.5	$767 \pm 31^{+69}_{-41}$	832^{+170}_{-102} (983)	0.78
3.5 : 5.0	$82.8 \pm 8.5^{+\ 6.3}_{-\ 4.1}$	$73.2^{+\ 9.2}_{-\ 5.5}$ (88.9)	0.80

$\lvert\cos\theta^*\rvert$	$d\sigma^b/d\lvert\cos\theta^*\rvert$ (pb)	$d\sigma^b_{NLO}/d\lvert\cos\theta^*\rvert \otimes C^b_{had}$ (pb)	C^b_{had}
0 : 0.2	$853 \pm 50^{+70}_{-41}$	721^{+170}_{-100} (838)	0.76
0.2 : 0.4	$865 \pm 53^{+69}_{-38}$	735^{+170}_{-110} (860)	0.75
0.4 : 0.6	$753 \pm 52^{+72}_{-34}$	743^{+200}_{-120} (875)	0.73
0.6 : 0.8	$780 \pm 59^{+74}_{-40}$	794^{+230}_{-130} (933)	0.75
0.8 : 1.0	$436 \pm 62^{+35}_{-21}$	$430^{+140}_{-\ 86}$ (507)	0.78

M^{jj} (GeV)	$d\sigma^b/dM^{jj}$ (pb/GeV)	$d\sigma^b_{NLO}/dM^{jj} \otimes C^b_{had}$ (pb/GeV)	C^b_{had}
14 : 18	$4.44 \pm 0.64^{+0.70}_{-1.17}$	$3.7^{+1.6}_{-1.2}$ (4.3)	0.13
18 : 22	$41.1 \pm 3.5^{+5.6}_{-6.5}$	$37.7^{+9.3}_{-5.1}$ (44.3)	0.61
22 : 26	$43.6 \pm 3.2^{+4.3}_{-3.5}$	$39.6^{+9.3}_{-5.3}$ (46.9)	0.87
26 : 30	$31.7 \pm 2.4^{+2.9}_{-1.9}$	$28.4^{+7.0}_{-4.0}$ (33.6)	0.94
30 : 35	$24.3 \pm 1.6^{+1.8}_{-1.1}$	$18.4^{+4.6}_{-2.9}$ (21.6)	0.95
35 : 40	$11.6 \pm 1.1^{+2.7}_{-1.3}$	$10.9^{+3.0}_{-1.6}$ (12.8)	0.94
40 : 45	$7.59 \pm 0.96^{+1.20}_{-0.42}$	$6.7^{+1.8}_{-1.1}$ (7.7)	0.94
45 : 100	$0.83 \pm 0.09^{+0.21}_{-0.11}$	$0.93^{+0.26}_{-0.17}$ (1.04)	0.89

Table D.4: Summary table of differential beauty dijet correlation cross sections as a function of ΔR, $|\cos\theta^*|$ and M^{jj} for events with $Q^2 < 1\,\mathrm{GeV}^2$, $0.2 < y < 0.8$, $P_T^{Jet\,1(2)} > 7(6)\,\mathrm{GeV}$ and $-2.5 \leq \eta^{Jet\,1(2)} < 2.5$ using jets with $-1.6 \leq \eta^{Jet\,1(2)} < 2.5$. Listed are the measurements and the NLO predictions using CTEQ5M as proton PDF including uncertainties as well as the hadronisation correction factors, C_{had}. The NLO predictions in brackets correspond to those using ZEUS-S instead of CTEQ5M.

D.3.2 Charm cross sections

$\lvert\Delta\phi\rvert$	$d\sigma^c/d\lvert\Delta\phi\rvert$ (pb)	$d\sigma^c_{NLO}/\lvert d\Delta\phi\rvert \otimes C^c_{had}$ (pb)	C^c_{had}
0 : 1.85	$79 \pm 13\ ^{+\ 12}_{-\ 9.3}$	$8.5^{+\ 24}_{-\ 3.6}$ (8.0)	0.24
1.85 : 2.2	$437 \pm 70\ ^{+\ 83}_{-\ 64}$	$131\ ^{+\ 70}_{-\ 50}$ (138)	0.76
2.2 : 2.5	$1307 \pm 110\ ^{+\ 170}_{-\ 140}$	$717\ ^{+1100}_{-\ 240}$ (814)	0.75
2.5 : 2.75	$3068 \pm 160\ ^{+\ 440}_{-\ 400}$	$1964\ ^{+1200}_{-\ 620}$ (2316)	0.67
2.75 : 3.0	$7740 \pm 240\ ^{+\ 940}_{-\ 780}$	$7170\ ^{+4100}_{-2200}$ (8428)	0.68
3.0 : π	$14934 \pm 430\ ^{+1800}_{-1500}$	$17745\ ^{+1600}_{-1800}$ (21533)	0.72

$\lvert\Delta\eta\rvert$	$d\sigma^c/d\lvert\Delta\eta\rvert$ (pb)	$d\sigma^c_{NLO}/d\lvert\Delta\eta\rvert \otimes C^c_{had}$ (pb)	C^c_{had}
0 : 0.4	$2668 \pm 120^{+330}_{-280}$	$2277^{+1900}_{-\ 370}$ (2693)	0.69
0.4 : 0.8	$2396 \pm 110^{+290}_{-240}$	$2199^{+1400}_{-\ 380}$ (2597)	0.68
0.8 : 1.2	$2604 \pm 110^{+310}_{-260}$	$2029^{+\ 300}_{-\ 350}$ (2397)	0.68
1.2 : 1.8	$2261 \pm 79^{+280}_{-230}$	$1765^{+\ 390}_{-\ 390}$ (2114)	0.69
1.8 : 2.5	$1231 \pm 67^{+160}_{-130}$	$1240^{+\ 960}_{-\ 300}$ (1473)	0.71
2.5 : 5.0	$168 \pm 15^{+\ 21}_{-\ 18}$	$200^{+\ 100}_{-\ 55}$ (244)	0.73

Table D.5: Summary table of differential charm dijet correlation cross sections as a function of $|\Delta\phi|$ and $|\Delta\eta|$ for events with $Q^2 < 1\,\mathrm{GeV}^2$, $0.2 < y < 0.8$, $P_T^{Jet\,1(2)} > 7(6)\,\mathrm{GeV}$ and $-2.5 \leq \eta^{Jet\,1(2)} < 2.5$ using jets with $-1.6 \leq \eta^{Jet\,1(2)} < 2.5$. Listed are the measurements and the NLO predictions using CTEQ5M as proton PDF including uncertainties as well as the hadronisation correction factors, C_{had}. The NLO predictions in brackets correspond to those using ZEUS-S instead of CTEQ5M.

ΔR	$d\sigma^c/d\Delta R$ (pb)	$d\sigma^c_{NLO}/d\Delta R \otimes C^c_{had}$ (pb)	C^c_{had}
0 : 2.0	$52 \pm 11^{+\ 9.0}_{-\ 6.9}$	$4.7^{+\ 3.7}_{-\ 2.0}$ (4.5)	0.22
2.0 : 2.5	$437 \pm 56^{+\ 66}_{-\ 58}$	$179\ ^{+730}_{-\ 63}$ (192)	0.66
2.5 : 3.0	$2726 \pm 100^{+330}_{-320}$	$1841\ ^{+860}_{-550}$ (2169)	0.66
3.0 : 3.5	$5544 \pm 130^{+650}_{-640}$	$5819\ ^{+370}_{-990}$ (6866)	0.70
3.5 : 5.0	$695 \pm 34^{+\ 85}_{-\ 82}$	$757\ ^{+650}_{-140}$ (939)	0.73

$\lvert\cos\theta^*\rvert$	$d\sigma^c/d\lvert\cos\theta^*\rvert$ (pb)	$d\sigma^c_{NLO}/d\lvert\cos\theta^*\rvert \otimes C^c_{had}$ (pb)	C^c_{had}
0 : 0.2	$5405 \pm 230^{+680}_{-570}$	$4620^{+3900}_{-\ 760}$ (5460)	0.69
0.2 : 0.4	$5393 \pm 230^{+650}_{-530}$	$4816^{+3100}_{-\ 830}$ (5680)	0.68
0.4 : 0.6	$6816 \pm 240^{+820}_{-680}$	5391^{+1300}_{-1100} (6327)	0.68
0.6 : 0.8	$7475 \pm 260^{+930}_{-780}$	6200^{+1200}_{-1300} (7561)	0.70
0.8 : 1.0	$3593 \pm 240^{+440}_{-380}$	4117^{+2700}_{-1100} (4887)	0.73

M^{jj} (GeV)	$d\sigma^c/dM^{jj}$ (pb/GeV)	$d\sigma^c_{NLO}/dM^{jj} \otimes C^c_{had}$ (pb/GeV)	C^c_{had}
14 : 18	$164 \pm 12\ ^{+19}_{-19}$	$172\ ^{+97}_{-31}$ (202)	0.35
18 : 22	$384 \pm 15\ ^{+42}_{-36}$	$300\ ^{+47}_{-54}$ (363)	0.74
22 : 26	$299 \pm 12\ ^{+45}_{-35}$	$241\ ^{+46}_{-53}$ (292)	0.85
26 : 30	$200.3 \pm 9.4\ ^{+37}_{-21}$	$166\ ^{+91}_{-34}$ (199)	0.87
30 : 35	$111.8 \pm 6.8\ ^{+30}_{-18}$	$111\ ^{+43}_{-26}$ (135)	0.87
35 : 40	$78.7 \pm 5.1\ ^{+17}_{-11}$	$66\ ^{+30}_{-15}$ (78)	0.88
40 : 45	$45.2 \pm 4.0\ ^{+16}_{-\ 9.3}$	$41.0\ ^{+\ 0.4}_{-10}$ (46.5)	0.87
45 : 100	$5.43 \pm 0.46^{+\ 1.58}_{-\ 0.84}$	$5.26^{+\ 0.40}_{-\ 1.17}$ (6.02)	0.84

Table D.6: Summary table of differential charm dijet correlation cross sections as a function of ΔR, $|\cos\theta^*|$ and M^{jj} for events with $Q^2 < 1\,\mathrm{GeV}^2$, $0.2 < y < 0.8$, $P_T^{Jet\,1(2)} > 7(6)\,\mathrm{GeV}$ and $-2.5 \leq \eta^{Jet\,1(2)} < 2.5$ using jets with $-1.6 \leq \eta^{Jet\,1(2)} < 2.5$. Listed are the measurements and the NLO predictions using CTEQ5M as proton PDF including uncertainties as well as the hadronisation correction factors, C_{had}. The NLO predictions in brackets correspond to those using ZEUS-S instead of CTEQ5M.

Appendix E

Systematics

In this appendix additional figures and information concerning some of the systematic checks discussed in Chapters 9 and 10 are presented. In Section E.1 the dependence of the scaling factors and the ratios with respect to the nominal scaling factors on the significance cut are displayed for all differential cross sections as a function of P_T^{Jet}. The corresponding distributions for η^{Jet} and the five correlation variables are not shown, as they do not contain additional information.

Table E.1 contains the weights for the charm m_{vtx} reweighting as explained in Chapter 10 for all differential P_T^{Jet} and η^{Jet} bins. This procedure was also repeated for the dijet correlation cross sections, but since the calculated weights were of a similar size as the ones listed here, they were not included in the table.

Finally, the variation of the differential beauty and charm cross sections as a function of the energy scale variation is displayed in Section E.3 for all P_T^{Jet} bins. The figures for the differential bins in η^{Jet} and the five correlation variables are again omitted, as they do not provide any further information.

E.1 Fit range

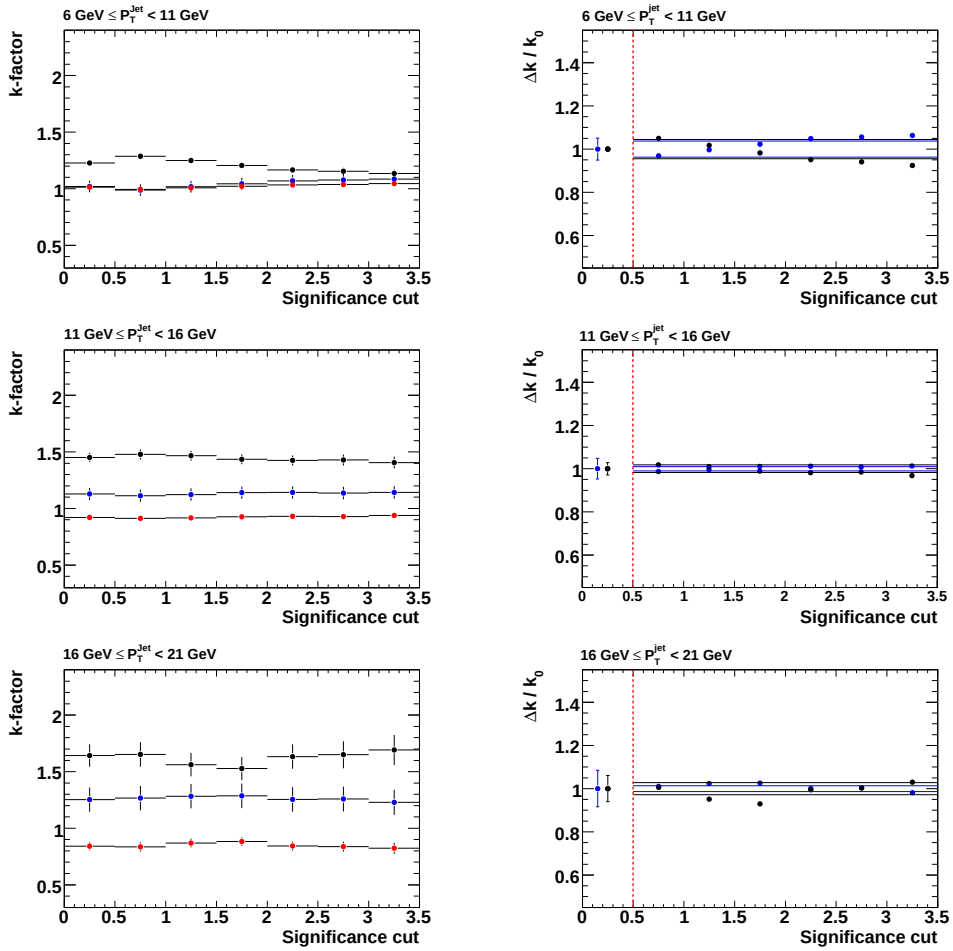

Figure E.1: Dependence of the scaling factors for beauty (blue points), charm (black points) and light flavours (red points) using jets with $6\,\text{GeV} \leq P_T^{Jet} < 11\,\text{GeV}$, $11\,\text{GeV} \leq P_T^{Jet} < 16\,\text{GeV}$ and $16\,\text{GeV} \leq P_T^{Jet} < 21\,\text{GeV}$ as a function of the lower cut on the mirrored decay-length significance, $S^+ - S^-$ (left). On the right, the ratios with respect to the nominal scaling factors, k_0, as well as the average deviations are shown for beauty and charm.

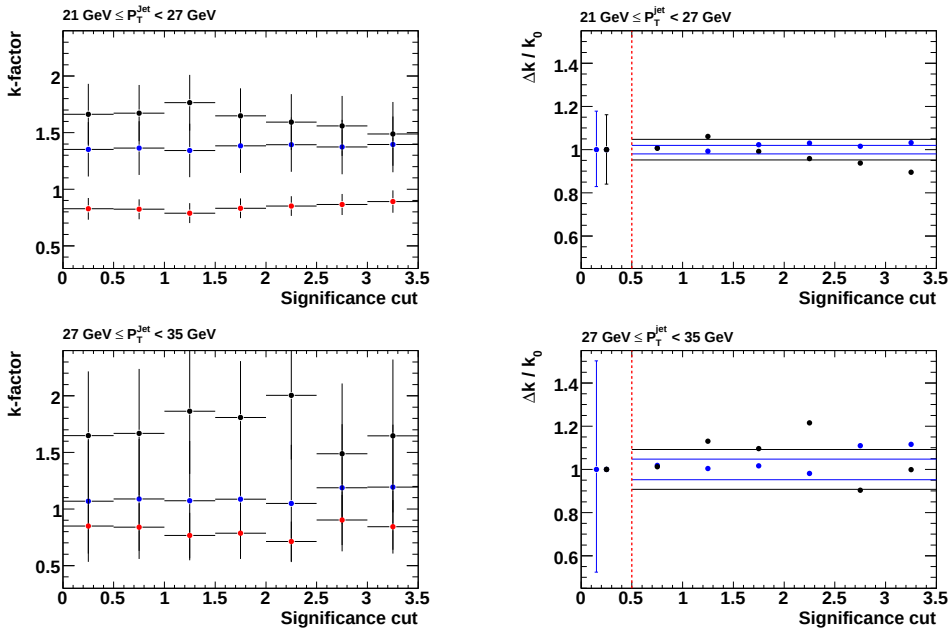

Figure E.2: Dependence of the scaling factors for beauty (blue points), charm (black points) and light flavours (red points) using jets with 21 GeV $\leq P_T^{Jet} <$ 27 GeV and 27 GeV $\leq P_T^{Jet} <$ 35 GeV as a function of the lower cut on the mirrored decay-length significance, $S^+ - S^-$ (left). On the right, the ratios with respect to the nominal scaling factors, k_0, as well as the average deviations are shown for beauty and charm.

E.2 Charm reweighting

	$m_{vtx} \leq 1.4$ GeV	$1.4 \leq m_{vtx} < 2$ GeV	$2 \leq m_{vtx} < 7.5$ GeV
Total	1.05 ± 0.09	1.03 ± 0.11	0.77 ± 0.15
$6 \leq P_T^{Jet} \leq 11$ GeV	0.96 ± 0.08	1.03 ± 0.12	1.14 ± 0.26
$P_T^{Jet} \geq 11$ GeV	1.11 ± 0.25	1.07 ± 0.25	0.76 ± 0.28
$-1.6 \leq \eta^{Jet} \leq 0.1$	1.02 ± 0.16	1.05 ± 0.13	1.08 ± 0.14
$0.1 \leq \eta^{Jet} \leq 0.9$	1.01 ± 0.19	1.02 ± 0.16	0.90 ± 0.19
$0.9 \leq \eta^{Jet} \leq 2.5$	0.91 ± 0.30	0.78 ± 0.24	0.91 ± 0.28

Table E.1: Factors for m_{vtx} reweighting [71].

E.3 Hadronic energy scale

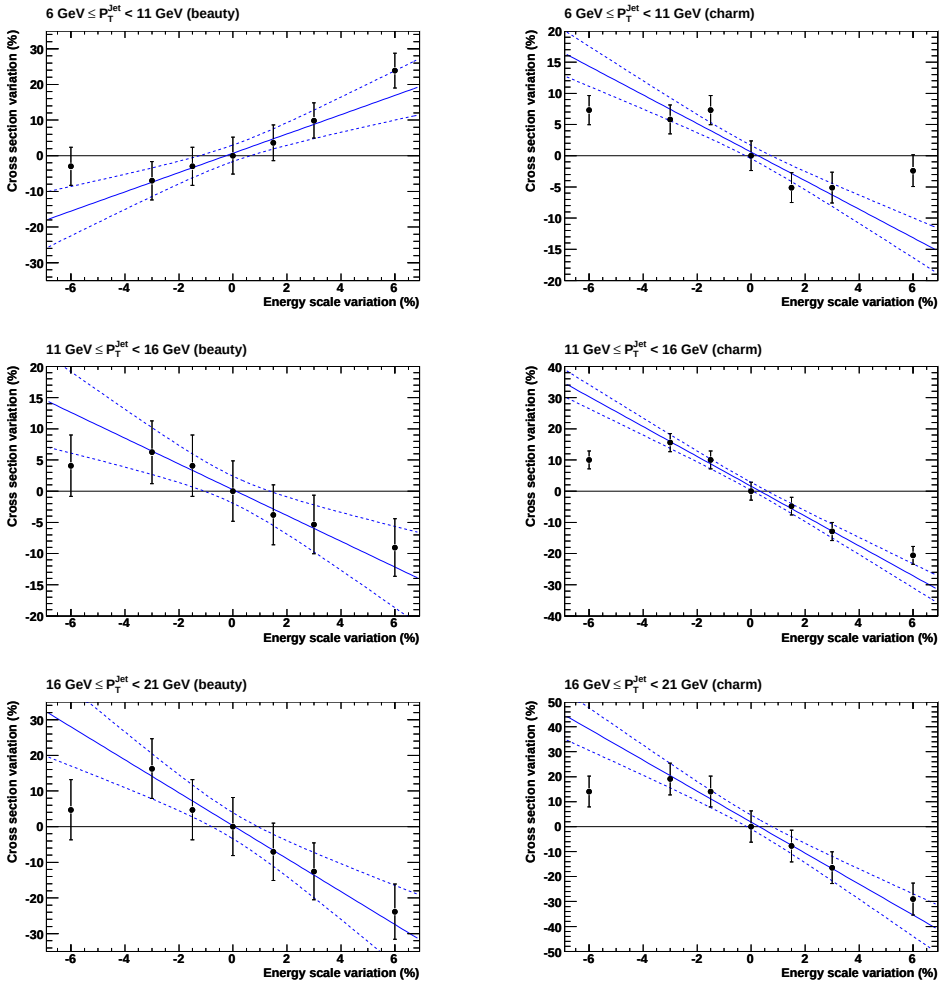

Figure E.3: Variation of the differential beauty (left) and charm (right) cross sections using jets with $6\,\mathrm{GeV} \leq P_T^{Jet} < 11\,\mathrm{GeV}$, $11\,\mathrm{GeV} \leq P_T^{Jet} < 16\,\mathrm{GeV}$ and $16\,\mathrm{GeV} \leq P_T^{Jet} < 21\,\mathrm{GeV}$ as a function of the energy scale variation. The linear fit is denoted by the solid line, its uncertainty by the dashed lines. The points corresponding to an energy scale variation of $\pm 6\,\%$ were excluded from the fits.

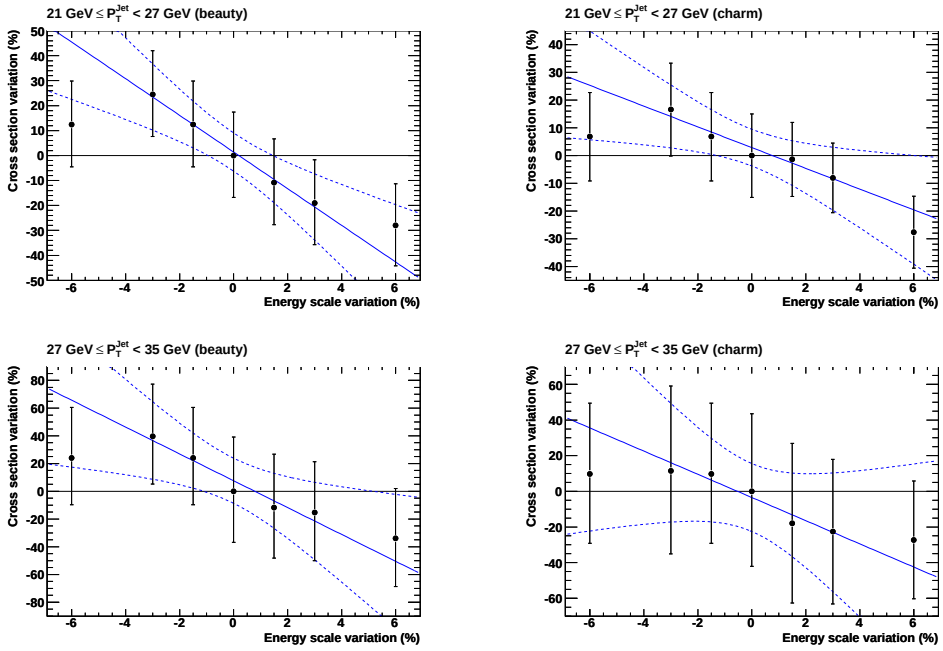

Figure E.4: Variation of the differential beauty (left) and charm (right) cross sections using jets with $21\,\text{GeV} \leq P_T^{Jet} < 27\,\text{GeV}$ and $27\,\text{GeV} \leq P_T^{Jet} < 35\,\text{GeV}$ as a function of the energy scale variation. For further details see the caption of Fig. E.3.

Acknowledgements

An dieser Stelle möchte ich mich gerne bei allen bedanken, die einen maßgeblichen Anteil am Gelingen dieser Doktorarbeit hatten.

In erster Linie danke ich Prof. Dr. Ian Brock dafür, daß er mir die Gelegenheit gegeben hat, nach der Diplomarbeit auch diese Doktorarbeit in seiner Gruppe zu schreiben, für seine kontinuierliche Unterstützung und auch für die Möglichkeit, im Rahmen meiner Arbeit an zahlreichen Konferenzen teilnehmen zu dürfen. Meinen weiteren Prüfern Herrn Prof. Dr. Wermes, Herrn PD Dr. Metsch und Herrn Prof. Dr. Cremers danke ich, daß sie sich als Mitglieder der Prüfungskomission und für die Bewertung meiner Arbeit zur Verfügung gestellt haben.

Des weiteren möchte ich mich bei den jetzigen und ehemaligen Kollegen aus der Arbeitsgruppe, die mich während meiner Arbeit sehr unterstützt haben, bedanken. Besonders nennen möchte ich in diesem Zusammenhang Oliver Kind, der den Grundstein für die Bonner Heavy-Flavour-Analysen gelegt hat und der trotz des Wechsels nach Berlin immer für Fragen und Diskussionen offen war. Detlef Bartsch gebührt ebenfalls ein großer Dank für viele hilfreiche Anregungen, Diskussionen und unermüdliches Korrekturlesen - und nicht zuletzt für die nötige Ablenkung durch regelmäßige Laufrunden. Bedanken möchte ich mich auch bei Torsten Held, der mit seiner Bachelorarbeit einen großen Beitrag zu dieser Analyse geleistet hat.

Namentlich erwähnen möchte ich weiterhin Markus Jüngst, Thomas Loddenkötter, Sebastian Mergelmeyer, Roger Renner, Jan Stillings und Robert Zimmermann - sie alle haben zusammen mit den bereits genannten für eine sehr angenehme Atmosphäre in der Arbeitsgruppe gesorgt und sind zu einem guten Teil schuld daran, daß mir meine Arbeit meist viel Freude bereitet hat.

Die zwei Jahre, die ich am DESY in Hamburg verbracht habe, möchte ich in keinem Fall missen, was nicht zuletzt an den "Desyanern" selber liegt. In diesem Sinne möchte ich mich bei Ana Yagües dafür bedanken, daß sie mit mir zusammen an dieser Analyse, die doch sehr viel Durchhaltevermögen und gute Nerven gefordert hat, arbeitet. Benjamin Kahle und Philipp Roloff danke ich für viele Diskussionen und Anregungen sowie interessante und aus-

gelassene Kaffeepausen und Kneipenabende.

Furthermore I'd especially like to thank Monica Turcato, Sasha Spiridonov and Andrea Parenti for their help concerning tracking-related issues, for providing MC samples and for their continuous support. Many thanks to all HFL coordinators, in particular Achim Geiser, for useful advice and helpful discussions.

Zu guter Letzt gebührt ein großer Dank meinen Eltern, die mich während der gesamten Doktorarbeit sehr unterstützt haben, in den besonders stressigen Zeiten eine enorme Geduld mit mir bewiesen und sich immer mitgefreut oder mitgelitten haben.

List of Figures

List of Tables

Bibliography

[1] ZEUS Collaboration, *The ZEUS Detector*. Status Report 1993

[2] H1 Collaboration, I. Abt et al., *The H1 detector at HERA. Nucl. Instr. and Meth.* **A386**, (1997) 310

[3] K. Ackerstaff et al., *The HERMES Spectrometer. Nucl. Instr. and Meth.* **A417**, (1998) 230 [arXiv:hep-ex/9703005]

[4] HERA-B Collaboration, E. Hartouni et al., *HERA-B Design Report*. DESY-PRC-95-01 (1995);

HERA-B Collaboration, *HERA-B Status Report*. DESY-PRC-00-04 (2000)

[5] ZEUS Coll., S. Chekanov et al., *Measurement of the Longitudinal Proton Structure Function at HERA. Phys. Lett.* **B 682**, (2009) 8

H1 Coll., F.D. Aaron et al., *Measurement of the Proton Structure Function $F_L(x, Q^2)$ at Low x. Phys. Lett.* **B 665**, (2008) 139

[6] E. Koffeman, *Mechanical Design and Construction of the ZEUS Microvertex Detector*. ZEUS-Note 00-028, October 2000

[7] M. Eckert, *TFRECON for F/RTD in Data Reprocessing 1996: Chamber Condition, Reconstruction and Output Information*. ZEUS-Note 97-027, April 1997

[8] I.C. Brock, V. Bashkirov et al. *A Straw-Tube Tracker for ZEUS*. ZEUS-Note 98-046, June 1998

[9] V. Schönberg, *Der ZEUS Straw-Tuber-Tracker - Auswertung erster Daten, Effizienzbestimmung und Anpassung der Simulation*. Diplom Thesis, Universität Bonn, November 2005

[10] S.M. Fisher, P. Palazzi *The ADAMO Data System, Programmers Manual - Version 3.2*. January 1992

M.G. Green, *The ADAMO Data System, An introduction for particle physicists*. ZEUS-Note 89-027, March 1987

[11] P. Bellan, A. Bertolin, R. Brugnera, M. Turcato, *The GTT05 SLT Filter*. ZEUS-Note 04-004, June 2004

[12] S.L. Glashow, *Partial-symmetries of weak interactions. Nucl. Phys. 22* (1961) 579

[13] S. Weinberg, *A Model of Leptons. Phys. Rev. Lett. 19* (1967) 1264

[14] D. Griffiths, *Introduction to elementary particles*. John Wiley & Sons, Inc. (1987)

[15] F. Halzen and A.D. Martin, *Quarks and Leptons: An Introductory Course in Modern Particle Physics*. John Wiley & Sons, Inc. (1984)

[16] C. Amseler (Particle Data Group), *Physics Letters* **B 667**, 1 (2008)

[17] DØ Collaboration, V.M. Abazov et al., *Determination of the strong coupling constant from the inclusive jet cross section in $p\bar{p}$ collisions at $\sqrt{s} = 1.96\,\text{TeV}$.* (2009) [arXiv:0911.2710v2]

[18] R.K. Ellis et al., *Perturbation Theory and the Parton Model in QCD. Nucl. Phys.*, **B 152** (1979) 285

[19] V. Gribov and L. Lipatov, *Deep inelastic ep scattering in perturbation theory.* , *Sov. J. Nucl. Phys.*, **15** (1972) 438

G. Altarelli and G. Parisi, *Asymptotic Freedom in Parton Language. Nucl. Phys.*, **B 126** (1977) 298

G. Altarelli, *Partons in quantum chromodynamics. Phys. Rep.*, **81** (1982) 1

L.N. Lipatov, *The parton model and perturbation theory. Sov. J. Nucl. Phys.*, **20** (1975) 94

Y.L. Dokshitzer, *Calculation of the Structure Functions for Deep Inelastic Scattering and e^+e^- Annihilation by Perturbation Theory in Quantum Chromodynamics. Sov. Phys. JETP*, **46** (1977) 641

[20] ZEUS Coll., S. Chekanov et al., *An NLO QCD Analysis of Inclusive Cross-Section and Jet-Production Data from the ZEUS Experiment. Eur. Phys. J.* **C 42**, (2005) 1

[21] H1 and ZEUS Coll., *Combined Measurement and QCD Analysis of the Inclusive $e^{\pm}p$ Scattering Cross Sections at HERA. DESY-Report* DESY 09-158 (2009)

[22] M. Jüngst, Private communication.

[23] B.J. Björken and S.L. Glashow, *Elementary Particles and SU(4). Phys. Lett.*, **11** (1964) 255

S.L. Glashow, J. Iliopoulos and L. Maiani, *Weak Interactions with Lepton-Hadron Symmetry. Phys. Rev.*, **D 2** (1970) 1285

[24] T. Sjöstrand et al., *High-energy physics event generation with PYTHIA 6.1. Comp. Phys. Comm.* **135**, (2001) 238

[25] CTEQ Coll., H.L. Lai et al., *Global QCD analysis of parton structure of the nucleon: CTEQ5 parton distributions. Eur. Phys. J.* **C 12**, (2000) 375

[26] M. Glück, E. Reya and A. Vogt, *Photonic parton distributions*, *Phys. Rev.* **D 46**, (1992) 1973

[27] B. Andersson et al., *Parton Fragmentation and String Dynamics. Phys. Rep.* **97**, (1983) 31

[28] B.R. Webber, *A QCD Model for Jet Fragmentation Including Soft Gluon Interference. Nucl. Physics* **B 238**, (1984) 492

[29] G. Marchesini et al., *HERWIG: A Monte Carlo event generator for simulating hadron emission reactions with interfering gluons. Comp. Phys. Comm.* **67**, (1992) 465

[30] C. Peterson et al., *Scaling violations in inclusive e^+e^- annihilation spectra. Phys. Rev.* **D 27**, (1983) 105

[31] ARGUS Collaboration, H. Albrecht et al., *Inclusive production of D^0, D^+ and $D^*(2010)^+$ mesons in B decays and nonresonant e^+e^- annihilation at* 10.6 GeV. *Z. Phys.*, **C 52** (1991) 353

ARGUS Collaboration, H. Albrecht et al., *Production of D_s^+ mesons in B decays and determination of f_{D_s}. Z. Phys.*, **C 54**, (1992) 1

CLEO Collaboration, D. Bortoletto et al., *Charm production in non-resonant e^+e^- annihilations at $\sqrt{s} = 10.55$ GeV. Phys. Rev.*, **D 37** (1988) 1719

OPAL Collaboration, K. Ackerstaff et al., *Measurement of $f(c \to D^{*+}X)$, $f(b \to D^{*+}X)$ and $\Gamma_{c\bar{c}}/\Gamma_{had}$ using $D^{*\pm}$ mesons. Eur. Phys. J.*, **C 1** (1998) 439

OPAL Collaboration, K. Ackerstaff et al., *Measurements of flavour-dependent fragmentation functions in $Z^0 \to q\bar{q}$ events. Eur. Phys. J.*, **C 7** (1999) 369

ALEPH Collaboration, R. Barate et al., *Study of charm production in Z decays. Eur. Phys. J.*, **C 16** (2000) 597

DELPHI Collaboration, P. Abreu et al., *Determination of $P(c \to D^{*+})$ and $BR(c \to l^+)$ at LEP 1. Eur. Phys. J.*, **C 12** (2000) 209

ZEUS Collaboration, S. Chekanov et al., *Measurement of the charm fragmentation function in D^* photoproduction at HERA. Eur. Phys. J.*, **C 12** (2000) 209

[32] B. Andersson, G. Gustafson and B. Söderberg, *A General Model for Jet Fragmentation. Z. Phys.* **C 20**, (1983) 317

[33] O.M. Kind, Private communication.

[34] T. Haas, *Generating Monte Carlo Events with MOZART* (unpublished). ZEUS-Note 92-021, February 1992

[35] R. Brun et al. *Geant 3, Technical Report.* CERN-DD/EE/84-1, CERN, 1987

[36] A. Parenti, Private communication.

[37] L. Wai and R. Yoshida, *Running MOZART-ZGANA-ZEPHYR chain using FUNNEL and Monte Carlo Environment (FMCE) for ZOW cluster* (unpublished). ZEUS-Note 93-065, June 1993

[38] S. Frixione et al., *Heavy quark correlations in photon-hadron collisions. Nucl. Phys.* **B 412**, (1994) 225

[39] I.C. Brock, Private communication.

[40] ZEUS Collaboration, *A ZEUS next-to-leading-order QCD analysis of data on deep inelastic scattering. Phys. Rev.* **D 67**, (2003)

[41] G. Hartner, *VCTRAK: STT(+CTD)+MVD Combined Pattern Recognition* (unpublished). Talk at ZEUS Collaboration Meeting, October 2005

[42] A. Spiridonov, *Mathematical Framework for Fast and Rigorous Track Fit for the ZEUS Detector. DESY-Report* DESY 08-182 (2008) [arXiv:0812.1245v1]

[43] G. Hartner, *VCTRAK Briefing, Program and Math.* ZEUS-Note 98-058, August 1998

[44] D. Nicholass, J. Loizides *The Reprocessed Beamspot* (unpublished). Talk at ZEUS Heavy Flavour Meeting, May 2006

[45] H. Stadie, *DAF Primary Vertex Reconstruction* (unpublished). Talk at ZEUS Collaboration Meeting, June 2006

[46] H. Stadie, *New Vertex Reconstruction Tools* (unpublished). Talk at ZEUS Tracking Meeting, August 2006

[47] H. Stadie, *Global Fitting of Vertex Final States* (unpublished). Talk at ZEUS Collaboration Meeting, October 2006

[48] ZEUS Collaboration, S. Chekanov et al., *Measurement of beauty production in deep inelastic scattering at HERA. Physics Letters* **B 599** (2004) 173

[49] ZEUS Collaboration, S. Chekanov et al., *Beauty photoproduction measured using decays into muons in dijet events in ep collisions at* $\sqrt{s} = 318\,\mathrm{GeV}$. *Phys. Rev.* **D 70** (2004) 012008

[50] ZEUS Collaboration, S. Chekanov et al., *Measurement of beauty photoproduction using decays into muons in dijet events at HERA. JHEP* **04** (2009) 133

[51] ZEUS Collaboration, S. Chekanov et al., *Beauty photoproduction using decays into electrons at HERA. Phys. Rev.* **D 78** (2008) 072001

[52] ZEUS Collaboration, S. Chekanov et al., *Measurement of open beauty production at HERA in the* $D^*\mu$ *final state. Eur. Phys. J.* **C 50**, (2007) 299

[53] H1 Collaboration, C. Adloff et al., *Measurement of Open Beauty Production at HERA. Physics Letters* **B 467**, (1999) 156

H1 Collaboration, A. Aktas et al., *Measurement of Beauty Production at HERA Using Events with Muons and Jets. Eur. Phys. J* **C 41**, (2005) 453

H1 Collaboration, A. Aktas et al., *Measurement of Charm and Beauty*

Photoproduction at HERA using $D^*\mu$ Correlations. Physics Letters **B 621**, (2005) 56

[54] ATLAS Collaboration, G. Aad et al., *Expected Performance of the ATLAS Experiment - Detector, Trigger and Physics.* CERN-OPEN-2008-020, Geneva (2008) [arXiv:0901.0512]

[55] M. Turcato, (unpublished). Talk at ZEUS Tracking Meeting, 2008

[56] M. Turcato, Private communication.

[57] T. Haas, *MVD Hit Resolution in the MC* (unpublished). Talk at ZEUS Physics Coordinators Meeting, March 2008

[58] N. Tuning, *ZUFOs: Hadronic final state reconstruction with calorimeter, tracking and backsplash correction.* ZEUS-Note 01-021, June 2001

[59] J. Chay and S.D. Ellis, *Cone Algorithm Jets in e^+e^- Collisions. Phys. Rev.* **D 55** (1997) 2728

S.D. Ellis, J. Huston and M. Tönnesmann, *On Building Better Cone Jet Algorithms. eConf C010630* (2001) 513

S. Catani, Y.L. Dokshitzer and B.R. Webber, *The K-perpendicular clustering algorithm for jets in deep inelastic scattering and hadron collisions. Phys. Lett.* **B 285** (1992) 291

S. Catani et al., *Longitudinally invariant K(t) clustering algorithms for hadron hadron collisions. Nucl. Phys.* **B 406** (1993) 187

M.H. Seymour, *Jets in QCD.* In *Proceedings for the* 10^{th} *Topical Workshop on Proton-Antiproton Collider Physics* (1995) [arXiv:hep-ph/9506421v2]

Y.L. Dokshitzer et al., *Better Jet Clustering Algorithms. JHEP* **9708** (1997) 1

S. Moretti, L. Lönnblad and T. Sjöstrand, *New and Old Jet Clustering Algorithms for Electron-Positron Events. JHEP* **9808** (1998) 1

[60] M. Cacciari, G.P. Salam and G. Soyez, *The anti-k_t jet clustering algorithm. JHEP*, **0804** (2008) 63

[61] G. Soyez, *The SISCone and anti-k_t jet algorithms.* (2008) [arXiv:0807.0021v1]

[62] S. Lammers and D. Chapin, *Jet Energy Scale Uncertainty.* ZEUS-Note 01-006, March 2001

[63] S. Boutle, Private communication.

[64] A. Lopez-Duran Viani and S. Schlenstedt, *Electron finder efficiencies and impurities. A comparison between SINISTRA95, EM and EMNET.* ZEUS-Note 99-077, Revised version, July 2000

[65] F. Jaquet and A. Blondel, in *Proceedings of the study of an ep facility for Europe*, (1979) 391, DESY-79/48

[66] A.G. Yagües Molina, *Study of Beauty Photoproduction with the ZEUS Experiment at the Electron-Proton Collider HERA.* Ph.D. Thesis, Humboldt-Universität zu Berlin, 2008

[67] A. Geiser, *Suggestion for decay length smearing* (unpublished). Talk at ZEUS Heavy Flavour Meeting, 26th March 2009

[68] A.G. Yagües Molina, Private communication.

[69] A.G. Yagües Molina, *Study of trigger efficiencies* (unpublished). Talk at ZEUS Heavy Flavour Meeting, July 2009

[70] A.G. Yagües Molina, *Beauty PhP with Inclusive Secondary Vertices* (unpublished). Talk at ZEUS Heavy Flavour Meeting, August 2009

[71] S. Mergelmeyer, Private communication.

[72] S. Mergelmeyer, Diplom Thesis in preparation, Universität Bonn, 2010.

[73] C. Glasman, *Rate studies in HERA II data* (unpublished). Talk at QCD Meeting, April 2008

[74] M. Wlasenko, *Measurement of neutral current deep inelastic e^+p scattering cross sections with longitudinally polarized positrons with ZEUS at HERA.* Ph.D. Thesis, Universität Bonn, Report BONN-IR-2009-05, 2009.

[75] R.Mankel, *Mathematical Framework for Alignment of the ZEUS Micro-Vertex Detector.* ZEUS-Note 07-002, 2007.

[76] O.M. Kind, *Production of Heavy Flavours with Associated Jets at HERA.* Ph.D. Thesis, Universität Bonn, BONN-IR-06-01, 2006

[77] U. Samson, *Beauty Photoproduction using Decays into Muons at HERA.* Ph.D. Thesis, Universität Bonn, BONN-IR-2008-06, 2008

[78] ZEUS Collaboration, S. Chekanov et al., *Measurement of beauty production from dimuon events at HERA*. *JHEP* **02** (2009) 032

[79] T. Held, *Dijet-Korrelationen in Photoproduktions-Ereignissen mit Beauty-Quarks bei HERA*. Bachelor Thesis, Universität Bonn, 2009

[80] A. Spiridonov, *MVD Hit Residuals with MC and Data* (unpublished). Talk at ZEUS Collaboration Meeting, February 2008